School of Engineering

PhD Thesis

Advanced polarization control for optimizing ultrafast laser micro-processing

Thesis submitted in accordance with the requirements of the University of Liverpool for the degree of Doctor in Philosophy

by

Olivier Allègre

February 2013

Declaration

I hereby declare that all the work contained within this dissertation has not been submitted for any other qualification.

Signed:

Date:

Summary

The ability to control and manipulate the state of polarization of a laser beam is becoming an increasingly desirable feature in a number of industrial laser micro-processing applications. Being able to control polarization would enable the improvement of the efficiency and quality of processes such as the drilling of holes for fuel-injection nozzles, the processing of silicon wafers or the machining of medical stent devices.

This thesis presents novel, liquid-crystal-based optical setups for controlling the polarization of ultrafast laser beams, and demonstrates how such optical setups can be used to improve laser micro-processing efficiency and quality. Two experimental strategies were followed: the first used dynamic control of the polarization direction of a linearly polarized beam; the second generated beams with complex polarization structures. Novel optical analysis methods were used to map the polarization structures in the focal region of these laser micro-processing setups, using Laser Induced Periodic Surface Structures (LIPSS) produced on stainless steel sample surfaces at low laser fluence (around 1.5J/cm^2), close to the ablation threshold of steel (i.e. 0.16J/cm^2). This helped to characterize and calibrate the optical setups used in this thesis.

The first experimental method used a fast-response, analogue, liquid-crystal polarization rotation device to dynamically control the direction of linear polarization of a laser beam during micro-processing. Thanks to its flexibility, the polarization rotator could be set-up in various synchronized configurations, for example keeping the polarization direction constantly perpendicular to the beam scanning motion. Drilling and cutting tests were performed on thin (~0.4mm thick) stainless steel sheets using a 775nm femtosecond laser at 24J/cm^2. The experimental results showed a consistent improvement in the micro-processing quality when the polarization direction was synchronized with the beam scanning motion. The sidewall surface roughness and edge quality of the machined structures were improved significantly, with the dimensions of ripples and distortions divided by a factor of two. The overall processing efficiency was also increased compared to that produced by linear or circular polarizations.

The second experimental method used a digital, Liquid-Crystal On Silicon (LCOS) Spatial Light Modulator (SLM) to generate polarization structures with a cylindrical geometry, or Cylindrical Vector Beams (CVBs). A Jones matrix analysis was used to model the optical setup and predict the ability to produce CVBs in this way. The setup was implemented in a 775nm femtosecond laser micro-processing bench and the resulting polarization analyzed with a polarizing filter, demonstrating a polarization purity better than 84%. The amplitude and polarization properties in the focal region of the setup were studied using LIPSS produced on the surface of stainless steel samples at low fluence (1.5J/cm^2), to check that the expected state of polarization had been achieved. An analytical model of the experimental setup was developed to explain the experimental results. The model predictions were in agreement with the

experimental results and clarified how the polarization and phase structures affect the focal properties of the produced laser beams.

Various types of CVBs were used with a high laser beam fluence (24J/cm²) for micro-machining 0.2-0.4mm thick stainless steel plates. A comparative analysis of micro-machining with radially, azimuthally, circularly and linearly polarized beams was carried out. It was shown that a radially polarized beam was more efficient at drilling and cutting high-aspect-ratio features when the plate thickness was above 0.2mm. The gain in processing speed was better than 5% compared with a circularly polarized beam and better than 10% compared with an azimuthally polarized beam, under the chosen processing parameters. However the processing speed was similar for all these polarization states (radial, azimuthal and circular) when machining 0.2mm thick plates. It was also shown that a radially polarized beam improved the processing quality, reducing the distortions affecting the edge quality of the machined structures.

List of publications to date by author

Allegre O. J., Perrie W., Edwardson S. P., Dearden G., Watkins K. G., 2012, *Laser microprocessing of steel with radially and azimuthally polarized femtosecond vortex pulses*, J. Optics **14** (8): 085601

Allegre O. J., Perrie W., Bauchert K., Liu D., Edwardson S. P., Dearden G., Watkins K. G., 2012, *Real-time control of polarisation in ultra-short-pulse laser micro-machining*, Appl. Phys. A **107** (2): 445-454

Allegre O. J., Perrie W., Edwardson S. P., Dearden G., Watkins K. G., 2011, *Ultra-short pulse laser micro-machining of metals with radial and azimuthal polarization*, Proc. ICALEO **2011**: 917-925

Allegre O. J., Perrie W., Bauchert K., Dearden G., Watkins K. G., 2010, *Real-time control of polarisation in high-aspect-ratio ultra-short-pulse laser micro-machining*, Proc. ICALEO **2010**: 1426-1433

Allegre O. J., Perrie W., Bauchert K., Liu D., Edwardson S. P., Dearden G., Watkins K. G., 2010, *Real-time control of polarization in ultra-short pulse laser micro-processing*, Proc. MATADOR **2010**: 553-556

Croft J., Edwardson S. P., Williams C. J., Allegre O. J., Dearden G., Watkins K. G., 2010, *Embedding arrays of microspheres with optical trapping for micro scale device manufacture*, Proc. ICALEO **2010**: 1450

Acknowledgements

I would like to thank Ken Watkins (my primary supervisor), Geoff Dearden, Stuart Edwardson and Walter Perrie, who have an inexhaustible supply of scientific insight and enthusiasm, which has meant that my Ph.D. has been not only interesting, but also enjoyable.

It is impossible to spend four years at the Laser Group without appreciating Doug Eckford, who has persistently made sure that the computers are running smoothly, as well as Eamonn Fearon who has tirelessly ensured the smooth running of the Lairdside Laser Engineering Centre, where most of the experimental work has been done. It has been lovely to meet and work alongside so many members of the Laser Group.

On a more personal note, I would like to thank Mary, as well as my family and friends for their unwavering support and acknowledge my proof-readers: Mary, my father and Walter Perrie (who all carefully red this thesis).

Contents

1 Introduction

1.1 Background to laser technology

The laser is undoubtedly the most important optical technology to be developed in the past 60 years. Soon after Theodore Maiman demonstrated the first ruby laser in 1960, there were tremendous developments in the field of laser technology. As a result, a wide range of basic laser applications quickly appeared in various domains such as surgery, bar-code scanning, telecommunication and industrial manufacturing (S. Perkowitz, 2010). The latter is the focus of this thesis.

1.1.1 Principle of the laser

A laser is a device that emits coherent electromagnetic radiation in the infrared, visible or ultraviolet spectrum, through a process of optical amplification based on the stimulated emission of photons. A laser is constructed from three principal elements: an energy source, a gain medium and an optical cavity (Figure 1.1).

- The energy source (also referred to as pump source) provides energy to the laser system. The energy source can be for example an electrical discharge, or the light from a flash lamp or another laser.
- The gain medium is a material (either a gas, liquid or solid) with optical properties that determines the characteristics of the laser light, such as its wavelength. Each electron in the gain medium carries some energy. Quantum mechanical effects dictate that electrons can only carry discreet energy levels. At a given time, an electron carries a defined level of energy, within the set of energy levels allowed by the material. In a laser gain medium, the electrons can be either in a ground state (they carry a minimum level of energy), or in an excited state (they carry a higher level of energy). The difference between the energy levels of the ground and excited states determines the wavelength of a laser. Typically, a laser gain medium does not have one, but multiple excited states (i.e. a multitude of allowed energy levels).
- The optical cavity (also referred to as optical resonator) is a set of mirrors placed around the gain medium so that photons can travel back and forth through it. Typically in a simple two-mirrors optical cavity, one of the mirrors is highly reflective and the other is partially reflective to allow some of the light to leave the cavity. It is noted that optical cavities can also use a more complex configuration, for example a ring cavity.

The laser is operated by pumping the gain medium i.e. transferring energy from the energy source to the gain medium. In this way, the gain medium becomes excited, with a large share of its electron population in an excited state. Typically, photons are initially emitted in the gain medium through a process of spontaneous emission. They are then amplified through a process of stimulated emission,

where the electrons in an excited states transfer their energy to incoming photons, producing more photons as a result (these electron-photon energy transfers are also called lasing transitions). The photons are reflected by the mirrors of the optical cavity, so that they travel back into the gain medium where they produce more stimulated emission. The photons may reflect back and forth inside the cavity many hundred times before exiting the cavity, through a partially reflective cavity mirror for example.

Although in principle lasers produce monochromatic light (electromagnetic radiation of a single wavelength), most lasers actually produce radiation in several modes, each having a slightly different frequency (wavelength). Some lasers even produce radiation in a wide spectral range, as much as 20nm in some cases. Lasers can operate in continuous mode, where the output beam power is constant over time. Such lasers are known as continuous wave lasers (CW lasers). Lasers can also operate in pulsed mode.

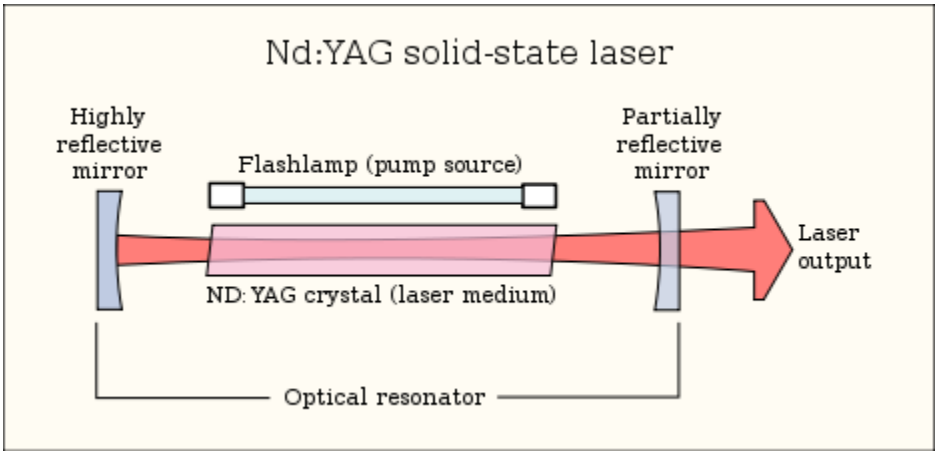

Figure 1.1: Schematic showing the three main elements in a laser, here a Nd:YAG laser. The energy source is a flash lamp. It is located next to the gain medium, here a Nd:YAG crystal. The flash lamp transfers energy to the electrons of the Nd:YAG crystal, so that they acquire a higher energy level. Photons are first emitted through spontaneous emission and then gradually amplified through stimulated emission, as they travel back and forth between the mirrors of the optical cavity. One of the mirrors is partially reflective and lets some of the optical radiation leave the cavity.

1.1.2 Industrial laser manufacturing

Right from the outset, the potential usefulness of laser-material interactions in industrial manufacturing applications was envisaged. Industrial laser manufacturing generally involves focusing a laser beam to melt or ablate material in a work-piece. Theoretical and experimental studies were soon undertaken to better understand these interactions. For industrial manufacturing processes such as cutting, welding and surface treatment, the quality of the laser source is of primary importance. In particular, achieving a good process efficiency requires the use of laser sources that produce a high average-power.

1.1.2.1 High-average-power laser sources for industry

Two early laser technologies demonstrated such high-average-power: CO_2 laser sources (which were first demonstrated by C. K. N. Patel, 1964) and Nd:YAG laser sources (first demonstrated by J. E. Geusic *et al.* 1964). Both technologies can produce continuous or pulsed output beams and work in the infrared spectrum (10.6µm for the CO_2 laser and 1.06µm for the Nd:YAG laser). CO_2 laser sources started being adopted in industry in the late 1960s, followed by the Nd:YAG laser sources in the 1970s.

Another technology, the Excimer laser (first demonstrated by N. Basov *et al.* 1970), produces a high-average-power, pulsed output beam in the ultraviolet spectrum. Excimer laser sources started being adopted for semiconductor wafer processing applications in the microelectronics industry from the early 1980s. In particular, the Excimer laser lithography technique, which was first demonstrated by K. Jain *et al.* (1982), is now arguably the only widely used technology for the manufacturing of microelectronic devices.

An additional technology, the laser diode, was initially demonstrated by both R. N. Hall *et al.* (1962) and M. I. Nathan *et al.* (1962). The laser diode started being used in telecommunication and information technologies from the 1980s. Since 1990, technology improvements enabled diode lasers to produce high-average-power beams. This led to their use for solid-state laser cavity pumping and enabled the advent of Diode-Pumped Solid-State (DPSS) lasers (J. Hecht, 2010). This also led to the use of laser diodes as direct sources for industrial processing applications such as surface hardening and welding, with diode arrays generating as much as 100W in average power, in continuous mode (first demonstrated by M. Sakamoto *et al.* 1992).

1.1.2.2 Emergence of integrated industrial laser processing systems

Apart from a high-average-power laser source, high-quality industrial laser processing also requires advanced beam quality control, in-process optimization of the output power and beam delivery, etc... All these areas saw rapid technological developments in the 1960s and 1970s (W. M. Steen, 1991; R. Crafer & P. J. Oakley, 1993).

Moreover, progress was being made in the understanding of laser-material interactions. These interactions are strongly dependant on the laser process parameters (fluence, wavelength, temporal pulse length, etc…) and the material properties (metals, semiconductors, etc…). These developments enabled the appearance of fully integrated laser processing systems (W. M. Steen, 1991; R. Crafer & P. J. Oakley, 1993). Thanks to accurate control of the process, precision manufacturing could be achieved at high speed. This led to the widespread use of laser manufacturing in the aerospace, automotive or textile industries for example.

1.1.2.3 Emergence of high-precision industrial laser micro-processing

Another area of development for industrial laser manufacturing is in high-precision micro-applications (for example in the microelectronics, photonics or medical industries), where ever more accurate processes are required. This fueled the development of short-pulse lasers, with pulse lengths in the nanosecond range. By concentrating the available energy into short time intervals, these short-pulse lasers provide a higher peak-power and enable a more accurate control of laser-material interactions. This, in turn, increases the machining quality by reducing recast and molten material during processing (D. Breitling *et al.* 2004a). A variety of such nanosecond-pulse laser sources have been developed since the 1980s. These include for example the Q-switched Nd: YAG lasers, the ytterbium-doped fiber lasers (J. Hecht, 2010), or the thin-disk lasers (first demonstrated by J. A. Abate *et al.* 1981).

More recently, laser sources producing pulse lengths in the picosecond and femtosecond range, referred to as ultrashort-pulse or ultrafast lasers, have been developed (A. Cavalieri, 2010). Laser sources producing ultrashort pulses include for example the titanium-doped sapphire laser (first introduced in P. F. Moulton, 1986), the fiber laser or the thin-disk laser. This has enabled even higher precision micro- and nano-manufacturing applications to be developed. Picosecond-pulse lasers are now explored in industries that typically require a very high process quality, as the ultrashort timescale on which laser energy is coupled to the material ensures sub-micron precision processing can be achieved with very little thermal damage. Potential future applications include for example the scribing of photovoltaic cells, the patterning of flexible displays and the fabrication of medical stent devices (N. H. Rizvi, 2003).

1.2 Introduction to ultrafast laser micro-processing

A laser source that produces light pulses with a duration in the picoseconds (10^{-12} s) or femtosecond (10^{-15} s) range is referred to as an ultrafast, or ultrashort-pulse laser. Shortly after their invention (P. F. Moulton, 1986), ultrafast lasers were mostly used for ultrafast spectroscopic applications, where their incredibly short pulse length facilitated the study of how the energy states and electron dynamics of molecules affect complex chemical or biological processes (A. Cavalieri, 2010). However it quickly emerged that their high peak power and very short laser-material interaction duration could also be beneficial to micro-manufacturing applications.

Producing such pulse durations at the level of pulse energy required for micro-manufacturing processes is generally achieved with a combination of advanced optical techniques, such as mode locking and chirped pulse amplification. Mode locking enables the production of extremely short, low energy (nJ) laser pulses, whereas chirped pulse amplification enables their amplification to achieve a pulse energy in the millijoule range, as required in micro-manufacturing applications. Most of the experimental work described in this thesis uses a femtosecond-pulse laser source, namely a Clark-MXR CPA2010 Ti-Sapphire laser. This laser source has a titanium-doped sapphire gain medium and uses mode locking and chirped pulse amplification to produce a femtosecond pulse train at a wavelength of 775nm.

1.2.1 Mode locking

1.2.1.1 Principle

Mode locking is a technique which is used to produce ultrashort laser pulses by inducing a fixed phase relationship between the oscillating electromagnetic field modes (i.e. the longitudinal modes) of the laser's optical cavity. By their nature, ultrashort-pulse lasers emit radiation over a broad range of wavelengths. For example a 180fs-pulse laser can have a wavelength range of 5nm around a central wavelength of 775nm (Z. Kuang *et al.* 2009a). Thanks to mode locking, the wavelength components are timed exactly so that their electromagnetic field modes nearly cancel each other out, except for during one tiny period of time when they combine constructively in one intense pulse (see Figure 1.2).

The wavelength of electromagnetic radiation modes that oscillate in a laser's optical cavity are determined by two factors. The first one is the lasing transitions that occur in the laser gain medium. In an ultrashort-pulse laser, the gain medium is chosen to have a broad range of lasing transitions (i.e. a large gain bandwidth Δν). For example, a titanium-doped sapphire has a lasing wavelength range of approximately 300nm centered near 800nm i.e. a gain bandwidth Δν of ∼130THz, and hence can support a temporal pulse-length $\tau \sim 1/\Delta\nu \sim 8$fs (A. Cavalieri, 2010). The second factor is the length of the optical cavity that surrounds the gain medium. The cavity length allows a set of discrete wavelength components (i.e. those that have an electromagnetic field mode with nodes at the cavity's end mirrors) to be amplified. By mode locking a broad range of wavelengths, an ultrashort pulse is produced at a dynamic point in the cavity, at which the many electromagnetic field modes interfere constructively. This point of coincidence moves back and forth in the cavity at the speed of light.

1.2.1.2 Methods to achieve mode locking

It is noted that mode locking does not occur naturally in a laser cavity. Without using an appropriate mode locking technique, the phase of each mode in the laser cavity would drift away from that of the

other modes and the resulting output beam power would fluctuate randomly. To achieve mode locking, two sets of methods have been developed, referred to as active and passive mode locking.

- Active mode locking uses a dynamic light modulation device in the laser cavity, externally driven with a synchronized signal. This is usually an acousto-optic modulator, which acts as a controllable attenuator. The light bouncing between the mirrors of the cavity is either attenuated when the device is “off”, or transmitted through when it is “on”. The modulator is “switched on” periodically each time the pulse has completed a cavity round trip.
- Passive mode locking uses a saturable absorber inside the cavity. A saturable absorber attenuates low-intensity light and transmits high intensity pulses.

Both active or passive, mode locking allows selective amplification of a high-intensity pulse travelling round trips between the cavity mirrors. As a result, a mode locked laser cavity produces a train of ultrashort pulses.

It is noted here that lasers which operate in a continuous wave fashion (CW laser) have their electromagnetic radiation modes oscillating randomly in the laser cavity, with no fixed relationship between each other. This leads to a near-constant output intensity with no laser pulses. Unlike pulsed lasers, continuous wave lasers generally emit radiation with a single monochromatic frequency.

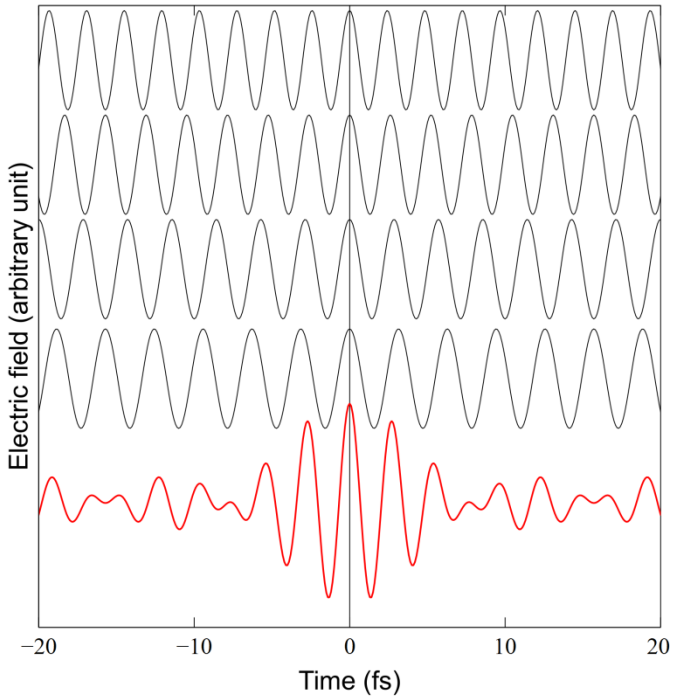

Figure 1.2: Plot showing an example of some of the electromagnetic radiation modes oscillating inside a laser’s optical cavity (plotted in black). The bottom curve (plotted in red), which is a sum of the four curves plotted in black, shows that the modes add up constructively only for a short time interval. In a femtosecond laser cavity, there are thousands of other modes interfering constructively at one moment in time before falling off quickly, thanks to mode locking. This produces a very short, high-intensity pulse travelling back and forth inside the laser cavity.

1.2.2 Chirped pulse amplification

For ultrafast laser material processing applications, ultrashort pulses need to be amplified in energy to the millijoule level. Amplifying an ultrashort laser pulse to these energy levels directly would damage the amplification crystal (gain medium), because of the very high peak power contained in the pulse. A chirped pulse amplification technique is used to avoid this.

In a chirped pulse amplifier, a seed ultrashort laser pulse is stretched in time to as long as a nanosecond by inducing a relative delay between its wavelength components (i.e. its longitudinal modes) to reduce peak intensity, prior to introducing it to the gain medium. This is usually achieved using a pair of gratings that are arranged so that the longer wavelength components of the laser pulse travel a shorter path than the shorter wavelength components. After the gratings, the shorter wavelength components lag behind the longer wavelength components (see Figure 1.3). The stretched pulse, which has a lower peak intensity, is then safely introduced to the gain medium for amplification. Depending on the design of the laser, the pulse can travel several times within the cavity, to deplete the amplification crystal (i.e. the gain medium) of its stored energy, before being released out of the laser cavity. Following amplification, the pulses are recompressed by temporally reversing the stretching process and removing the relative delay between the wavelength components. In this way, ultrashort laser output pulses achieve much higher peak powers, as the amplification is not limited by the damage threshold of the amplifying crystal.

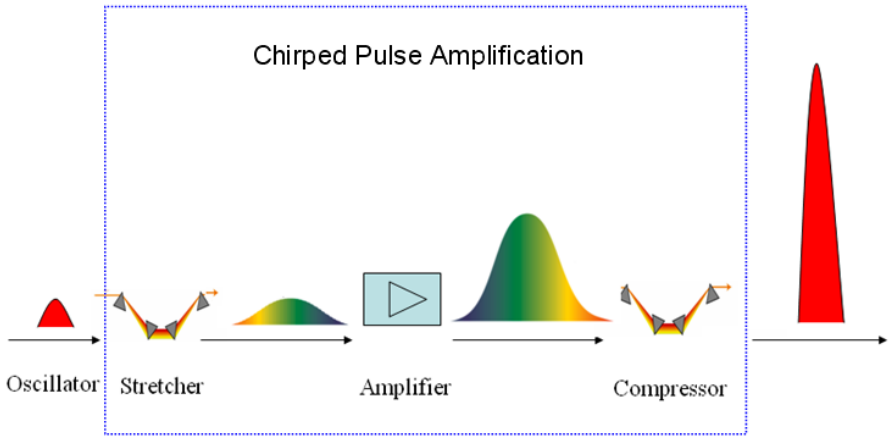

Figure 1.3: Schematic showing the principle of Chirped Pulse Amplification. An ultrashort seed pulse is stretched by a set of gratings before amplification in the laser cavity, here referred to as "Amplifier". After amplification, the pulse is compressed by another set of gratings to produce a high-intensity, ultrashort pulse. This schematic was taken from J. Cheng (2010).

1.2.3 Laser-material interactions mechanisms

This section gives a brief overview into various types of laser-material interaction mechanisms which occur when a pulsed laser beam is used to process a material. A distinction is made between two types of processing regimes. The first is when a laser beam with a "long" pulse duration (i.e. down to the nanosecond range) is used. This is typically referred to as the long-pulse regime. The second is when a pulse duration in the picosecond or femtosecond range is used. This is sometimes referred to as the ultrashort-pulse regime. Each of these regimes produces different types of laser-material interactions.

1.2.3.1 Long-pulse regime

Micro-machining materials such as metals or semiconductors in the long-pulse regime is a dynamic process where the material close to the surface of the work-piece is heated, molten and finally vaporized within the duration of each pulse (S. T. Hendow & S. A. Shakir, 2010). In this regime, laser pulses transfer most of their energy thermally by melting the material. However, energy losses occur due to thermal diffusion within the pulse duration. Thermal diffusion causes heat to flow to the bulk substrate material outside the processing area and reduces the efficiency of the process.

To improve efficiency, high-precision industrial processes often use pulse lengths in the nanosecond range, since they produce less thermal losses than longer pulses in the microsecond range or above. This results in a comparatively high processing speed. However even with nanosecond pulses, melting inevitably produces recast layers on the sidewalls of the machined structures, which limits the end quality of the process achievable in this regime (N. H. Rizvi, 2003).

For any given micro-machining process, a balance has to be found between efficiency and quality. For example by increasing the pulse energy, more material is ablated by each pulse, making the process more efficient; however, this also produces more recast material on the sidewalls of the machined structures (Figure 1.4) and this reduces the process quality.

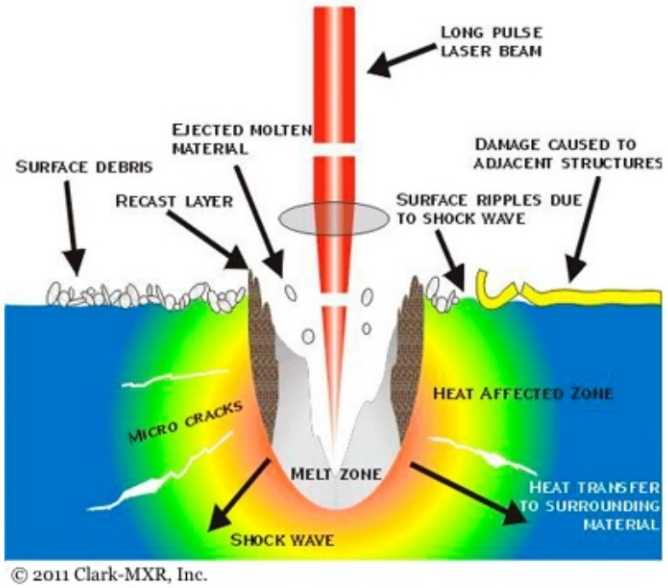

Figure 1.4: Schematic showing the various phenomenon which occur in the long-pulse laser-material interaction regime. This schematic is taken from the Clark-MXR website (www.cmxr.com/Education).

1.2.3.2 Ultrashort-pulse regime

In the ultrashort-pulse regime, the heat deposited by the laser into the material does not have enough time to move away from the processing area within the duration of the pulse. This reduces thermal diffusion and energy losses. As soon as a laser pulse reaches the surface, the temperature at the focal spot rises very quickly past the melting point and then the evaporation point of the material, soon reaching the plasma regime (C. Fohl & F. Dausinger, 2006; D. Breitling *et al.* 2004b). As a result, ultrashort-pulses increase the share of vaporized material at the expense of molten material. They enable many materials to be processed with a very high quality and minimal thermal damage (see Figure 1.5).

The physics of laser material interactions in this regime can be described as follows: when an ultrashort pulse reaches the target surface, the laser radiation energy is absorbed locally in the electron system of the target material. Depending on the fluence and peak power of the laser pulse and on the properties of the target material, various laser-material energy transfer mechanisms can occur:

- In some semiconductors or dielectric materials, the intense energy transfer to the electrons causes their separation from the bulk material, leaving behind ions which repel each other and leave the bulk substrate material. This process is referred to as a Coulomb explosion (F. Dausinger, 2003).
- Another example of an energy transfer mechanism is multi-photon absorption, which occurs in some dielectrics. Here, the high peak power of the ultrashort pulses causes the laser photons to excite molecules within the target material to their higher energy state.
- In metals, each laser pulse locally heats electrons. Contrary to the light-weight electrons, the heavier ion lattice of the material cannot absorb optical radiation energy directly since they cannot follow the fast oscillations of the electromagnetic field. However, by collisions with the energetic electrons, the ion lattice is also heated up eventually. Due to the large mass difference between electrons and ions, only a small energy portion can be transmitted by each electron-ion collision (D. Breitling *et al.* 2004a). Thermodynamic equilibrium between the electron system and the lattice is only reached after a time delay in the nanosecond range, after which the transferred energy vaporizes the material. Since the duration of the laser pulse is shorter than this time delay, it does not transfer its energy to the lattice directly. This reduces melt formation and thermally induced stress and it leads to a better process quality.

It is noted that thermal damages sometimes occur when processing with ultrashort-pulses, especially at higher fluences. For example melting does take place in metals, caused by a residual thermal diffusion when the pulse energy is very high (D. Breitling *et al.* 2004a).

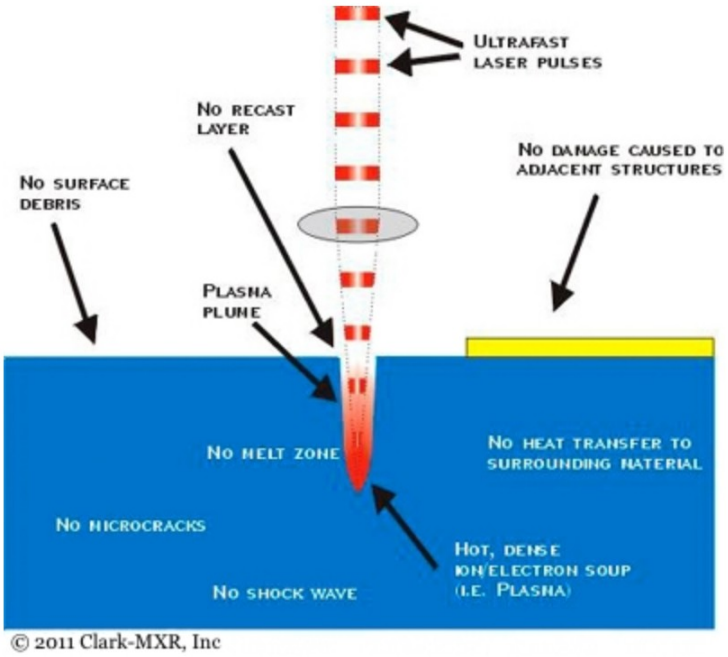

Figure 1.5: Schematic showing some of the benefits obtained by processing in the ultrashort-pulse laser-material interaction regime. Thermal damages are minimal in this regime. This schematic is taken from the Clark-MXR website (www.cmxr.com/Education).

1.2.4 Techniques for laser micro-machining

Laser micro-machining (also referred to as laser micro-processing) is a general term that includes a variety of processes, such as surface marking, hole drilling, cutting and milling. This section gives a brief overview of some of the processes used to micro-machine metals with short- and ultrashort-pulse lasers.

1.2.4.1 Low aspect-ratio processing

Low-aspect-ratio processing includes the marking or texturing of the surface of a work-piece, as well as drilling or cutting structures through thin sheets of material (thin semiconductor wafers, metal sheets etc…). It involves the gentle surface ablation of target materials. Ultrashort pulses with a fluence just above the ablation threshold can be used to produce virtually melt-free structures (D. Breitling *et al.* 2004a). The low processing efficiency associated with low pulse energy can be compensated by increasing the pulse repetition rate of the laser source. The laser is scanned across the surface to produce the desired geometry. The number of pulses at each position determines the depth of the structures.

1.2.4.2 High-aspect-ratio micro-drilling

For high-aspect-ratio laser drilling, a high enough fluence is necessary to maintain a good ablation efficiency. Experimental evidence shows that deep hole drilling generally requires a high fluence level to enable full material penetration (D. Breitling *et al.* 2004b). Therefore thermal damages such as the formation of melt and heat affected zones, which occur during high-fluence laser processing, can be problematic even with ultrashort pulses (F. Dausinger, 2003; D. Breitling *et al.* 2004b). Specific machining techniques have been developed to limit these effects.

There are four principal techniques for laser drilling: single-pulse, percussion, trepanning and helical drilling (see Figure 1.6). Single-pulse and percussion are simpler and faster drilling methods since they use only the focused laser beam for machining, without any further optics. The resulting hole is roughly the same diameter as the laser beam's spot size. These methods can deliver aspect ratios as large as 10; however, they do not produce the best hole quality. Trepanning and helical drilling are more complex as they involve moving the laser beam with regard to the work-piece. As a result these methods produce holes wider than the laser beam spot size.

Laser trepanning involves piercing the work-piece in the same way as in percussion drilling and then cutting a round hole in one circular movement. Laser trepanning is comparable to a cutting process. Again, this method can suffer from melt formation and heat affected zones.

In helical drilling, the beam does not pierce through the material initially. Rather, it follows a recurring circular path where laser pulses ablate layers of material gradually, meaning that the ablation front follows a helical path. Since the laser spot diameter is smaller than the final bore, material expulsion becomes easier and thus recast layers, which are deposited on the sidewalls, do not accumulate to thick layers and can be removed by successive passes of the beam, thus improving the end process quality. Furthermore, helical drilling has proven to be beneficial also in terms of increased geometrical accuracy, since the rotational beam movement produces a hole shape that does not depend on the beam profile but rather on the accuracy of the scanning motion. Although it is not the fastest drilling method, helical drilling produces the best process quality and geometrical accuracy of the resulting structures, compared to other drilling methods (D. Breitling *et al.* 2004b). It is also the only option for drilling holes

with a very high aspect-ratio (i.e. above 10). The hole quality can also be further improved by using an assist gas during drilling to reduce oxidation, or by drilling at reduced atmospheric pressure to facilitate ablation and molten material ejection. It is noted that in some cases helical drilling can be used to produce non-circular holes. Instead of repeatedly scanning along a circular path, the laser beam can follow a specific path to produce the desired hole geometry.

1.2.4.3 Micro-milling and cutting

For machining more general shapes which are not necessarily circular or do not go through the full thickness of the work-piece, various methods can be used, such as milling or cutting. For example micro-machining non-circular holes through the work-piece can be achieved by cutting out, removing a core in the centre of the scanned beam path. As in helical drilling, the beam scans repeatedly over the work-piece. However unlike in helical drilling, there is a core left which is removed after machining.

In some cases, blind structures are desired, which do not go all the way through the thickness of the work-piece. As before, the laser is scanned across the surface to produce the desired structures (N. H. Rizvi, 2003). The number of pulses at each position determines the depth of the structure. This process is often referred to as micro-milling.

1.2.4.4 Further developments in current micro-machining techniques

In all laser micro-machining applications, the quality of the produced features has to be balanced with the process efficiency and cost. Thus, current industrial applications require a careful adjustment of process parameters such as the fluence, pulse duration, wavelength or pulse repetition rate of the incident laser beam (S. Hahne *et al.*2007).

The polarization and phase of laser beams have been largely unexploited in current industrial applications, although they significantly affect the efficiency and quality of laser processing. Structuring laser beams in polarization and phase or controlling them in real-time during a process would allow a far more advanced level of control of laser-material interactions, impacting on the efficiency and quality of processes and potentially enabling applications previously not achievable. This thesis explores the use of advanced methods to control the polarization and phase of a laser beam and optimize micro-machining processes.

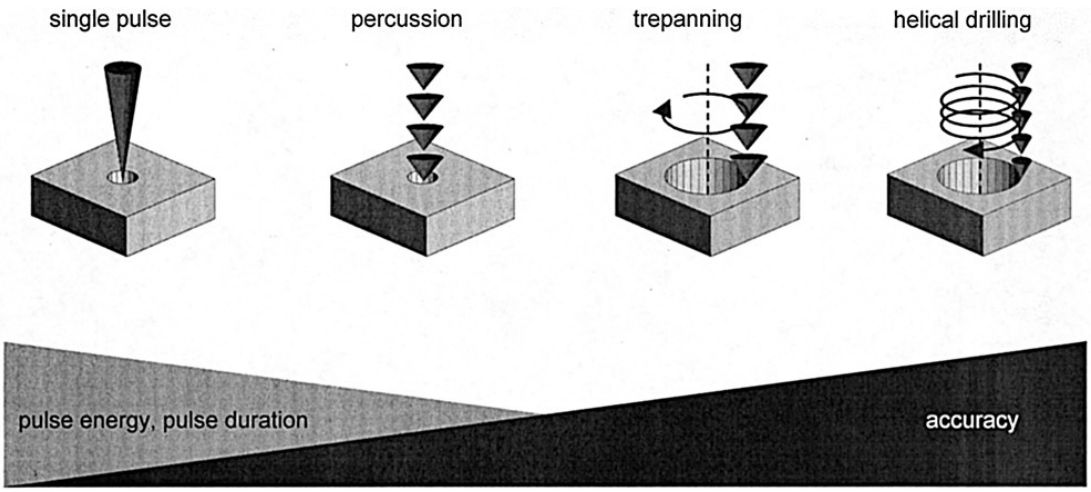

Figure 1.6: Schematic showing the four most common techniques for laser drilling. Single-pulse drilling usually involves a large pulse energy and/or longer pulse duration. As a result it is not a very accurate process. Percussion drilling involves using a laser pulse train to gradually ablate deep holes. Trepanning consists of a percussion drilling, followed by a cutting procedure. Helical drilling usually involves low pulse energies and shorter pulses and produces the most accurate structures (D. Breitling *et al.* 2004b).

1.3 Introduction to phase and polarization

In this thesis, novel methods are used to control the phase and polarization of laser beams. This section gives an overview into the physical meaning of phase and polarization and describes how these physical quantities can be described mathematically.

1.3.1 Definition of phase and polarization

An electromagnetic wave produced by laser radiation can be described as a self-propagating, transverse oscillating wave of electric and magnetic fields. The electric and magnetic fields both oscillate perpendicularly to the direction of wave propagation and perpendicularly to each other. Each of these fields can be described as a sinusoidal function, oscillating in both space and time (see Figure 1.7).

1.3.1.1 Phase

If we plot the electric field along the axis of propagation of the laser beam at a given time, there are places along the axis where the field is at a maximum amplitude (i.e. a maximum positive field), places where it is zero and other places where the field is at a minimum amplitude (i.e. a maximum negative field), forming a sinusoidal function overall (Figure 1.8-a). These places along the axis of propagation represent different phases of the wave (D. C. O'Shea, 1985). In other words, the phase of an electromagnetic wave can be defined as the location where the sinusoidal function has a given amplitude value (see Figure 1.8-b). The concept of phase is valuable in the context where a group of coherent electromagnetic waves travel together in the same direction, as is the case in a laser beam. In such cases, it can be useful to describe a phase front (also referred to as wavefront) as a surface defined by the locations in space where all the sinusoidal functions have the same amplitude. In an undisturbed collimated laser beam, the phase front is generally a planar surface. In a focused laser beam, for example, the phase front has a convex shape (Figure 1.9).

1.3.1.2 Polarization

The polarization of electromagnetic waves is a property related to the orientation in which they oscillate. By definition, it is described by specifying the orientation of the wave's electric field at a point in space, over one period of oscillation of the wave (D. C. O'Shea, 1985). For example, an ultrafast laser source typically produces a beam where the field is oriented in a single direction (i.e. it always oscillates along a fixed line in space; see D. Breitling *et al.* 2004b). This is referred to as linear polarization. However other types of laser sources can produce a field that rotates as the wave travels, producing polarization configurations called either circular or elliptical depending on the way the field rotates. It is noted that some laser sources produce beams where the direction of the electric field changes randomly over time. These beams are said to be randomly polarized. Laser sources that generate random polarization typically cannot produce ultrashort pulses for material processing (D. Breitling *et al.* 2004b), therefore random polarization is not investigated further in this thesis.

When a collimated laser beam travels in free space, it propagates as a transverse wave: the electric field (polarization) is perpendicular to the wave's direction of travel. It is noted that, unlike laser radiation, ordinary light is not usually polarized. This is because ordinary light is produced by a number of independent atomic sources whose radiation is not synchronized, and with an electric field that does not oscillate in any preferred orientation.

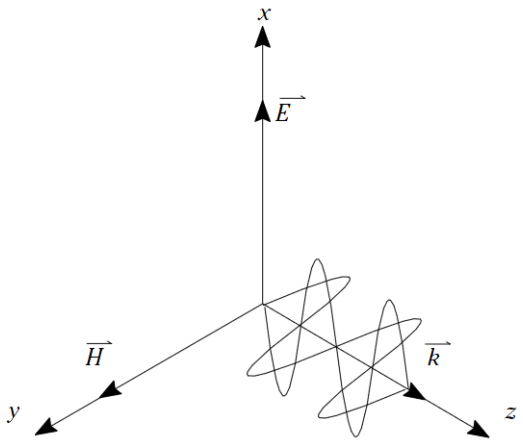

Figure 1.7: Schematic showing an electromagnetic wave represented in a coordinate system (x, y, z) and propagating along the z axis. An electromagnetic wave can be pictured as a combination of electric ($\vec{E}$) and magnetic ($\vec{H}$) fields whose directions are perpendicular to the direction of propagation of the wave ($\vec{k}$). This schematic is taken from D. C. O'Shea (1985).

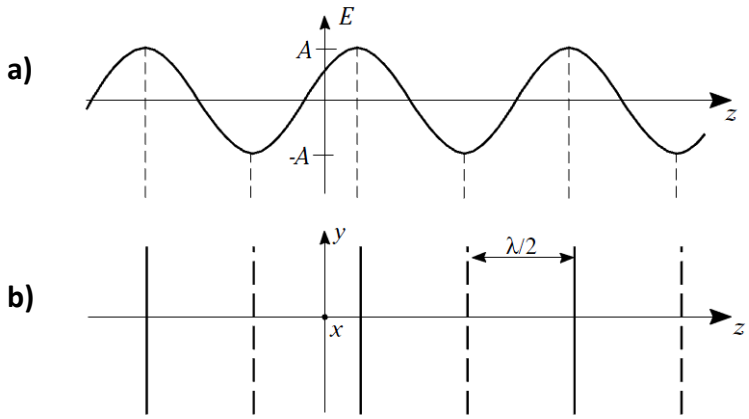

Figure 1.8: (a) Schematic showing how the amplitude of the electric field *E* of an electromagnetic wave oscillates along the direction of propagation *z*. **(b)** Schematic showing phases of the wave. The solid lines indicate the places where the field is at a maximum *+A*, the dashed lines indicate the places where it is at a minimum *–A*. Each of these places represents a phase of the wave.

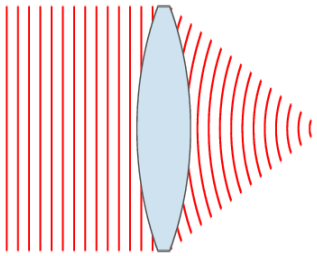

Figure 1.9: Schematic showing the planar wavefronts of a collimated laser beam (left), converging after a focusing lens (right).

1.3.2 Mathematical representation of polarized light: Jones vectors

This section gives a brief reminder of Jones formalism, which uses complex vectors to describe polarization. For a more detailed description of Jones formalism, see for example F. L. Pedrotti & L. S. Pedrotti (1993) or J. P. Perez (1996). For a description of complex numbers, see for example K. F. Riley *et al.* (2002). It is noted here that I use the notation j as an imaginary (i.e. complex) number and the notation $\boldsymbol{J}$ as a Jones vector.

1.3.2.1 Reference coordinate system

To explain Jones vectors, we consider a ray of linearly polarized light, with its direction of propagation oriented perpendicularly out of this page and situated at the origin of the reference coordinate system defined in Figure 1.10. The electric field of the light is represented by a vector in this coordinate system. Here, it is chosen to be at +45˚ of the coordinate axes (x and y). The field oscillates periodically like a sinusoidal function along the direction indicated by the dotted line (see Figure 1.10). For convenience the vector is represented with the amplitude when the field is at its (positive) maximum. The vector is described in the coordinate system by the sum of its projections on the x and y axes of the coordinate system:

$$\vec{\boldsymbol{E}} = E_X.\vec{\boldsymbol{X}} + E_Y.\vec{\boldsymbol{Y}} \qquad (1.1)$$

$\vec{\boldsymbol{X}}$ and $\vec{\boldsymbol{Y}}$ are unit vectors along the x and y axes of the coordinate system. E_X and E_Y are often referred to as the components of the electric field vector.

Here, the Jones vector representing the polarization of the light is noted $\boldsymbol{J}$ and is defined as: $\boldsymbol{J} = \begin{pmatrix} E_X \\ E_Y \end{pmatrix}$. Each component E_X and E_Y of the Jones vector is expressed as complex numbers: $E_X = r_X.e^{j(\varphi_X)}$ and $E_Y = r_Y.e^{j(\varphi_Y)}$, where r_X and φ_X, are the amplitude and phase of E_X respectively, and similarly for E_Y. The state of polarization is completely determined by the relative amplitudes and phases of these components. Therefore, Jones vectors are convenient to mathematically describe polarized laser beams. It is noted that the electric field vector $\vec{\boldsymbol{E}}$ is fully defined by the corresponding Jones vector $\boldsymbol{J}$. Henceforth in this thesis, I refer to Jones vectors using either the notation $\boldsymbol{J}$ or $\vec{\boldsymbol{E}}$, for clarity, depending on the circumstances.

In this example, the electric field vector $\vec{\boldsymbol{E}}$ is oriented at +45˚ of the axes of the coordinate system. Therefore the amplitudes r_X and r_Y are equal.

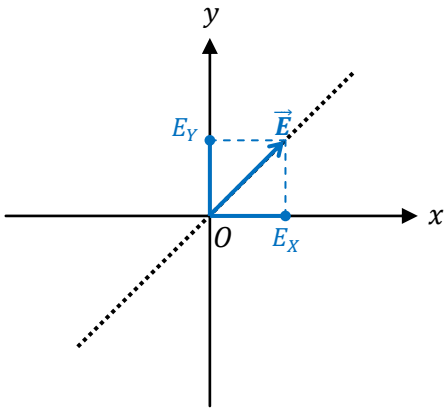

Figure 1.10: Schematic showing the vector $\vec{\boldsymbol{E}}$ of a linearly polarized ray of light directed perpendicularly to the plane of this page, represented in a coordinate system $(\boldsymbol{O}, \vec{\boldsymbol{X}}, \vec{\boldsymbol{Y}})$.

1.3.2.2 Jones vector for linearly polarized light

With a linearly polarized light (see Figure 1.10), both phase components φ_X and φ_Y are equal (for convenience, they are both set equal to zero). In this case, both electric field components E_X and E_Y are in phase and oscillate together, reaching their maximum amplitude at the same time, decreasing and reaching their minimum amplitude at the same time and so on (see Figure 1.11). Therefore, the resulting vector $\vec{\boldsymbol{E}}$ oscillates only within one orientation (i.e. along the dotted line in Figure 1.10). If we define for example $r_X = r_Y = 1$, the Jones vector representing linear polarization is: $\boldsymbol{J} = \binom{1}{1}$.

1.3.2.3 Jones vector for elliptically polarized light

If the two phase components φ_X and φ_Y are not equal, the electric field components E_X and E_Y are not in phase and do not oscillate together. For example when E_X reaches a maximum, E_Y is still increasing. When E_Y reaches its maximum E_X has already started decreasing and so on (see Figure 1.12). This, in general causes the electric field vector $\vec{\boldsymbol{E}}$ to change its orientation and amplitude over time. As the field vector forms an elliptical pattern over a period of oscillation, this type of polarization configuration is called elliptical. This is generally described by defining $\varphi_X = 0$ and $\varphi_Y = \Delta_\varphi$. If we define for example $r_X = r_Y = 1$, we have the following Jones vector: $\boldsymbol{J} = \binom{1}{e^{j\Delta_\varphi}}$, which defines in general an elliptical polarization.

1.3.2.4 Jones vector for circularly polarized light

A particular case is where the two phase components φ_X and φ_Y have a relative shift of a quarter of the period of oscillation: $\varphi_Y - \varphi_X = \pi/2$. This means that the phase of E_X leads that of E_Y by a quarter of period (i.e. a phase of $\pi/2$). At the instant E_X has reached its maximum amplitude, E_Y is zero. Then E_X decreases as E_Y increases. E_X is zero when E_Y is maximum and so on (see Figure 1.13). This causes the electric field vector $\vec{\boldsymbol{E}}$ to change its orientation continuously, while keeping a constant amplitude over time. In this case, the field vector forms a circular pattern over a period of oscillation and this type of polarization configuration is called circular. The corresponding Jones vector is: $\boldsymbol{J} = \binom{1}{e^{j\frac{\pi}{2}}}$.

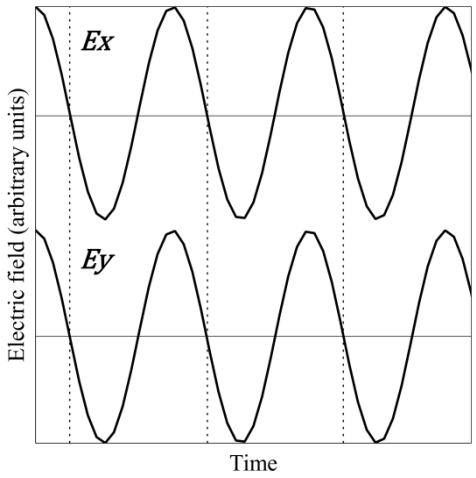

Figure 1.11: Plot showing the time dependence of the components E_X and E_Y of an electric field vector $\vec{\boldsymbol{E}}$ representing a linearly polarized ray of light. Here, $\varphi_X = \varphi_Y, r_X = r_Y = 1$.

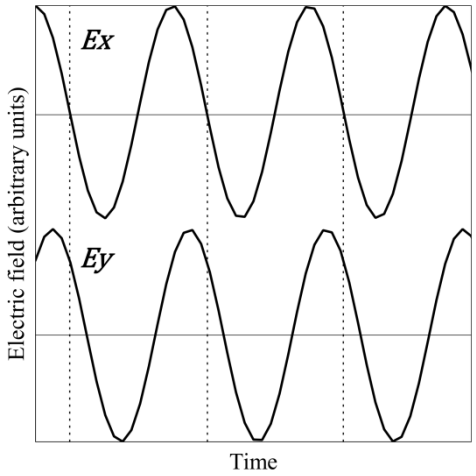

Figure 1.12: Plot showing the time dependence of the components E_X and E_Y of an electric field vector $\vec{\boldsymbol{E}}$ representing a elliptically polarized ray of light. Here, $\varphi_X = 0, \varphi_Y = \Delta_\varphi, r_X = r_Y = 1$.

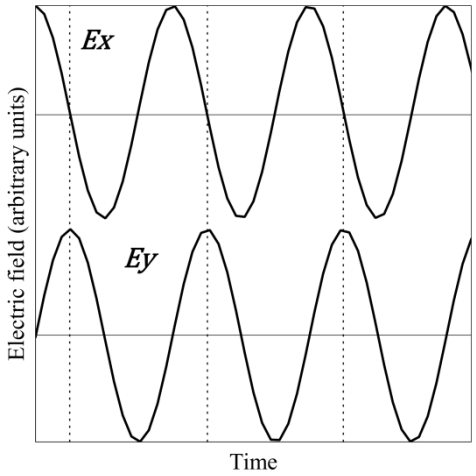

Figure 1.13: Plot showing the time dependence of the components E_X and E_Y of an electric field vector $\vec{\boldsymbol{E}}$ representing a circularly polarized ray of light. Here, $\varphi_X = 0, \varphi_Y = \pi/2, r_X = r_Y = 1$.

1.3.3 Mathematical representation of waveplates: Jones matrixes

In this section we explain, using matrices, how birefringent optical components such as waveplates affect the polarization of light transmitted through them. For a detailed description of matrix mathematics, see K. F. Riley *et al.* (2002).

1.3.3.1 Waveplates and Jones matrixes

A waveplate, or phase retarder, is an optical element that introduces a phase difference between the electric field components E_X and E_Y (A. Yariv & P. Yeh, 1984). It works by making each component of the electromagnetic wave (corresponding to the electric field E_X or E_Y) travel through it with a different speed. As a result, there is a cumulative phase difference Δ_φ between the two wave components as they emerge from the waveplate. The phase difference Δ_φ is the main attribute of a waveplate. The physical phenomenon that causes each component of the electromagnetic wave to travel at different speeds is called birefringence and will be further detailed in Section 1.3.4.

Here we are interested in mathematically describing waveplates by using matrixes. A matrix that represents a waveplate is called a Jones matrix, and can be defined as:

$$\boldsymbol{P} = \begin{bmatrix} 1 & 0 \\ 0 & \mathrm{e}^{j\Delta_\varphi} \end{bmatrix} \tag{1.2}$$

We describe the polarization of the electromagnetic wave incident on a waveplate using a Jones vector noted $\boldsymbol{J}_i$. The polarization of the wave that emerges from this waveplate is noted $\boldsymbol{J}_o$. By definition, the relation between the Jones vectors $\boldsymbol{J}_i$ and $\boldsymbol{J}_o$ is as follows:

$$\boldsymbol{J}_o = \boldsymbol{P} \times \boldsymbol{J}_i \tag{1.3}$$

1.3.3.2 Case where linearly polarized light is incident on a waveplate

If $\boldsymbol{J}_i$ is the linearly polarized light described in Section 1.3.2.2 above, we have $\boldsymbol{J}_i = \binom{1}{1}$. Then we can derive $\boldsymbol{J}_o$ in the following way:

$$\boldsymbol{J}_o = \boldsymbol{P} \times \boldsymbol{J}_i = \begin{bmatrix} 1 & 0 \\ 0 & \mathrm{e}^{j\Delta_\varphi} \end{bmatrix} \times \binom{1}{1} = \binom{1}{\mathrm{e}^{j\Delta_\varphi}} \tag{1.4}$$

Equation (1.4) is the mathematical expression that the waveplate introduces a phase difference Δ_φ between the electric field components E_X and E_Y of the incident wave.

For example if the linearly polarized light described in Section 1.3.2.2 above, $\boldsymbol{J}_i = \binom{1}{1}$, is incident on a waveplate with a Δ_φ value of $\frac{\pi}{2}$, the resulting Jones vector is $\boldsymbol{J}_o = \binom{1}{\mathrm{e}^{j\frac{\pi}{2}}}$. In other words, the waveplate has introduced a phase shift of $\frac{\pi}{2}$ (i.e. a quarter of periodic oscillation) between the components of the electric field. As a result, the incident linear polarization has been converted to circular polarization, defined by the Jones vector $\binom{1}{\mathrm{e}^{j\frac{\pi}{2}}}$, as the field emerges from the waveplate. This type of waveplate is called quarter-waveplate, as it induce a phase retardance of a quarter of the period of oscillation of the electric field (i.e. a phase of $\pi/2$).

1.3.3.3 Case where circularly polarized light is incident on a waveplate

If the incident light, $\boldsymbol{J}_i$, is the circularly polarized light described in Section 1.3.2.4 above, we have $\boldsymbol{J}_i = \binom{1}{\mathrm{e}^{j\frac{\pi}{2}}}$. As before, we can derive $\boldsymbol{J}_o$ in the following way:

$$\boldsymbol{J}_o = \boldsymbol{P} \times \boldsymbol{J}_i = \begin{bmatrix} 1 & 0 \\ 0 & e^{j\Delta_\varphi} \end{bmatrix} \times \begin{pmatrix} 1 \\ e^{j\frac{\pi}{2}} \end{pmatrix} = \begin{pmatrix} 1 \\ e^{j(\Delta_\varphi + \frac{\pi}{2})} \end{pmatrix} \quad (1.5)$$

Here, the waveplate introduces an extra phase shift Δ_φ between the electric field components E_X and E_Y of the incident wave. As the incident polarization was circular (i.e. with an existing phase shift of $\frac{\pi}{2}$ between E_X and E_Y), the resulting overall phase shift after emerging from the waveplate will be $\frac{\pi}{2} + \Delta_\varphi$.

If the waveplate has a phase retardance Δ_φ value of $\frac{\pi}{2}$ (i.e. a quarter-waveplate), the overall phase shift of the resulting wave will be $\frac{\pi}{2} + \frac{\pi}{2} = \pi$. Therefore the resulting Jones vector will be $\boldsymbol{J}_o = \begin{pmatrix} 1 \\ e^{j\pi} \end{pmatrix}$. In complex number formalism, $e^{j\pi} = -1$. Thus we have $\boldsymbol{J}_o = \begin{pmatrix} 1 \\ -1 \end{pmatrix}$, which defines a linear polarization, with a direction of electric field oscillation oriented orthogonally to that of the incident light. Here, we have shown that a circularly polarized beam incident on a quarter-waveplate is converted into a linearly polarize beam.

In this thesis, various phase retardance optics are used to introduce a phase shift between the two electric field components of a laser beam and convert its polarization state.

1.3.4 Birefringence

Certain materials have anisotropic optical properties. For example, birefringent materials are so named because they have two distinct values for refractive index. This is due to the anisotropic forces binding the electrons of these materials, causing anisotropic response to a stimulating electromagnetic wave propagating through them. In other words, the electrons tend to oscillate preferentially along one direction, where the binding force is weaker (see F. L. Pedrotti & L. S. Pedrotti, 1993).

We can define a reference coordinate system with x and y axes directed perpendicularly to the light propagation, so that the x axis corresponds to the direction of the strong binding force, where the electron oscillation is weaker (also called the optical axis of the material) and y is perpendicular to x (i.e. along the preferential direction of electron oscillation). The presence of anisotropic binding forces along the x and y directions leads to different refractive indexes: n_X corresponding to the component of electric field oscillation along the x axis and n_Y corresponding to that along the y axis. This results in different velocities of light propagation along each axis: light travel faster along the x axis, where the interaction with the electrons of the material is weaker (the x axis is sometimes referred to as the fast axis).

This type of optical behavior occurs in materials such as calcite crystal, which have an anisotropic crystalline structure. It is noted that birefringence is also dependant on wavelength and that a given material is only birefringent within a portion of the electromagnetic spectrum. Birefringence is used to make phase retardance optics, such as waveplates. This is done by cutting and polishing a birefringent material in a direction parallel to its optical axis.

1.3.5 Fresnel's coefficients and Brewster's angle

When a laser beam is incident on the surface of a material, a fraction of the beam power is absorbed by the material and the remainder is reflected from the surface. The reflectivity of a material is the fraction of power in the incident beam that is reflected from a planar surface of the material. The reflectivity of a material depends on a number of parameters. Of particular relevance in this thesis is the dependence of reflectivity with the angle of incidence of the incident light, as well as its polarization.

To describe this, we can consider the case where a narrow beam of polarized light is incident at an arbitrary angle α on a flat surface, as represented in Figure 1.14. A distinction is made between light which is polarized parallel to the plane of incidence (i.e. with the electric field oscillating within the plane of the page, see Figure 1.14) and light which is polarized orthogonal to the plane of incidence (i.e. with the electric field oscillating in a direction perpendicular to the plane of the page). The former is often referred to as *p*-polarization, or E_p and the latter as *s*-polarization, or E_s . The incident light can consists of a combination of a *p*-polarized component an *s*-polarized one.

The reflectivity of a material illuminated under *p*-polarized light is not always the same as that of the same material under *s*-polarized light. These reflectivities can be calculated using the well-known Fresnel formula (S. Nolte *et al.* 1999; F. Dausinger & J. Shen, 1993):

$$\boldsymbol{q}_p = \frac{\boldsymbol{Er}_p}{\boldsymbol{Ei}_p} = \frac{n^2\cos\alpha - \sqrt{n^2 - \sin^2\alpha}}{n^2\cos\alpha + \sqrt{n^2 - \sin^2\alpha}} \tag{1.6}$$

$$\boldsymbol{q}_s = \frac{\boldsymbol{Er}_s}{\boldsymbol{Ei}_s} = \frac{(\sqrt{n^2 - \sin^2\alpha} - \cos\alpha)^2}{1 - n^2} \tag{1.7}$$

$\boldsymbol{q}_p$ and $\boldsymbol{q}_s$ are the amplitude ratios of the reflected to incident electric fields for *p*- and *s*-polarized light respectively, with $\boldsymbol{Ei}$ and $\boldsymbol{Er}$ as the electric field amplitude of the incident and reflected light respectively. α is the angle between the direction of the incident light and the surface normal. The reflectivity for both *p*- and *s*-polarized light is then obtained from:

$$\boldsymbol{R}_p = \left|\boldsymbol{q}_p\right|^2 \tag{1.8}$$

$$\boldsymbol{R}_s = \left|\boldsymbol{q}_s\right|^2 \tag{1.9}$$

In this thesis, we are especially interested in the reflectivity of absorbing materials such as metals. In this case, the index of refraction n in the Fresnel Equations 1.6 and 1.7 has to be replaced with a complex value $n - jk$, where k is the so-called extinction coefficient that describes the exponential decay of the electric field inside the material. The index of refraction and extinction coefficient depend on the material and wavelength. For example, the typical values for steel are n=0.9 and k=2.25 in the visible spectrum (S. Nolte *et al.* 1999). Replacing these values in Equations 1.6 and 1.7 and the results in Equations 1.8 and 1.9 above enables deriving the reflectivity of steel under *p*- and *s*-polarized light illumination as a function of the angle of incidence. The results are plotted in Figure 1.15. It can be seen that when the angle of incidence is close to normal ($\alpha \sim 0^\circ$), the influence of the direction of polarization is negligible. However when the angle of incidence is around 80˚, the reflectivity for *p*-polarized light is close to its minimum value around 47%, whereas the reflectivity for *s*-polarized light is around 94% (S. Nolte *et al.* 1999). In this case, the intensity of light reflected from the surface is higher by approximately a factor of two compared to the previous case. This angle is called Brewster angle. This consideration is important since laser drilling high-aspect-ratio holes in metals generally produces internal reflections on the sidewalls around the hole with an angle of incidence close to 80˚. This means that controlling the state of polarization of the beam is important to ensure a good quality and efficiency of the drilling process.

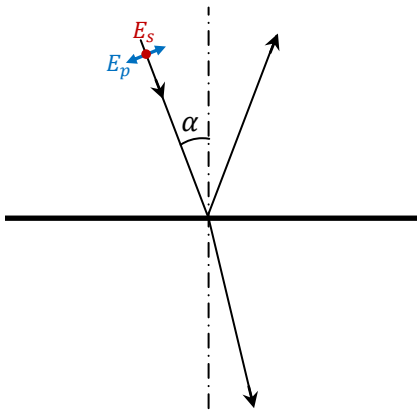

Figure 1.14: Schematic showing a beam of light (top left) incident on the surface of a material. The incident beam consists of both a *p*-polarized component and an *s*-polarized one. Some of the incident power is absorbed by the material and some is reflected from the surface. Depending on the angle of incidence α, the value of reflectivity is not always identical for the *p*-polarized component and for the *s*-polarized one.

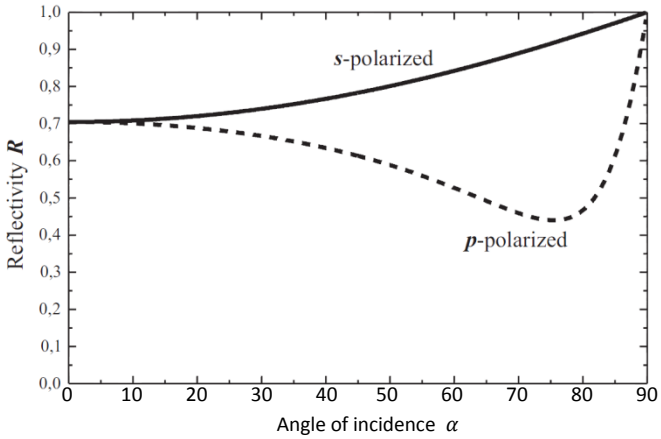

Figure 1.15: Reflectivity of steel as a function of the angle of incidence α, for *p*- and *s*-polarized light illumination. Various types of steel have slightly different value of reflectivity. This plot is taken from S. Nolte *et al.* 1999.

1.3.6 Cylindrical Vector Beams

Most past research in industrial laser processing dealt with spatially uniform states of polarization, such as linear, elliptical and circular polarizations. In each of these cases, the state of polarization does not depend on the spatial location within the profile of the laser beam: the state of polarization is the same at all locations within a given beam cross-section. Recently, there has been an increasing interest in laser beams with a spatially varying state of polarization (Q. Zhan, 2009). Spatially structuring the state of polarization of a laser beam affects its focal properties, when focused by a lens, as well as the way it interacts with materials.

Of particular interest is the case where the oscillating electric field vectors are cylindrically symmetric around the cross-section of the laser beam. Such beams are often referred to as Cylindrical Vector Beams (CVBs). Two particular cases of CVBs are those with a radial or an azimuthal polarization structure (Figure 1.16). For example, the Jones vector representing an azimuthally polarized laser beam can be written as:

$$\boldsymbol{J}_a(\theta) = \begin{pmatrix} \sin\theta \\ \cos\theta \end{pmatrix} \tag{1.10}$$

θ represents the polar angle in a Cartesian coordinate system (see Figure 1.16-c). In this configuration, the Jones vector (which varies spatially with the polar angle θ) represents an electric field always oscillating in an azimuthal orientation, regardless of θ. It is noted that this Jones vector should not be confused with that representing a linear polarization oriented at an angle θ. The latter does not vary spatially with the polar angle θ.

In the example describe in Equation 1.10 above, the CVB only has a polarization structure (azimuthal in that case). It does not have a phase structure (i.e. the beam has a planar wavefront). CVBs can also be produced with a spatially varying phase structure such as a vortex phase. A beam with a vortex phase structure can be described as if it had a helical phase front, or a topological charge in its phase structure. This is why these types of beams are said to carry an Orbital Angular Momentum (OAM). Laser beams can have both a polarization and a phase structure (M. Beresna *et al.*2011). For example, the Jones vector representing an azimuthally polarized vortex phase beams can be written as:

$$\boldsymbol{J}_v(\theta) = \mathrm{e}^{j\theta} \times \begin{pmatrix} \sin\theta \\ \cos\theta \end{pmatrix} \tag{1.11}$$

The second term in Equation 1.11 represents an electric field oscillating azimuthally as detailed in Equation 1.10 above. The first term is the phase vortex element. For example the electric field oscillating at a polar angle $\theta = 0$ in the coordinate system has a Jones vector $\boldsymbol{J}_v(0) = \mathrm{e}^{j\times 0} \times \begin{pmatrix} 0 \\ 1 \end{pmatrix} = \begin{pmatrix} 0 \\ 1 \end{pmatrix}$, whereas the electric field oscillating at an angle $\theta = \theta_1$ has a Jones vector $\boldsymbol{J}_v(\theta_1) = \mathrm{e}^{j\theta_1} \times \begin{pmatrix} \sin\theta_1 \\ \cos\theta_1 \end{pmatrix}$. This means $\boldsymbol{J}_v(\theta_1)$ has a phase delay of θ_1 compared to $\boldsymbol{J}_v(0)$. The overall phase structure of the beam forms a vortex pattern (Q. Zhan, 2009).

The transformative properties of CVBs such as those with a radial or azimuthal polarization and/or a vortex phase structure include their isotropic laser-material interactions, controllable laser-material energy coupling, and sub-diffraction limited focal spot size. Moreover, they also enable a greater control over the focal energy distribution (Q. Zhan, 2009). Some of these structured beams are starting to be explored for microscopy and telecommunication applications. The field of laser manufacturing is another very promising and yet not very well explored application.

A wide range of CVBs can be produced. A CVB is defined by its polarization and phase structures. Four types of CVB are of special importance in this thesis: radially and azimuthally polarized beams with a

planar phase and radially and azimuthally polarized beam with a 2π pitch phase vortex (i.e. a topological charge of 1).

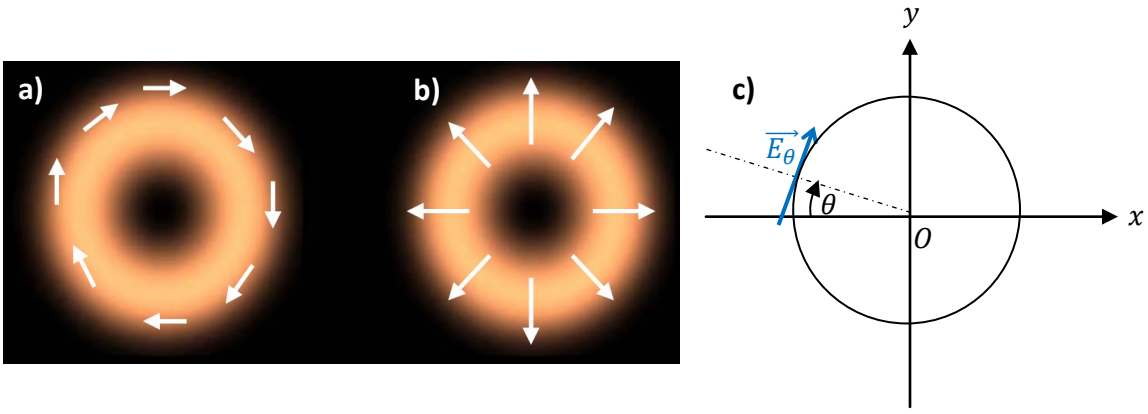

Figure 1.16: (a) Schematic showing the overall polarization structure (i.e. the vectors $\vec{E}$) in the cross-section of an azimuthally polarized beam. **(b)** Schematic showing the polarization structure of a radially polarized beam. These schematics are taken from Q. Zhan, 2009. **(c)** Schematic of the cross-section of an azimuthally polarized beam, showing a vector $\overrightarrow{E_\theta}$ represented in a coordinate system $(\boldsymbol{O}, \vec{\boldsymbol{X}}, \vec{\boldsymbol{Y}})$. For each value of θ, the vector $\overrightarrow{E_\theta}$ is azimuthally oriented.

1.4 Introduction to liquid-crystal technology

Liquid-crystal-based devices have been used for display applications since the early 1970s (G. W. Gray *et al.* 1973). Following tremendous technological developments, their use has spread to advanced control of the phase and polarization of laser beams in a number of scientific applications (P. De-Genne, 1974; M. Stalder & M. Schadt, 1996; Z. Kuang *et al.* 2009a). However due to the sensitivity of liquid-crystals to high laser power, it was believed that they could not be used in industrial laser manufacturing. Nevertheless, the most recent generation of liquid-crystal devices has proven to be resilient to high-average-power laser beams. In this thesis, liquid-crystal devices are demonstrated for use in industrial laser manufacturing applications.

1.4.1 Liquid-crystals

1.4.1.1 Definition and properties

Liquid-crystals are a type of material which, under certain conditions, has properties between those of a conventional liquid and those of a solid crystal. By definition, they are liquids in which an ordered arrangement of molecules exists (A. Yariv & P Yeh, 1984). Liquid-crystal materials generally consist of organic substances with sharply anisometric molecules, that is, large elongated molecules or flat molecules. The molecule size is typically larger than 1 nm. It is noted that liquid-crystal materials are not always in a liquid-crystal state. For example, varying the temperature and concentration of liquid crystals can drive them into either a conventional solid or liquid state. A very large number of chemical compounds are known to have liquid crystalline states. Although liquid-crystal materials can be synthesized by chemical processes, they also exist in the natural world. For example, many proteins and cell membranes are liquid-crystals.

Because of their physical properties, the application of an external electric field to liquid-crystals alters their arrangement. Thanks to the orientational ordering of the anisometric molecules, liquid-crystals are generally birefringent and affect the polarization of light transmitted through them. Liquid-crystals exist in various arrangements, or phases.

1.4.1.2 Nematic phase

The most widely used phase of liquid-crystals is the nematic phase, where rod-shaped organic molecules have no positional order, but self-align to have a long-range directional order with their long axes roughly parallel (see Figure 1.17). Most nematic liquid-crystals are uniaxial: they have one axis that is longer and the other two being equivalent.

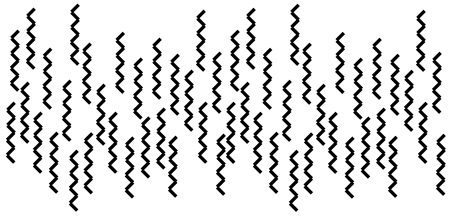

Figure 1.17: Schematics representing nematic liquid-crystal molecules aligned preferentially along their long axis. In this example, all the liquid-crystal molecules point roughly along the vertical direction.

1.4.1.3 Smectic phase

Other phases of liquid-crystals exist, such as the smectic phases, which are generally found at lower temperatures than the nematic. Smectic phases have molecules oriented preferentially along one direction, like in a nematic phase. Like their nematic counterparts, the orientation of smectic liquid-crystals can be altered by applying an external electric field. However they also have well-defined layers that can slide over one another (see Figure 1.18). In some types of smectic phases, the liquid-crystal molecules are tilted at an angle from the direction normal to the layers. This type of phase is called smectic C. It has been shown that, under certain conditions, smectic C liquid-crystals feature a ferroelectric behavior. This means they have a spontaneous electrical polarization, even when no external electrical field is applied. This type of liquid-crystals is referred to as ferroelectric liquid-crystals (FLC).

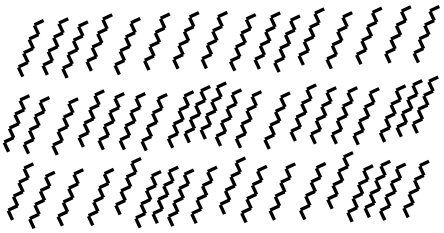

Figure 1.18: Schematics representing smectic liquid-crystals, where the molecules are arranged in multiple layers. In this example, the molecules are pointing along an average direction that is tilted from the direction normal to the multiple layers. This is called a smectic C phase.

1.4.2 Ferroelectric liquid-crystal polarization rotator

Some of the experimental research in this thesis used a liquid-crystal polarization rotation device manufactured by Boulder Nonlinear Systems Inc. (Figure 1.19). This polarization rotation device is based on a ferroelectric liquid-crystal technology: a thin active layer of ferroelectric liquid-crystals is sandwiched between two optically flat protective glass plates, each coated with a transparent electrode (indium tin oxide, or ITO). A summary of the manufacturing method used to make these devices is given in Figure 1.20. Applying an electric field to the electrodes surrounding the active layer of liquid-crystals modifies their birefringent properties. As a result, the device rotates the direction of polarization of light transmitted through it. Applying an appropriate analog electric voltage signal to the device can produce a fast switching speed between two orthogonal polarization directions i.e. the polarization of the transmitted light can be quickly rotated between two orthogonal directions. The response time of the device is typically less than 100μs and the produced polarization purity is 99%. The analog driving voltage signal is typically applied and controlled using a programmable function generator.

Figure 1.19: Polarization rotation device manufactured by Boulder Nonlinear Systems Inc. These devices are based on a ferroelectric liquid-crystal technology and rotate the polarization of transmitted light when a analogue voltage is applied. The polarization rotation device has a clear aperture of 25mm and its optical surfaces are coated with an anti-reflection layer for maximum transmission efficiency.

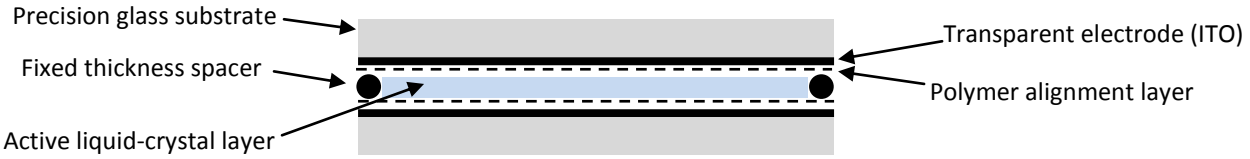

Figure 1.20: Cross sectional representation of the polarization rotator. The assembly of the polarization rotator includes several stages. Transparent conductive layers (ITO) are first coated on a pair of optically flat glass substrates. Each substrate is subsequently coated with a polymer layer. These polymer layers are then rubbed to form tiny micro-grooves along one direction, so as to provide a preferred alignment direction for the liquid crystals. The two substrates are assembled with spacers, so that they are parallel to each other and with a few microns gap between them. The cavity between the substrates is then filled with the liquid-crystal material and sealed.

1.4.3 Nematic liquid-crystal spatial light modulator

Part of the experimental work described in this thesis uses a Liquid-Crystal On Silicon (LCOS) Spatial Light Modulator (SLM) manufactured by Hamamatsu Photonics K.K. (Figure 1.21). This SLM is a reflective device made of a two-dimensional array of pixels, where a thin layer of nematic liquid-crystals is sandwiched between a protective glass substrate with a coated transparent electrode, and a reflective silicon substrate. A schematic of the device can be seen in Figure 1.22. When no voltage is applied, the liquid-crystals are all aligned parallel to each other. Thus, this technology is called “parallel-aligned nematics”.

Thanks to its liquid-crystal pixel array, the SLM can locally modify the optical properties of an incident laser beam. Each pixel is independently controlled by a direct, accurate voltage from the controller driving the SLM (Figure 1.23). The SLM controller is itself controlled from a PC via a standard DVI connection. A graphical user interface enables dynamic control of the SLM pixel array from the PC. Typically, a bitmap file is used to express the required voltage for each pixel. The bitmap file, displayed in the graphical user interface, enables to visualize each pixel voltage as a grey level. Depending on the chosen optical configuration, the liquid-crystals can either modify the wavefront, or the state of polarization of the laser beam.

In a first type of configuration, the state of polarization of the laser beam incident on the SLM is linear, with the direction of the electric field vector set parallel to optical axis of the liquid-crystals. Each pixel of the two-dimensional array induces a phase delay, proportional to the voltage applied by the controller. Inducing a relative phase delay between the pixels of the SLM shapes the wavefront of the laser beam. It is noted that only the phase of the incident laser beam is modulated; its polarization is unaffected (i.e. it remains linear). Therefore, this type of SLM is sometimes referred to as “phase-only” SLM as it only affects the phase of the beam. This approach is used for example to produce dynamic holograms that shape the amplitude distribution at the focal plane of a laser micro-processing bench (Z. Kuang *et al.* 2009b, D. Liu *et al.* 2010).

A second type of optical configuration uses an incident laser beam with a linear polarization, the direction of which is oriented at 45˚ from the optical axis of the liquid-crystals. This configuration enables to spatially modify the polarization of the incident laser beam by using the birefringence properties of the liquid-crystals. Applying the appropriate voltage to each pixel enables to precisely set its birefringence. This configuration, which enables to spatially control the polarization of a laser beam, will be further detailed later in this thesis.

Figure 1.21: Nematic liquid-crystal Spatial Light Modulator (SLM) from Hamamatsu Photonics K.K. This SLM is made of reflective liquid-crystal pixels arranged in a two-dimensional array. The SLM is driven by a controller which provides the appropriate voltage required to drive the liquid-crystal pixels.

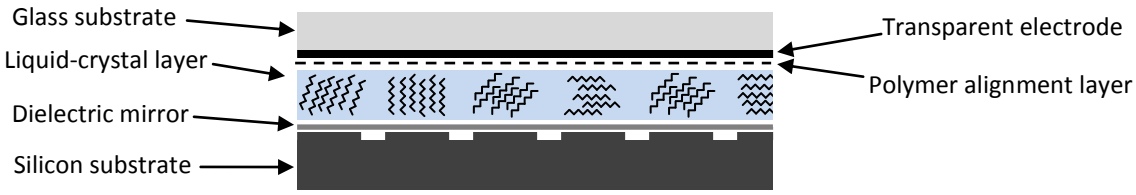

Figure 1.22: Cross sectional representation of the LCOS-SLM device. The device is made from a glass substrate, a transparent electrode, alignment polymer films, a layer of nematic liquid-crystals, a dielectric mirror and a silicon substrate.

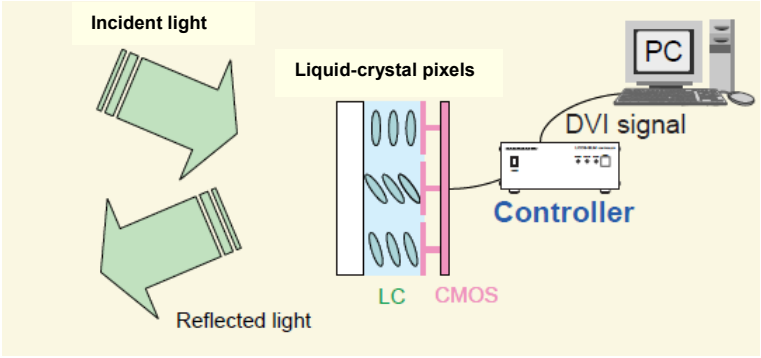

Figure 1.23: Schematics showing a cross-section of the liquid-crystal pixels of the SLM (three pixels are shown here). The liquid-crystals are sandwiched between a reflective CMOS chip in the pack-plane (in pink on the right) and a transparent film in the front (in white on the left). Applying an electric field to the liquid-crystals changes their orientation. This, in turn, affects the optical properties of the incident light. This schematic is taken from www.hamamatsu.com.

1.5 This thesis

This thesis presents a study of ultrafast laser micro-processing using advanced, liquid-crystal-based technologies for controlling the state of polarization of the laser beam and improve the processing efficiency and quality.

In this chapter, I have given a basic introduction to the relevant fields of optics and laser engineering. In Chapter 2, I introduce advanced optical measurement methods to analyze the phase and polarization response of the optical setups designed in this thesis. In Chapter 3, I use a polarization rotation device to control the polarization direction dynamically during laser processing of stainless steel. In Chapter 4, I present an optical setup which enables to produce Cylindrical Vector Beams. Chapter 5 details an analytical method to model the state of polarization in the focal region of the optical setup presented in Chapter 4. Chapter 6 details the experimental results obtained when micro-machining stainless steel plates with the optical setup shown in Chapter 4. The final chapter (Chapter 7) sums up the results presented in the rest of this work and maps out potential future industrial applications. A number of areas where future studies could enable to further improve the quality and efficiency of micro-processes are suggested.

2

Innovative optical diagnostic techniques: verifying phase stability of SLMs and analyzing polarization

2.1 Introduction

Polarization and phase are physical quantities which cannot be measured easily. To characterize the polarization and phase of a laser beam, indirect methods have to be used (see for example S. F. Nee, 2000 and P. Schlup *et al.* 2008). In the research presented in this thesis, innovative optical setups are designed to control the polarization and phase of laser beams. In order to characterize these optical designs, their polarization and phase response under various experimental conditions has been measured, using indirect methods.

The state of polarization in the focal region of the optical setups presented in this thesis is of particular importance and needs to be analyzed. In the experimental methods described in the literature (see for example P. L. Fuhr, 1984), the polarization of a laser-based optical setup is always analyzed in the regions of the beam path where the beam is collimated i.e. before any focusing optics. Several types of polarizing filters can be used to analyze a collimated beam. For example a Glan-laser polarizing filter produces an excellent polarization purity by splitting the beam between its *s*- and *p*-polarized components, using the differential in reflectivity between *s*-and *p*-polarization at Brewster's angle in a calcite crystal. However this method is only appropriate for analyzing the polarization of a collimated laser beam, not that of a focused beam. Although some experimental methods have been demonstrated for studying the focal properties of beams with various polarization modes (for example Y. H. Fu *et al.* 2003), no experimental methods exist for analyzing polarization in the focal region of an optic. On the other hand, several theoretical models have been proposed to predict the state of polarization in the focal volume of various optics using numerical methods (see for example J. Lekner, 2003 and Q. Zhan & J. R. Leger, 2002). However, these theoretical methods cannot be verified experimentally. To analyze the state of polarization in the focal region of an optical setup, a new experimental method is required.

This chapter presents a novel technique for analyzing polarization in the focal region of an ultrashort-pulse laser processing system. This technique involves using ultrashort laser pulses to produce wavelength-sized Laser Induced Periodic Surface Structures (LIPSS) on the surface of stainless steel samples placed at, above or below the focal plane. As LIPSS develop in a direction orthogonal to that of the local polarization vectors (Z. Guosheng *et al.* 1982), they enable one to deduce indirectly the local polarization vector field at any given plane of interest. The advantages and limitations of this technique are discussed and several experimental examples are given in Section 2.2.

In this thesis, novel optical setups based on SLMs are introduced and implemented in ultrafast laser processing benches. Various configurations of these optical setups are used in Chapters 3, 4 and 6. As the average beam power P available on the ultrafast laser processing benches was generally limited to P<0.5W, these experiments had therefore to be carried out using low average powers. However, industrial applications often use high-average-power laser beams (P>5W). If high-average-power beams were to affect the optical properties of the SLMs (e.g. by inducing phase instability), it would invalidate the transferability of this research to industry. Hence the compatibility of SLMs with high-average-power beams needs to be demonstrated. An SLM works by modulating the phase of a laser beam. Demonstrating that exposure to high-average-power beams does not affect the phase modulation induced by an SLM would establish the transferability to industry of the experimental results presented in Chapters 3, 4 and 6. Therefore, the SLMs used in this research need to be tested at high average-power and a phase diagnostic of the beam is required. As the ultrafast laser processing benches used in Chapters 3, 4 and 6 do not have sufficient average beam power, a high-average-power nanosecond-pulse laser source is used to test the phase stability of the SLM.

Measuring the phase of a laser beam is more complicated than measuring its polarization. One method for analyzing a beam phasefront is using a Shack–Hartmann sensor, where the beam is passed through a two-dimensional array of tiny lenses followed by a CCD detector. The local tilt of the phasefront causes a shift in the position of the focal spot on the CCD detector. The phase of the original beam can be reconstructed by measuring the focal spot shift in each location (see for example S. G. Garanin *et al.* 2012). However, this type of detector is sensitive to high-average-power beams. Implementing a Shack-Hartmann sensor in the laser bench used for high-average-power tests is therefore complicated.

To measure the phase stability of the SLMs used in this research, an alternative method is used. An SLM is programmed to induce a phase grating that splits the beam between a zero- and a first-order beam. The SLM is then exposed to a high-average-power beam for several hours and the diffraction efficiency monitored for the duration of the experiments. The observed variation of the diffraction efficiency gives an indication of the stability of the phase modulation induced by the SLM. The details of this technique, the experimental results and the applicability to industry of the SLM-based optical setups are discussed in Section 2.3.

2.2 Development of a novel polarization mapping technique

2.2.1 Laser Induced Periodic Surface Structures (LIPSS)

Spontaneous periodic surface structures produced by laser irradiation of a solid material close to its ablation threshold have been widely observed since the early 1970s. Henceforth in this thesis, I refer to them as Laser Induced Periodic Surface Structures (LIPSS). As detailed in the literature (see for example Z. Guosheng *et al.* 1982), LIPSS have been produced on metals, semiconductors and dielectrics. They always develop initially along a direction perpendicular to that of the local polarization vector and their period is often close to the wavelength of the incident laser beam. Early research focused on characterizing LIPSS under various experimental conditions, and explaining the physical phenomenon that produced them. Although a variety of mechanisms had been suggested to explain their formation, it

is now widely acknowledged that they are produced by the interference between the incident laser beam and the surface scattered wave (see R. Le Harzic *et al.* 2011). As LIPSS are now well understood, more recent research focused on making use of LIPSS in various applications. For example, diffractive gratings were produced on titanium in L. Mellor (2011). The tribological properties of surfaces textured with LIPSS for mechanical lubrication applications were also studied in J. Eichstadt *et al.* (2011).

Thanks to their size close to laser wavelength and their orientation perpendicular to polarization, LIPSS can also be used as a high-resolution diagnostic tool to check the local state of polarization in the focal region of a focused laser beam. In this chapter, I will show that LIPSS are a useful tool for verifying the polarization properties of the optical setups presented in this thesis.

2.2.2 Experimental setup

To demonstrate that LIPSS can be used as a polarization mapping tool, I used a micro-processing bench with a Clark-MXR CPA2010 femtosecond-pulse laser source. The laser has a minimum pulse width of 160fs, a 775nm central wavelength, a spectral bandwidth of 5nm, a 1mJ maximum pulse energy, a 1kHz pulse repetition rate and a horizontal linear polarization. The laser output was attenuated by a half-waveplate and a Glan laser polarizer. A quarter-waveplate was used to produce either a linear or circular polarization. As shown in Figure 2.1, after reflection on Mirrors 3 and 4 the beam entered the 10mm aperture of a scanning galvanometer system (made by GSI Lumonics) with a flat field lens (f = 100mm, NA=0.03), driven by a programmable PC interface board (Scanlab). Samples were mounted on a precision 4-axis (x, y, z, θ) motion control system (Npaq system, produced by Aerotech) allowing accurate positioning of the sample in the focal plane.

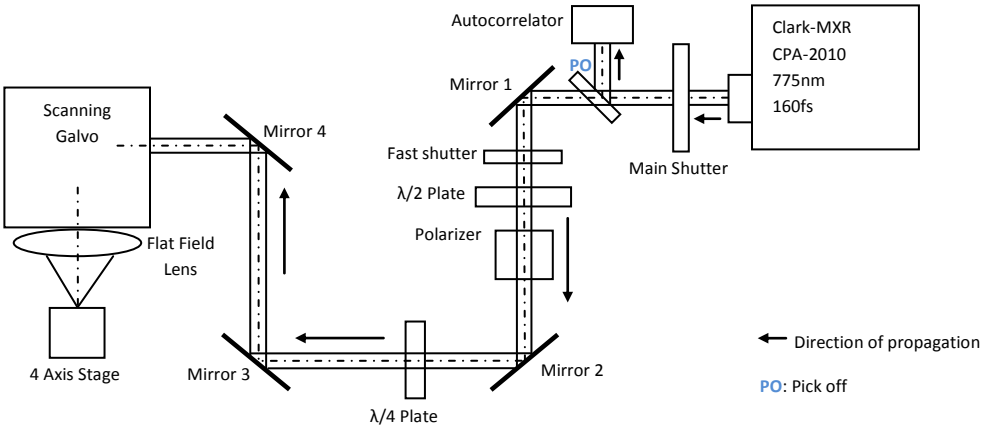

Figure 2.1: Schematic of the experimental setup used to produce LIPSS on stainless steel samples. The quarter-waveplate fast axis is rotated to produce either a linearly or a circularly polarized beam.

2.2.3 Mapping the polarization in the focal region of a laser beam

To produce the LIPSS, the polished surface of a stainless steel work-piece was marked with the laser pulse energy attenuated to 6µJ (1.8J/cm²), using the setup described in Figure 2.1. Each point was exposed to ~15 laser pulses, producing spot diameters of 40+/-5µm. In this thesis, a wider focal spot is desirable as it is convenient for micro-processing larger areas. The fast axis of the quarter-waveplate (Figure 2.1) was oriented to produce a linearly or circularly polarized beam in turn.

After processing, I analyzed the laser-marked spots with an optical microscope. Figure 2.2-a shows the LIPSS within the laser spot produced with a linearly polarized beam. The LIPSS formed as recurring linear structures oriented perpendicular to the direction of polarization. This is consistent with the experimental results described in the relevant literature (such as R. Le Harzic *et al.* 2011). Figure 2.2-b shows the laser spot produced with a circularly polarized beam. No structures could be clearly identified within the spot. LIPSS are absent in this case because the direction of the polarization vector rotates many times within each femtosecond laser pulse, preventing the formation of LIPSS (Z. Guosheng *et al.* 1982).

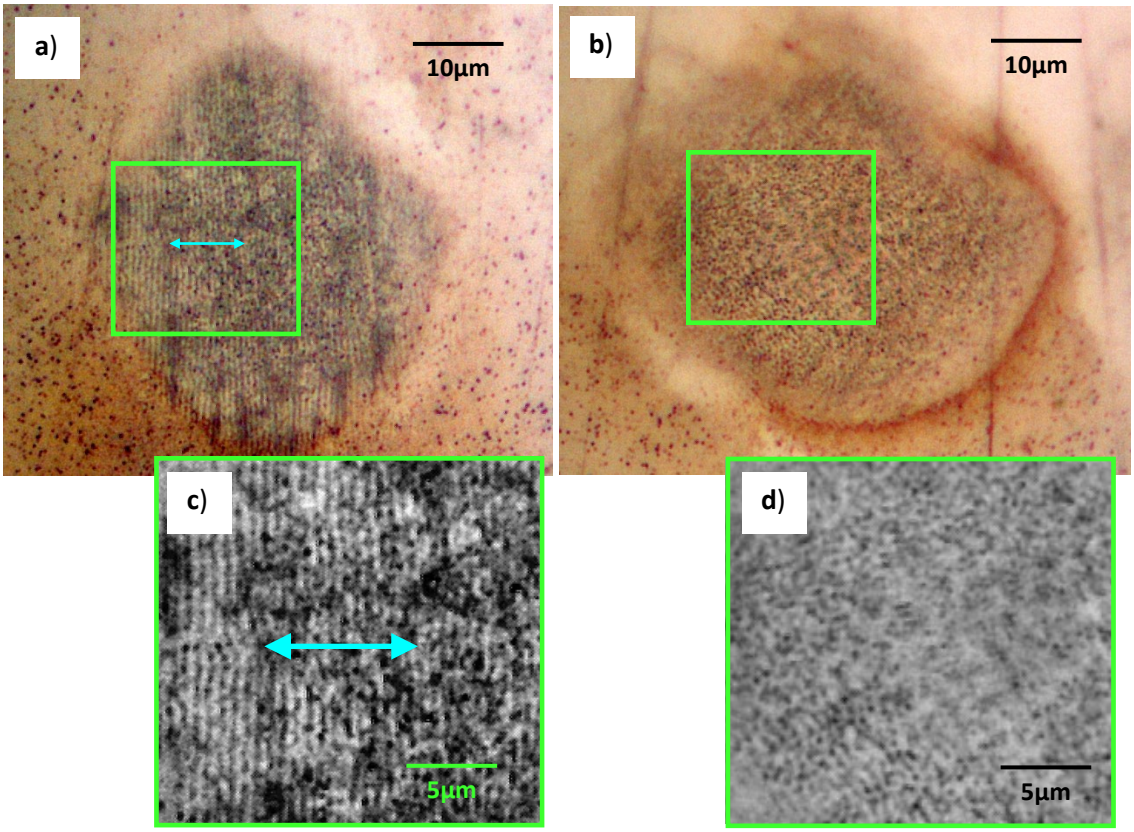

Figure 2.2: Optical micrographs showing laser-marked spots produced on a stainless steel surface by 15+/-5 femtosecond pulses at energy E=6µJ per pulse (1.8J/cm²). A linearly polarized beam was used in **(a)**, where the blue arrow indicates the polarization direction. A circularly polarized beam was used in **(b)**. The highlighted areas (green rectangles) are magnified in **(c)**: linear polarization and **(d)**: circular polarization. Only the linear polarization produced clearly visible LIPSS, oriented perpendicular to the direction of polarization.

The results in Figure 2.2 confirm that, thanks to LIPSS, a microscopic analysis of laser-marked spots enables us to find out the state of polarization at the focal plane of a laser micro-processing setup. For example, we can discriminate between circular and linear polarization, or determine the direction of incoming linear polarization. However, experimental evidence also shows that if the incident polarization is elliptical with a strong elongation (for example if the ellipse that describes polarization has its axial-ratio < 0.3), the LIPSS develop perpendicularly to the long axis of the ellipse. This makes it difficult to discriminate between linear polarization and an elliptical polarization with a strong elongation and could be seen as a limitation in this method of analyzing polarization. For material processing, an elliptical polarization with a strong elongation (i.e. an ellipse with axial ratio < 0.3) couples almost in the same way (within 10%) as a linear polarization oriented parallel to the long axis of the ellipse (Figure 2.3). The irradiance induced from the electric field component oriented parallel to the long axis of the ellipse carries over 90% of the total beam irradiance in such a case. Hence this drawback is not considered too problematic, as far as material processing is concerned.

LIPSS can be used for analyzing a static, uniform polarization at the focal plane, as shown in Figure 2.2 above. However, they are especially powerful when analyzing complex, structured polarization modes such as CVBs. Thanks to their small size (~λ), LIPSS enable high-resolution analysis of the structure of CVBs in the focal regions. In the example shown in Figure 2.4, from U. Klug *et al.* (2010), the space-dependent structures of the polarization vectors at the focal plane are clearly visible. This method will be further detailed in Chapter 4.

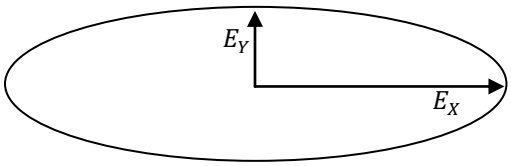

Figure 2.3: Schematic representing an elliptical polarization, where $E_X$and E_Y are the electric field vectors along the long and short axis respectively. In this example we define $E_X = 3 \times E_Y$. By definition, the irradiance components induced from the electric field vectors E_X and E_Y, are $I_X = {E_X}^2$ and $I_Y = {E_Y}^2$ respectively. Furthermore, we have ${E_X}^2 = 3^2 \times {E_Y}^2$. Therefore we can write $I_X = 9 \times I_Y$. This means the overall irradiance is dominated by its component I_X.

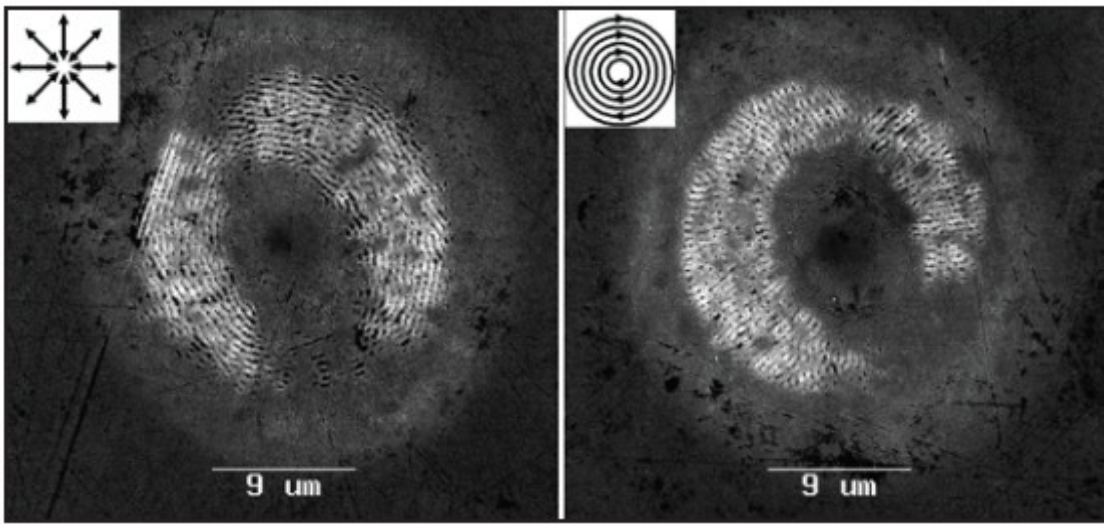

Figure 2.4: SEM images of steel surfaces exposed to picosecond-laser pulses (532nm) with radial (left) and azimuthal (right) polarization. These images are taken from U. Klug *et al.* (2010).

2.2.4 LIPSS as a dynamic polarization diagnostic

Some industrial laser processes, such as *polarization trepanning*, use a linear polarization with a direction that varies during the scanning of the laser beam. An example of this is shown in Figure 2.5-a. LIPSS can be produced at low pulse energies prior to laser machining, to check the appropriate orientation of polarization in each region of the beam path. This enables one to calibrate a laser processing bench and verify the polarization of a focused beam along a chosen scanning path.

To demonstrate this, a polished stainless steel surface was processed with the beam scanning path shown in Figure 2.5-a, using the femtosecond-pulse laser processing bench described above (see Figure 2.1). In this case the quarter-waveplate was replaced with dynamic polarization optics, which are further detailed in Chapter 3. The pulse energy was attenuated to E=5µJ per pulse (1.5J/cm²) and the chosen scan speed was 2mm/s. The overall exposure to the laser beam was around 1 second, corresponding to approximately 10 overscans. After processing, the produced laser beam track was analyzed with an optical microscope. A high-resolution optical micrograph of the beam track is shown in Figure 2.5-b.

The microscopic analysis allowed me to verify the direction of the LIPSS in each region of the beam path and to confirm the relevant orientation of the polarization. However, this method involves using a high-magnification microscope and can be time consuming. To stream-line the verification process, I used the diffractive properties of the LIPSS (which were studied in details in L. Mellor, 2011). When the laser track was illuminated with low-angle lights located on either side of the sample, only the regions where the polarization was parallel (i.e. where the LIPSS were perpendicular) to the direction of illumination diffracted the light and were visible in the microscope images (Figure 2.5-c). This method enables one to quickly check the polarization configuration of several beam tracks simultaneously without the need for high-magnification microscopy. In the example shown in Figure 2.6, several beam tracks were produced. The experimental parameters were similar to those used to produce the beam track shown above in Figure 2.5, except for the direction of polarization within the beam path, which was varied between each track shown in Figure 2.6. For each of these tracks, a synchronization delay is introduced between the polarization rotation optic and the beam scanning optics.

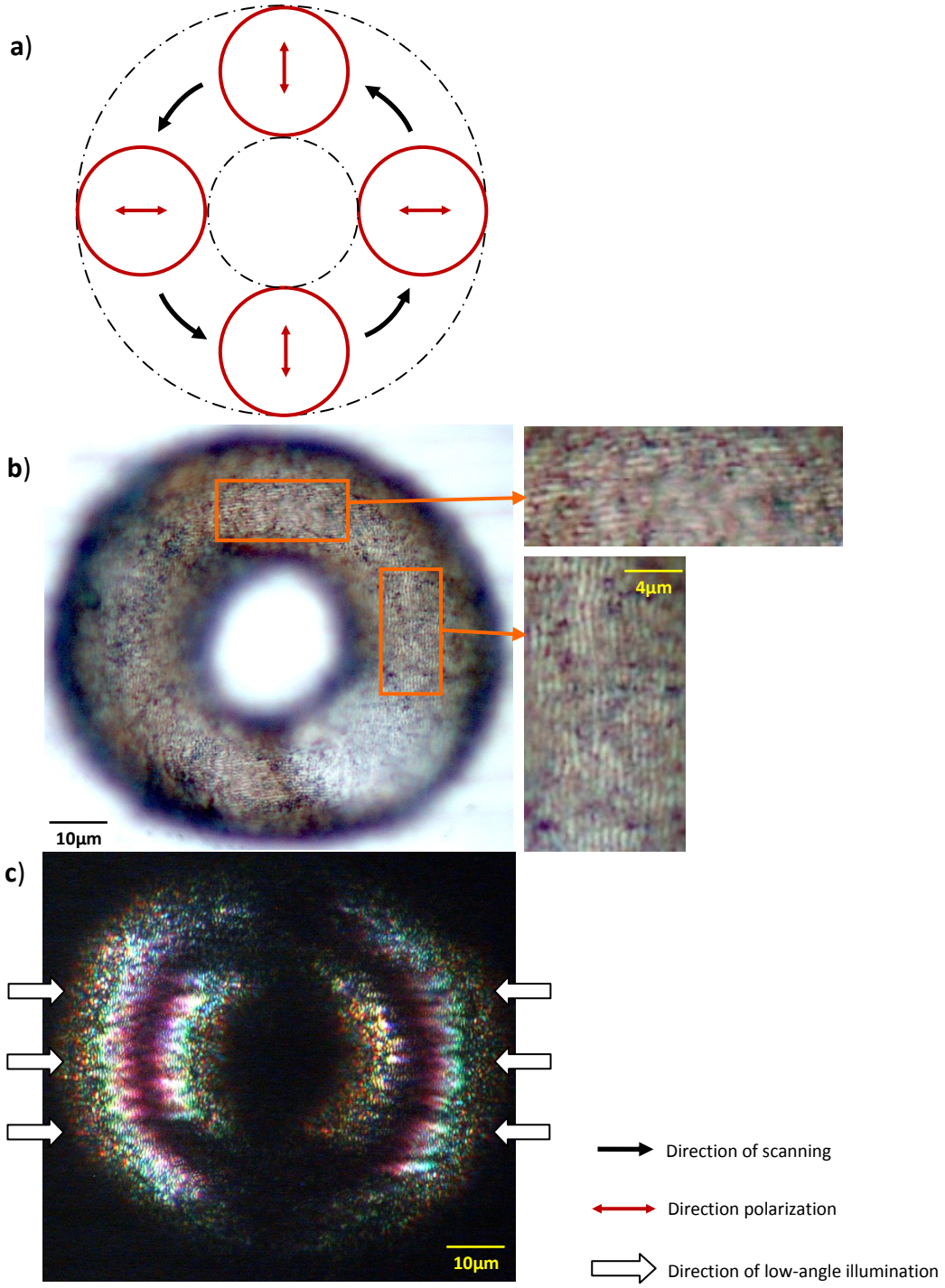

Figure 2.5: (a) Schematic showing the laser beam scanning path (black arrows). The direction of polarization in each region of the beam path is also shown (red arrows). **(b)** Optical micrographs showing the laser beam track produced on a stainless steel surface by scanning at 2mm/s with 5µJ per pulse (1.5J/cm²), for 1s (~10 overscans). **(c)** Optical micrograph showing the laser beam track under low-angle side illumination (white arrows). Thanks to the diffractive properties of the LIPSS (L. Mellor, 2011), only the regions of the beam track with a polarization parallel to the direction of illumination reflect the low-angle light. It is noted that, as the centre of the beam track is deeper than the edges, it reflects less light.

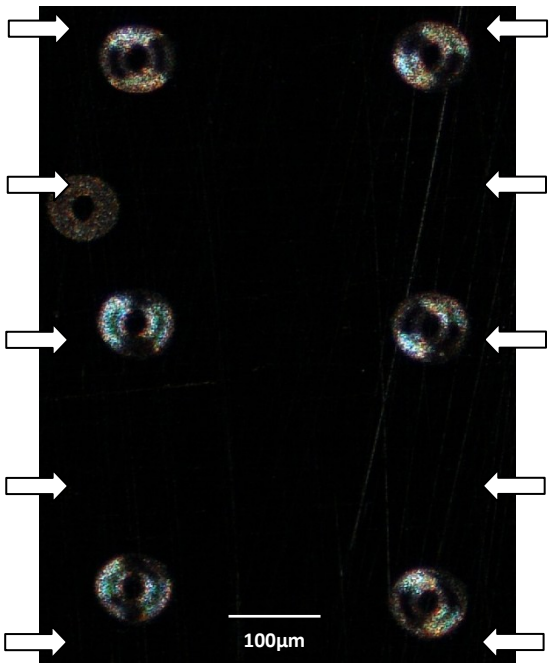

Figure 2.6: Optical micrograph showing several circular laser beam tracks under low-angle side illumination (white arrows). Thanks to the diffractive properties of the LIPSS, the polarization configuration of each track can be quickly determined.

2.2.5 Discussion

In this section it was shown that LIPSS can be used to analyze the polarization in the focal region of a laser micro-processing bench, which is a notoriously difficult thing to do. Producing LIPSS requires applying ultrashort laser pulses to a surface, using laser fluences close to the ablation threshold of the material. As a consequence of incubation effects, the contrast of the LIPSS can be improved by applying several pulses to each region. For example, an overscan of 10 at the appropriate scan speed enables one to produce clearly visible LIPSS. The produced LIPSS' orientation is orthogonal to the polarization vectors of the beam and their pitch is similar to the wavelength. This method can be used for analysing a static, uniform polarization such as linear or circular at the focal plane. However there are several restrictions:

- An elliptical polarization cannot be characterized accurately using this method.
- This method can only analyse the transverse components of the polarization. Therefore, it is not accurate for analysing the polarization in the focal region of a high NA optic.
- This method cannot be used to analyse the polarization of collimated beams, since LIPSS can only be produced in the focal region of an optic, where the fluence is appropriate i.e. slightly above the ablation threshold of the target material.

In spite of these restrictions, this method is very powerful when analysing complex, structured polarization modes, or dynamically controlled polarizations, focused with a low NA lens. LIPSS enable to clearly visualize the state of polarization in the focal region. In this thesis, novel optical setups are designed to produce CVBs or dynamically controlled states of polarization and LIPSS are used to help characterizing and calibrating these new optical setups (see Chapters 3 and 4).

2.3 Diagnostic technique for verifying the phase stability of SLMs under high-average-power laser exposure

2.3.1 Aim of the experiment

The aim of the research presented in this thesis is to control the polarization and phase of laser beams to improve industrial micro-processes. In order to optimize efficiency, industrial processes often use high-average-power beams. These high-average powers can be incompatible with some of the delicate optics used in a research laboratory. Here, I will demonstrate that the optics I use for polarization and phase control are sufficiently robust to be used at high-average-power in an industrial environment. One of the key optics used in the experimental setups here is a phase-only liquid-crystal SLM from Hamamatsu. This type of SLM has often been used with low-average-power beams in a research environment, but its suitability for high-average-power (and hence industrial) use needs to be confirmed. An SLM works by modulating the phase of a laser beam. In this section I will verify if exposure to a high-average-power beam affects the phase modulation induced by an SLM. This is done by programming an SLM to induce a phase grating which splits the beam into a zero- and a first-order component. The resulting diffraction efficiency, which is defined as the power-ratio between first-order beam and full reflected beam (i.e. first-order plus zero-order), is used to evaluate the stability of the phase modulation. A fluctuation of diffraction efficiency as a result of a long exposure to a high-average-power beam would imply that the phase modulation is affected by the exposure to the beam. Here, the diffraction efficiency is measured while the SLM used in this experiment is exposed to a laser beam with 8W of average power for 4.5 hours.

2.3.2 Experimental setup

Figure 2.7 shows the optical setup used to check the phase stability of the SLM. A 532nm, 150ns pulse laser beam set at 8W of average power output is incident on a reflective phase-only SLM from Hamamatsu (model X10468-04). The SLM induces a diffractive phase grating which splits the reflected beam into a zero-order beam and a first-order beam. After the SLM, an iris is used to discriminate the first-order beam against the zero-order beam. When the iris aperture diameter is reduced, only the first-order beam is transmitted, while the zero-order beam is blocked. When the iris aperture diameter is at its fully open position, both the zero- and first-order beams are transmitted (i.e. the full beam power reflected from the SLM). A power meter is placed after the iris to measure either the first-order or the full reflected beam power, depending on the chosen aperture of the iris. A beam splitter is also inserted in the beam path before the SLM to pick-off a fraction of the beam. Another power meter measures the power from this beam pick-off. In this way, the stability of the output from the laser source can be verified during the experiment. The readings from the three power measurements are plotted against the duration of exposure in Figure 2.8-a. A slight increase in all three power readings is noted in the first 30 minutes. This is due to a ~5% power increase in the output from the laser source, demonstrated by the power measurements from the pick-off (not visible in Figure 2.8 due to the chosen scale). It is therefore irrelevant to this experiment. A value for the diffraction efficiency is derived by dividing the

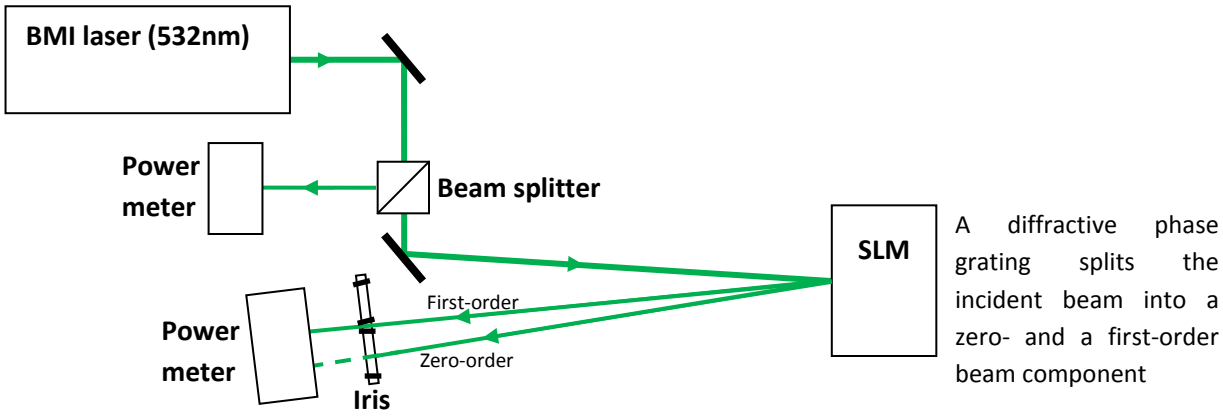

Figure 2.7: Schematic showing the experimental setup used to check the phase behavior of the SLM under high-average-power laser exposure. The laser source is a 532nm, 12kHz repetition frequency, 150ns pulse laser. For these tests, the average output power is set at 8W. The iris aperture diameter is reduced to measure the first-order beam power, or fully open to measure the full reflected beam power.

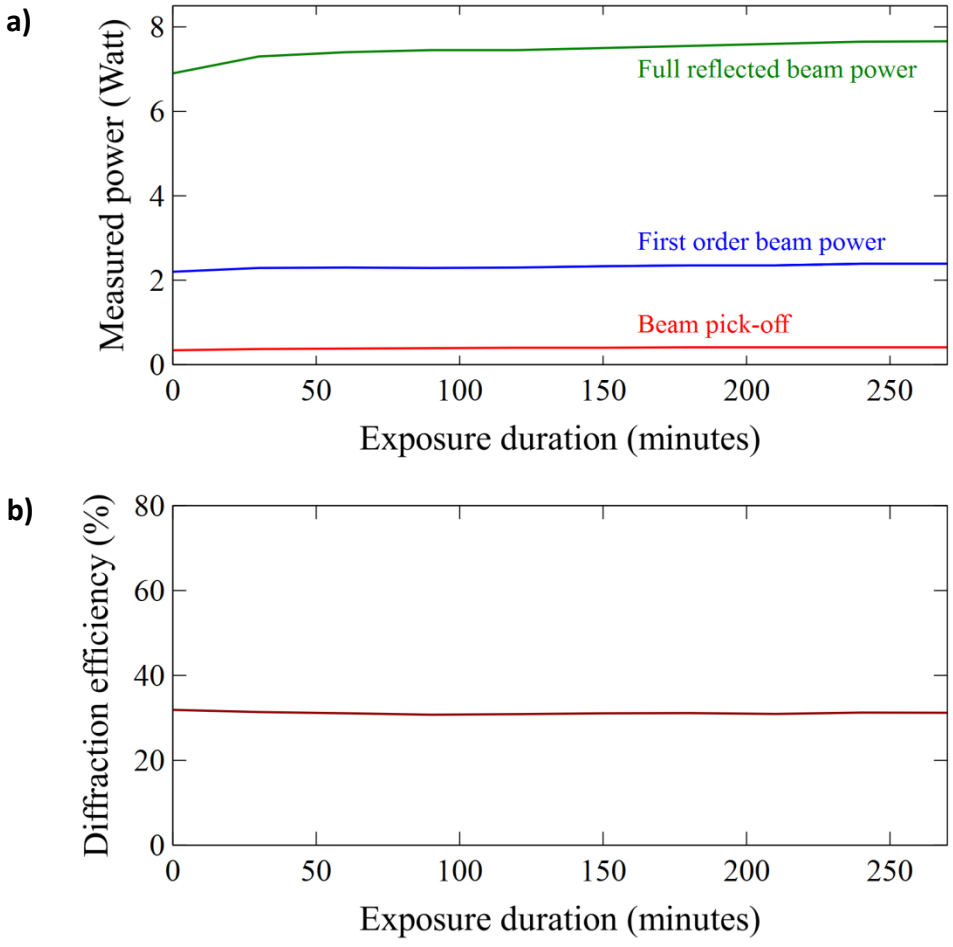

Figure 2.8: (a) Power meter readings during laser exposure. **(b)** Diffraction efficiency derived from the power measurements.

power value for the first-order beam by that of the full reflected beam. The diffraction efficiency is plotted in Figure 2.8-b.

2.3.3 Results and discussion

It can be seen from Figure 2.8-b that the diffraction efficiency is relatively stable (within +/-3.5%) over the duration of the exposure (4.5 hours). If the phase response of the SLM was affected by a continuous high-average-power laser beam exposure at the 8W level, the diffraction efficiency would be expected to change significantly. As the diffraction efficiency remains reasonably constant for the duration of the experiment, we can conclude that the phase response of the SLM is unaffected under these experimental conditions.

Here, I have demonstrated that the SLMs used in this research are compatible with an average beam power of 8W, which is representative of the average-power used in some industrial applications. In the rest of this thesis, the experiments that use SLMs will involve lower average beam powers. However the experimental results above give confidence that the SLM-based optical setups introduced in this thesis are potentially transferable to industrial applications.

In the rest of this thesis, several experiments use SLMs exposed to high-peak-power ultrashort-pulse laser beams (with a low average-power P<3W). The phase modulation induced by the SLMs has remained constant throughout and no optical damage has been noticed on the active liquid-crystal layers of the SLMs. As for high-average-power beams, there is no evidence to suggest that high-peak-power beams affect the phase response of the SLMs in these experiments. It is noted that Hamamatsu has tested its SLMs to peak power densities above 10GW/cm² without producing any damage to the liquid-crystal layers.

2.4 Chapter summary

The conclusions of this chapter will be discussed in Chapter 7, but as an *aide-mémoire*, they are outlined briefly here.

- I have detailed two original optical diagnostic techniques which are relevant throughout this thesis. These techniques enable me to characterize some of the polarization and phase properties of the new optical setups designed as part of my research.

- A polarization mapping technique enables one to analyze polarization by imprinting LIPSS on a sample placed in the focal region of a low NA lens. This technique can be used to visualize the state of polarization of CVBs around the focal region. It can also be used to calibrate a laser processing bench where dynamic polarization control is used to vary the direction of polarization along the beam scanning path.

- A phase analysis technique involves high-power testing of the SLMs used in my research to confirm their ability to sustain high-average beam powers without influencing their phase modulation properties. In this way I have demonstrated that the SLMs, which are a key element used in several setups in this thesis, are suitable for high-average-power industrial applications.

3
Real-time control of polarization

3.1 Introduction

The key parameters influencing the quality and efficiency of a laser process are the fluence, pulse duration, wavelength, beam quality and polarization (P. S. Banks *et al.* 1999, S. Hahne *et al.* 2007). The influence of polarization on micro-machining has been demonstrated experimentally in S. Nolte *et al.* 1999, showing that drilling high-aspect-ratio (depth/diameter) microscopic holes in metal with linearly polarized ultra-short-pulse lasers produces anisotropic profiles. This is due to the higher reflectivity of the *s*-polarized radiation, relative to the *p*-polarized radiation (S. Nolte *et al.* 1999). As the hole develops through the material, the *p*-polarized radiation is more readily absorbed by the sidewalls, whereas the *s*-polarized radiation tends to be reflected down to the base of the hole. This results in a distorted intensity profile, affecting the shape of the hole when the beam reaches the exit side. The simplest way to reduce these distortions is to use a circularly polarized beam, which removes the differential in reflectivity during drilling. In some cases however, the remaining distortions associated with circular polarization are problematic. In particular, ripple formation on the surface of the side wall cannot be avoided (C. Föhl & F. Dausinger, 2003). Another aspect of importance for micro-machining is the laser process efficiency. The influence of polarization on this has been studied for example in V. G. Niziev & A. V. Nesterov, 1999 and in F. Dausinger & J. Shen, 1993. When drilling or cutting high-aspect-ratio microscopic features, neither circular nor static linear polarization offers the optimum process efficiency.

To overcome these limitations, a technique referred to as *polarization trepanning* was developed (S. Nolte *et al.* 1999). It consists of rotating linear polarization during drilling, further improving the hole quality (see for example H. K. Tönshoff *et al.* 2000). The trepanning optic developed in C. Föhl *et al.* 2003 produced holes of remarkable quality using this technique. However, these methods involve mechanical rotation of optical components and could be adversely affected by vibrations and prone to mechanical failure, leading to potentially expensive maintenance. An alternative laser-specific polarization switching method is detailed in S. Hahne *et al.* 2007. It is based on an intra-cavity polarization chopper wheel synchronised to the laser pulse train. However, as this method requires the laser cavity to be re-designed, it cannot be easily applied to existing laser systems.

In this chapter, I introduce a flexible method for rapidly switching the linear polarization of a laser beam between two orthogonal directions during micro-processing, using a fast-response liquid-crystal polarization rotator. This novel method provides an alternative to those mentioned above, resolving the issues related to linear polarization (poor process quality), circular polarization (ripple formation and poor process efficiency) and the traditional method of *polarization trepanning* (reliance on mechanical rotation stages). As a proof of principle, helical drilling and cutting tests were performed on stainless steel sheets using various polarization configurations. Experimental results using a femtosecond laser

show a consistent improvement in the micro-processing quality compared to that produced by linear polarization configurations.

3.2 Experimental setup

A schematic of the experimental setup is shown in Figure 3.1. The output from a femtosecond laser (Clark-MXR CPA2010, with a minimum pulse width of 160fs, 775nm central wavelength, spectral bandwidth of 5nm, 1mJ maximum pulse energy, 1kHz repetition rate and horizontal linear polarization) is attenuated by a halfwave-plate and a Glan laser polarizer. The resulting linear polarized beam is incident on a transmissive, ferroelectric liquid-crystal polarization rotator developed by Boulder Nonlinear Systems, Inc. (MS Series). The liquid-crystal polarization rotator offers a switching frequency of up to 20kHz between two orthogonal output states, with a response time of typically less than 100µs. Varying the electric field applied to the device results in a non-linear rotation of the output polarization. The liquid-crystal device can be operated in a binary mode, where the polarization is periodically flipped between orthogonal directions, or operated in a quasi-linear mode. The polarization rotator is driven by a programmable, DC-balanced, periodic voltage signal from a function generator (Tektronix AFG3021B). After reflection on Mirrors 3 and 4 (see Figure 3.1), the beam enters the 10mm aperture of a scanning galvo system (GSI Lumonics) with a flat field lens (f = 100mm), driven by a programmable PC interface board (Scanlab). Samples are mounted on a precision 4-axis (x, y, z, θ) motion control system (Aerotech Npaq) allowing accurate positioning of the sample at the laser focus.

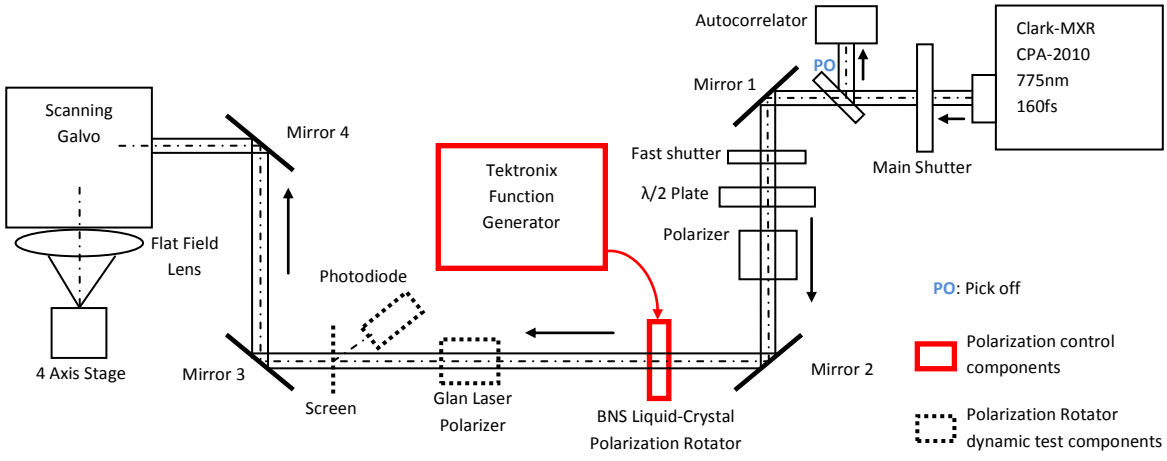

Figure 3.1: Micro-machining experimental setup showing how the liquid-crystal polarization rotator was used. For the processing tests, the dashed components were removed.

3.3 Proof of concept

This section describes how some of the optical characteristics of the polarization rotator were tested.

3.3.1 Testing response time

The response time of the liquid-crystal device was tested by placing a Glan laser polarizer behind it. Thus, a rotation in polarization direction was translated into a modulation of the amplitude transmitted through the polarizer. The resulting beam amplitude was measured with a photodiode (see dashed components in Figure 3.1). In order to obtain a clearer signal from the photodiode, the polarization rotator driving signal was synchronised with the 1kHz femtosecond laser pulse train. This was achieved by triggering the function generator with a synchronised TTL signal from the femtosecond laser's Pockels cell driver (DT-505). A DC-balanced, 4V peak-to-peak square-wave signal was programmed on the function generator, triggered by this synchronised signal. Oscilloscope traces from the photodiode and the driving signal of the liquid-crystal device are shown in Figure 3.2. When the driving voltage is positive (+2V), the resulting polarization is parallel to the transmission axis of the Glan laser polarizer. The transmitted laser pulse train measured by the photodiode shows a residual amplitude shift due to the inertia of the liquid-crystal device. When the driving voltage is negative (-2V), the laser pulse train is blocked by the polarizer. The response time of the polarization rotator was found to be less than 0.5ms (manufacturing specification: 0.1ms). In the Clark laser system, the period between each femtosecond pulse is ~1ms (1kHz repetition rate). The response time of the liquid-crystal device is therefore sufficient to provide accurate control over the polarization direction of each individual pulse. When a polarising filter is placed behind the liquid-crystal rotator, this pulse-train-synchronised mode enables dynamic pulse-to-pulse amplitude control, with potential applications in surface machining of periodic structures.

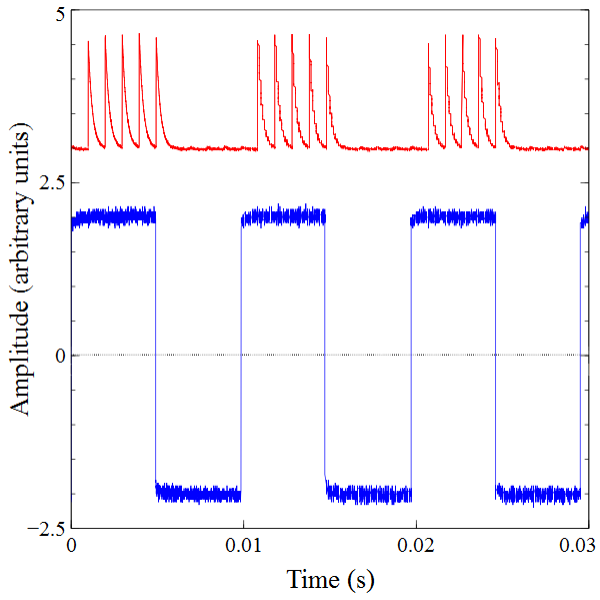

Figure 3.2: Oscilloscope traces showing the amplitude of the femtosecond pulse train (output signal from the photodiode in red on top) modulated by a polarization rotator with a Glan laser polarizer behind it (driving signal in blue at the bottom).

3.3.2 Polarization diagnostic

In this section, I demonstrate that *polarization trepanning* is achievable with the liquid-crystal device. *Polarization trepanning* requires synchronising the polarization rotation with the beam scanning motion so that the direction of polarization is constantly perpendicular to the direction of scanning (C. Föhl & F. Dausinger, 2003). This is normally achieved by placing a wave-plate in the optical path and mechanically rotating it with the beam. In order to obtain a similar effect, the driving signal from the function generator was synchronised with the galvo scanning head (see Figure 3.1). The test procedure described in Chapter 2 was used to visualise the direction of polarization along the scanned beam paths, using the setup shown in Figure 3.1 (without the dashed components). These tests make use of LIPSS, which provide a marker for the direction of polarization of the incoming laser beam (see Section 2.2.4 in Chapter 2).

Due to its design characteristics, the response time of the liquid-crystal device is shorter when the polarization is flipped between two perpendicular directions and longer when it is gradually rotated. The former case applies a DC-balanced square-wave driving signal, the latter applies a sinusoidal one. In the tests described here, a square-wave signal was used to obtain the best polarization switching speeds. Synchronisation routines were programmed into the PC interface board driving the galvo head to maintain the desired polarization state while scanning along pre-defined geometries on a steel sample surface (Figure 3.3-a). The scanning programmes were run with the laser pulse energy attenuated to 2μJ and the sample was exposed to the laser beam for a few seconds. As a result, LIPSS were produced and then imaged with an optical microscope (Figure 3.3-b).

As detailed in Chapter 2 (Section 2.2.4), the microscopic investigation of the resulting figures used low-angle illumination to distinguish between the two directions of laser polarization that produced the LIPSS. Two illumination sources were used, located on each side of the sample, with the axis of illumination set parallel to one of the polarization directions and perpendicular to the other. Due to the diffractive properties of the LIPSS, only the direction of polarization parallel to the direction of illumination reflected the low-angle light (see Figure 3.3-c), the other remained dark. Therefore, each microscope image shows the part of the scanned geometry that reflected the illumination. Rotating the axis of illumination by 90˚ reveals the remainder of the scanned geometry (Figure 3.3-d). These tests demonstrated that the desired direction of polarization had been successfully applied to each region, giving confidence that a good approximation of *polarization trepanning* is achievable using a liquid-crystal polarization rotator.

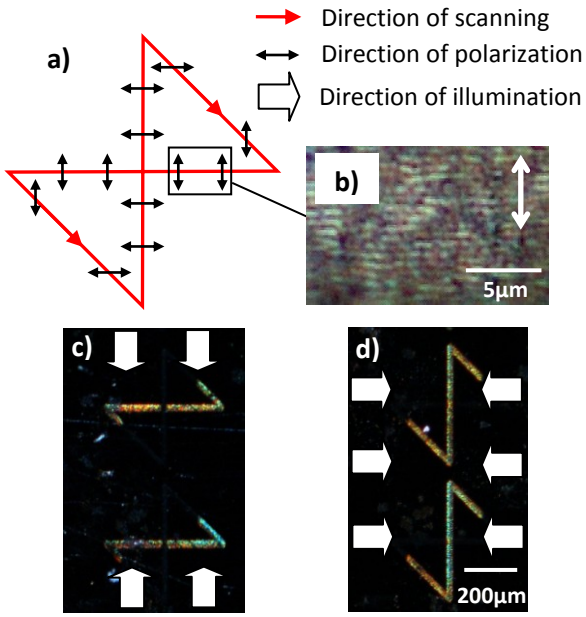

Figure 3.3: (a) Programmed laser beam path showing the expected state of polarization for each region. (**b**) LIPSS formation on the surface of the work-piece. The direction of polarization is indicated by the white arrows. **(c)** Optical micrograph of the scanned beam path after laser exposure, under low-angle illumination. **(d)** The same region after the illumination was rotated by 90˚, revealing the remainder of the scanned geometry.

3.4 Helical drilling

In helical drilling, the laser beam moves in a periodic fashion following a pre-defined geometry. As material is removed by each pulse, the beam works its way through the sample, as shown in Figure 3.4. If the chosen beam scanning motion is circular, the ablation front follows a helical path overall. The parameters influencing the geometry of the machined hole include the dimensions of the programmed beam path, the laser spot size and the polarization (C. Föhl & F. Dausinger, 2003).

To check the benefits of using a liquid-crystal polarization rotation device in helical drilling, tests were performed on 380µm thick, type 302 (austenitic chromium-nickel alloy) stainless steel samples in air, using circular and square beam paths. Prior to the tests, the sample surfaces were polished to a 320 grade abrasive grit.

3.4.1 Circular beam path

Circular beam paths with diameters of 65µm and a 5mm/s scan speed were programmed into the PC interface board driving the scanning galvanometer. A laser pulse energy of 75µJ was used, corresponding to a peak fluence of ~24J/cm², much higher than the ablation threshold which is around 0.16J/cm² for stainless steel (P. Mannion *et al.* 2003). This fluence value was appropriate since it produced a high ablation efficiency and low thermal damages. The focal spot diameter (calculated where the intensity has fallen to $1/e^2$ of its central peak value) is 30µm and the focal depth is ±300 µm. The sample was placed on a holder on the multi-axis motion control stage (see Figure 3.1), so that the focal plane lied ~100µm below the sample top surface. The chosen drilling time per hole was 150s. The

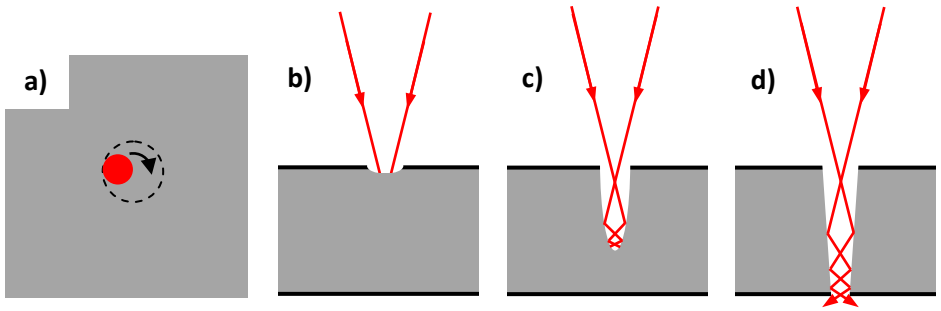

Figure 3.4: (a) Schematic showing a helical drilling process, where the laser beam scans with a circular motion. **(b)** Initially, the laser ablation occurs with a nearly normal beam incidence. **(c)** As the ablation front penetrates deeper, internal reflections occur at increasingly large incidence angles. **(d)** Once the hole is fully developed, multiple internal reflections occur with a high incidence angle. The state of beam polarization, which strongly influences reflectivity at high incidence angles (see Figure 1.15 in Chapter 1), affects the efficiency and quality of the process.

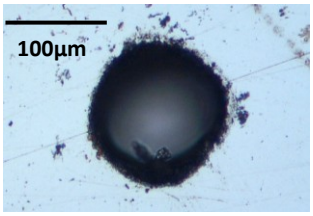

Figure 3.5: Optical micrograph of the hole entrance. The shape of the hole does not depend on polarization.

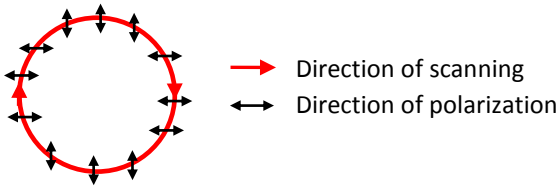

Figure 3.6: Laser scanning path with corresponding direction of polarization used in *polarization trepanning*.

test strategy consisted of using the various polarization modes available with the liquid-crystal polarization rotator, varying the operating parameters to improve circularity and reduce the taper of the micro-holes. Linear and circular polarized beams were used to provide comparative data for subsequent tests. The experimental configuration of the setup for each test is summarised in Table 3.1. It is noted that each drilling test was performed a number of times and the figures in Table 3.1 were obtained by averaging the results from all the tests.

All these tests produced tapered holes with an entrance opening diameter of typically 110±10μm. The entrances of the holes showed no dependence on polarization, but were slightly elliptical in shape due to the slight astigmatism of the incident laser beam profile (Figure 3.5). On the exit side, the shape and taper of the holes varied with polarization, with a typical half-angle sidewall taper ranging between 4˚ and 5˚ and a diameter of typically 65±10μm. A summary of the test results as well as optical micrographs of the exit holes for the various polarization modes are given in Table 3.1.

3.4.1.1 Linear and circular polarizations

Drilling with a linearly polarized laser beam produces elliptical exit holes, elongated in the direction of the polarization vector (see Table 3.1). As the laser beam reflects against the internal sidewalls during drilling, the light is *p*-polarized in the regions where the sidewalls are perpendicular to the polarization vector (i.e. where the plane of incidence is parallel to the polarization vector) and *s*-polarized in the regions where the sidewalls are parallel to it (i.e. where the plane of incidence is perpendicular to the polarization vector). The laser energy is more readily absorbed in the regions with *p*-polarization, producing more ablation which results in an elliptical profile with a long axis parallel to the polarization vector. *s*-polarization tends to be reflected down to the base of the hole. As the sidewalls are not optically flat, these internal reflections sometimes produce distortions around the exit hole, perpendicular to the polarization vector as can be seen on the hole drilled with a linearly polarized beam in Table 3.1. As expected, circular polarization produced a clear, circular hole exit due to the isotropic coupling of the beam energy to the material in this case.

3.4.1.2 Scanner-synchronised polarization switching

In *polarization trepanning*, the direction of linear polarization rotates synchronously with the beam around the hole so that it is always oriented in the same way with regard to the wall (C. Föhl & F. Dausinger, 2003). To obtain a similar effect, the galvo scanner was synchronised with the liquid-crystal polarization rotator, driven with a 4V peak-to-peak square-wave. This test produced an approximation of *polarization trepanning* by maintaining the direction of polarization as close as possible to a *p*-polarization during helical drilling (see Figure 3.6). The experimental results obtained are described in Table 3.1. It can be seen that the exit apertures of the holes drilled using this method have an increased surface area (~10%) compared to circular polarization, demonstrating an improved coupling of the laser energy to the stainless steel and an increase in the machining efficiency. However, the quality is limited by only having two directions of polarization; it is more promising for drilling geometrical shapes with straight edges, such as those shown in Table 3.2.

3.4.1.3 Un-synchronised polarization switching

In these tests, the square-wave signal driving the polarization rotator was not synchronised with the beam motion. During helical drilling, the laser beam rotates about the central axis of the hole. When the

polarization rotator is not synchronised with the scanner system, a given location in the circular beam path will see the polarization direction vary over time. The resulting reflectivity of the laser beam at this location will vary accordingly. This is known to lead to an averaging effect which tends to reduce the distortions in the exit hole (S. Nolte *et al.* 1999). As expected, our un-synchronised helical drilling tests showed reduced distortions compared to the other polarization modes (see Table 3.1). It is noted that the slight increase in ellipticity is due to the rotation span of the liquid-crystal device, which is limited to 90˚.

3.4.1.4 Polarization modulated geometry

In the drilling tests described so far in Section 3.4.1, real-time polarization control was used to improve the circularity of the exit holes. However, some applications require drilling non-circular holes (C. Föhl & F. Dausinger, 2003). Consequently, I investigated whether polarization control could be used for drilling pre-defined non-circular holes, using the same circular beam path as in the previous tests. Instead of using a square-wave signal as before, I used a sinusoidal one to drive the polarization rotator. This results in a gradual rotation of polarization between orthogonal directions, instead of binary switching as is the case when a square-wave signal is used. The same synchronisation setup as in *polarization trepanning* was used and the other laser drilling parameters were similar. These tests produced a repeatable exit hole geometry. This geometry (see Table 3.1) did not result from the (circular) beam scanning path but from the modulation of polarization. This technique could provide more flexibility in micro-drilling non-circular holes.

Table 3.1: Description and results of helical drilling tests on a 380µm-thick stainless steel plate, including a comparison of the exit holes surface area and ellipticity (775nm, 160fs pulses, 1kHz repetition rate, pulse energy: 75µJ). The figures for the axial ratio and surface area were obtained by averaging the results from ten drilling tests for each polarization state.

	Linear polarization	**Circular polarization**	**Scanner-synchronised polarization switching**	**Un-synchronised polarization switching**	**Polarization-modulated geometry**
Configuration of the setup	Polarization rotator removed. The linear polarized laser beam is used to drill the sample.	Polarization rotator removed. A quarterwave-plate is used to produce circular polarization.	Polarization rotator driven with a 10Hz square wave synchronised with the galvo scanner.	Polarization rotator driven with an un-synchronised 10Hz square wave.	Polarization rotator driven with a 10Hz sine wave synchronised with the galvo scanner.
Optical micrographs of the holes exit aperture (arrows indicate the direction of polarization)	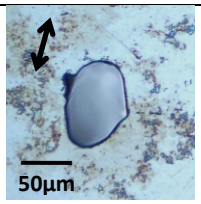	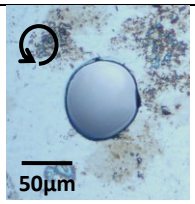	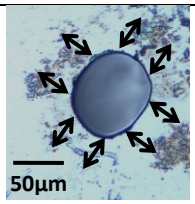	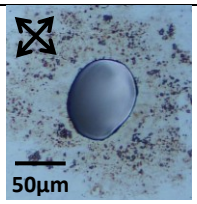	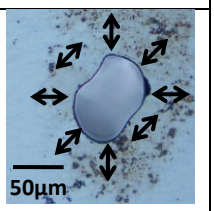
Axial ratio of elliptical hole exit aperture	35±5%	10±5%	15±5%	16±5%	N/A
Surface area	3000±300µm²	3400±300µm²	3700±300µm²	3400±300µm²	3300±300µm²

3.4.2 Square beam path

The limitation on the available rotation span (90˚ with this device) means that the quality of straight orthogonal edged geometries is likely to be most improved. To confirm this prediction, I drilled and analyzed square holes. The liquid-crystal device was configured in scanner-synchronised polarization switching mode (using a 10V peak-to-peak square-wave driving signal) so that *polarization trepanning* could be achieved. Both *p*- and *s*-polarizations were tested i.e. the polarization direction during drilling was always maintained at *p*- or *s*- respectively. Prior to drilling, a synchronisation program was developed and tested by producing LIPSS on a sample, using the polarization diagnostic procedure described earlier.

The programmed square beam paths had a side length of 130µm and 2mm/s scan speed. For the drilling tests, a laser pulse energy of 75µJ was used (F~24J/cm²). This produced square holes with an entrance side length of ~200µm and an exit side length of ~120µm, corresponding to a ~6˚ half-angle sidewall taper. The entrance of the square holes showed no dependence on polarization (Figure 3.7). The distortions in the corners at the entrance were due to the limited resolution of the scanning galvo. The exit holes obtained are shown in Table 3.2. It is noted that *s*-polarization produces the worst machining quality, with distorted exit holes. This is due to the relatively poor coupling of the laser beam energy to the sidewalls. A larger share of the beam energy is reflected away through the exit aperture of the hole compared with *p*-polarization, where the coupling to the sidewalls is better. As the *p*-polarization achieved similar drilling quality as circular polarization, these results suggest that this *polarization trepanning* technique could be a viable alternative to static linear or circular polarization.

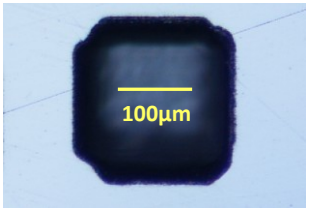

Figure 3.7: Optical micrograph of the hole entrance. The shape of the hole does not depend on polarization.

Table 3.2: Description and results of square-shaped helical drilling tests on a 380µm-thick stainless steel plate (775nm, 160fs pulses, 1kHz repetition rate, pulse energy: 75µJ).

	Linear polarization	**Circular polarization**	***p*-polarization**	***s*-polarization**
Configuration of the setup	Polarization rotator removed. The linear polarized laser beam is used to drill the sample.	Polarization rotator removed. A quarterwave-plate is inserted into the beam path to produce circular polarization.	Polarization rotator driven with an 8Hz square wave synchronised with the galvo scanner, using the *p*-polarization mode.	Polarization rotator driven with an 8Hz square wave synchronised with the galvo scanner, using the *s*-polarization mode.
Optical micrographs of the holes exit aperture (arrows indicate the direction of polarization)	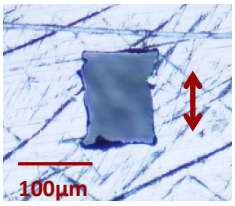	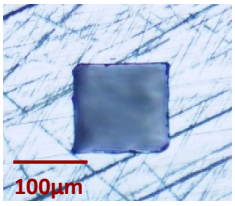	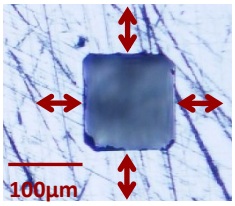	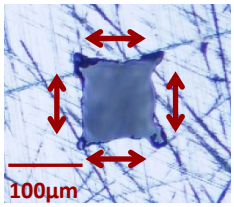

3.5 Micro-cutting

In the helical drilling tests described above, the chosen dimension for the holes was such that the resulting figure dimensions were not significantly larger than the laser spot size (~120μm and ~30μm respectively in Section 3.4.2). The relatively small hole dimension to spot size ratio (~4 here) means that all the material within the scanned figure is ablated. As a result, there is a continuous ablation front across the hole and this ablation front is wider than the laser spot itself. As material is removed by each laser pulse, the ablation front penetrates deeper inside the thickness of the material while maintaining an entrance opening that is wider than the spot size. This is essential in maintaining a high processing efficiency while drilling high-aspect-ratio holes, as it enables effective channelling of laser energy inside the hole by avoiding excessive reflections on the walls. It also facilitates ejection of the ablated material outside of the hole.

In the case of micro-cutting, where the scanned figure is much larger than the laser spot size, only the material along the beam path is ablated. This means that high-aspect-ratio grooves are produced (see Table 3.3). As the ablation front is of a similar size to the laser spot, micro-cutting can suffer from poor process efficiency: multiple reflections on the groove walls lead to poor channelling of laser energy to the bottom of the groove. As the laser beam's polarization can have a strong effect on these internal reflections, I investigated whether polarization control is beneficial in improving laser micro-cutting efficiency and quality. The tests described below were performed on 380μm thick stainless steel samples.

3.5.1 Cross-shaped beam path

A cross-shaped geometry was used, which is equivalent to cutting two orthogonal linear slots. As in the square drilling tests described earlier, the liquid-crystal device was configured in scanner-synchronised polarization switching mode, using a 10V peak-to-peak square-wave driving signal to achieve *polarization trepanning*. As before, both *p*- and *s*-polarization modes were used as well as a static linear polarization for comparison purposes. A synchronisation program was developed and tested at low pulse energies (2μJ) to produce LIPSS on the sample (see Figure 3.3).

The micro-cutting tests used pulse energies of 75μJ (F~24J/cm²). The length of each slot was 450μm and the scan speed was 2mm/s. The entrance and exit sides of the resulting incisions can be seen in Figure 3.8 and Table 3.3 respectively. Static linear polarization produced varying degrees of anisotropic machining features. Visual inspection showed the regions of the beam path with *p*-polarized internal reflections were of much better quality (i.e. less distorted and with straighter edges) than the *s*-polarized regions. The synchronisation program, which ensured that *p*-polarization is used on both arms of the cross, improved both the straightness and the accuracy of the machined slots by minimising internal reflections and maintaining an optimum coupling of the laser beam energy to the sidewalls. It is noted that the bulge-shaped distortions at the end of each arm (see optical micrographs in Table 3.3) were not caused by polarization, but rather resulted from the beam path geometry and the deceleration at the ends due to the inertia of the galvo mirrors (see Figure 3.3 for beam path).

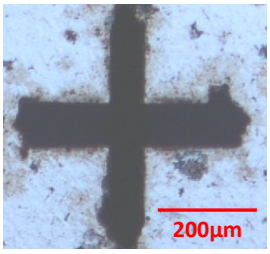

Figure 3.8: Optical micrograph of the entrance side of the cross-shaped incisions. Polarization does not affect the shape of the entrance side.

Table 3.3: Description and results of cross-shaped cutting tests on a 380µm-thick stainless steel plate (775nm, 160fs pulses, 1kHz repetition rate, pulse energy: 75µJ).

	Linear polarization	***p*-polarization**	***s*-polarization**
Polarization configuration during machining	The polarization direction (yellow arrow) is *p*- for the horizontal branch and *s*- for the vertical one.	The polarization direction was maintained at *p*- (see yellow arrows).	The polarization direction was maintained at *s*- (see yellow arrows).
Optical micrographs of the holes exit aperture (arrows indicate the direction of polarization)	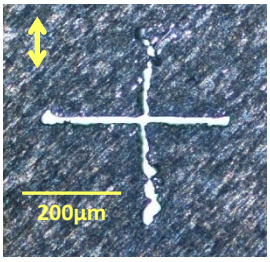	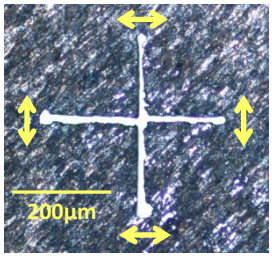	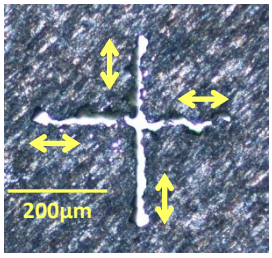

3.5.2 Square beam path

To further investigate the gains in cutting efficiency and quality, square holes were produced by cutting micro-grooves through the stainless steel plates and removing the remaining square cut-out in the centre after laser exposure.

3.5.2.1 Experimental procedure

As in the previous tests, the laser pulse energy was set at 75µJ (F~24J/cm²). The side length of the scanned figures was 650µm and the scan speed was 2mm/s. The same *polarization trepanning* technique was used as before. Both *p*- and *s*-polarization modes were tested as well as circular polarization for comparison purposes. The chosen processing time per hole was 540s. After laser processing, the samples were placed in an ultrasonic bath for three minutes, so that the pressure waves would remove the central squares if the cutting process had been successful. The exit side of the resulting holes are shown in Table 3.4.

3.5.2.2 Results

The cutting process was successful with both circular and *p*-polarization, where the central cut-outs were removed by the ultrasonic waves. The optical micrographs in Table 3.4 show the exit holes after the central square cut-outs have been removed. *s*-polarization failed to cut out the central square, demonstrating a poorer process efficiency in that case. The optical micrographs in Table 3.4 show the exit grooves produced with *s*-polarization, with the central cut-out still in place. When the test was repeated with a 10% shorter processing time, only the *p*-polarization successfully cut out the central square, suggesting this polarization mode provides a further improvement in cutting efficiency compared with circular polarization under these experimental conditions. Of these two configurations, microscopic investigation revealed that the surface quality of the sidewalls was better with *p*-polarization (Figure 3.9), whereas circular polarization produced ripples and distortions on the sidewalls of the hole (Figure 3.10). Figures 3.9-b and 3.10-b show the amplitude of these ripples on selected regions of the sidewalls for *p*- and circular polarization respectively, measured with an optical surface profiling system (WYKO NT1100). The average peak-to-peak amplitude between the valleys (in dark blue) and the peaks (in light red) was found to be 2.5±1µm for *p*- and 5±1µm for circular polarization.

3.5.2.3 Discussion

The better process efficiency and quality obtained with *p*-polarization can be explained by the increased coupling of the laser beam energy to the sidewalls during the machining of the micro-channels, compared with circular or *s*-polarization. For a typical high-aspect-ratio channel geometry, the angle of incidence on the walls is around 80˚. The corresponding value for the reflectivity of steel is around 47% for *p*-polarization and 94% for *s*-polarization (S. Nolte *et al.* 1999). Therefore, the intensity of the light reflected from the walls is approximately twice as much with *s*-polarization compared with *p*-polarization. This results in a higher loss of energy through the exit of the channels machined with *s*-polarization. The extra reflections on the non-optically flat walls inside the channels also induce a non uniform energy distribution resulting in distorted exit channels produced with *s*-polarization. In the case of circular polarization, the *p*- and *s*-polarizations are averaged over time. This produces an average value for reflectivity which results in an intermediate quality and efficiency for micro-machining.

Table 3.4: Description and results of square-shaped cutting tests on a 380µm-thick stainless steel plate (775nm, 160fs pulses, 1kHz repetition rate, pulse energy: 75µJ).

	Circular polarization	***p*-polarization**	***s*-polarization**
Polarization configuration during machining	A quarterwave-plate is inserted into the beam path to produce circular polarization.	The polarization direction was maintained at *p*-.	The polarization direction was maintained at *s*-.
Optical micrographs of the holes exit aperture	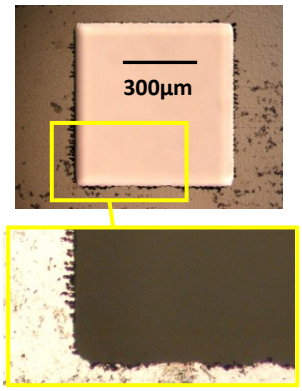	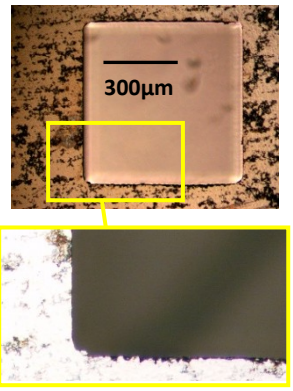	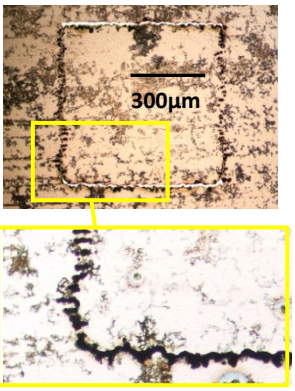
Description of the results	The central cut-out was successfully removed after a 540s laser exposure. Significant distortions are present on the exit side of the cut-out.	The central cut-out was successfully removed after a 540s laser exposure. Minor distortions are present on the exit side of the cut-out.	The central cut-out could not be removed after a 540s laser exposure. Significant distortions are visible along the exit channels.

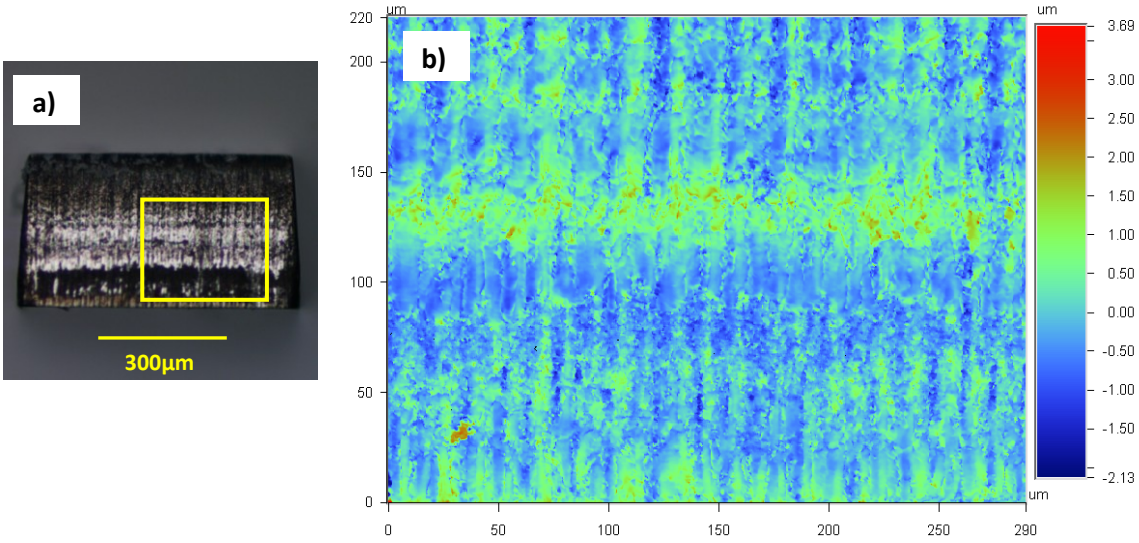

Figure 3.9: (a) Optical micrograph of a square cut-out with *p*-polarization after removal by ultrasonic waves (see Table 3.4). The sidewall of the cut-out is shown here, with magnified area (yellow square). **(b)** Magnified area observed with an optical surface profiling system, showing vertical periodic ripples on the sidewall. The dark blue regions are the valleys and the light orange regions are the peaks. The colour-coded scale shows the distance from an average mid-plane, in µm. The measured average peak-to-peak amplitude of the ripples was 2.5±1µm.

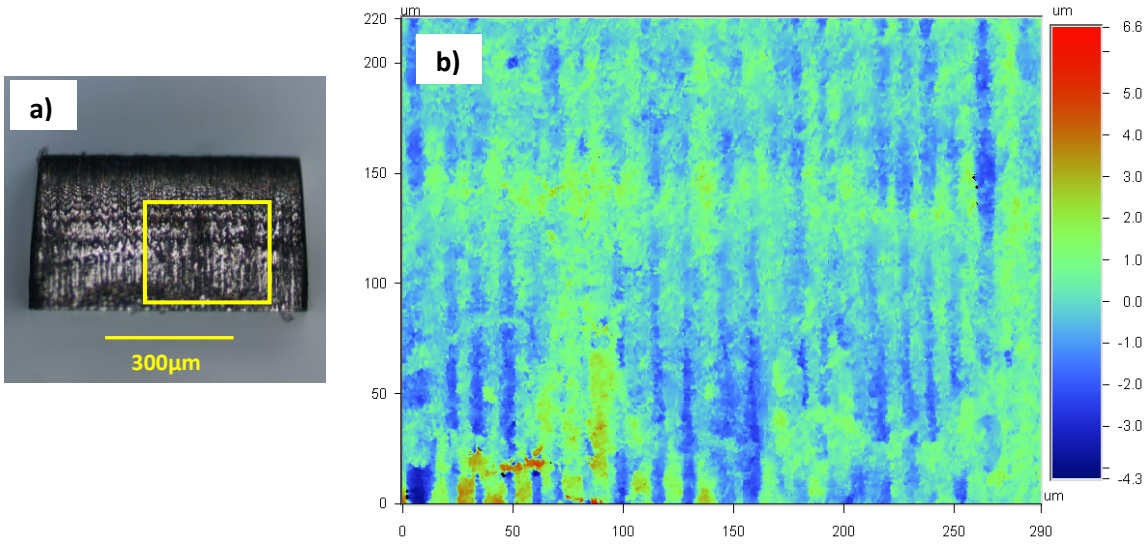

Figure 3.10: (a) Optical micrograph of a square cut-out with circular polarization after removal by ultrasonic waves (see Table 3.4). The sidewall of the cut-out is shown here, with magnified area (yellow square). **(b)** Magnified area observed with an optical surface profiling system, showing vertical periodic ripples on the sidewall. The dark blue regions are the valleys and the light orange regions are the peaks. The colour-coded scale shows the distance from an average mid-plane, in µm. The measured average peak-to-peak amplitude of the ripples was 5±1µm.

3.6 Chapter summary

The chief points of this chapter are summarized below. A more comprehensive discussion of these results is outlined in Chapter 7.

- A method for dynamically switching the polarization direction of a femtosecond laser beam with a fast-response, transmissive, ferroelectric liquid-crystal device was presented.

- Helical drilling and cutting of high-aspect-ratio microscopic structures in a steel plate were carried out using various polarization modes, such as linear, circular, *p*- or *s*-polarization. Various machining geometries were tested, i.e. circular, square and cross-shaped beam paths. Microscopic investigation of the resulting features revealed that *polarization trepanning* with the liquid-crystal device offers better levels of machining quality than circular or static linear polarizations.

- Due to its design characteristics, the liquid-crystal device used in this research had an angular rotation range limited to 90˚ and required a DC-balanced, 50% duty-cycle periodic driving voltage. As a result, the tests were restricted to machining axi-symmetric features.

4

Spatial control of polarization: producing Cylindrical Vector Beams

4.1 Introduction

In Chapter 3, I have shown how uniform states of polarization (i.e. linear or circular) affect the laser-material energy coupling and influence the quality/efficiency of laser micro-processing. I used a liquid-crystal device to control these effects dynamically and improve the process. In the rest of this thesis, I am interested in exploring the use of CVBs (such as radial or azimuthal polarizations) for industrial ultrafast-laser micro-processing. Due to the limited average beam power available on the ultrafast-laser processing benches used in this thesis, the experiments had to be carried out using low average powers (<0.5W). However the results are still transferable to high-average-power, industrial applications as demonstrated in Chapter 2.

The potential benefits of using radially or azimuthally polarized laser beams for various applications have been studied theoretically for several years (see for example V. G. Niziev & A. V. Nesterov, 1999, M. Stalder & M. Schadt, 1996 and I. Iglesias & B. Vohnsen, 2007). This led to predictions that the use of a radially polarized beam could enhance the efficiency of cutting processes by more than 50% compared to circular polarization (V. G. Niziev & A. V. Nesterov, 1999). However, producing radially or azimuthally polarized beams has been difficult until recently, making it complicated to verify these claims experimentally (M. Stalder & M. Schadt, 1996 and I. Iglesias & B. Vohnsen, 2007). In the last few years, a range of methods has been developed to produce these modes of polarization. Recent experimental work using these methods confirmed the benefits of processing with a radial or azimuthal polarization (for example K. Venkatakrishnan & B. Tan, 2006 or M. Meier *et al.* 2007). The most recent work in this area is concurrent to the research presented in this thesis (M. Kraus *et al.* 2010, R. Weber *et al.* 2011, C. Hnatovsky *et al.* 2011). However, the methods used in these publications either required a cumbersome re-design of the laser cavity, or used static extra-cavity polarization converters which can lack flexibility. Thanks to the latest technological developments in dynamic programmable liquid-crystal devices such as SLMs, it is now possible to produce such polarization modes in a more flexible and cost effective manner. Although this approach has been used for high-resolution microscopy applications (E. Y. S. Yew & C. J. R. Sheppard, 2007; M. R. Beversluis *et al.* 2006; K. Yoshiki *et al.* 2005), until recently SLMs were unable to sustain the high average power required for laser machining applications.

In this thesis I demonstrate for the first time that modern SLMs, capable of sustaining a high average power as detailed in Chapter 2, are well suited for producing radially or azimuthally polarized beams in a micro-machining bench. I use a simple optical setup designed as part of this research project. In this chapter, I aim to show how CVBs produced in this way influence the properties of the laser focal region.

In Chapter 6, I will show how they are used to improve the quality and efficiency of industrial laser micro-processes.

This chapter is split into two sections. In the first section, I introduce an optical setup that uses a liquid-crystal SLM to generate a CVB. A Jones Matrix analysis of the setup is used to predict the ability to produce CVBs in this way. The setup is implemented in a laser test bench and the resulting polarization analyzed with a polarizing filter. In the second section, the setup is implemented in an ultrafast laser micro-processing bench. The amplitude and polarization properties in the focal region of the setup are studied using LIPSS, as described in Chapter 2. This enables me to check if the expected state of polarization is achieved in the focal region.

4.2 Principle and proof of concept for a Polarization Mode Converter

4.2.1 Polarization Mode Converter

Here, I introduce a simple optical setup design that comprises a reflective, phase-only, liquid-crystal SLM and a quarter-waveplate to convert a linearly polarized laser beam into a CVB. These two components are referred to as "Polarization Mode Converter" henceforth. The basic setup of the Polarization Mode Converter is shown in Figure 4.1. The SLM is mounted so that the long axis of its liquid-crystals lies in the horizontal plane. The quarter-waveplate is mounted with its fast axis tilted at 45˚. The angle between the SLM's incident and reflected beams is less than 20˚, so that the phase response of the liquid-crystals is linear. The Polarization Mode Converter also requires the direction of the incident linear polarization to be oriented at +45˚ with respect to the (horizontal) liquid-crystals axis of the SLM. This can be achieved either with a half-waveplate or using a polarizing filter. In principle, this setup design can be implemented on any laser micro-processing bench, hence its potential as a powerful new tool.

4.2.2 Theoretical analysis of the Polarization Mode Converter using Jones matrices

In Chapter 1, phase-only, liquid-crystal SLMs were introduced. If the direction of the incident linear polarization is set parallel to the liquid-crystals axis of the SLM, only the phase of the incident laser beam is modulated, the polarization is unaffected (i.e. it remains linear). In this case, inducing a relative phase delay between the pixels of the SLM shapes the wavefront of the laser beam. This approach is used for example to produce dynamic holograms that shape the amplitude distribution at the focal plane of a laser micro-processing bench (Z. Kuang *et al.* 2009a, D. Liu *et al.* 2010).

In the Polarization Mode Converter detailed here, the direction of the incident linear polarization is set at 45˚ with respect to the (horizontal) liquid-crystals axis of the SLM. In this case, each pixel of the SLM induces a relative phase delay between the horizontal and vertical components of the polarization.

To explain how the Polarization Mode Converter works, we look at a single pixel of the SLM, using Jones vector formalism. We first define a reference coordinate system with horizontal (x) and vertical (y) axes, centered on the optical axis of the laser beam. The location of the pixel of interest in this coordinate system is: (x_p, y_p). As described above, the incident linearly polarized beam has its polarization direction tilted at +45˚. In this analysis, this is described as a Jones vector with equal

amplitude horizontal and vertical components ($E_X = E_Y = 1$, see Figure 4.2). For our pixel of interest the incident Jones vector is defined as: $\boldsymbol{J}inc_{x_p y_p} = \frac{1}{\sqrt{2}}\binom{1}{1}$.

Each pixel on the SLM generates a horizontal phase delay Φ_{xy} at the corresponding location (x, y). Therefore after reflection on the SLM, the vertical component of the polarization vector is phase-shifted by an amount Φ_{xy} relative to the horizontal component (M. R. Beversluis *et al.* 2006). For our pixel of interest we express this vertical phase shift as Φ_p. We can express the Jones matrix of our pixel as:

$$\boldsymbol{P}_{x_p y_p} = \begin{bmatrix} 1 & 0 \\ 0 & \mathrm{e}^{j\Phi_p} \end{bmatrix} \tag{4.1}$$

The resulting Jones vector after the SLM is noted $\boldsymbol{J}slm_{x_p y_p}$. To obtain $\boldsymbol{J}slm_{x_p y_p}$, we multiply the matrix $\boldsymbol{P}_{x_p y_p}$ by the incident Jones vector defined above:

$$\boldsymbol{J}slm_{x_p y_p} = \boldsymbol{P}_{x_p y_p} \times \boldsymbol{J}inc_{x_p y_p} = \frac{1}{\sqrt{2}}\binom{1}{\mathrm{e}^{j\Phi_p}} \tag{4.2}$$

In general, this represents an elliptical polarization. However if $\Phi_p = 0$, the polarization after the SLM is linear, oriented at +45˚ (the derivation is in Appendix A): $\boldsymbol{J}slm_{x_p y_p} = \frac{1}{\sqrt{2}}\binom{1}{1}$. If $\Phi_p = \pi/2$, the resulting polarization is circular: $\boldsymbol{J}slm_{x_p y_p} = \frac{1}{\sqrt{2}}\binom{1}{\mathrm{e}^{j\frac{\pi}{2}}}$.

To produce CVBs, a quarter-waveplate is required after the SLM. The quarter-waveplate needs to have its fast axis oriented at -45˚ relative to the horizontal. The Jones matrix of a quarter-waveplate is:

$$\boldsymbol{Q} = \begin{bmatrix} 1 & 0 \\ 0 & \mathrm{e}^{-j\frac{\pi}{2}} \end{bmatrix} \tag{4.3}$$

It is noted that the Jones matrix $\boldsymbol{Q}$ is expressed in a reference coordinate system with one of its axes parallel to the fast axis of the quarter-waveplate, which is oriented at -45˚ here. As a result, the polarization vectors incident on this waveplate need to be converted so that they are expressed in this tilted coordinate system (see Figure 4.2). This is done by multiplying them with the following rotation matrix:

$$\boldsymbol{R} = \frac{1}{\sqrt{2}}\begin{bmatrix} 1 & -1 \\ 1 & 1 \end{bmatrix} \tag{4.4}$$

The Jones matrix representing the Polarization Mode Converter (i.e. the system comprising the SLM and waveplate) is obtained by multiplying the three Jones matrices above (see for example M. R. Beversluis *et al.* 2006, where an SLM-based optical system is analyzed using Jones matrices). At the coordinate of our pixel of interest (x_p, y_p), the resulting Jones matrix is:

$$\boldsymbol{T}_{x_p y_p} = \boldsymbol{Q} \times \boldsymbol{R} \times \boldsymbol{P}_{x_p y_p} \tag{4.5}$$

It is noted that the rotation matrix $\boldsymbol{R}$ changes the reference coordinate system. As a result, the vectors before (i.e. on the right-hand side of) the second term $\boldsymbol{R}$ are expressed in a coordinate system with horizontal and vertical axes. The vectors after (i.e. on the left-hand side of) the second term $\boldsymbol{R}$ are expressed in a coordinate system with its axes tilted at 45˚(see Figure 4.2).

The resulting Jones vector after the Polarization Mode Converter, noted $\boldsymbol{J}pmc_{x_p y_p}$, is obtained by multiplying the matrix $\boldsymbol{T}_{x_p y_p}$ by the incident Jones vector defined above:

$$\boldsymbol{J}pmc_{x_p y_p} = \boldsymbol{T}_{x_p y_p} \times \boldsymbol{J}inc_{x_p y_p} = \mathrm{e}^{-j\frac{\pi}{2}} \times \mathrm{e}^{j\frac{\Phi_p}{2}} \times \begin{pmatrix} \sin\frac{\Phi_p}{2} \\ \cos\frac{\Phi_p}{2} \end{pmatrix} \tag{4.6}$$

The details of the derivation are in Appendix A. It is noted that the incident vector $\boldsymbol{J}inc_{x_p y_p}$ is expressed in the reference coordinate system with horizontal and vertical axes, while the resulting vector

$\boldsymbol{J}pmc_{x_p y_p}$ is expressed in the reference coordinate system tilted at 45˚ (Figure 4.2). As shown in Equation (4.6), $\boldsymbol{J}pmc_{x_p y_p}$ includes three terms. The first term $e^{-j\frac{\pi}{2}}$ is a constant. This does not vary with the pixel-induced phase delay so it is not relevant to this analysis. The second term $e^{j\frac{\Phi_p}{2}}$ represents a residual phase delay which varies with the phase shift Φ_p. The implications of this will be discussed later. The third term $\begin{pmatrix} \sin\frac{\Phi_p}{2} \\ \cos\frac{\Phi_p}{2} \end{pmatrix}$ represents a linear polarization with a direction rotated by an angle $\frac{\Phi_p}{2}$ relative to the incident polarization (i.e. an angle of $\frac{\pi}{4}+\frac{\Phi_p}{2}$ relative to the vertical axis). For example, varying the amplitude of phase shift Φ_p between 0 and 2π, rotates the polarization direction by an angle between 0 and π.

In this example, Φ_p was the phase shift induced by a chosen pixel at a location (x_p, y_p) in the pixel array of the SLM. As each pixel independently generates a phase shift Φ_{xy} at the corresponding location (x, y), the Polarization Mode Converter enables a spatially dependant rotation of the polarization.

Of particular interest is the case where a vortex phase pattern is created on the pixel array of the SLM by instigating a gradual change in the phase shift between adjacent pixels. For example if Φ_{xy} varies from 0 to 4π depending on the (x, y) pixel coordinates, it can produce a 4π pitch vortex phase overall. In such case, we can infer from the third term $\begin{pmatrix} \sin\frac{\Phi_p}{2} \\ \cos\frac{\Phi_p}{2} \end{pmatrix}$ in Equation (4.6), that the resulting polarization has a cylindrical symmetry, i.e. it is a CVB. The second term $e^{i\frac{\Phi_{xy}}{2}}$ in Equation (4.6) means that a residual phase vortex is still present after the quarter-wave plate in such case (i.e. the beam has an orbital angular momentum). The pitch (topological charge) of this residual phase vortex is half that of the overall vortex phase induced by the SLM. For example if the SLM induces a 4π pitch overall phase vortex, the residual phase vortex after the quarter-waveplate has a 2π pitch (i.e. a topological charge of one). The implications of the residual phase vortex will be discussed in the following chapters.

4.2.3 Principle of the Polarization Mode Converter

Figure 4.1 shows the principle of the Polarization Mode Converter. Two configurations are described. In Figure 4.1-a, a uniform polarization rotation configuration is shown, where the SLM induces a planar phase shift of Φ_0 (i.e. all the liquid-crystal pixels of the SLM induce the same phase shift value Φ_0). After transmission through the quarter-waveplate, the polarization of the beam is expected to be linear with its direction rotated by an angle $\frac{\Phi_0}{2}$ with regard to the direction of incident polarization.

In Figure 4.1-b, a spatially dependant polarization rotation configuration is shown. A vortex phase pattern is created on the pixel array of the SLM as described in Section 4.2.2. The resulting polarization is expected to have a cylindrical symmetry around the optical axis. In the example shown in Figure 4.1-b, the resultant beam has a radial polarization and a vortex phase.

In the following sections, the Polarization Mode Converter will be demonstrated experimentally, using each of these two configurations. It is noted that all the phase patterns used with the SLMs in this thesis were produced using a software originally designed for the control of SLM-based optical tweezers at the University of Glasgow (see for example A. Curran *et al.* 2012).

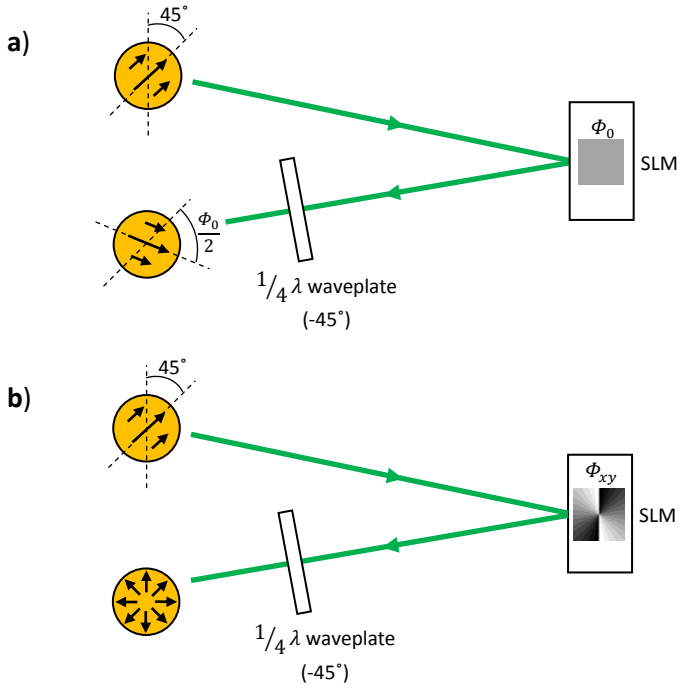

Figure 4.1: Schematics showing how the Polarization Mode Converter is used. A linearly polarized beam with its polarization direction tilted at 45˚ is incident on the SLM. **(a)** When the SLM induces a planar phase shift of Φ_0, the resulting polarization is linear with its direction rotated by $\frac{\Phi_0}{2}$. **(b)** When the SLM induces a 4π vortex phase shift, the resulting polarization has a cylindrical symmetry. In this example, the resultant polarization is radial.

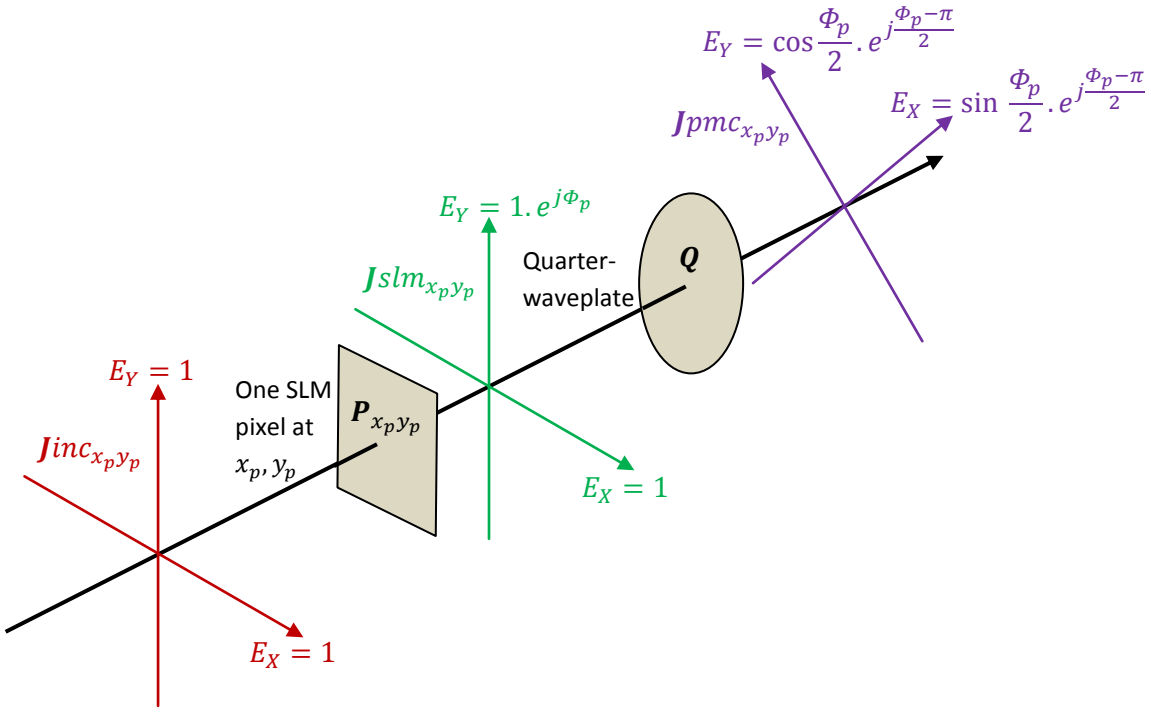

Figure 4.2: Schematic illustrating how the Jones vectors are used to analyze the Polarization Mode Converter. $\boldsymbol{J}inc$, $\boldsymbol{J}slm$ and $\boldsymbol{J}pmc$ are represented in red, green and purple respectively.

4.2.4 Experiments producing a uniform rotation of polarization with the Polarization Mode Converter

4.2.4.1 Aim

By using the Polarization Mode Converter in its uniform polarization rotation configuration, I aim to confirm experimentally the theoretical results from the Jones vectors calculation outlined in Section 4.2.2. In other words, I aim to show that the Polarization Mode Converter effectively rotates the polarization direction of a linearly polarized beam in a controllable manner.

4.2.4.2 Experimental setup

I used the experimental setup shown in Figure 4.3. A linearly polarized 532nm laser beam produced by a nanosecond-pulse laser source from BMI, is incident on a liquid-crystal SLM (model X10468-04) from Hamamatsu. The SLM consists of a 16x12mm, 800x600 pixel array of horizontally oriented liquid-crystal phase retarders. Before the SLM, a zero-order half-waveplate (Newport) is used so that the direction of incident polarization it is tilted at +45˚ with respect to the horizontal axis of the liquid-crystals of the SLM. After the SLM, a zero-order quarter-waveplate (Newport) with its axis oriented at -45˚, a polarizing filter and a power meter are inserted into the beam path. The SLM and quarter-waveplate constitute the Polarization Mode Converter. The polarizing filter, with its transmission axis oriented at -45˚ with regard to the horizontal, is used to analyze the polarization of the beam after the Polarization Mode Converter. This means that, for example if the induced rotation of polarization is zero, the resulting polarization will be oriented at +45˚ (i.e. parallel to the incident polarization) and no power will be transmitted through the polarizing filter.

4.2.4.3 Experimental procedure

We set the SLM to induce a planar phase shift, where all the pixels induce the same phase shift value: $\Phi_{xy} = \Phi_0$. As shown in Equation (4.6), the resulting beam is expected to be linearly polarized, but with the direction of its polarization rotated by an angle of $\frac{\Phi_0}{2}$ relative to that of the incident polarization. In the experiments, the phase shift Φ_0 will be gradually increased. The resulting beam will be analyzed with the polarization filter. The beam power transmitted through the polarizing filter will be measured with the power meter.

It is noted that the SLM control software expresses phase shifts as a range of 256 discrete values, referred to as “grey levels”. As part of this experiment, the correlation between the grey levels and the induced phase shifts Φ_0 needs to be clarified. The scale factor between grey levels and phase radians has to be determined. This requires finding out which grey level values induce 0, π and 2π radians phase shifts.

4.2.4.4 Results

In the experiment, the grey level was given a set of values between 0 and 255. For each value, the beam power was measured after the polarizing filter (Figure 4.3). The transmitted beam power plotted against the grey level is shown in Figure 4.4. Two sets of measurements were taken to verify consistency in the results. The two sets of measurements were consistent within the accuracy of the power measurements (+/-5%). The measured beam power was at a minimum (i.e. most of the beam was blocked by the polarizing filter) when the grey levels were at 25 or 225. It was at a maximum (i.e. most

of the beam was transmitted through the polarizing filter) when the grey level was at 125 (Figure 4.4). It is noted that the minimum measured power is above zero watts. Also, the maximum measured power was below the full beam power. In both cases, the discrepancy was within 5% of full beam power. This could be due to residual distortions in the SLM phase modulation, which affect the polarization purity. It is also possible that the actual minimum and maximum fall between the measurement points.

4.2.4.5 Discussion

These results are consistent with a polarization direction oriented at ~+45˚ (i.e. a rotation angle of ~zero or $\sim\pi$ radians) when the grey level is 25 or 225, and a polarization direction oriented at ~-45˚ (i.e. a rotation angle of $\sim\frac{\pi}{2}$ radians) when the grey level is 125. These results are also consistent with a polarization direction rotating by an angle of $\sim\pi$ radians as the grey level increases by 200 (see model in Figure 4.4). Table 4.1 summarizes the polarization rotation angle for each value of grey level. It is estimated that the angles are accurate within 5%, due to the accuracy of the power measurements.

From the rotation angle, the SLM-induced phase shift Φ_0 can be derived. As inferred from Equation (4.6), the amplitude of phase shift Φ_0 is twice the angle of rotation. Therefore if a grey level of 25 produces a rotation angle of ~0, Φ_0 is also ~0. If a grey level of 125 produces a rotation angle of $\sim\frac{\pi}{2}$ radians, the phase shift Φ_0 is $\sim\pi$. A grey level of 225 produces a rotation angle of $\sim\pi$ radians and a phase shift Φ_0 of $\sim 2\pi$. There is a scale factor of $\frac{\pi}{100}$ between the grey levels and the phase shift Φ_0. Table 4.1 summarizes the correlation between the grey level, the polarization rotation angle and the SLM-induced phase shift Φ_0. It can be seen that the SLM has a phase modulation range of around $\frac{5\pi}{2}$ at the wavelength of the laser (532nm). These results confirm that the Polarization Mode Converter enables to rotate the polarization direction of a linearly polarized beam and give us confidence that it behaves as expected.

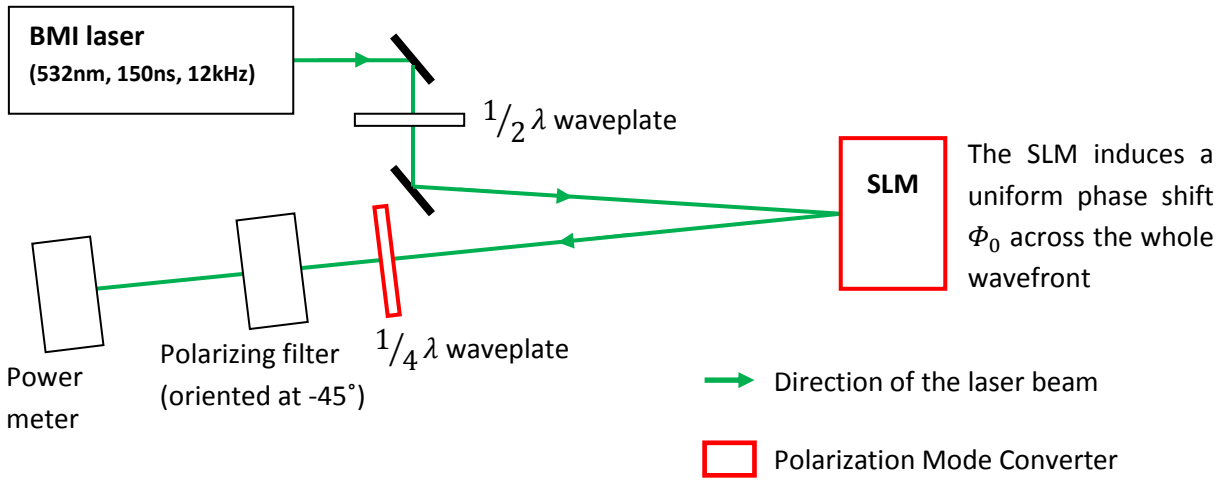

Figure 4.3: Schematic of the experimental setup used to test the Polarization Mode Converter. Before the Polarization Mode Converter, a half-waveplate is used to produce a linearly polarized beam oriented at +45˚. The SLM is programmed to induce a planar phase shift Φ_0. After the Polarization Mode Converter, a polarizing filter with its transmission axis tilted at -45˚ is used as an analyzer. A power meter measures the resulting beam amplitude for each phase shift value Φ_0.

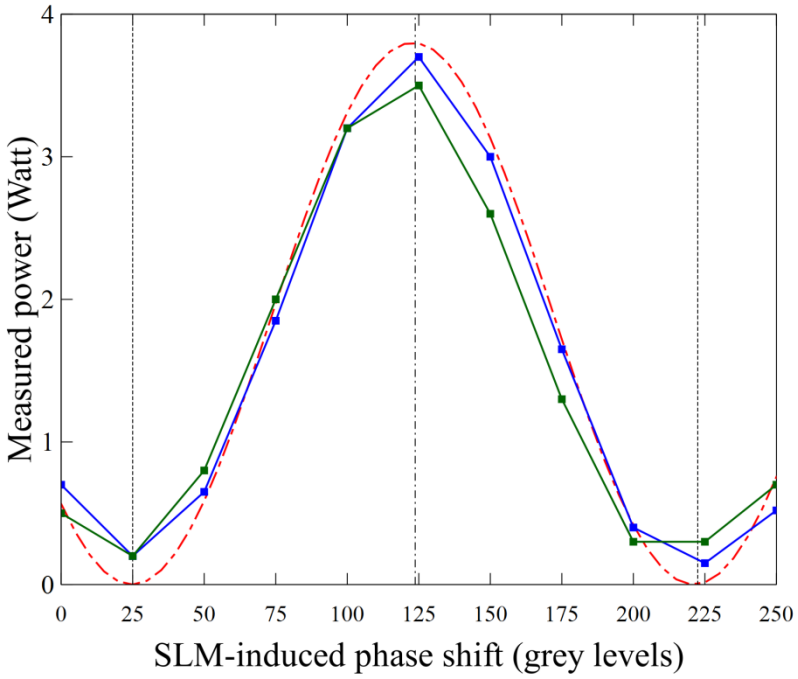

Figure 4.4: Power measurements obtained by analyzing the laser beam after the Polarization Mode Converter. The transmission axis of the polarization analyzer is tilted at -45˚ and the SLM-induced phase shift is varied between grey levels 0 and 255. The experiment was carried out twice to check consistency. The two sets of measurements, which are plotted in blue and green, are in agreement within 10%. This is consistent with the +/-5% accuracy of the power measurements. The red dashed line is a model of a linearly polarized beam with a polarization direction rotating by just over π radians overall. The experimental results are consistent within 10% with the model.

Table 4.1: Correlation between the control software input to the SLM (expressed in grey levels), the polarization rotation angle induced by the Polarization Mode Converter (in radians) and the phase shift Φ_0 induced by the SLM (in radians). The induced phase shift and polarization rotation angle, which are inferred from the experimental results shown in Figure 4.3, are accurate within 5%.

Software input to the SLM (grey levels)	0	25	50	75	100	125	150	175	200	225	250
Polarization rotation angle induced by the Polarization Mode Converter (radians)	$-\frac{\pi}{8}$	0	$\frac{\pi}{8}$	$\frac{\pi}{4}$	$\frac{3\pi}{8}$	$\frac{\pi}{2}$	$\frac{5\pi}{8}$	$\frac{3\pi}{4}$	$\frac{7\pi}{8}$	π	$\pi+\frac{\pi}{8}$
Phase shift Φ_0 induced by the SLM (radians)	$-\frac{\pi}{4}$	0	$\frac{\pi}{4}$	$\frac{\pi}{2}$	$\frac{3\pi}{4}$	π	$\frac{5\pi}{4}$	$\frac{3\pi}{2}$	$\frac{7\pi}{4}$	2π	$2\pi+\frac{\pi}{4}$

4.2.5 Experiments producing Cylindrical Vector Beams with the Polarization Mode Converter:

4.2.5.1 Aim

The experiments in Section 4.2.4 confirmed the ability to rotate polarization direction by using the Polarization Mode Converter in a uniform rotation configuration. I now aim to confirm experimentally the ability to produce CVBs. This time the Polarization Mode Converter is used in a spatially dependent rotation configuration, where polarization rotation is adjusted pixel by pixel. An overall vortex phase pattern is created on the pixel array of the SLM as detailed in Section 4.2.2. The resulting beam is expected to be cylindrically polarized (i.e. a CVB), with a residual phase vortex (i.e. an orbital angular momentum).

4.2.5.2 Experimental setup

The same experimental setup is used as described in Section 4.2.4 (see Figure 4.3) except that the power meter is replaced with a projection screen. A digital camera is used to capture optical images of the beam profiles transmitted through the analyzer (polarizing filter) and projected on the screen (see Figure 4.5).

4.2.5.3 Results

The beam profiles transmitted through the polarization analyzer, shown on the sixth line in Table 4.2 are obtained by setting the SLM to induce a 4π phase vortex, producing various types of CVB with a residual 2π phase vortex. The regions of the beam with polarization vectors that are parallel to the transmission axis of the polarization analyzer are transmitted through the analyzer and are visible on the screen. The regions where the polarization vectors are perpendicular to the transmission axis of the analyzer are blocked.

When the linear polarization incident on the Polarization Mode Converter was oriented at +45˚, a radial or azimuthal polarization was obtained. Changing between a radial and an azimuthal polarization state was achieved by adding a constant planar phase term π to the overall phase vortex induced by the SLM. The beam profiles transmitted through the polarizing filter are consistent with analyzing a radial or azimuthal polarization (Table 4.2). When the incident polarization was oriented at -45˚, a hybrid polarization was produced (see Table 4.2). By rotating the polarizing filter used to analyze the beam, I can discriminate between a radial/azimuthal polarization and a hybrid polarization. With a radial/azimuthal polarization, rotating the polarizing filter clockwise causes the transmitted beam pattern to rotate clockwise. With a hybrid mode, rotating the polarizing filter clockwise causes the transmitted beam pattern to rotate anticlockwise.

The polarization patterns shown in Table 4.3 are obtained by setting the mode converter to produce CVBs with a residual vortex phase of higher pitch (i.e. topological charge) than 2π. It is noted that in all cases, the phase singularity at the center of the beam produces a small area of zero field amplitude near the optical axis. This area is too small to be visible in the images in Tables 4.2 and 4.3.

4.2.5.4 Discussion

As the experiments described here were carried out before achieving a detailed calibration of the SLM, residual distortions of the beam fluence profiles were visible in the results (see Tables 4.2 and 4.3).

However these preliminary experiments allowed me to verify the ability of the proposed optical setup design to produce a wide range of CVBs in a flexible manner. They also enabled me to calibrate the SLM and find the appropriate phase offsets to produce the desired CVBs without distortions. Profiles of CVBs obtained after calibrating the SLM will be shown in Section 4.3.

It is noted that all the produced CVBs have a residual vortex phase (i.e. an orbital angular momentum). Although the effects of this phase vortex are not visible in the experimental results described here, they are important in the laser processing experiments described in later chapters.

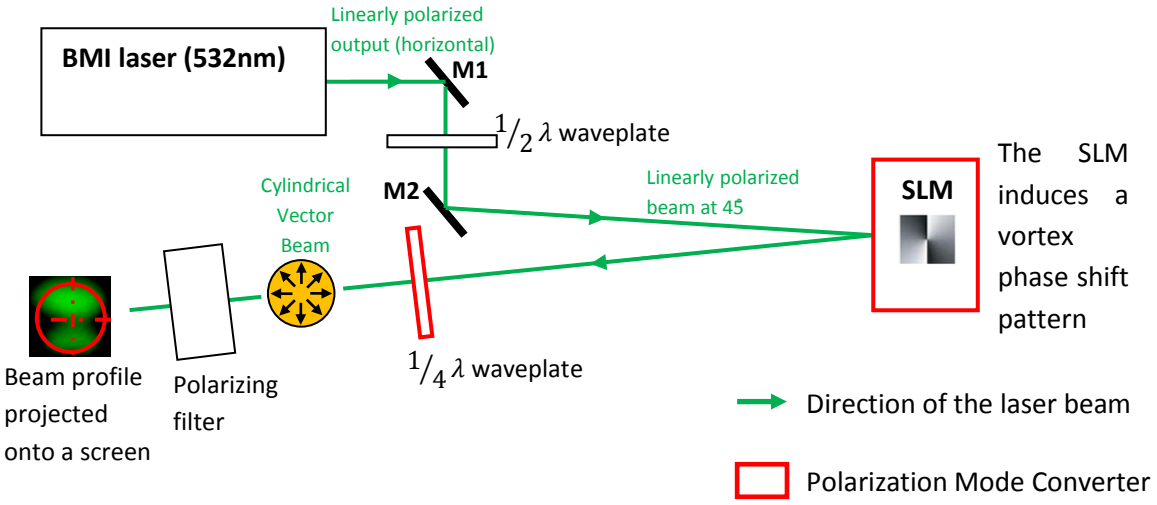

Figure 4.5: Schematic of the experimental setup used to analyze the Cylindrical Vector Beams produced with the Polarization Mode Converter.

Table 4.2: Summary of the experimental parameters, expected polarization modes and resulting beam profiles obtained when analyzing various types of CVBs with a 2π phase vortex.

Desired state of polarization	Radial (with 2π phase vortex)	Azimuthal (with 2π phase vortex)	Hybrid (with 2π phase vortex)
Direction of linear polarization incident on the Polarization Mode Converter	**+ 45°** with regard to horizontal axis	**+ 45°** with regard to horizontal axis	**- 45°** with regard to horizontal axis
SLM induced vortex phase pattern			
Expected cross-sectional polarization pattern			
Polarizing filter transmission axis	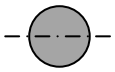	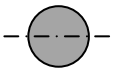	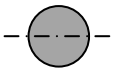
Beam profile patterns after polarizing filter (the beam diameter is shown as a red circle)	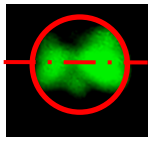	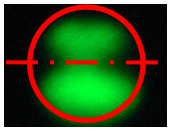	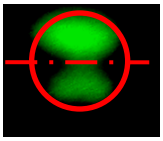

Table 4.3: Summary of the experimental parameters, expected polarization modes and resulting beam profiles obtained when analyzing CVBs with a phase vortex at various pitches.

Desired state of polarization	Hybrid (with 3π phase vortex)	Hybrid (with 4π phase vortex)	Hybrid (with 6π phase vortex)
Direction of linear polarization incident on the Polarization Mode Converter	**+ 45°** with regard to horizontal axis	**- 45°** with regard to horizontal axis	**+ 45°** with regard to horizontal axis
SLM induced vortex phase pattern		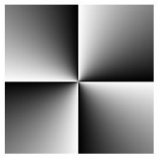	
Expected cross-sectional polarization pattern	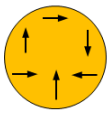	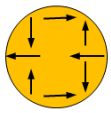	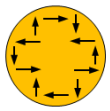
Polarizing filter transmission axis	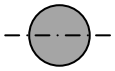	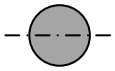	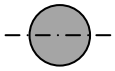
Beam profile patterns after polarizing filter (the beam diameter is shown as a red circle)	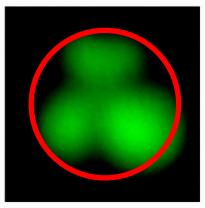	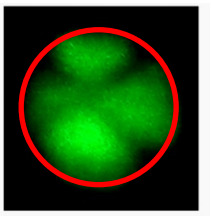	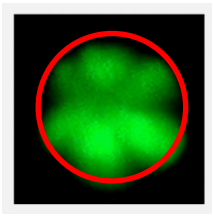

4.3 Analysis of Cylindrical Vector Beams in the focal region of a femtosecond laser setup

The experiments described in Section 4.2.5 confirm that the desired CVBs can be produced using the Polarization Mode Converter. I now set up a similar Polarization Mode Converter on a femtosecond-pulse laser processing bench and use it for laser marking the polished surface of stainless steel samples. The aim is to characterize the amplitude and polarization properties of the CVBs produced in the focal region of the optical setup. In this way, I can investigate how using specially designed CVBs has the potential to improve the efficiency and quality of industrial micro-processes.

4.3.1 Experimental setup

A schematic of the experimental setup is shown in Figure 4.6. This setup is a modified version of the one used in Chapters 2 and 3. The output from a femtosecond laser (Clark-MXR CPA2010, with a minimum pulse width of 160fs, 775nm central wavelength, spectral bandwidth of 5nm, 1mJ maximum pulse energy, 1kHz repetition rate and horizontal linear polarization) was attenuated by a half-wave plate and a Glan laser polarizer. The resulting linearly polarized beam was incident on the Polarization Mode Converter, which consists of a Hamamatsu X10468-02 SLM and a zero-order quarter-waveplate. As before, a vortex phase shift pattern was instigated by the SLM, producing the desired phase front. A polarizing filter and a SPIRICON beam profiler were used to analyze the beam and verify that the desired CVBs were produced. They were removed when the micro-processing experiments were carried out. As shown in Figure 4.6, after reflection on Mirrors 4 and 5 the beam entered the 10mm aperture of a scanning galvanometer system with a flat field lens (f = 100mm, NA = 0.03). Samples were mounted on a precision 4-axis (x, y, z, θ) motion control system (Npaq system, produced by Aerotech) allowing accurate positioning of the sample in the focal plane.

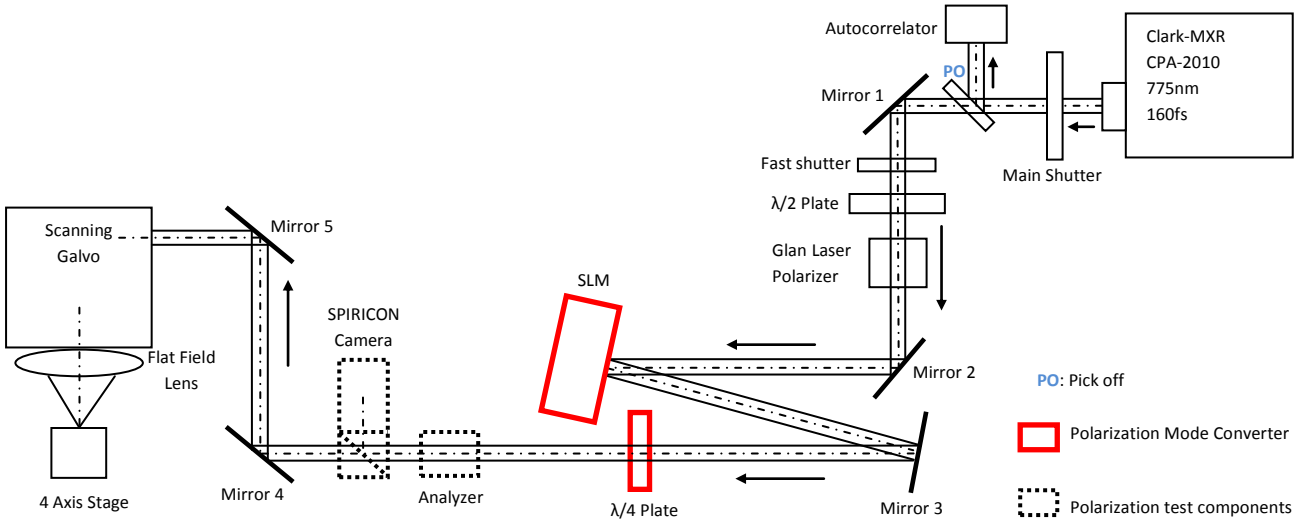

Figure 4.6: Schematic of the micro-processing experimental setup showing how the Polarization Mode Converter is used. The Polarization Mode Converter consists of an SLM and a quarter-wave plate. Together these components convert the linearly polarized femtosecond laser beam into a radially, azimuthally or circularly polarized beam. The "polarization test components" consist of a polarizing filter (analyzer) and a SPIRICON (CCD) camera, used to verify the state of polarization of the collimated beam. They are removed when the micro-processing tests are carried out.

4.3.2 Polarization analysis of the collimated beams

I first checked that the collimated beam after the Polarization Mode Converter (i.e. before the focusing optics) had the expected polarization. The Polarization Mode Converter was set to produce a radially and an azimuthally polarized beam in turn. As described earlier in Section 4.2.3, this is achieved by setting the orientation of the incident polarization at +45˚ and inducing a 4π pitch vortex phase pattern with the SLM. The linear-to-radial/azimuthal mode conversion was then checked using a polarization analyzer and a SPIRICON camera placed in the beam path, after the Polarization Mode Converter (dotted components in Figure 4.6). This is essentially the same experiment as was carried out in Section 4.2.5, except that this time the SLM control software used a phase calibration factor and a phase offset to improve the polarization purity and remove distortions in the beam profiles. The beam intensity profiles transmitted through the polarization analyzer can be seen in Figure 4.7. These beam profiles are consistent with what is typically expected from analyzing a radially (Figure 4.7-a) or azimuthally (Figure 4.7-b) polarized beam, as demonstrated in Table 4.2. As anticipated with such beams, rotating the polarization analyzer (anti)clockwise causes the detected beam profiles to rotate (anti)clockwise.

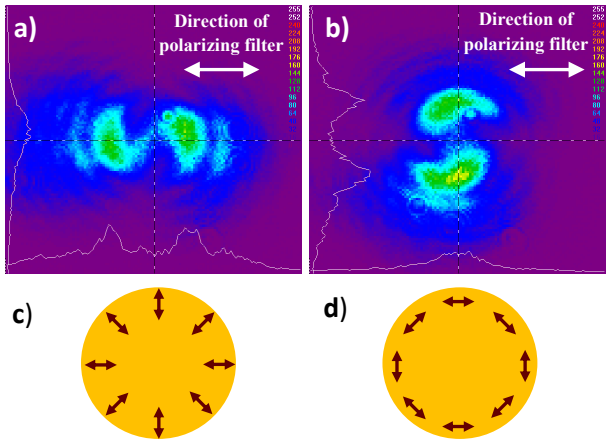

Figure 4.7: Beam intensity profiles observed with a CCD camera (SPIRICON beam profiler) after transmission through a horizontally oriented polarization analyzer. The colour coded scale (in arbitrary units) represents the amplitude of the beam. Only the components of the polarization vectors that are parallel to the analyzer are transmitted through. **(a)** is the profile of a radially polarized beam and **(b)** is the profile of an azimuthally polarized beam. **(c)** is a schematic of the vectorial structure of a radially polarized beam and **(d)** is a schematic of the structure of an azimuthally polarized beam.

4.3.3 Measuring polarization purity

By placing a power meter after the polarization analyzer, in front of the SPIRICON camera (see Figure 4.6), the polarization purity of the CVBs can be measured. The polarization purity was determined by the following method (which is also described in T. Moser *et al.* 2006). The laser power was measured when the analyzer was oriented at different angles. A maximum transmitted power, referred to as $\boldsymbol{P_{max}}$, was measured when the transmission axis of the analyzer was oriented at $\sim +50^{\circ}$ with regard to the horizontal. A minimum transmitted power, referred to as $\boldsymbol{P_{min}}$, was measured when the axis of the analyzer was oriented at $\sim -40^{\circ}$ (i.e. rotated by 90° from the orientation of the maximum transmitted

power). It was found $\boldsymbol{P_{max}} \approx 81\text{mW}$ and $\boldsymbol{P_{min}} \approx 59\text{mW}$. The polarization purity, noted $\boldsymbol{PP}$, was derived from the following formula:

$$\boldsymbol{PP} = 1 - \frac{\boldsymbol{P_{max} - P_{min}}}{\boldsymbol{P_{max} + P_{min}}} \quad (4.7)$$

Using to this formula, the polarization purity was found to be $\sim 84\%$. It is noted that if the through power was independent of the direction of the polarization analyzer and was always half of the incident power, the polarization purity would be 100%.

4.3.4 Polarization analysis in the focal plane

4.3.4.1 Aim

Having confirmed that the collimated beam after the Polarization Mode Converter had the expected state of polarization as described above, I then looked at the focal properties of the processing bench. The aim is to characterize the intensity distribution and polarization properties of the CVBs produced in the focal plane.

4.3.4.2 Experimental procedure

I used the method described in Chapter 2 to produce LIPSS on polished stainless steel surfaces and imprint the polarization vectors in the focal plane.

The Polarization Mode Converter was used to produce a linearly, circularly, radially and azimuthally polarized beam in turn. Summarizing from Chapter 2, the laser pulse energy was attenuated to 5µJ (1.5J/cm²) and each point was exposed to ~15 laser pulses, producing spot diameters of 38+/-10µm.

4.3.4.3 Results

After processing, I analyzed the laser marked spots with an optical microscope. High-magnification optical micrographs of the laser spots can be seen in Figure 4.8.

- Figure 4.8-a shows the LIPSS within the laser spot produced with a *linearly* polarized beam. As expected, the LIPSS formed as recurring linear structures oriented perpendicular to the direction of polarization. This is consistent with the results described in Chapter 2. It is noted that the region in the centre of the spot has no LIPSS. This is thought to be because the higher fluence at the tip of the Gaussian beam (i.e. in the middle of the spot) prevented the formation of LIPSS. This will be investigated further in Section 4.3.5.
- Figure 4.8-b shows the laser spot produced with a *circularly* polarized beam. No structure could be clearly identified within the spot. This is also consistent with the previous results in Chapter 2.
- Figure 4.8-c shows the laser spot produced with a *radially* polarized beam. The resulting LIPSS formed recurring curved structures centred on the middle of the laser spot. As the direction of the LIPSS is perpendicular to that of the electric field vectors (Z. Guosheng *et al.* 1982), the geometry of the structures inside the laser spot seems to imply that the electric field vectors are *azimuthally* oriented i.e. *azimuthal* polarization is likely to be dominant around the focal point.
- Figure 4.8-d shows the laser spot produced with an *azimuthally* polarized beam. The LIPSS appear to form an approximate circular pattern around the centre of the laser spot. This implies that *radial* polarization is likely to be dominant around the focal point.

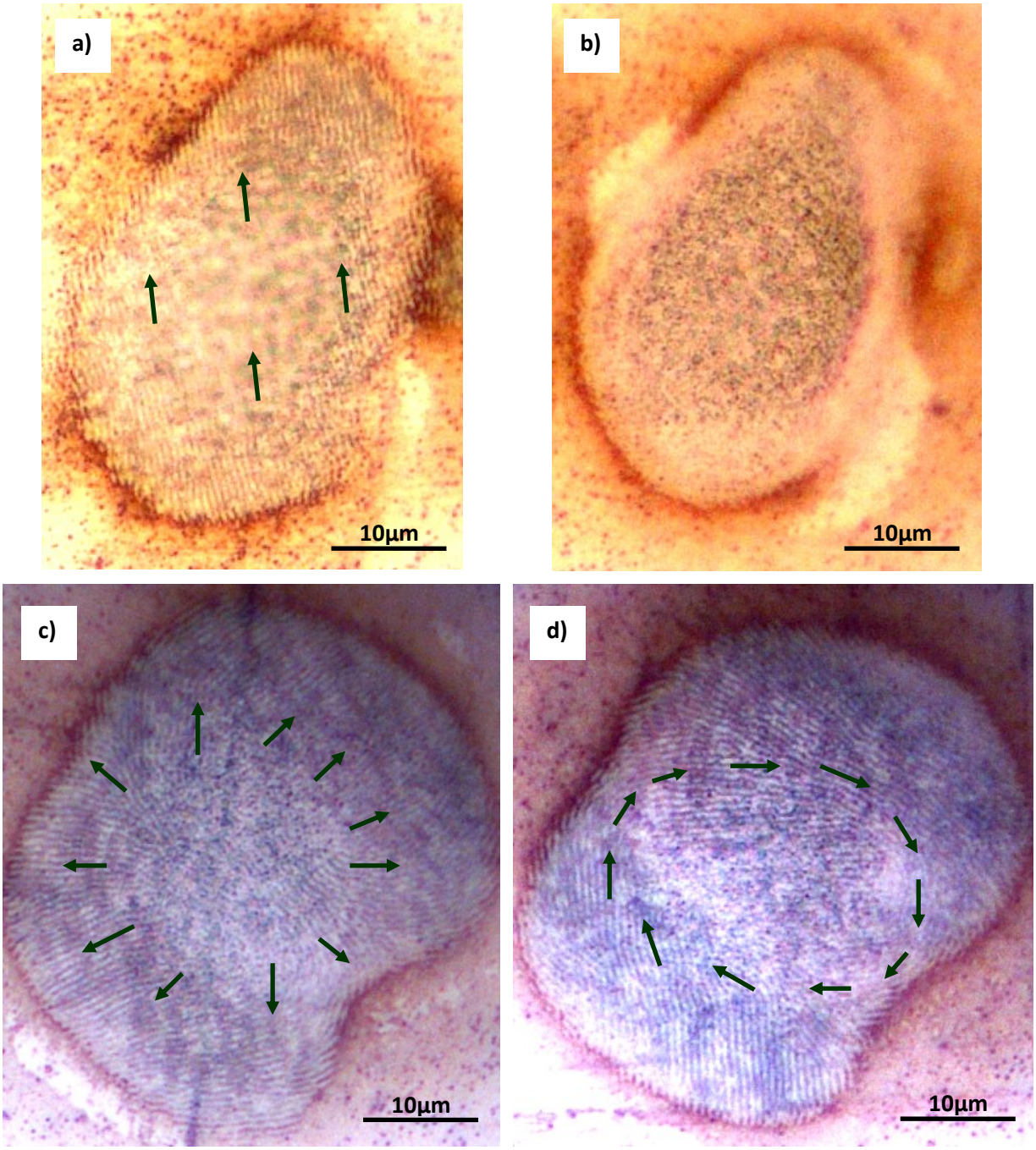

Figure 4.8: Optical micrographs showing the structures of the polarization vectors around the focal point of the micro-processing setup. The structures are imprinted into the surface of a stainless steel work-piece using LIPSS produced by 15+/-5 femtosecond pulses at 5µJ per pulse (1.5J/cm²). The arrows show the direction of the LIPSS and are perpendicular to that of the polarization vectors. The Polarization Mode Converter successively produced laser beams polarized linearly, circularly, radially and azimuthally, producing the laser spots shown in **(a)**, **(b)**, **(c)** and **(d)** respectively.

As expected, the radially and azimuthally polarized beams shown in Figures 4.8-c and 4.8-d produce patterns of LIPSS that are perpendicular to each other. This is most visible at the edges of the laser spots. It is noted that the laser spots produced with radially and azimuthally polarized beams are elliptical, tilted at ~45˚. It is also noted that there is a ~10μm diameter region in the centre of these laser spots where no LIPSS are visible. The reason for the absence of LIPSS in the central region will be discussed further in Chapter 5.

The experimental results obtained when focusing radially and azimuthally polarized beams are repeatable with other materials. Experiments using the same setup have been carried out on silicon wafers, producing the same patterns of LIPSS as in Figure 4.8 (see J. Ouyang, 2011).

Figure 4.9 summarizes the polarization analysis of CVBs at the focal plane, by splitting the laser-marked spots into three regions with different properties. It is noted that the elliptical shape of the beam affects the polarization purity, since the amplitude of the polarization vectors appears to be higher along the long axis of the ellipse.

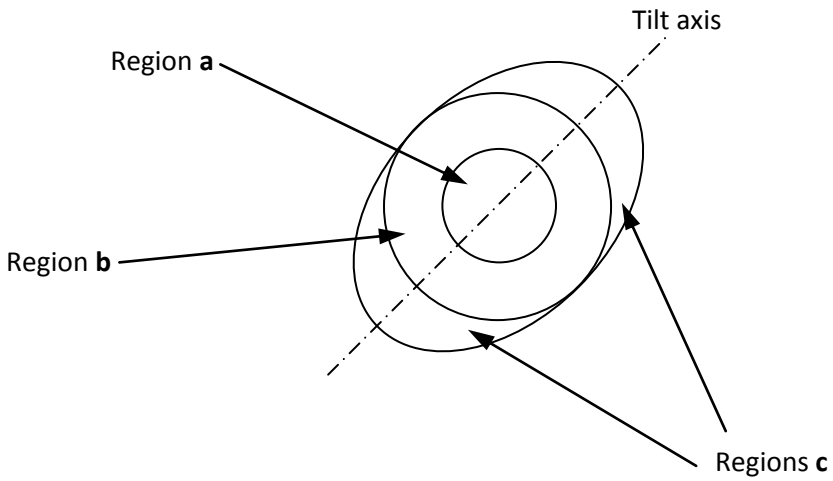

Figure 4.9: Schematic showing the overall geometry of the laser spots marked by focusing CVBs produced using the Polarization Mode Converter. The laser spots are always elliptical and tilted at ~45˚. They can be split into three regions, referred to as Regions a, b and c. In Region a, the LIPSS are not clearly visible. The reason for this will be discussed in Chapter 5. In Region b, the LIPSS are clearer and reveal the dominant polarization at the focal plane. In Region c, the LIPSS generally follow the same direction as those in the tangential areas of region b (i.e. along the tilt axis). It is noted that the polarization purity is affected by the ellipticity of the beams.

4.3.4.4 Discussion

The investigation of the LIPSS outlined above revealed that the radially polarized collimated beam from the Polarization Mode Converter seemed to produce an azimuthally polarized focal region and vice versa. It is interesting to consider why the state of polarization in the focal plane appears to be orthogonal to that of the collimated beam after the Polarization Mode Converter. In Chapter 5, I will present an analytical model explaining that an inversion in the state of polarization is expected in the focal plane when focusing CVBs with a phase vortex. However it is also noted here that a numerical simulation of a microscopy setup predicted that a radially polarized beam with a vortex phase becomes azimuthally polarized in the focal plane, whereas a radially polarized beam with a planar phase remains radially polarized in the focal plane (H. Kang *et al.* 2010). It is likely that the polarization inversion effect observed in my experiments above is also related to the vortex phase of the beam and it is anticipated that it would not occur when focusing a beam with a planar phase (i.e. without residual vortex phase).

The size and shape of the laser spots were also affected by the vortex phase structure of the radially and azimuthally polarized beams. The radially/azimuthally polarized vortex beams focused as elliptical spots with two lobes. This is consistent with theoretical predictions in G. Machavariani *et al.* 2007, where the focusing properties of a radially polarized vortex beam are investigated using a numerical simulation (although the geometry of the polarization vectors is not analyzed). The linearly and circularly polarized beams, which do not have a vortex phase structure, produced slightly smaller spots without lobes (32+/-5µm for linearly/circularly polarized beams versus 40+/-5µm for radially/azimuthally polarized vortex beams).

4.3.5 Comparative analysis of intensity profiles in the focal plane

In the experiments described in Section 4.3.4 above, the linearly and circularly polarized beams were produced by setting the incident polarization in a direction perpendicular to the axis of the liquid-crystals of the SLM. In this configuration, the SLM behaved like a mirror and no change in the phase or polarization of the beam occurred. Therefore, the linearly and circularly polarized laser beams had a phase that remained planar. In Section 4.3.4, these beams produced smaller spot sizes in the focal plane compared with radially and azimuthally polarized vortex phase beams, although they were marked using the same value of energy per pulse. A possible explanation for this is that there is a difference in the focal intensity (i.e. fluence) profiles between these beams, due to the difference in their phase structures.

To test this hypothesis, I marked laser spots on the surface of a stainless steel sample using the experimental setup described above (Figure 4.6) and I used an optical surface profiling system (WYKO NT1100) to measure the laser spots diameter and depth. The Polarization Mode Converter was used to produce a linearly, radially and azimuthally polarized beam in turn, as described in Section 4.3.4. However this time, the laser pulse energy was further attenuated to 1µJ (0.3J/cm^2) and each point was exposed to ~1500 laser pulses.

After processing, I analyzed the resulting laser marked surface with an optical microscope (see optical micrograph in Figure 4.10). The sample was also analyzed with the surface profiling system to measure the laser spots diameter and depth. It was found that the radially and azimuthally polarized beams both produced spots diameters of 15+/-3µm and a depth of 5.5+/-0.5µm (i.e. a depth/diameter ratio of

~0.37), whereas the linearly polarized beam produced spots diameters of 22+/-4µm and a depth of 12.0+/-1.0µm (i.e. a depth/diameter ratio of ~0.55).

The results above confirmed that the radially and azimuthally polarized beams produced a different spot diameter and depth compared with the linearly polarized beam, although all these beams had the same value of energy per pulse (1µJ). For example the spot diameter was 15+/-3µm for a radially or azimuthally polarized beam whereas it was 22+/-4µm for a linearly polarized beam. Interestingly, these results seem to be inconsistent with the previous experimental results in Section 4.3.4, where the radially or azimuthally polarized beam produced wider spot diameters (40+/-5µm) than the linearly polarized ones (32+/-5µm). However, the hypothesis outlined above where the beams have different intensity profiles, could resolve the apparent inconsistency.

The experimental results may indeed be explained if the linearly polarized beam had a comparatively steep Gaussian fluence profile while the radially and azimuthally polarized beams both had a comparatively wide fluence profile with a lower peak than the linearly polarized beam. The experimental results obtained when marking with a pulse energy of 1µJ (0.3J/cm²) are consistent with a linearly polarized beam having a peak fluence that is well above the ablation threshold of the stainless steel sample (0.16J/cm²), producing deeper and wider holes as a result. These results are also consistent with radially/azimuthally polarized beams having a peak fluence that is just above the ablation threshold, producing shallower holes. The suggested beam profiles are shown in Figure 4.11-a.

In Section 4.3.4, the experiments used a higher pulse energy of 5µJ (1.5J/cm²). As a result, the suggested intensity profiles are effectively shifted “upwards” in the fluence scale (see Figure 4.11-b). The diameter of all the laser spots increases, those produced with radially/azimuthally polarized beams become the widest.

This comparative analysis provides an insight into how the phase structure of the beams affects their intensity profiles. This analysis could not easily be carried out using a beam profiler, such as the SPIRICON camera shown in Figure 4.6. A beam profiler generally uses a beam splitter to pick-off a fraction of the beam power. With CVBs, these beam splitters effectively behave like polarizing filters producing profiles such as the ones shown in Figure 4.7 and making it difficult to compare with linearly or circularly polarized beams.

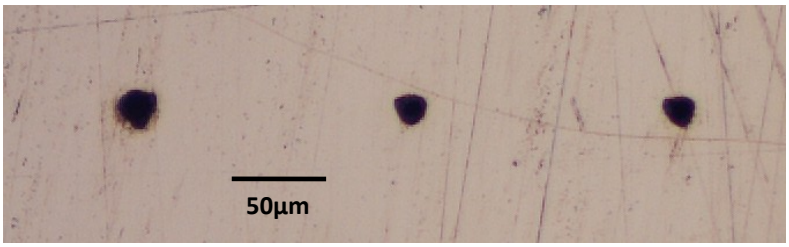

Figure 4.10: Optical micrograph showing the laser spots produced with ~1500 femtosecond pulses at 1µJ per pulse (0.3J/cm²). The spots were produced with a linearly (left), azimuthally (centre) and radially (right) polarized beam

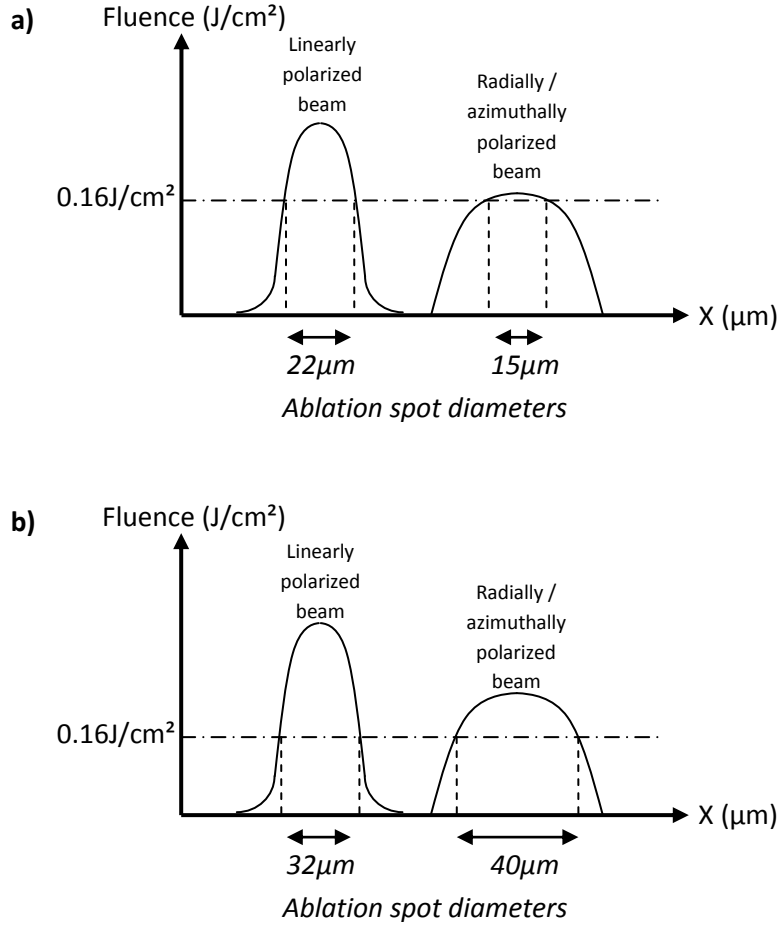

Figure 4.11: Schematics representing the suggested beam intensity profiles in the focal plane, inferred from the experimental results. The profiles in **(a)** are consistent with experimental results obtained with a laser pulse energy of 1μJ. The profiles in **(b)** are consistent with a laser pulse energy of 5μJ. The horizontal dotted line represents the ablation threshold of stainless steel. The diameter of the profile at the ablation threshold is determined from the diameter of the laser ablation spot, which is obtained experimentally.

4.3.6 Effect of the phase vortex on the focusing properties of CVBs

4.3.6.1 Optical aberrations

In the experimental setup used for laser micro-processing with CVBs (see Figure 4.6 in Section 4.3.1), some of the optical components induce aberrations that affect the focal properties. Here, these aberrations are sorted into five types:

- Beam mode: slight aberrations in the laser beam mode affect the polarization purity of the CVBs produced in the experiments. Here the laser beam quality factor, measured with a SPIRICON beam profiler, is $M^2 = 1.3$. The beam profile can be seen in Figure 4.12. The polarization purity, measured in Section 4.3.3, was $\sim 84\%$.
- Astigmatism in the laser beam: this affects the morphology of the laser spot above and below the focal plane.
- SLM surface distortions: due to constraints in the manufacturing of the active liquid-crystal layers, phase distortions are induced by the SLM. Some, but not all of these distortions are corrected using a

phase correction pattern provided by the SLM manufacturer (see Figure 4.13). This phase correction pattern is superimposed on the desired phase patterns such as the ones shown in Tables 4.2 and 4.3.

- Residual phase divergence induced by the Polarization Mode Converter: the phase vortex induced by the SLM produces a phase singularity at the optical axis. The pixels of the SLM that are very close to this central phase singularity induce significant diffraction effects, because of the rapid transverse spatial phase variations associated with the singularity (L. Marrucci *et al.* 2011). These diffraction effects produce a residual divergence of the beam. The residual phase divergence is further discussed in Chapter 5.
- Residual phase vortex induced by the Polarization Mode Converter: although the residual phase vortex is not an optical aberration, it affects the focusing properties of the CVBs.

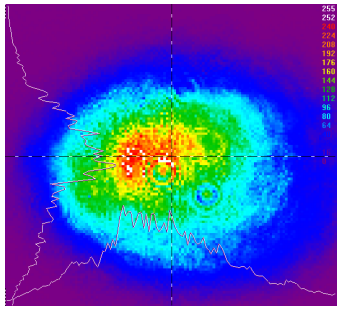

Figure 4.12: Laser beam profile observed with a CCD camera (SPIRICON beam profiler). The experimental setup is shown in Figure 4.6. The colour coded scale (in arbitrary units) represents the amplitude of the beam.

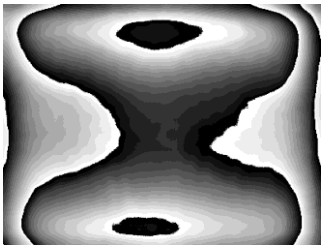

Figure 4.13: Phase correction pattern induced by a Hamamatsu X10468-02 SLM, to correct for phase distortions induced from the imperfect surface flatness of its LCOS chip. This phase correction pattern was provided by Hamamatsu Photonics K.K.

4.3.6.2 Residual phase vortex

In this section, I look at how the residual vortex structure of the phase affects the laser fluence amplitude profile (i.e. the intensity distribution) in the focal plane. This is done by using the experimental setup described in Section 4.3.1 (Figure 4.6) to produce CVBs with a vortex phase pitch (topological charge) of π, 2π and 3π successively.

The resulting beams were first analyzed with a polarizing filter and a SPIRICON camera. The beam profiles can be seen in Figure 4.14. These beams were then used to process the surface of polished stainless steel samples placed at the focal plane, with the laser pulse energy attenuated to 10μJ (3J/cm²), using the setup described in Figure 4.6 (without the dashed components). Each point was exposed to ~15 laser pulses.

After processing, the resulting laser marked surface was observed with an optical surface profiling system (WYKO NT1100). The measured surface profiles can be seen in Figure 4.15. It is noted that all the produced laser spots have LIPSS that reveal their polarization structure. However this analysis aimed at studying the laser fluence amplitude profile at the focal plane, so the LIPSS were not analyzed further.

Here, I look at the morphology of the produced laser spots, since it gives an indication of the laser amplitude profile at the focal plane. All the produced laser spots have a "Z" shaped structure with two lobes. It can be seen that increasing the vortex pitch moves the lobes further away from the centre of the spots. The maximum depth of the laser spots was found to be 1.0±0.5μm in all cases. The lobes are also found to be deeper (1.0±0.5μm) than the centre of the spot (0.6±0.4μm) when a vortex phase pitch of π was applied. The lobes are shallower than the center of the spot with higher vortex pitches (0.2±0.2μm at the lobes versus 1.0±0.5μm at the centre when a 3π pitch phase vortex was used). This means that the lobes carry less energy with higher vortex pitches.

It is noted that the laser spot produced with a 2π phase vortex in Figure 4.15-b is not exactly similar to the ones shown in Figure 4.8, which were also produced with CVBs with a 2π phase vortex. This is because the SLM was used in a different mode between the two experiments. The laser spots shown in Figure 4.8 were produced with the SLM using a corrective phase pattern (see Figure 4.13). The laser spots sown in Figure 4.15 were produced without using any corrective phase pattern.

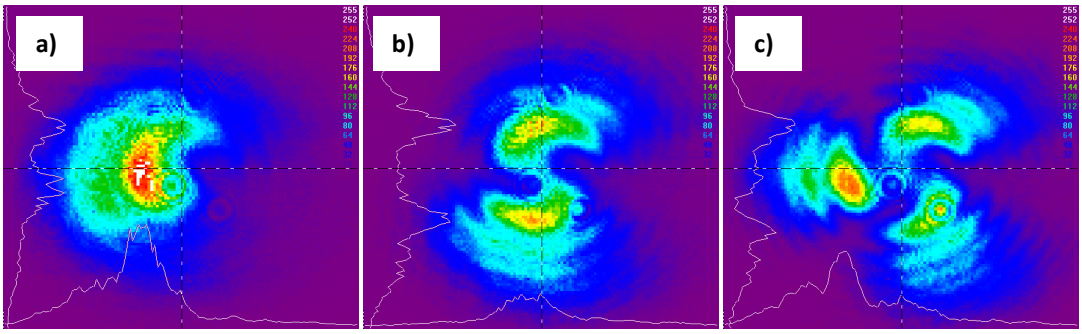

Figure 4.14: Beam profiles observed with a CCD camera (SPIRICON beam profiler) after transmission through a horizontally oriented polarization analyzer. The colour coded scale (in arbitrary units) represents the amplitude of the beam. Only the components of the polarization vectors that are parallel to the analyzer are transmitted through. **(a)** is the profile of a CVB with a phase vortex pitch of π. **(b)** is the profile of a CVB with a phase vortex pitch of 2π. **(c)** is the profile of a CVB with a phase vortex pitch of 3π.

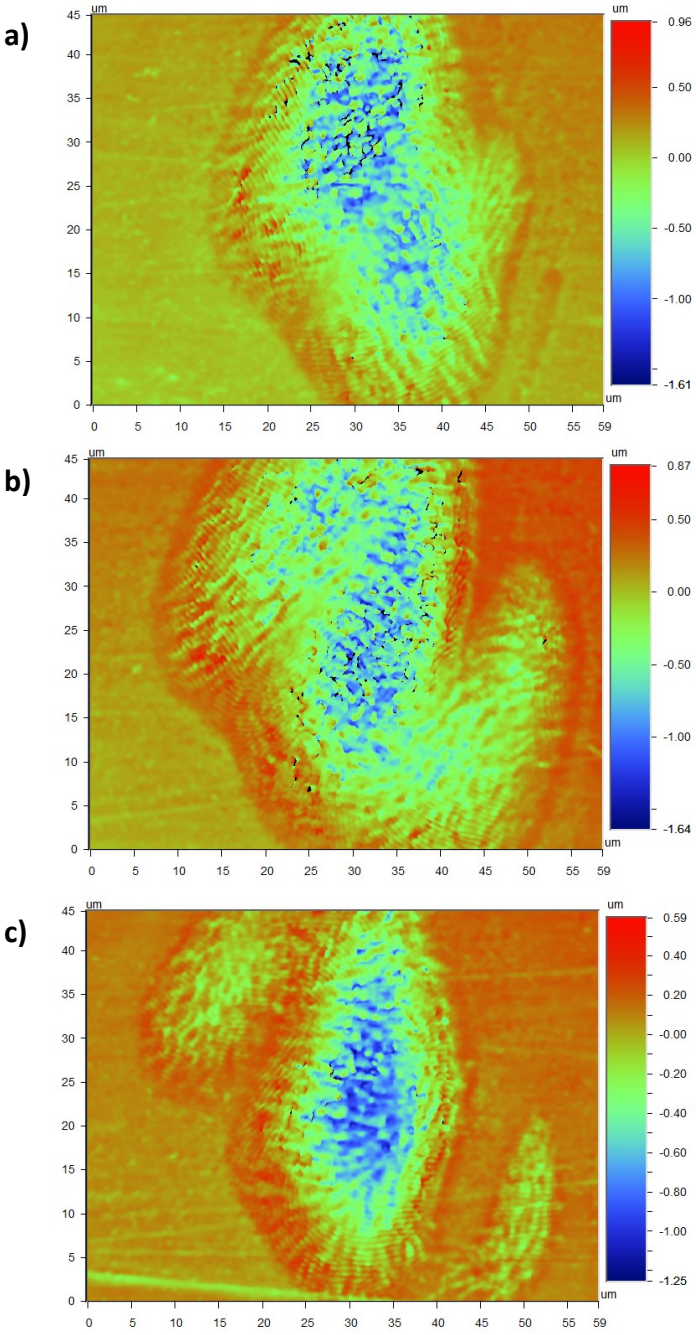

Figure 4.15: Laser marked spots observed with an optical surface profiling system. All the laser spots were produced on a polished stainless steel surface by 15+/-5 femtosecond pulses at 10µJ per pulse (3J/cm²), using CVBs with a phase vortex. The colour-coded scale shows the distance from the surface of the sample, in µm. The dark blue regions are the deepest regions. The morphology of the laser spots is an indirect indication of the intensity distribution at the focal plane. **(a)** was produced with a phase vortex pitch of π. **(b)** was produced using with a phase vortex pitch of 2π. **(c)** was produced with a phase vortex pitch of 3π.

4.3.7 Three dimensional mapping of the polarization structure of CVBs in the focal region

4.3.7.1 Aim

In the experiments in Section 4.3.4, I found that a radially polarized vortex phase collimated beam produced an azimuthally polarized focal spot and vice versa. This suggests that the state of polarization of the focused beam varies along the optical axis of the focusing lens. In order to better understand this phenomenon, I use the LIPSS analysis method to imprint the polarization vectors at various planes above and below the focal plane of the focusing lens. In this way, I can build a three dimensional map of the polarization vectors in and around the focal plane.

4.3.7.2 Experimental procedure

I used the same experimental procedure as described in Section 4.3.4, except that the stainless steel sample was placed at various positions above and below the focal plane (see Figure 4.16). After processing, the resulting laser marked spots were imaged with an optical microscope.

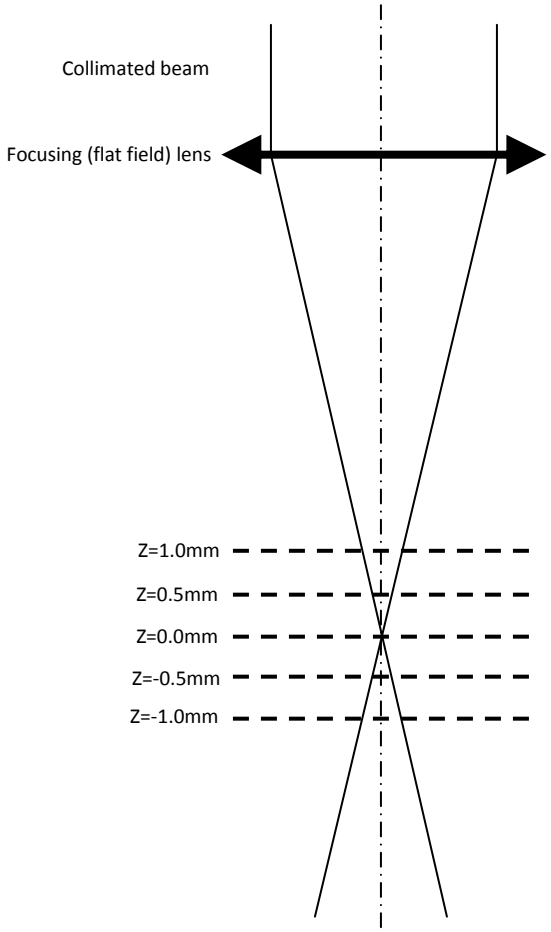

Figure 4.16: Schematic showing the focused beam and the planes where the sample was positioned to mark the LIPSS. The focal plane of the lens is set at Z=0mm.

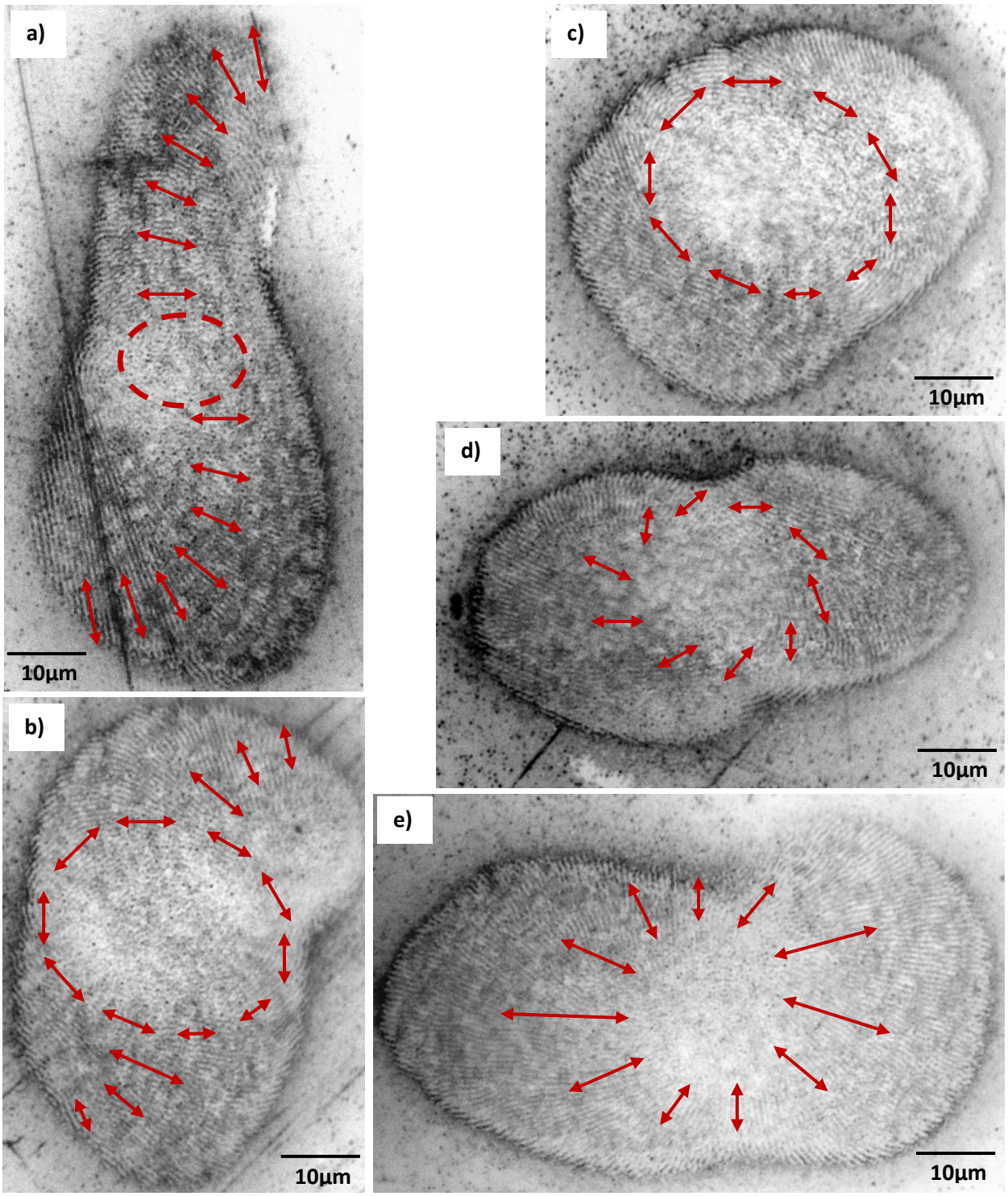

Figure 4.17: Optical micrographs showing the structure of the polarization vectors in various planes along the optical axis of the focusing lens. The polarization vectors are imprinted into the surface of a stainless steel work-piece using LIPSS produced by 15+/-5 femtosecond pulses at 5µJ per pulse (1.5J/cm²). The incident collimated vortex phase beam is azimuthally polarized. The arrows show the direction of the LIPSS and so are perpendicular to the polarization vectors. The sample surface was positioned 1mm above the focal plane in **(a)**, 0.5mm above the focal plane in **(b)**, at the focal plane in **(c)**, 0.5mm below the focal plane in **(d)** and 1mm below the focal plane in **(e)**.

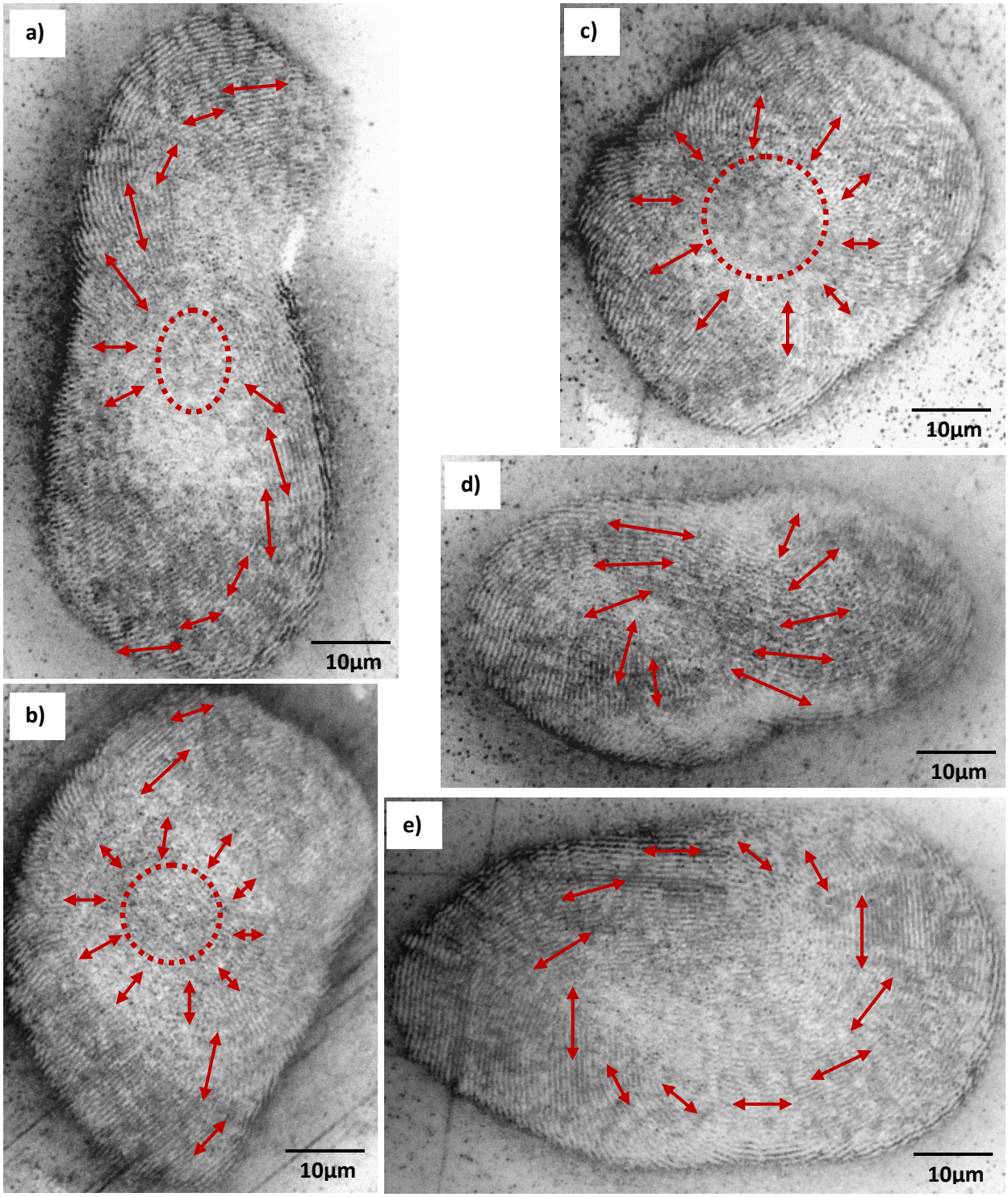

Figure 4.18: Optical micrographs showing the structure of the polarization vectors in various planes along the optical axis of the focusing lens. The polarization vectors are imprinted into the surface of a stainless steel work-piece using LIPSS produced by 15+/-5 femtosecond pulses at 5µJ per pulse (1.5J/cm²). The incident collimated vortex phase beam is radially polarized. The arrows show the direction of the LIPSS and so are perpendicular to the polarization vectors. The sample surface was positioned 1mm above the focal plane in **(a)**, 0.5mm above the focal plane in **(b)**, at the focal plane in **(c)**, 0.5mm below the focal plane in **(d)** and 1mm below the focal plane in **(e)**.

4.3.7.3 Results

Figure 4.17 shows the LIPSS within the laser marked spots at each position along the optical axis. The Polarization Mode Converter was set to generate an azimuthally polarized vortex phase collimated beam in this instance. Figure 4.18 shows the LIPSS within the laser marked spots for a radially polarized vortex phase collimated beam.

Figures 4.17 and 4.18 show that the morphology of the laser spots and the geometry of the LIPSS vary around the focal plane of the laser beam. This means that both the intensity and polarization of the focused vortex phase beams have a geometrical structure that varies along the optical axis after the focusing lens.

4.3.7.4 Morphology of the laser spots

I first look at the morphology of the laser spots, which is an indirect indication of the intensity structure of the focused beam:

- The laser spots above the focal plane, shown in Figures 4.17-a, 4.17-b, 4.18-a and 4.18-b, have lobes that are larger further away from the focal plane (Figures 4.17-a and 4.18-a). The lobes are fairly small 0.5mm above the focal plane (Figures 4.17-b and 4.18-b) and they almost disappear at the focal plane (Figures 4.17-c and 4.18-c).
- Below the focal planes, small lobes are visible which are perpendicular to those above the focal plane (Figures 4.17-d, 4.17-e, 4.18-d and 4.18-e).

These lobe structures are not visible when laser marking samples with a planar phase (i.e. without a phase vortex), as was shown in Figure 4.8. Therefore, it is thought that they are related to the phase vortex produced by the Polarization Mode Converter. The current design of the Polarization Mode Converter does not allow a CVB to be produced without a residual phase vortex. Furthermore in this experimental setup, a slight astigmatism of the produced laser beam influences the shape of the laser spots produced above and below the focal plane. However, the effect of the phase vortex is thought to dominate the distortions in the spot morphology.

4.3.7.5 Geometry of the LIPSS

Now I look at the structure of the LIPSS (i.e. the polarization vectors):

- The LIPSS at the focal plane (Figures 4.17-c and 4.18-c) are consistent with those presented in Section 4.3.4 (see Figure 4.8).
- Above the focal plane, the center of the beam has approximately the same LIPSS structure as in the focal plane. This is especially visible in Figures 4.17-b and 4.18-b. However, the lobes have LIPSS that gradually curve away from the center of the beam, as seen in Figures 4.17-a and 4.18-a. This implies that the polarization vectors also curve perpendicularly to the LIPSS.
- Below the focal plane, the structure of the LIPSS varies along the optical axis. The LIPSS gradually change the further away from the focal plane in such a way that, 1mm below the focal plane, they are approximately orthogonal to those at the focal plane (see Figures 4.17-e and 4.18-e). This implies that the state of polarization is also orthogonal to that at the focal plane. Coincidentally, the state of polarization 1mm below the focal plane is similar to that of the collimated beam after the Polarization Mode Converter.

4.3.7.6 Discussion

The analysis of the LIPSS implies that, when focusing CVBs with a vortex phase, the polarization vectors appear to "twist" along the optical axis of the focusing optics. This analysis allowed me to confirm that the state of polarization of the focused beam indeed varies along the optical axis of the focusing lens. This phenomenon is thought to be related to the vortex phase of the CVBs produced with the Polarization Mode Converter. It is anticipated that it would not occur when focusing a beam with a planar phase. This is an important result for laser material processing, where only the state of polarization within the focal region is relevant. It highlights the necessity to check the state of polarization of a CVB at the focal plane, because it is not necessarily the same as that of the collimated beam, where polarization is typically analyzed. However the implications of these results go beyond laser machining. These results give an insight into CVBs with an orbital angular momentum (i.e. a phase vortex) and could contribute to improve the understanding of laser-material interactions with these beams.

The phenomenon that leads to the variation of the polarization state along the optical axis is not trivial. To better understand this phenomenon and the polarization properties of focused vortex beams, I developed an analytical model that describes these beams. The model is detailed in Chapter 5.

4.4 Chapter summary

The chief points of this chapter are outlined below. A discussion of the wider context of these results is outlined in Chapter 7.

- I have introduced a Polarization Mode Converter that comprises a liquid-crystal SLM and a quarter-waveplate and demonstrated theoretically, using Jones vector formalism, how it can produce CVBs.

- The Jones vector calculations show that there is a residual phase vortex after the Polarization Mode Converter. For example if radially or azimuthally polarized beams are produced, the residual phase vortex has a 2π pitch.

- As a proof of concept, the Polarization Mode Converter was implemented in a nanosecond-pulse laser test bench, demonstrating experimentally that CVBs can be produced.

- The Polarization Mode Converter was implemented in an ultrafast laser micro-processing bench. The intensity distribution and polarization properties around the focal point of the micro-processing bench were studied.

- At the focal plane, the state of polarization was found to be orthogonal to that of the collimated beam before the focusing lens. This polarization rotation effect is thought to be caused by the residual vortex phase structure induced with the Polarization Mode Converter.

- Analyzing polarization above and below the focal plane revealed that the polarization vectors “twist” along the optical axis of the focusing optics. This is an interesting development in the study of CVBs with an orbital angular momentum (i.e. a phase vortex). It could contribute to improve the understanding of laser-material interactions with these beams.

- The phase vortex affects the intensity distribution at the focal plane, producing lobes around the center of the focal spot. Changing the pitch of the phase vortex affects the intensity distribution and the size of the lobes.

5

Geometrical analysis of the polarization state in the focal plane

5.1 Introduction

The experimental results described in Chapter 4 indicate that the state of polarization at the focal plane is orthogonal to that of the collimated vortex phase beams before the focusing optics. For example, a collimated vortex phase beam polarized radially after the Polarization Mode Converter becomes azimuthally polarized at the focal plane and vice versa. In this chapter, I present an analytical model of the optical components in the experiments described in Chapter 4 aimed at investigating this phenomenon.

Numerical models are frequently used to predict the structure of the polarization vectors around the focal point of optical setups. These models help us to understand the focal properties of various polarization modes (for example Q. Zhan & J. R. Leger, 2002 studied focused laser spots produced with CVBs with a planar phase, H. Kang *et al.* 2010 modeled several types of radially polarized beams with a vortex phase, focused with a high NA microscope setup and D. P. Biss & T. G. Brown, 2004 looked at aberrations produced by focusing radially polarized beams). These models indicate that the state of polarization of a collimated CVB with a planar phase is maintained at the focal plane. However, the focal behavior of CVBs with a vortex phase is more complicated as it depends on the optical properties of the experiment (topological charge of the phase vortex, NA of the focusing optic, etc). The publications above involved models of optical setups where high NA objectives are used to focus the beam, producing very small focal spots, so their results are not directly transferable to my own optical setup. In my experiments, I used a 100mm focal length f-theta lens with a NA of 0.03. Numerical simulations using similar low NA optics are available in the literature (for example Y. V. Krylenko *et al.* 2011 modelled an optical setup with a 100mm focal length, using two different numerical calculation methods and compared the results between the two methods). However, none of the published results address the polarization properties at the focal plane of radially or azimuthally polarized vortex phase beams, focused with a low NA optic similar to the one used in my experiments. Since no numerical simulation available in the literature can explain the experimental results found in Chapter 4, I have developed an analytical model of these beams. Analytical calculations rather that numerical ones are used, thanks to the simple geometry of the setup.

This chapter describes how I represent my optical setup using a geometrical approach to analyze the Jones vectors at the focal plane. This model explains the inversion in the state of polarization at the focal plane between a radial and an azimuthal mode. This chapter is structured as follows:

- I first describe how the geometry of the experimental setup can be modeled analytically, using approximations where appropriate.

- I detail how the model describes various types of CVBs using complex Jones vectors.
- I study the focusing properties of a radially polarized beam with a planar phase.
- I also study the focusing properties of a radially polarized beam with a 2π vortex phase.
- The focusing properties of azimuthally polarized beams with a planar or a 2π vortex phase are also studied.
- The resulting model predictions are discussed and compared with the experimental results presented in Chapter 4.

To aid clarity, some of the derivations in this chapter are summarized. The full derivations are available in Appendix B.

5.2 Outline of the model

5.2.1 Geometry of the experimental setup

The geometrical properties of the beams produced in the experiments allow me to make a number of approximations in the model, keeping my analysis simple without compromising the accuracy of the predictions. Here, I describe some of the geometrical properties of these beams. In the next section, I discuss the resulting simplifications in the model.

- The Polarization Mode Converter produces an annular beam. This is because the SLM induces a phase singularity at the optical axis, where the beam amplitude is zero.
- The Polarization Mode Converter produces a CVB with a discrete polarization structure, because of the finite number of pixels on the SLM (see schematic in Figure 5.1-a).
- The focusing optic after the Polarization Mode Converter is a low NA lens (NA = 0.03).
- The SLM induces a residual unwanted phase divergence, which is superimposed on the desired phase pattern. This phase divergence, caused by diffraction effects in the liquid-crystal layer near the phase singularity (Marrucci *et al.* 2011), induces a spread of the laser beam energy at the focal plane. Figure 5.2 shows the phase spread which is cylindrically symmetric around the optical axis: the resulting widened laser spot is centered on the focal point, noted ***O*** in Figure 5.2. It is noted that these SLM-induced diffraction effects dominate the overall diffraction at the focal plane. Therefore other sources of diffraction, such as the focusing optics, are ignored in the model.

5.2.2 Approximations

To mimic the experimental setup, my model represents the annular beam with eight polarization vectors equally spread around the beam profile (Figure 5.1-b). Although approximate, this model reflects the annular, pixelated structure of the CVBs produced in the experiments. Also, because of the low NA of the focusing optic, the longitudinal components of the polarization vectors (i.e. along the optical axis) at the focal plane are ignored in the model, since their contribution is negligible. This makes the geometrical calculations simpler.

To mimic the residual unwanted phase spread induced by the SLM, I assume that each point in the focal plane is reached by a separate planar component of the overall wavefront (Figure 5.2).

5.2.3 Principle of the model

The resulting polarization and amplitude at the focal plane are studied using the complex Jones vector technique (which was first used in Chapter 4). I sum the contribution from each of the annular beam's eight vectors at various points in the focal plane. My study first looks at two specific points in the focal plane: at the optical axis (shown as Point ***O*** in Figure 5.2) and at a location in the focal plane where the optical path difference between two cylindrically opposite vectors is equal to half of a wavelength (as is the case at Points ***A*** or ***B*** for example in Figure 5.2). Thanks to the cylindrical symmetry of this problem, the polarization properties at other points in the focal plane can then be extrapolated from those at Points ***O*** and ***A***. This analysis gives me a good approximation of the polarization and amplitude in the focal plane, without requiring an advanced numerical simulation.

In this analysis, I look at four types of CVB. I first look at a radially polarized beam with a planar phase. Then I look at a radially polarized beam with a 2π vortex phase (i.e. a topological charge of one). The polarization properties at the focal plane are compared between these two beams to show how the phase vortex influences the focal properties. The focal properties of azimuthally polarized beams with planar and 2π vortex phase structures are also derived. It is noted that the model described here could in principle predict the focal polarization of CVBs other than radially or azimuthally polarized beams. However, as the model relies on vectorial symmetry, the CVBs have to have a cylindrical symmetry. This is the case, for example, for CVBs with a vortex phase pitch that is an even multiple of π (i.e. 0, 2π, 4π, etc...).

Although the Polarization Mode Converter used in the experiments can only produce radially or azimuthally polarized beams with a 2π vortex phase, modeling planar phase CVBs allows me to check the model by comparing its prediction with the existing publications available in the literature. As discussed above in Section 5.1, the focal properties of planar phase CVBs are better understood than those of CVBs with a vortex phase.

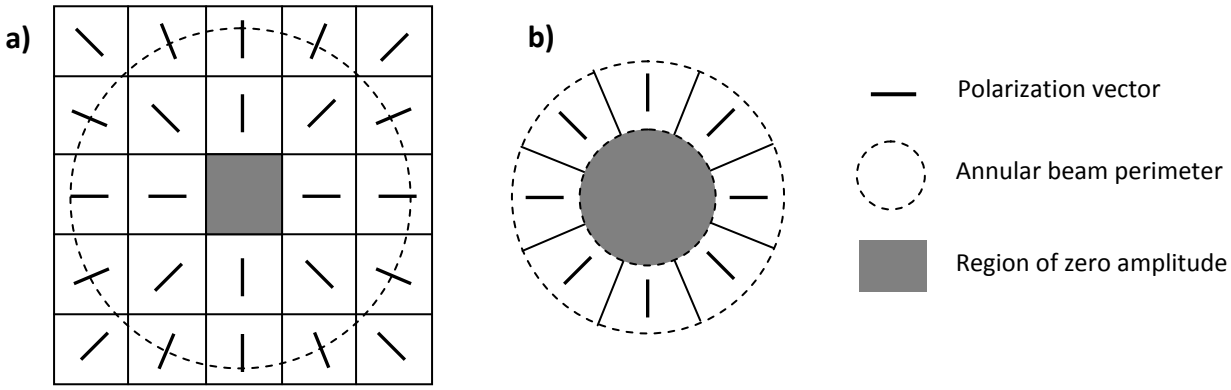

Figure 5.1: (a) Simplified schematic showing the pixel structure of the SLM used in the experiments. The beam perimeter is shown as a dotted line (not to scale). Each pixel produces a polarization angle that is slightly different from that of its neighbours. In this example, the overall polarization is radial. At the center of the beam, a zero amplitude region is caused by the phase singularity. In the experimental setup, the beam diameter is ~6mm and the pixel size is 50µm, so there are ~120 pixels across the beam diameter. **(b)** Schematic showing how the model represents the annular beam with eight polarization vectors surrounding a region of zero amplitude.

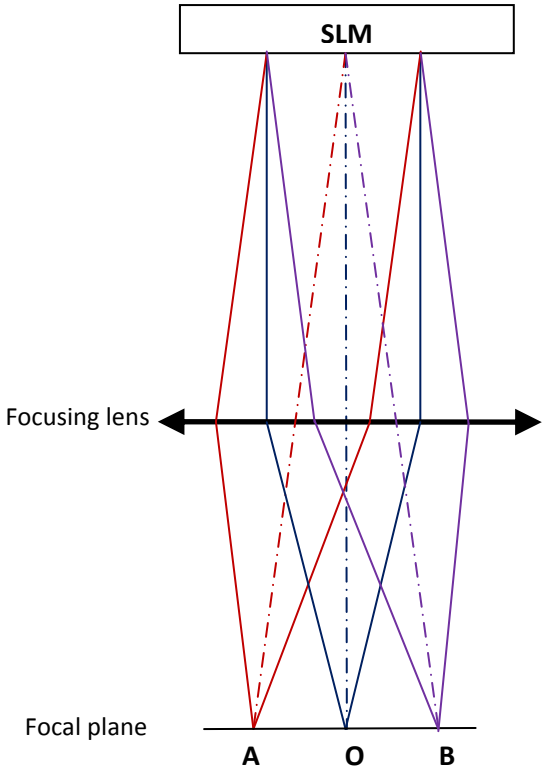

Figure 5.2: Schematic showing how the residual unwanted phase divergence produced by the SLM induces a spread of the laser beam energy at the focal plane. In the model described here, each point at the focal plane is reached by a separate planar wavefront component. For clarity, the quarter-waveplate after the SLM is not represented here, since it does not affect the phase divergence.

5.3 Vectorial calculation

It is noted here that I use i as an index number and j as an imaginary number.

5.3.1 Geometry of the model

Figure 5.3 shows the geometry of the model. The annular CVB is represented by eight Jones vectors $\vec{E}_i$ (Figure 5.3-a). The CVB focused with a low NA objective is studied at two specific points in the focal plane: at Points ***O*** and ***A*** (Figure 5.3-b). Point ***O*** is on the optical axis, where some of the laser energy is focused. Because of the residual unwanted phase divergence induced by the SLM, some of the laser energy is also focused at Point ***A***.

The resulting Jones vector at each of these points is derived by summing the contribution from all the vectors and normalizing the sum: $\frac{1}{8}\sum_{i=0}^{i=7}\vec{E}_i$. Because of the very low NA of the focusing optic, I ignore the longitudinal components of the vectors (i.e. along the optical axis) at these points.

5.3.2 Jones vector coordinates definition

I first define a reference coordinate system in the focal plane $(\boldsymbol{O}, \vec{\boldsymbol{X}}, \vec{\boldsymbol{Y}})$ to express the Jones vectors (Figure 5.3-c). Each Jones vector $\vec{E}_i$ is defined within this coordinate system as (E_{iX} ; E_{iY}). The vector coordinates E_{iX} and E_{iY} are expressed as complex numbers: $E_{iX} = r_{iX}.e^{j(\varphi_{iX})}$ and $E_{iY} = r_{iY}.e^{j(\varphi_{iY})}$, where r_{iX} and φ_{iX}, are the amplitude and phase of E_{iX} respectively. The relation between the amplitude of $\vec{E}_i$ and the amplitude of its coordinates E_{iX} and E_{iY} is: $\left\|\vec{E}_i\right\| = \sqrt{{r_{iX}}^2 + {r_{iY}}^2}$. For convenience we choose $\left\|\vec{E}_i\right\| = 1$.

It is noted that, thanks to the quarter-waveplate inserted after the SLM in the optical setup, the phase of both complex coordinates E_{iX} and E_{iY} is the same: $\varphi_{iX} = \varphi_{iY} = \varphi_i$ (this could be seen in Equation 4.6 in Chapter 4, where there was no phase difference between the horizontal and vertical coordinates). Without the quarter-waveplate, φ_{iX} and φ_{iY} would have different values (this could also be seen in Equation 4.2 in Chapter 4, where there was a phase difference between the horizontal and vertical coordinates).

The resulting Jones vector at any given point in the focal plane is ($\frac{1}{8}\sum_{i=0}^{i=7}E_{iX}$; $\frac{1}{8}\sum_{i=0}^{i=7}E_{iY}$). To derive the Jones vector at that point, I use the "Complex Plane" method. It is noted that the "Complex Plane" method enables to sum complex vectors and derive geometrically the resulting amplitude and phase. However this method requires all the vectors in the sum to be parallel to each other. Therefore in this analysis, I sum all the vector components parallel to $\vec{\boldsymbol{X}}$ together ($\frac{1}{8}\sum_{i=0}^{i=7}E_{iX}$) and all the vector components parallel to $\vec{\boldsymbol{Y}}$ together ($\frac{1}{8}\sum_{i=0}^{i=7}E_{iY}$), as two separate calculations. The "Complex Plane" method also requires the phase of all the vectors to be expressed with regard to the same reference origin. In the next section, I define the origin of the phase.

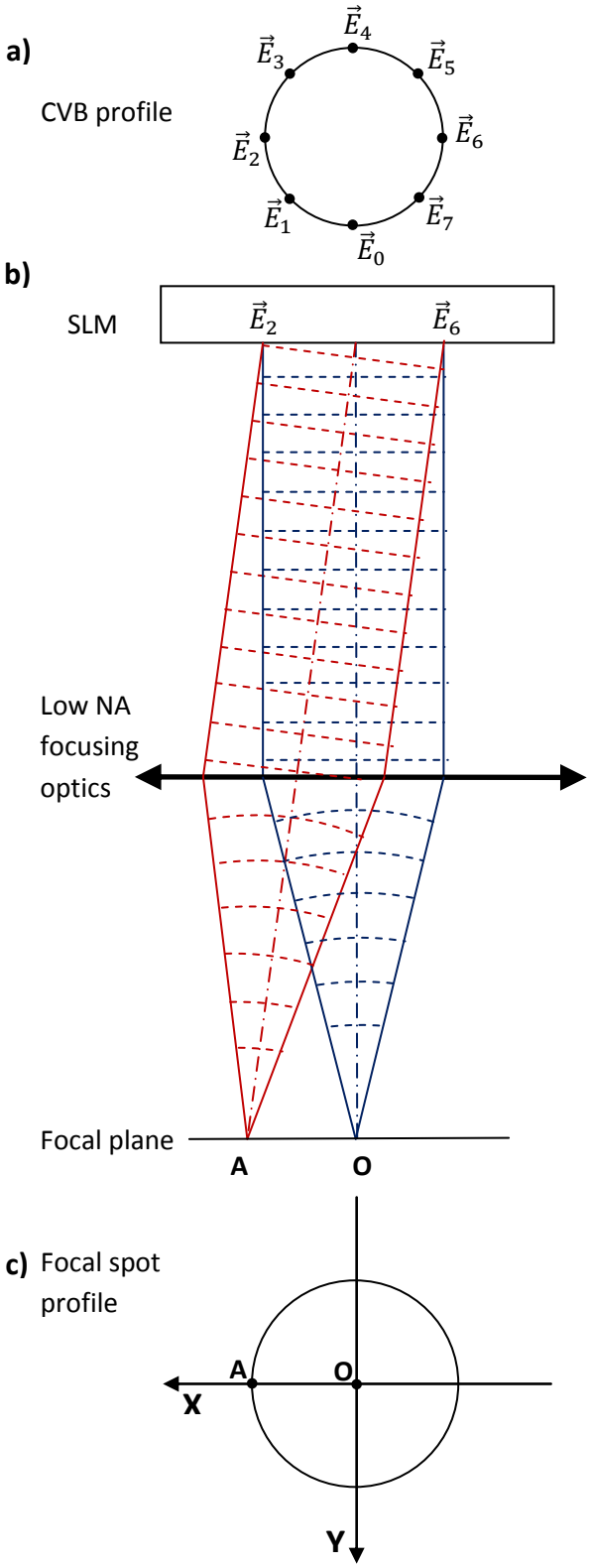

Figure 5.3: Schematics showing: **(a)** the eight polarization vectors in the CVB profile, **(b)** the side-view of the phase fronts focusing at the focal plane and **(c)** the reference coordinate system (***O***, ***X***, ***Y***) describing the focal plane. It is noted that the quarter-waveplate after the SLM is not represented here as it does not affect the divergence of the phase fronts.

5.3.3 Jones vectors phase definition

To use the "Complex Plane" method, the model needs to define each phase φ_i according to the structure of the phase front (i.e. planar or vortex) and the location where the phase front focuses (i.e. Point ***O*** or Point ***A***). For clarity, each phase term φ_i is defined as the sum of a phase term φ_{1i} related to the structure of the phase front and a phase term φ_{2i} related to the tilt angle of the phase front: $\varphi_i = \varphi_{1i} + \varphi_{2i}$.

5.3.4 Phase term $\boldsymbol{\varphi_{1i}}$

In this analysis, I am interested in two types of phase front geometry: a planar phase front and a vortex phase front with a pitch of 2π (i.e. a topological charge of one).

- If the beam has a planar phase front, all the eight phase terms φ_{1i} are equal. For simplicity, they are defined as: $\varphi_{1i} = 0$. This case is further investigated in Section 5.4.
- If the beam has a vortex phase front with a topological charge of one, the phase terms are defined as: $\varphi_{1i} = i \times \frac{\pi}{4}$. This case is further investigated in Section 5.5.

5.3.5 Phase term $\boldsymbol{\varphi_{2i}}$

The phase tilt factor φ_{2i} has to be added to each phase term φ_i if the phase front is not perpendicular to the optical axis (as is the case for the component of the phase front that focuses at Point ***A***).

Here, I need to derive the phase tilt factor φ_{2i} for each incident vector $\vec{E}_i$ in the case of the phase front component that focuses at Point ***O*** and the one that focuses at Point ***A***.

5.3.5.1 Phase front that focuses at Point **O**

Figure 5.3-b shows the component of the phase front that focuses at Point ***O***, from the SLM to the focal plane. The phase front is perpendicular to the optical axis of the setup and there is no optical path (i.e. phase) difference between the contributing incident polarization vectors $\vec{E}_i$ that focus at Point ***O***. This means there is no need for any phase tilt factor to be included when adding the contribution from each vector at Point ***O***: $\varphi_{2i} = 0$.

5.3.5.2 Phase front that focuses at Point **A**

Figure 5.3-b shows the component of the phase front that focuses at Point ***A***, from the SLM to the focal plane. This phase front diverges linearly away from the optical axis of the setup (i.e. it is tilted from the optical axis). The tilt angle implies that there is an optical path (i.e. phase) difference between each contributing incident vector $\vec{E}_i$ that focuses at Point ***A***. Figure 5.4 illustrates how the phase front tilt at the SLM induces an optical path difference at Point ***A***. In my model, Point ***A*** has specific geometrical properties: its location is chosen so that the contributions from $\vec{E}_2$ and $\vec{E}_6$ are out of phase i.e. the optical path difference between $\boldsymbol{E_2A}$ and $\boldsymbol{E_6A}$ is half a wavelength. This is shown in Figure 5.4: the distance $\boldsymbol{E_6F}$ is λ/2.

Here, I am interested in the phase tilt factor φ_{2i} associated with each contributing incident vector $\vec{E}_i$. I define a tilted plane that contains Points $\boldsymbol{E_0}$, $\boldsymbol{E_4}$ and $\boldsymbol{E_4}'$, and is parallel to the tilted phase front that focuses at Point ***A*** (see Figure 5.4). This plane is used as a reference and each phase tilt factor φ_{2i} is expressed against this tilted plane. Henceforth, this tilted plane is referred to as Origin Plane**.** Each

phase tilt factor φ_{2i} is derived from the optical path differences between the corresponding Point $\boldsymbol{E_i}$ and the Origin Plane. The details of these calculations are in Appendix B. Table 5.1 summarizes these results.

In this analysis, I first look at a radially polarized beam with a planar phase and a radially polarized beam with a 2π pitch vortex phase. In each case, I derive the polarization state (i.e. Jones vector) at Point ***O*** and at Point ***A***, by summing the contributions from the eight vectors $\vec{E}_i$ using vectorial calculations in the Complex Plane.

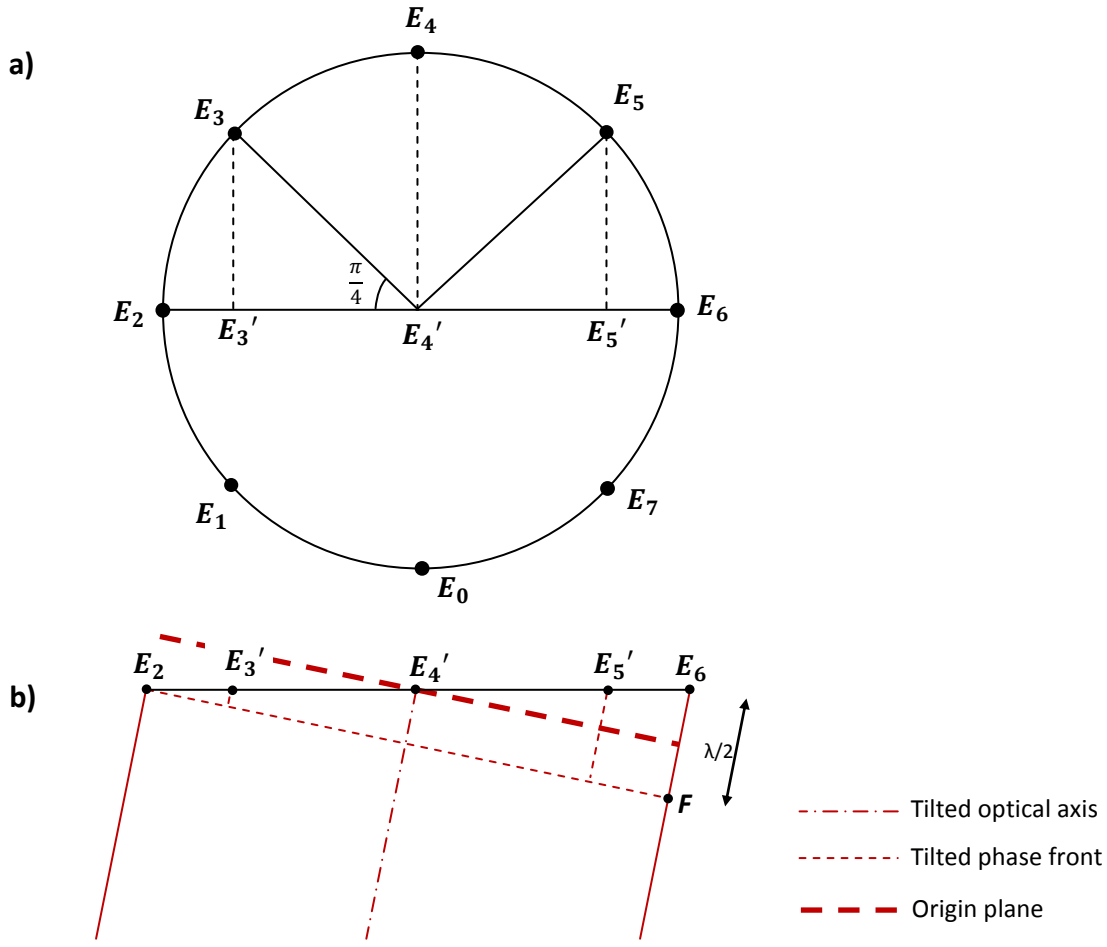

Figure 5.4: Schematics showing the geometry of the model. **(a)** Collimated beam profile showing the eight origin points $\boldsymbol{E_i}$ of the vectors $\vec{E}_i$ used to model the beam. **(b)** Side-view of the tilted phase front that focuses at Point ***A***. To mimic a planar phase front that focuses at Point ***A***, the model uses a set of Jones vectors $\vec{E}_i$ that each includes an appropriate phase tilt factor φ_{2i}. The phase tilt factors φ_{2i} are derived using the geometrical properties of this model. The derivations are in Appendix B.

Table 5.1: Optical path difference and corresponding phase tilt factor φ_{2i} induced by the phase front tilt, derived for each vector $\vec{E}_i$ that focuses at Point ***A***. The derivations are in Appendix B. This table summarizes the results in Table B.1.

Vectors $\vec{E}_i$ (all these vectors focus at Point ***A***)	Optical path difference from Origin Plane	Phase tilt factor φ_{2i}
$\vec{E}_0$	0	0
$\vec{E}_1$	$\frac{\sqrt{2}}{8}.\lambda$	$\frac{\sqrt{2}}{4}.\pi$
$\vec{E}_2$	$\frac{1}{4}.\lambda$	$\frac{1}{2}.\pi$
$\vec{E}_3$	$\frac{\sqrt{2}}{8}.\lambda$	$\frac{\sqrt{2}}{4}.\pi$
$\vec{E}_4$	0	0
$\vec{E}_5$	$-\frac{\sqrt{2}}{8}.\lambda$	$-\frac{\sqrt{2}}{4}.\pi$
$\vec{E}_6$	$-\frac{1}{4}.\lambda$	$-\frac{1}{2}.\pi$
$\vec{E}_7$	$-\frac{\sqrt{2}}{8}.\lambda$	$-\frac{\sqrt{2}}{4}.\pi$

5.4 Model of a radially polarized beam with a planar phase

5.4.1 Vectorial representation

In the case a radially polarized beam with a planar phase, all the polarization vectors $\vec{E}_i$ within the beam profile have the same amplitude at any given time. In other words, the amplitude of all these vectors reaches a maximum at the same time, decreases and reaches a minimum at the same time and so on (Figure 5.5).

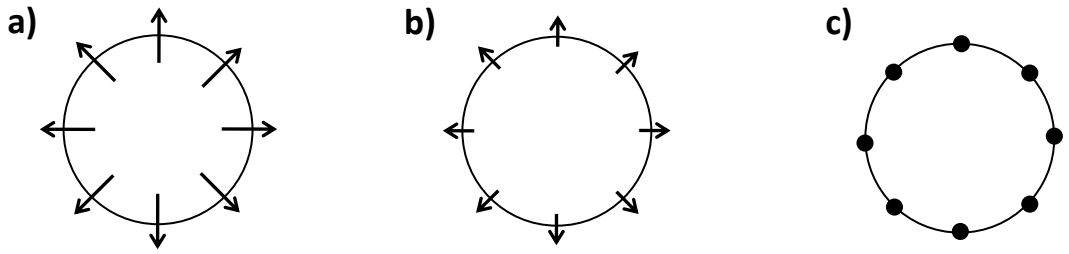

Figure 5.5: Schematics of the profile of a radially polarized beam with a planar phase, showing the amplitude of the electric field vectors **(a)** at a maximum at t=0, **(b)** at an intermediate value at t=T/8 and **(c)** at zero at t=T/4.

5.4.2 Calculation of the Jones vector at Point *O* for a radially polarized beam with a planar phase

I first look at the Jones vector produced by a radially polarized beam with a planar phase at Point ***O***, on the optical axis. I have derived the complex values of the coordinates E_{iX} and E_{iY} for each of the eight contributing vectors, taking into account the phase structure of the beam (in this case, all the phase terms are nil). The details of the calculation are in Appendix B. Table 5.2 summarizes the results.

To derive the resulting Jones vector at Point ***O***, I then need to sum the X and Y coordinates of the eight contributing vectors: ($\frac{1}{8}\sum_{i=0}^{i=7} E_{iX}$; $\frac{1}{8}\sum_{i=0}^{i=7} E_{iY}$). I derive these sums geometrically, using the Complex Plane method. Figure 5.6 shows the vectors plotted in the Complex Plane. Figure 5.6-a shows all the vectors E_{iX} and E_{iY}. Figure 5.6-b shows the results obtained after summing all the contributing vectors. Therefore, the vectors plotted in Figure 5.6-b are the X and Y components of the Jones vector at Point ***O***.

As seen in Figure 5.6-b, the amplitude resulting from summing all the contributing vectors is zero in both X and Y, so the Jones vector at Point ***O*** is (0 ; 0). From this result, we can conclude that the focal spot has a zero irradiance amplitude at Point ***O***. This result was anticipated since the contribution from each vector is compensated by that of another vector of equal amplitude and phase, and opposite direction (see Figure 5.5).

Table 5.2: Coordinates of the vectors $\vec{E}_i$ for a radially polarized beam with a planar phase focusing at Point ***O***. The derivations are in Appendix B. This table summarizes the results in Tables B.2 and B.3.

Vectors $\vec{E}_i$ (all these vectors focus at Point ***O***)	E_{iX}	E_{iY}
$\vec{E}_0$	0	1
$\vec{E}_1$	$\frac{1}{\sqrt{2}}$	$\frac{1}{\sqrt{2}}$
$\vec{E}_2$	1	0
$\vec{E}_3$	$\frac{1}{\sqrt{2}}$	$-\frac{1}{\sqrt{2}}$
$\vec{E}_4$	0	-1
$\vec{E}_5$	$-\frac{1}{\sqrt{2}}$	$-\frac{1}{\sqrt{2}}$
$\vec{E}_6$	-1	0
$\vec{E}_7$	$-\frac{1}{\sqrt{2}}$	$\frac{1}{\sqrt{2}}$

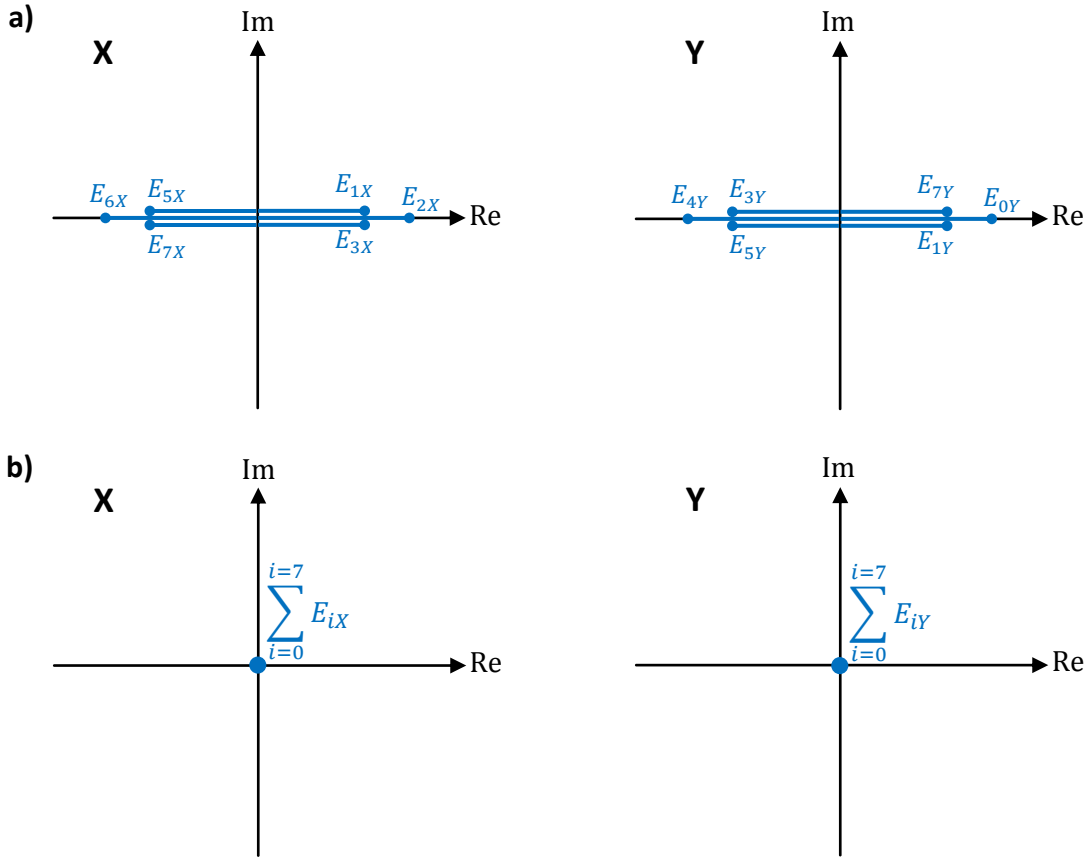

Figure 5.6: (a) Complex Planes showing the X and Y components (E_{iX} and E_{iY}) of the Jones vectors $\vec{E}_i$ at Point ***O*** and **(b)** the resulting Jones vector obtained after summing all the contributing vectors.

5.4.3 Calculation of the Jones vector at Point *A* for a radially polarized beam with a planar phase

The Jones vector produced by the radially polarized beam with a planar phase at Point ***A*** is derived by summing the X and Y components from all the complex vectors $\vec{E}_i$. I have derived the complex values of the coordinates E_{iX} and E_{iY} for each of the eight contributing vectors, taking into account the phase front tilt. The details of the calculation are in Appendix B. Table 5.3 summarizes the results.

To derive the Jones vector at Point ***A***, I then need to sum the X and Y components of the eight contributing vectors: ($\frac{1}{8}\sum_{i=0}^{i=7} E_{iX}$; $\frac{1}{8}\sum_{i=0}^{i=7} E_{iY}$). Figure 5.7 shows the vectors plotted in the Complex Plane. Figure 5.7-a shows all the vectors E_{iX} and E_{iY}. Figure 5.7-b shows the results obtained after summing all the contributing vectors. The vectors plotted in Figure 5.7-b are the X and Y components of the Jones vector at Point ***A***.

A geometrical calculation in the Complex Plane shows that the amplitude resulting from summing all the contributing vectors is $\sim 0.57 e^{j(\frac{\pi}{2})}$ in X and 0 in Y. It is noted that the results have been normalized by dividing the amplitude of the sum of all the contributing vectors by the number of contributing vectors (eight here). Therefore, the Jones vector is $0.57 e^{j(\frac{\pi}{2})} \times (1\ ;\ 0\ )$. This means that, at Point ***A***, the polarization is linear and its direction is oriented along the X axis (see Figure 5.3-c). In other words, the polarization vector at Point ***A*** is oriented radially (i.e. away from the center).

5.4.4 Discussion

Given the cylindrical symmetry of the optical setup, we can infer that all the points located at the same distance as Point ***A*** from the center Point ***O*** will have a polarization vector radially oriented. Therefore, the focal spot is expected to have a radially polarized component in the annular region around the optical axis. In the previous section, I found a zero irradiance amplitude at Point ***O***. We can now conclude that, when focusing a radially polarized beam with a planar phase, the focal spot has a radially polarized annular structure with a zero amplitude at the center, as shown in Figure 5.8-c.

Table 5.3: Coordinates of the vectors $\vec{E}_i$ for a radially polarized beam with a planar phase focusing at Point ***A***. The derivations are in Appendix B. This table summarizes the results in Tables B.4 and B.5.

Vectors $\vec{E}_i$ (all these vectors focus at Point ***A***)	E_{iX}	E_{iY}
$\vec{E}_0$	0	1
$\vec{E}_1$	$\frac{1}{\sqrt{2}} . e^{j\frac{\sqrt{2}}{4}.\pi}$	$\frac{1}{\sqrt{2}} . e^{j\frac{\sqrt{2}\pi}{4}}$
$\vec{E}_2$	$e^{j\frac{\pi}{2}}$	0
$\vec{E}_3$	$\frac{1}{\sqrt{2}} . e^{j\frac{\sqrt{2}}{4}.\pi}$	$-\frac{1}{\sqrt{2}} . e^{j\frac{\sqrt{2}\pi}{4}}$
$\vec{E}_4$	0	-1
$\vec{E}_5$	$-\frac{1}{\sqrt{2}} e^{j(-\frac{\sqrt{2}}{4}.\pi)}$	$-\frac{1}{\sqrt{2}} e^{j(-\frac{\sqrt{2}\pi}{4})}$
$\vec{E}_6$	$-e^{j(-\frac{\pi}{2})}$	0
$\vec{E}_7$	$-\frac{1}{\sqrt{2}} . e^{j(-\frac{\sqrt{2}}{4}.\pi)}$	$\frac{1}{\sqrt{2}} . e^{j(-\frac{\sqrt{2}\pi}{4})}$

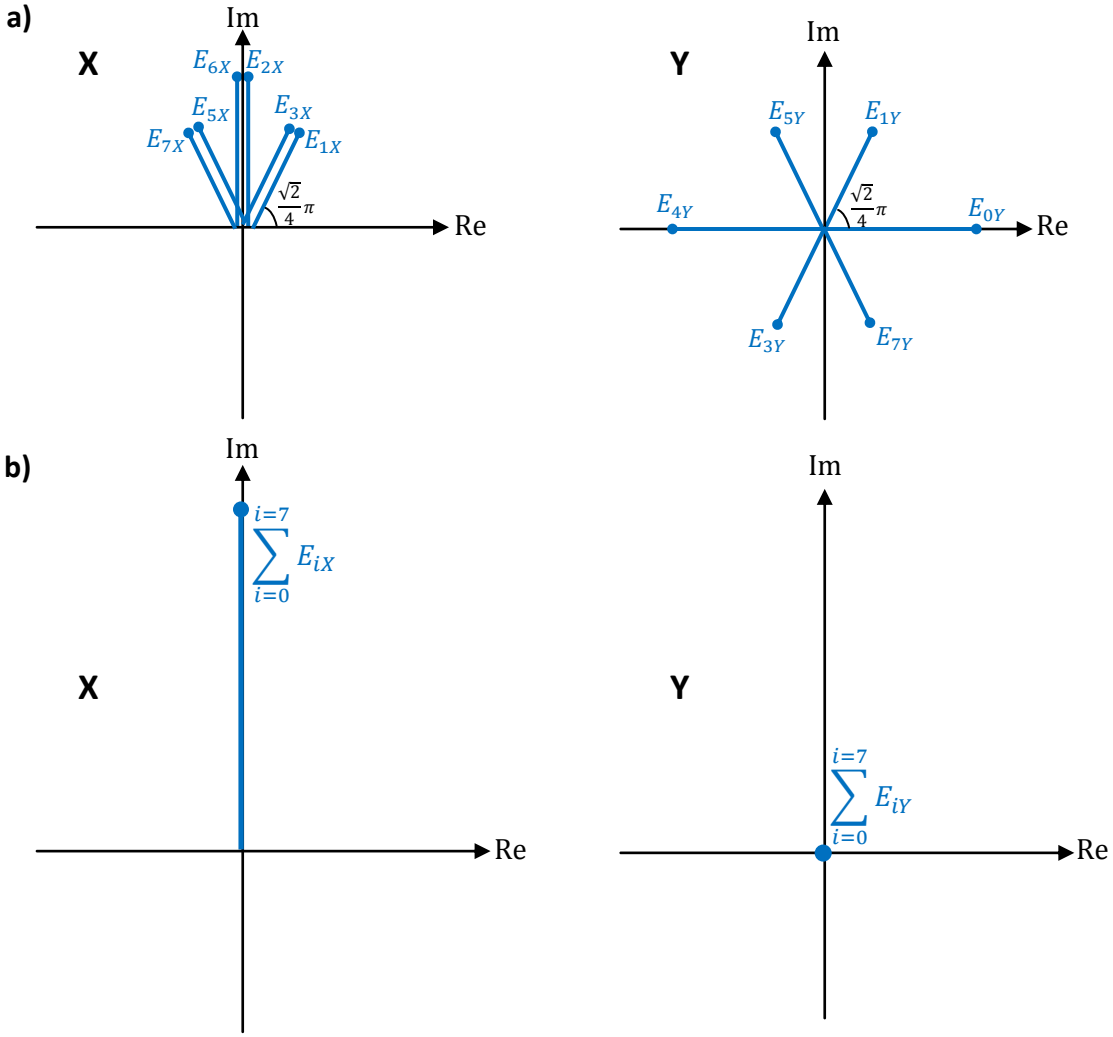

Figure 5.7: (a) Complex Planes showing the X and Y components (E_{iX} and E_{iY}) of the Jones vectors $\vec{E}_i$ at Point ***A*** and **(b)** the resulting Jones vector obtained after summing all the contributing vectors. It is noted that the amplitude scale is not the same in **(a)** and **(b)**.

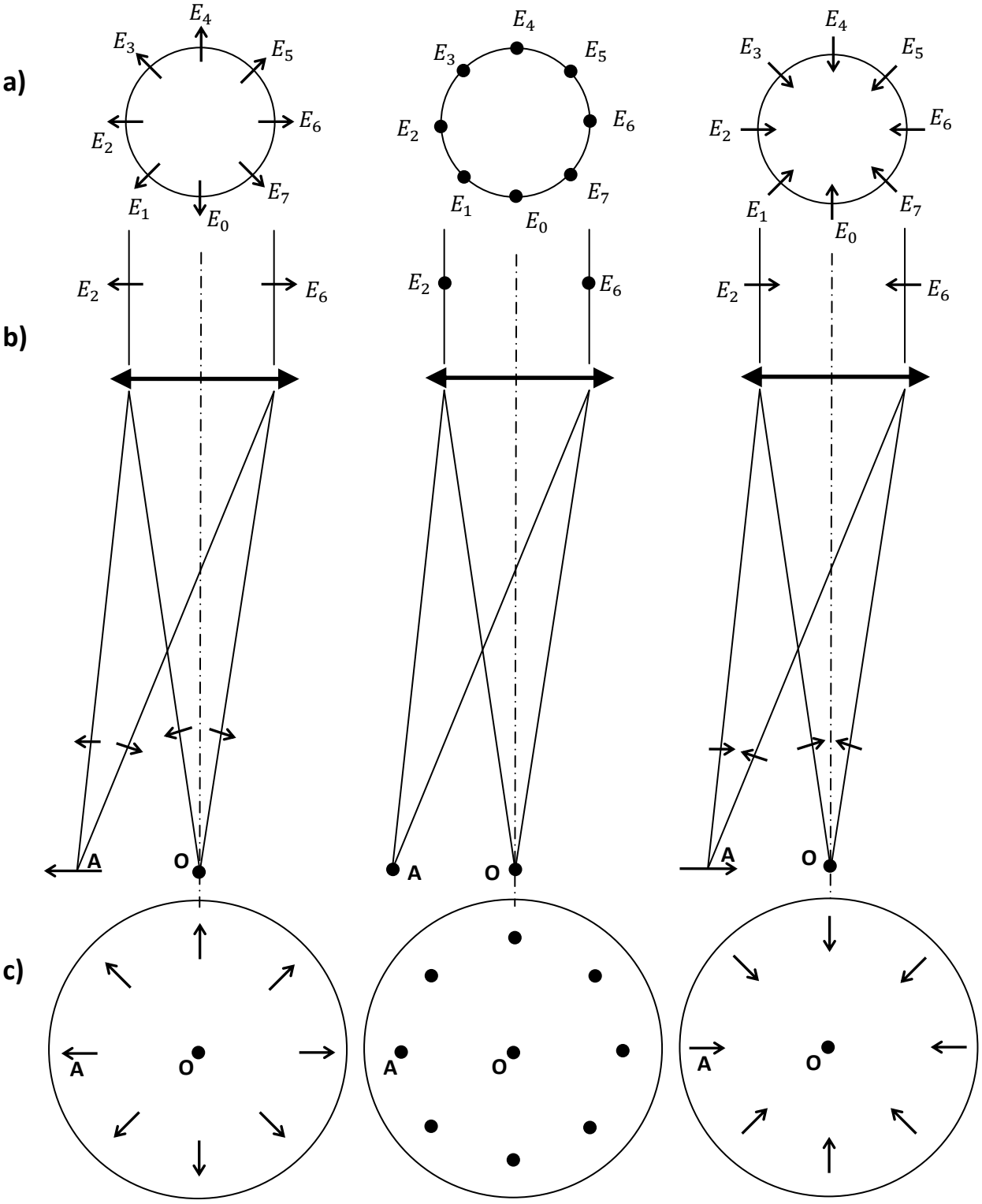

Figure 5.8: (a) Schematics of the profile of a radially polarized beam with a planar phase, showing the electric field vectors at t=0 (left), t=T/4 (middle) and t=T/2 (right). **(b)** Side-view showing the beam focusing at Points ***O*** and ***A***, with the resulting electric field vectors at each of these points. **(c)** Focal spot profile (not to scale) showing the electric field vectors at t=0 (left), t=T/4 (middle), t=T/2 (right). The amplitude of the electric field vector is always zero in the center (black dot at ***O***).

5.5 Model of a radially polarized beam with a vortex phase

5.5.1 Vectorial representation

In the case of a radially polarized beam with a vortex phase, all the Jones vectors $\vec{E}_i$ within the annular beam profile do not have the same amplitude at a given time. Figure 5.9 shows schematics of the polarization vectors of a radially polarized beam with a phase vortex pitch of 2π, for t=0, t=T/8 and t=T/4. With this type of CVB, there is a constant phase offset between each Jones vector $\vec{E}_i$. These phase offsets are defined as: $\varphi_{1i} = i \times \frac{\pi}{4}$. Table 5.4 summarizes these phase terms.

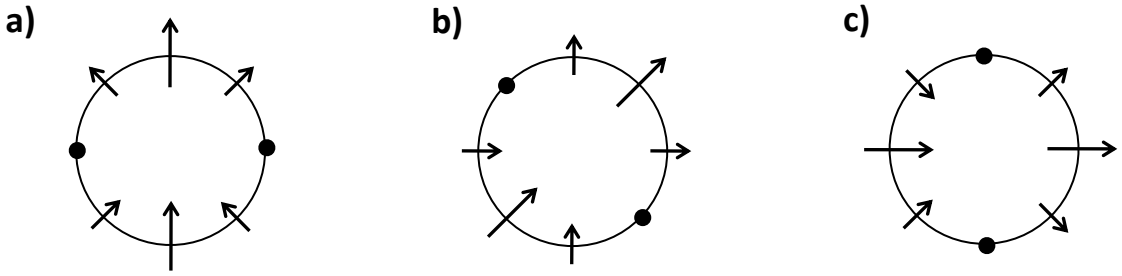

Figure 5.9: Schematics of the profile of a radially polarized beam with a vortex phase pitch of 2π (i.e. a topological charge of one), showing the amplitude of the electric field vectors **(a)** at t=0, **(b)** at t=T/8 and **(c)** at t=T/4.

5.5.2 Calculation of the Jones vector at Point *O* for a radially polarized beam with a vortex phase

I first look at the Jones vector produced by a radially polarized beam with a 2π pitch vortex phase at Point ***O***. I have derived the complex values of the coordinates E_{iX} and E_{iY} for each of the eight contributing vectors, taking into account the vortex phase terms described in Table 5.4. The details of these calculations are in Appendix B. Table 5.5 summarizes the results.

I then sum the X and Y components of the contributing vectors to derive the Jones vector at Point ***O***: $(\frac{1}{8}\sum_{i=0}^{i=7} E_{iX}\ ;\ \frac{1}{8}\sum_{i=0}^{i=7} E_{iY}\ )$. Figure 5.10 shows the vectors plotted in the Complex Plane. Figure 5.10-a shows all the vectors E_{iX} and E_{iY}. Figure 5.10-b shows the results obtained after summing all the contributing vectors. The vectors plotted in Figure 5.10-b are the X and Y components of the Jones vector at Point ***O***.

A geometrical calculation shows that the amplitude resulting from summing all the contributing vectors is $0.5e^{j(\frac{\pi}{2})}$ in X and 0.5 in Y. It is noted that the amplitudes have been normalized by dividing the amplitude of the sum of all the contributing vectors by the number of contributing vectors (eight here). The resulting Jones vector is $0.5 \times (e^{j(\frac{\pi}{2})}; 1)$, which defines circular polarization. This means the polarization is circular at Point ***O***.

Table 5.4: Phase factors induced by the 2π pitch vortex phase structure of the beam. These phase factors are also detailed in Table B6, in Appendix B.

Vectors $\vec{E}_i$	Vortex phase factors: φ_{1i}
$\vec{E}_0$	0
$\vec{E}_1$	$\frac{\pi}{4}$
$\vec{E}_2$	$\frac{\pi}{2}$
$\vec{E}_3$	$\frac{3\pi}{4}$
$\vec{E}_4$	π
$\vec{E}_5$	$\frac{5\pi}{4}$
$\vec{E}_6$	$\frac{3\pi}{2}$
$\vec{E}_7$	$\frac{7\pi}{4}$

Table 5.5: Coordinates of the vectors $\vec{E}_i$ for a radially polarized beam with a 2π pitch vortex phase structure focusing at Point ***O***. The derivations are in Appendix B. This table summarizes the results in Tables B.7 and B.8.

Vectors $\vec{E}_i$ (all these vectors focus at Point ***O***)	E_{iX}	E_{iY}
$\vec{E}_0$	0	1
$\vec{E}_1$	$\frac{1}{\sqrt{2}}.e^{j\frac{\pi}{4}}$	$\frac{1}{\sqrt{2}}.e^{j\frac{\pi}{4}}$
$\vec{E}_2$	$e^{j\frac{\pi}{2}}$	0
$\vec{E}_3$	$\frac{1}{\sqrt{2}}.e^{j\frac{3\pi}{4}}$	$-\frac{1}{\sqrt{2}}.e^{j\frac{3\pi}{4}}$
$\vec{E}_4$	0	1
$\vec{E}_5$	$-\frac{1}{\sqrt{2}}e^{j\frac{5\pi}{4}}$	$-\frac{1}{\sqrt{2}}.e^{j\frac{5\pi}{4}}$
$\vec{E}_6$	$-e^{j\frac{3\pi}{2}}$	0
$\vec{E}_7$	$-\frac{1}{\sqrt{2}}e^{j\frac{7\pi}{4}}$	$\frac{1}{\sqrt{2}}e^{j\frac{7\pi}{4}}$

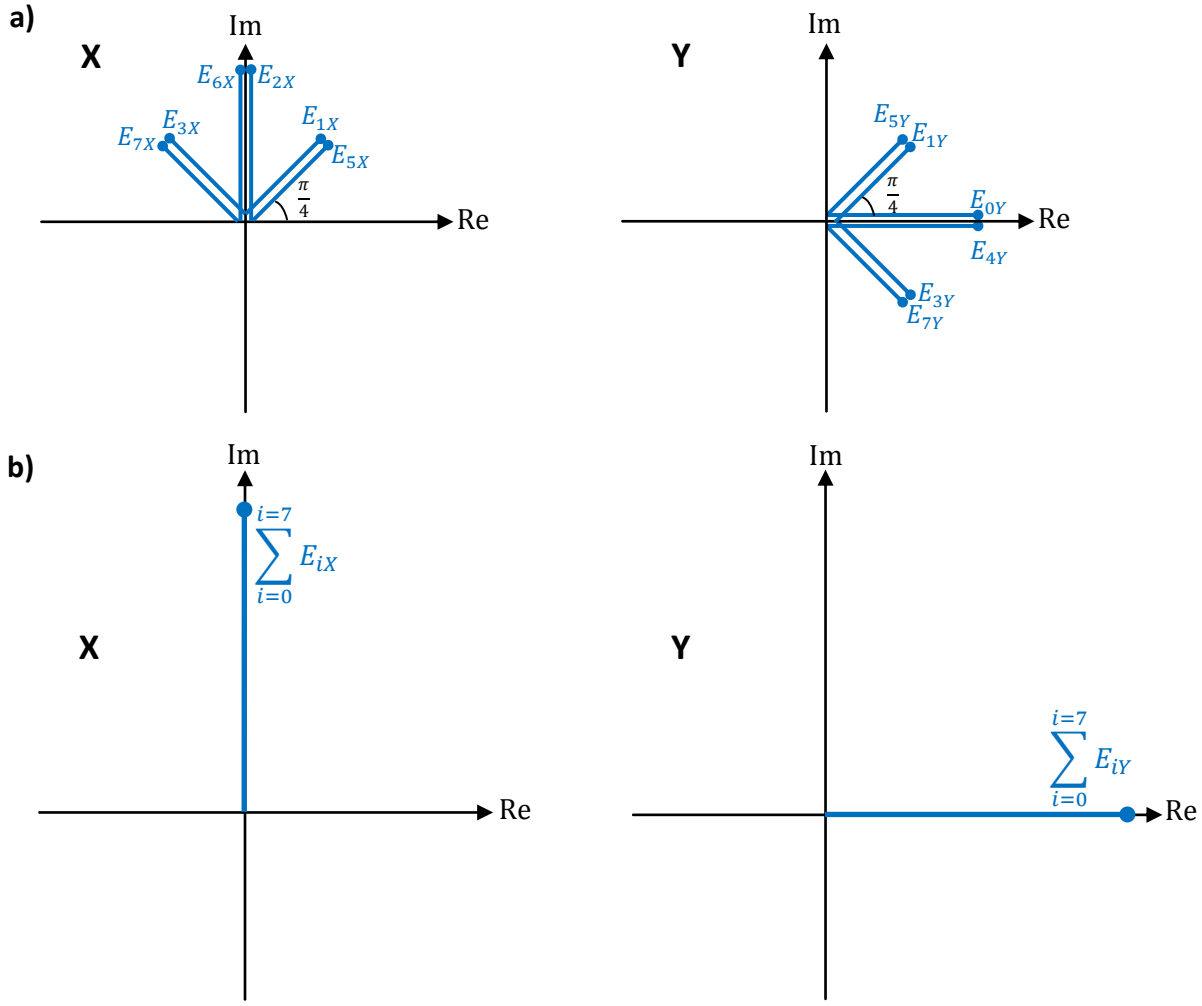

Figure 5.10: (a) Complex Planes showing the X and Y components (E_{iX} and E_{iY}) of the Jones vectors $\vec{E}_i$ at Point ***O*** and **(b)** the resulting Jones vector obtained after summing all the contributing vectors. It is noted that the amplitude scale is not the same in **(a)** and **(b)**.

5.5.3 Calculation of the Jones vector at Point *A* for a radially polarized beam with a vortex phase

I now derive the Jones vector produced by the radially polarized, vortex phase beam at Point ***A***, by summing the X and Y components of all the complex vectors $\vec{E}_i$. As before, I have derived the complex values of the coordinates E_{iX} and E_{iY} for each of the eight contributing vectors, taking into account the vortex phase terms described in Table 5.4. The details are in the Appendix B. Table 5.6 summarizes the results.

I then sum the X and Y components of the contributing vectors to derive the Jones vector at Point ***A***: ($\frac{1}{8}\sum_{i=0}^{i=7} E_{iX}$; $\frac{1}{8}\sum_{i=0}^{i=7} E_{iY}$). Figure 5.11 shows the vectors plotted in the Complex Plane. Figure 5.11-a shows all the vectors E_{iX} and E_{iY}. Figure 5.11-b shows the results obtained after summing all the contributing vectors and thus the vectors plotted in Figure 5.11-b are the X and Y components of the Jones vector at Point ***A***.

A geometrical calculation shows that the amplitude resulting from summing all the contributing vectors is $0.1e^{j(\frac{\pi}{2})}$ in X and 0.4 in Y. The resulting Jones vector at Point ***A*** is ($0.1e^{j(\frac{\pi}{2})}$; 0.4). This describes an elliptical polarization with a strong elongation along the Y axis (Figure 5.3-c), that is, the polarization vector at Point ***A*** is mostly oriented azimuthally (i.e. tangentially from the center).

5.5.4 Discussion

Given the cylindrical symmetry of the optical setup, we can infer that all the points located at the same distance as Point ***A*** from the center Point ***O*** have a polarization vector predominantly oriented azimuthally. Therefore, the focal spot has a dominant azimuthally polarized component in the annular region around the optical axis. In the previous section, I had found a circular polarization at Point ***O***. We can now conclude that the profile of the focal spot has a circularly polarized central region and a strong azimuthally polarized annular region. This is shown in Figure 5.12-c.

Table 5.6: Coordinates of the vectors $\vec{E}_i$ for a radially polarized beam with a with a 2π pitch vortex phase structure focusing at Point ***A***. The derivations are in Appendix B. This table summarizes the results in Tables B.9 and B.10

Vectors $\vec{E}_i$ (all these vectors focus at Point ***A***)	E_{iX}	E_{iY}
$\vec{E}_0$	0	1
$\vec{E}_1$	$\frac{1}{\sqrt{2}} \cdot e^{j\frac{1+\sqrt{2}}{4}.\pi}$	$\frac{1}{\sqrt{2}} \cdot e^{j\frac{1+\sqrt{2}}{4}.\pi}$
$\vec{E}_2$	-1	0
$\vec{E}_3$	$\frac{1}{\sqrt{2}} \cdot e^{j\frac{3+\sqrt{2}}{4}.\pi}$	$-\frac{1}{\sqrt{2}} \cdot e^{j\frac{3+\sqrt{2}}{4}.\pi}$
$\vec{E}_4$	0	1
$\vec{E}_5$	$-\frac{1}{\sqrt{2}} e^{j\frac{5-\sqrt{2}}{4}.\pi}$	$-\frac{1}{\sqrt{2}} e^{j(\frac{5-\sqrt{2}}{4}.\pi)}$
$\vec{E}_6$	1	0
$\vec{E}_7$	$-\frac{1}{\sqrt{2}} \cdot e^{j\frac{7-\sqrt{2}}{4}.\pi}$	$\frac{1}{\sqrt{2}} \cdot e^{j(\frac{7-\sqrt{2}}{4}.\pi)}$

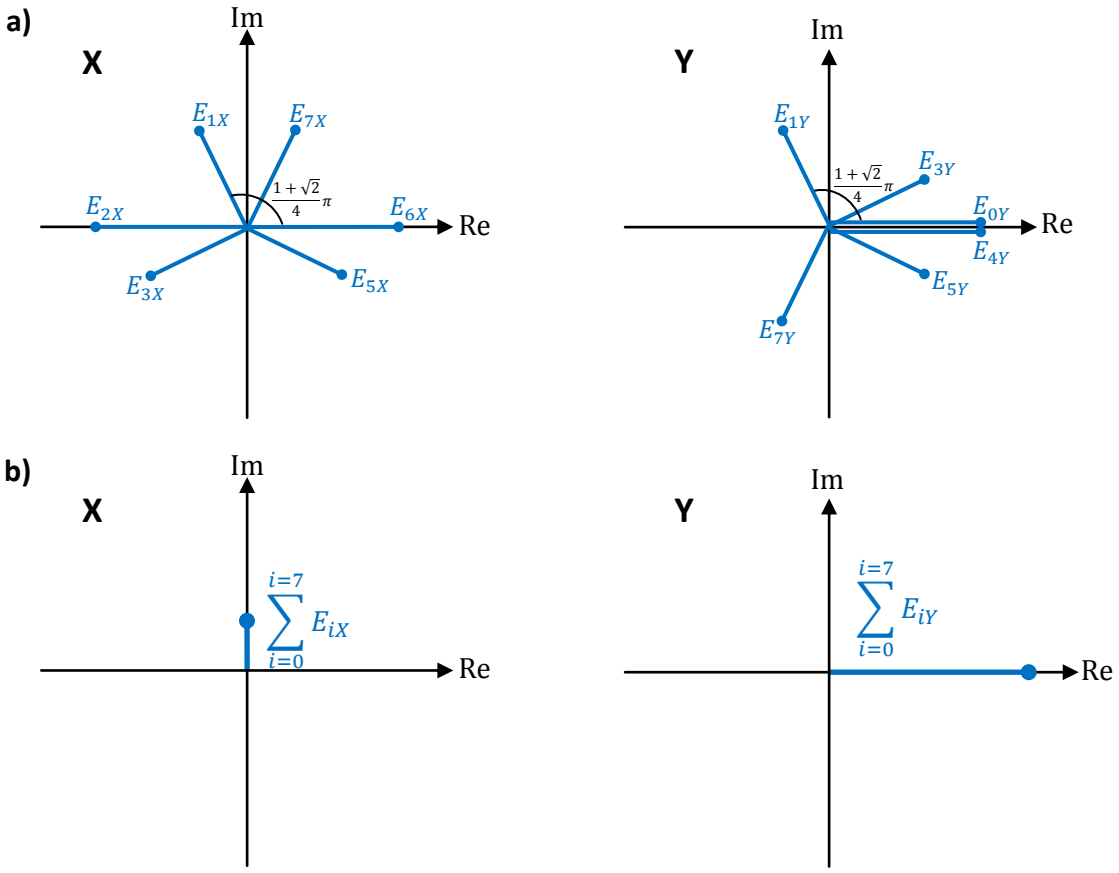

Figure 5.11: (a) Complex Planes showing the X and Y components (E_{iX} and E_{iY}) of the Jones vectors $\vec{E}_i$ at Point ***A*** and **(b)** the resulting Jones vector obtained after summing all the contributing vectors. It is noted that the amplitude scale is not the same in **(a)** and **(b)**.

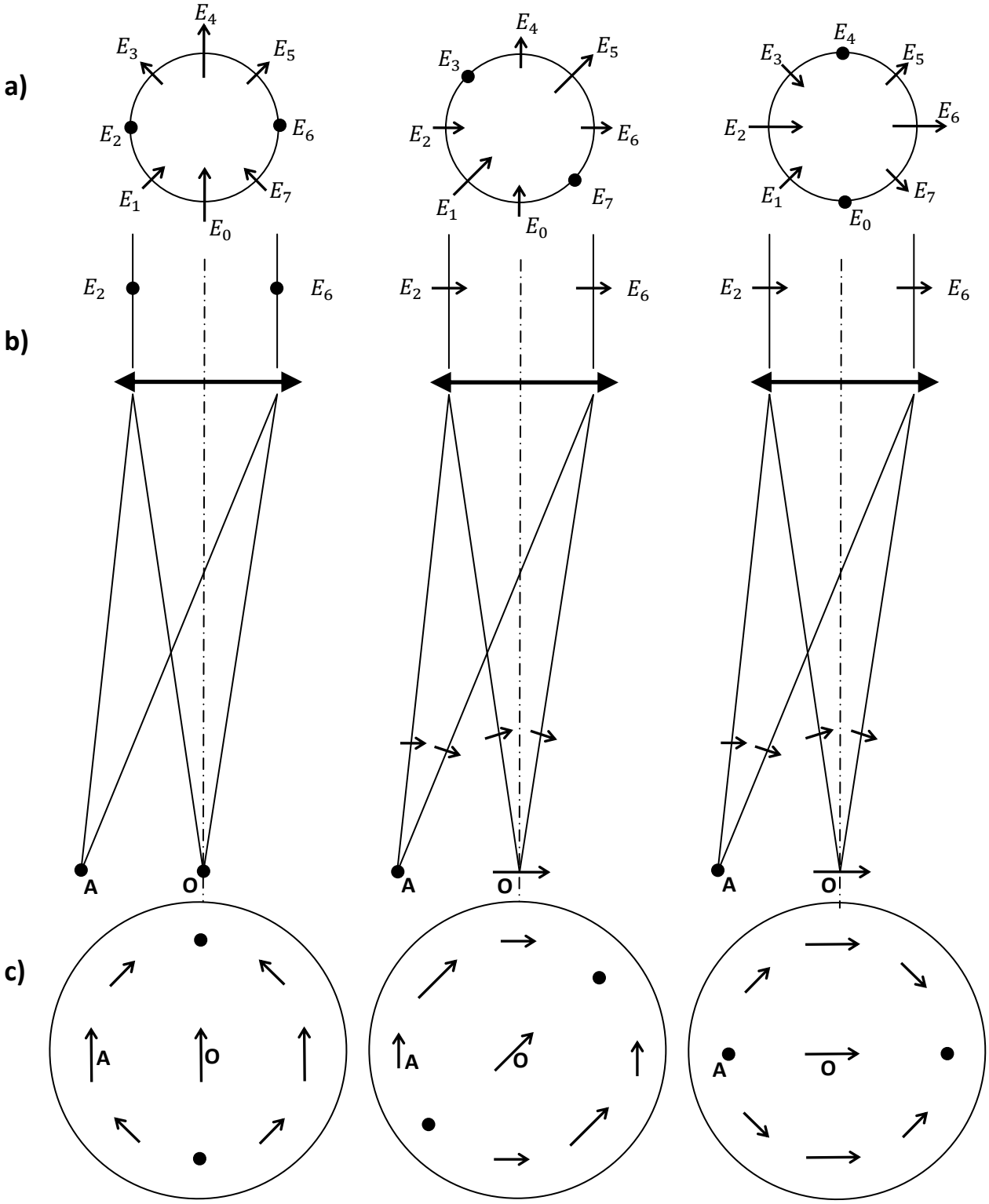

Figure 5.12: (a) Schematics of the profile of a radially polarized beam with a vortex phase, showing the electric field vectors at t=0 (left), t=T/8 (middle) and t=T/4 (right). **(b)** Side-view showing the beam focusing at Points ***O*** and ***A***, with the resulting electric field vectors at each of these points. **(c)** Focal spot profile (not to scale) showing the electric field vectors at t=0 (left), t= T/8 (middle) and t= T/4 (right). In the center, the polarization is circular.

5.6 Comparison of the beams' intensity profile at the focal plane

Due to its simplicity, the model cannot predict the full beam intensity profile at the focal plane. However the experimental results described in Chapter 4 were consistent with Gaussian beam profiles. In the model described here, I assume that the irradiance profile (or intensity profile) at the focal plane is indeed Gaussian. The model allows deriving a normalized value of irradiance at Point ***O***, noted I_O and one at Point ***A***, noted I_A. The ratio I_O/I_A illustrates how steep the Gaussian profile is and allows comparisons between various types of beams. Here, the ratio I_O/I_A is derived for a radially polarized beam with a vortex phase and for a beam with a uniform polarization (i.e. linear or circular) and a planar phase. The results are compared between these two beams. In this way, I can check if the model can explain the experimental results described in Section 4.3.5 in Chapter 4.

I first derive the ratio I_O/I_A for a radially polarized beam with a 2π pitch vortex phase. The amplitude of the electric field E at any given coordinates (X, Y) in the focal plane is obtained from the Jones vector coordinates (E_X ; E_Y) in the following way: $E = \sqrt{{E_X}^2 + {E_Y}^2}$. Therefore, the irradiance at that location is: $I = E^2 = {E_X}^2 + {E_Y}^2$. At Point ***O***, I have $E_X = E_Y = 0.5$ (see results in Section 5.5.2). Hence the irradiance at Point ***O*** is: $I_O = 0.5^2 + 0.5^2 = 0.5$. At Point ***A***, I have $E_X = 0.1$ and $E_Y = 0.4$ (see results in Section 5.5.3). Hence the irradiance at Point ***A*** is: $I_A = 0.1^2 + 0.4^2 = 0.17$. The ratio I_O/I_A is 2.9 . A Gaussian fit to this irradiance profile is plotted in Figure 5.13 (red curve).

The irradiance obtained with a uniform (i.e. linear or circular) polarized beam at Points ***O*** and ***A***, have been derived in Appendix B, using the same method as described above: the Jones vectors at these points were derived in the same way as in Sections 5.4 and 5.5; their coordinates (E_X ; E_Y) were used to obtain the irradiance. With a uniform polarization, I have $I_O = 1$ and $I_A = 0.22$. Here, the ratio I_O/I_A is 4.5 . A Gaussian fit to this irradiance profile is plotted in Figure 5.13 (blue curve).

The ratio I_O/I_A obtained with a uniform polarization is ~55% higher than that obtained with a radially polarized vortex beam. This suggests that a uniform polarization produces a comparatively steep Gaussian profile at the focal plane, whereas a radially polarized, vortex beam produces a Gaussian profile with a lower peak in the center and wider wings around it (see Figure 5.13). These predictions are consistent with experimental results in Section 4.3.5 in Chapter 4. They explain the variations in the size of the laser spots obtained with radially polarized, vortex phase beams and linearly polarized beams with a planar phase at different value of fluence, which were seen in the experiments. These variations are indeed related to the amplitude profiles of the beams.

It is noted that, in principle, the amplitude of an electric field is expressed in Newton per Coulomb and the amplitude of an irradiance is expressed in Watts per squared centimeters. However as the electric field vectors used here are normalized, their absolute amplitude does not have a physical meaning, only their relative amplitudes are relevant. In the calculation of electric field and irradiance here, I did not include these units.

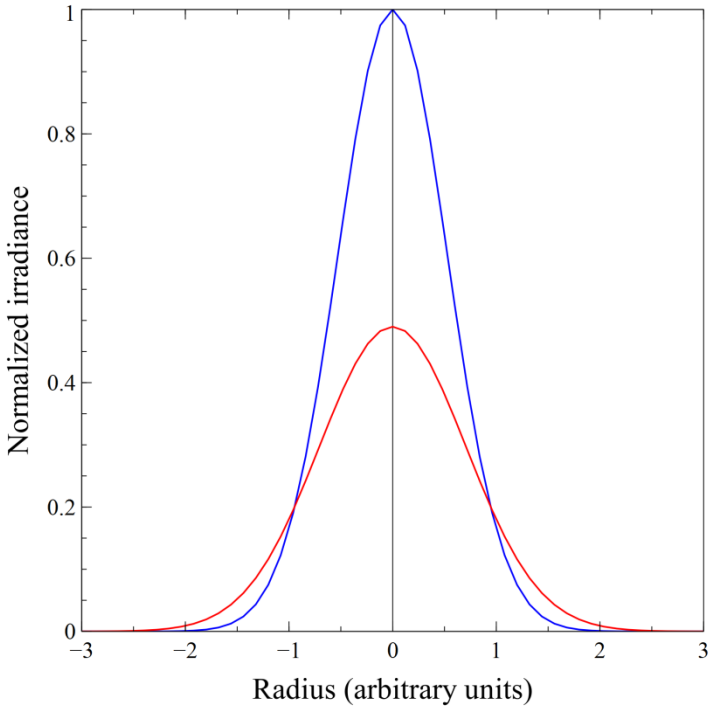

Figure 5.13: (a) Gaussian fit to the irradiance profiles predicted by the model. The profiles produced by a radially polarized vortex beam and a linearly polarized beam are plotted in red and blue respectively. At Point ***O***, the normalized irradiance produced by the vortex beam is 0.5 and that produced by the linearly polarized beam is 1. At Point ***A*** (where the radius is 1 in the chosen scale) it is ~0.17 and ~0.22 respectively.

5.7 Model of azimuthally polarized beams with a planar or a vortex phase

The model presented here also enables to predict the focal properties of azimuthally polarized beams. To derive the Jones vectors at the focal plane of azimuthally polarized beams, I apply the same method as described in Sections 5.4 and 5.5, except that the vectors $\vec{E}_i$ are azimuthally oriented (essentially, their X and Y coordinates are swapped compared with the radially polarized beams). Here, I only detail the results of these derivations.

- Azimuthally polarized beam with a planar phase; component focusing at Point ***O***: The resulting Jones vector is $(0\ ;\ 0\ )$. This means that the focal spot has a zero irradiance amplitude at Point ***O***.
- Azimuthally polarized beam with a planar phase; component focusing at Point ***A***: The resulting Jones vector is $0.57e^{j(-\frac{\pi}{2})} \times (0\ ;\ 1\ )$. This means that, at Point ***A***, the polarization is linear and its direction is oriented along the Y axis. In other words, the polarization vector at Point ***A*** is oriented azimuthally (i.e. tangentially to the beam).
- Azimuthally polarized beam with a vortex phase pitch of 2π; component focusing at Point ***O***: The resulting Jones vector is $0.5 \times (1\ ;e^{j(-\frac{\pi}{2})})$, which defines circular polarization. This means the polarization is circular at Point ***O***.

- Azimuthally polarized beam with a vortex phase pitch of 2π; component focusing at Point ***A***: The resulting Jones vector is $(0.4\ ;0.1e^{j(-\frac{\pi}{2})})$. This describes an elliptical polarization with a strong elongation along the X axis, that is, the polarization vector at Point ***A*** is mostly oriented radially (i.e. away from the center).

These results are consistent with those obtained with radially polarized beams. Therefore, we can infer that an azimuthally polarized beam with a planar phase produces an annular focal spot that is azimuthally polarized. An azimuthally polarized beam with a 2π pitch vortex phase produces a focal spot polarized circularly in the center and with a dominant radially polarized component in the annular region around the center.

5.8 Discussion

My model predicts that a radially (azimuthally) polarized beam with a planar phase focuses as an annular spot with a zero intensity in its center and radial (azimuthal) polarization. These predictions are in agreement with recent experimental results that used CVBs with a planar phase, focused with a low NA optic to imprinting LIPSS (U. Klug *et al.* 2010, see Figure 2.4 in Chapter 2). They are also consistent with existing models that describe these beams, focused with low NA optics and producing annular focal spots (see G. Wu *et al.* 2007). Although the Polarization Mode Converter used in my experiments cannot produce CVBs with a planar phase (see Chapter 4), modeling these beams enabled me to compare my model predictions with existing results available in the literature. The consistency between my model predictions and the results available in the literature in the case of CVBs with a planar phase, gives confidence that my simplified analytical model describes the focal behavior of the beams accurately. In the case of CVBs with a vortex phase, there is no consensus in the literature since the focal properties of these beams depend on the experimental parameters.

My model predicts that a radially polarized beam with a 2π pitch vortex phase produces a Gaussian type of profile at the focal plane, with a focal spot which is circularly polarized in its central region and mostly azimuthally polarized in the annular region around its centre. Similarly, an azimuthally polarized beam with a 2π pitch vortex phase produces a focal spot which mostly radially polarized in the annular region around its centre. It is noted that the polarization purity at the focal plane is not 100% in this case as it includes circularly and elliptically polarized regions. Importantly, the model successfully explains the polarization patterns imprinted with the LIPSS experiments in Chapter 4. The results in Chapter 4 appeared to show an inversion of polarization at the focal plane. The model confirms that the optical setup indeed induces an inversion in the overall state of polarization at the focal plane compared to the state of polarization of the collimated beam. It also explains why there are no LIPSS in the center of the focal spots: the circular polarization prevents their formation in this region (see Figures 4.8, 4.17 and 4.18 in Chapter 4).

The inversion in the dominant state of polarization at the focal plane studied here is related to a divergence of the phase fronts, which is mainly caused by diffraction effects at the SLM, near the phase singularity at the optical axis (L. Marrucci *et al.* 2011). These effects can be minimized by modifying the experimental setup, for example by adding a 4F correlator (i.e. a telescope with two identical lenses) after the SLM to minimize the divergence. In this way, it is thought that the inversion in the state of

polarization at the focal plane can be avoided. However this analysis gives an insight into how, under some experimental conditions, diffraction effects can cause an inversion in the state of polarization at the focal plane of a CVB with a vortex phase. It is thought that diffraction limited focusing optics could also produce an inversion of polarization (such phenomenon were predicted in H. Kang *et al.* 2010, where the focusing properties of a microscopy setup illuminated with radially polarized beams with a phase vortex were modeled numerically).

It is noted that the model described in this chapter is limited to cylindrical symmetries. Therefore, it cannot describe the elliptical structures, or the lobes found within laser spots described in Chapter 4 (Figures 4.8, 4.17 and 4.18). Table 5.7 summarizes the focal properties of different types of CVBs.

Table 5.7: Summary of focal properties of different types of CVB.

	Uniform states of polarization with a planar phase	**CVB with a vortex phase (topological charge of 1)**	**CVB with a planar phase**
Intensity profile	Gaussian	Widened Gaussian	Annular
Polarization structure	No inversion in the state of polarization	Inversion in the state of polarization	No inversion in the state of polarization
Polarization purity	~100%	Hybrid polarization	~100%

5.9 Chapter summary

The chief points of this chapter are outlined below. A more comprehensive discussion of these results is outlined in Chapter 7.

- I have introduced an analytical model of the experimental setup used in Chapter 4 to produce radially and azimuthally polarized vortex beams.

- The model is used to predict the focal properties of four types of CVBs, focused with a low NA optic: radially polarized beams with a planar phase or a 2π vortex phase and azimuthally polarized beams with a planar phase or a 2π vortex phase.

- The model predicted that a radially polarized beam with a planar phase produces an annular, radially polarized focal spot. A radially polarized beam with a vortex phase produces a Gaussian intensity profile with a hybrid polarization: circularly polarized in the center and azimuthally polarized in the annular region around the center. The Gaussian profile is wider than that produced with a uniform polarization.

- The model also predicts the properties of focal spots produced with azimuthally polarized beams. A beam with a planar phase produces an annular, azimuthally polarized focal spot. A beam with a vortex phase produces Gaussian intensity profile with a hybrid polarization (circular in the center and radial in the wings).

- The results from the model are consistent with results published in the existing literature in the case of CVBs with a planar phase.

- The results from the model are also consistent with the experimental results described in Chapter 4. They explain the patterns or LIPSS and confirm the inversion in the state of polarization at the focal plane found in the experiments.

- The model clarifies the behavior of radially/azimuthally polarized vortex phase beams focused with low NA optics. Theoretical studies of this type of optical setups are currently not available in the literature.

6

Ultrafast laser processing with Cylindrical Vector Beams

6.1 Introduction

In the previous chapters, I have introduced a Polarization Mode Converter and demonstrated how it can produce a radial or an azimuthal polarization state at the focal plane of a low NA focusing optic. The Polarization Mode Converter was studied both experimentally and theoretically, indicating that an inversion in the state of polarization occurs, i.e. the state of polarization at the focal plane is orthogonal to that of the collimated beam before the focusing optic. For material processing, only the state of polarization within the focal region is relevant. Therefore in the processing tests described in this chapter, I refer to the state of polarization at the focal plane only and not the polarization of the collimated beam.

In this chapter, the Polarization Mode Converter is used with a high laser beam fluence to micro-machine stainless steel plates. Recent experimental work (see M. Meier *et al.* 2007, M. Kraus *et al.* 2010 or R. Weber *et al.* 2011) also investigates micro-machining with radial and azimuthal states of polarization, suggesting that the potential benefits of using these states of polarization are more subtle than predicted in early theoretical studies (such as V. G. Niziev *et al.* 1999, for example). Depending on the material, processing parameters and aspect-ratio of the machined structures, either a radial, an azimuthal or a circular polarization is most efficient. In particular, Meier *et al.* 2007 demonstrated experimentally, using a nanosecond-pulse laser source, that a radial polarization is usually more efficient than other modes at drilling through 1-3mm thick brass and copper plates, whereas an azimuthal polarization is more efficient at drilling mild steel plates of similar thicknesses. M. Kraus *et al.* 2010 compared the efficiency of drilling 0.5-1mm thick steel plates with a radially and an azimuthally polarized beam, using a picosecond-pulse laser source. It was shown that the azimuthally polarized beam was more efficient at micro-drilling high-aspect-ratio holes when the plate thickness was above 0.5mm.

The work presented in this chapter focuses on micro-machining 0.2-0.4mm thick stainless steel plates using a femtosecond-pulse laser source with the Polarization Mode Converter described in earlier chapters. A comparative analysis of micro-machining with radially, azimuthally, circularly and linearly polarized beams is carried out. Two types of micro-machining processes are tested: helical drilling and cutting. In each case, the results are compared between the various states of polarization.

Thanks to the SLM, the state of polarization can be programmed and modified to better suit an industrial process, without requiring any mechanical rotation of the polarization optics. Hence, compared with the other methods for producing CVBs used in the experimental work described above, the Polarization Mode Converter allows further flexibility.

6.2 Helical drilling

6.2.1 Aim of the experiment

During a laser micro-machining process such as helical drilling, multiple internal reflections occur inside the holes. Polarization affects the laser-material energy coupling at each reflection. In this section, various polarization states (such as radial, azimuthal, circular and linear) are compared with each other in a helical drilling process. Stainless steel plates are drilled with each polarization state. The resulting entrance and exit holes are investigated using an optical microscope to compare the process quality and efficiency in each case.

6.2.2 Experimental setup

The same femtosecond laser processing setup presented in Chapter 4 (see Figure 4.6) was used. However in the experiments here, a beam expanding telescope with a magnification of two was used to reduce the fluence at the SLM. This beam expanding telescope was placed before the SLM (Figure 4.6).

6.2.3 Experimental procedure

In these experiments, 380µm thick, type 302 stainless steel plates were drilled with four square holes, one for each polarization mode (the Polarization Mode Converter was set to produce either a linearly, circularly, radially or azimuthally polarized focal region). Apart from the polarization state, the same process parameters were used for each hole so that the results can be compared. Prior to the tests, the sample surfaces were polished to a 320 grade abrasive grit.

The laser pulse energy was 75µJ, corresponding to a peak fluence of ~24J/cm². This is much higher than the ablation threshold of stainless steel which is around 0.16J/cm² (P. Mannion *et al.* 2003). The laser focal spot diameter was calculated according to the parameters of the optical setup, where f=100mm, D=6mm and M^2=1.3 (M^2 was measured with a SPIRICON beam profiler, as detailed in Section 4.3.6 in Chapter 4). The spot diameter is $2\omega_0 = \frac{4\lambda M^2 f}{\pi D} = 28 \mp 2\mu\text{m}$. Each hole was machined using a helical drilling process, where the laser beam is continuously scanned along the chosen geometry for the chosen exposure duration. The beam path geometry was a 120µm sided square and the exposure duration was 2.5 minutes. The scanning speed was 2mm/s. The sample was placed on a holder on the multi-axis motion control stage (see Figure 4.6), so that the focal plane lied ~100µm below the sample top surface.

6.2.4 Results

After processing, the produced holes were analyzed with an optical microscope. The square holes had an entrance opening of ~220µm and exit opening of ~110µm. The entrance of the holes showed no dependence on polarization. Optical micrographs of the exit holes, which were affected by polarization, are shown in Figure 6.1.

- Figure 6.1-a shows the exit of the hole produced with a *linearly* polarized focal region. The exit hole is rectangular, elongated in the direction of the polarization vector (125+/-5µm x 80+/-5µm).

- Figure 6.1-b shows the exit of the hole produced with a *circularly* polarized focal region. The size of the hole is 110+/-10µm. Distortions can be seen on the edges of the exit hole.
- Figure 6.1-c shows the exit of the hole produced with a *radially* polarized focal region. The size of the hole is 100+/-5µm. The sides of the hole are more regular, with fewer distortions than with the other modes of polarization.
- Figure 6.1-d shows the exit of the hole produced with an *azimuthally* polarized focal region. The size of the hole is 115+/-10µm. Distortions are visible, similar to those produced with a circularly polarized focal region.

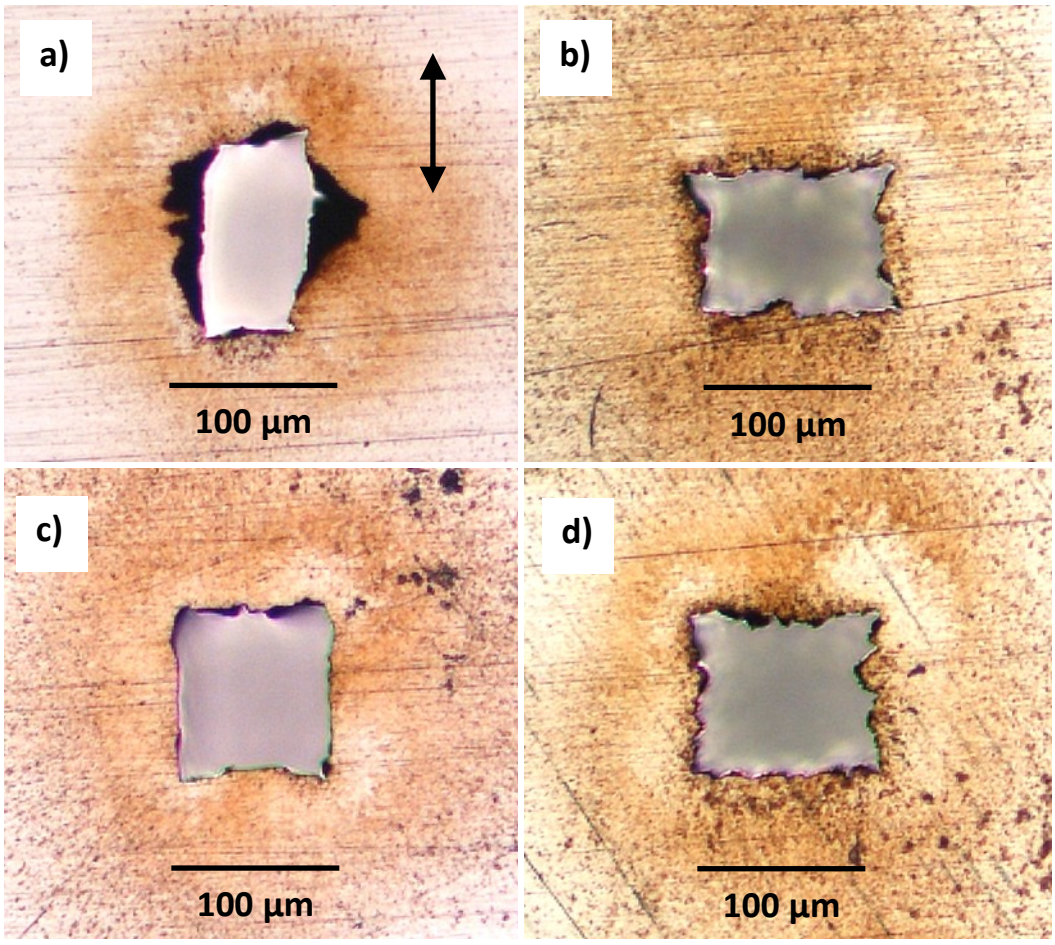

Figure 6.1: Optical micrographs of the exit holes obtained from drilling square holes of in a 380µm thick stainless steel plate, using a **(a)** linearly, **(b)** circularly, **(c)** radially and **(d)** azimuthally polarized focal region (775nm, 160fs pulses, 1kHz repetition rate, laser scanning speed: 2mm/s, pulse energy: 75µJ, duration of laser exposure: 2.5 minutes per hole). The arrow in **(a)** indicates the direction of incident polarization.

6.2.5 Discussion

The exit holes produced here with a linearly polarized focal region are consistent with the experimental results presented in Chapter 3. The holes are elongated along the direction of the polarization vector (Figure 6.1-a). This is due to the laser-material energy coupling being higher along that direction, where the internal reflections on the sidewalls during machining are *p*-polarized.

A circularly polarized focal region produced exit holes with distorted edges. It is noted that the experimental results obtained when drilling with a circularly polarized beam in Chapter 3, showed a better hole quality (Table 3.2) than here. In Chapter 3, the circularly polarized beam was produced using a zero-order quarter-waveplate, whereas here the circularly polarized beam was obtained by setting the SLM to induce a quarter-wave phase shift. An SLM sometimes induces diffraction noise which affects the beam quality. The distortions seen on the hole exit in Figure 6.1-b are thought to be related to these SLM-induced diffraction effects.

When drilling with a radially polarized focal region, the internal reflections on the sidewalls of the hole are mostly *p*-polarized. This leads to a better absorption of the laser energy and reduces internal reflections during machining. This also leads to a poorer channelling of the laser energy to the bottom of the hole, which results in an increased sidewall taper angle and a smaller exit hole (100+/-5µm with a radial polarization versus 110+/-10µm with a circular polarization). These results are consistent with those obtained when drilling with *p*-polarization in Chapter 3 (Table 3.2).

With an azimuthally polarized focal region, the internal reflections on the sidewalls of the hole are mostly *s*-polarized. This is expected to increase internal reflections during machining. As these reflections occur on non-optically flat surfaces inside the hole, they tend to produce an irregular ablation front and a distorted hole exit. The results in Figure 6.1-d are consistent with those obtained when drilling with *s*-polarization in Chapter 3 (Table 3.2).

Overall, these results showed that a radial polarization at the focal plane is best suited for helical drilling in steel under these experimental conditions. With comparatively fewer internal reflections, the radially polarized focal region produces the best machining quality albeit with a slightly higher taper angle. However, it is noted that the comparatively poorer channelling of the laser energy to the bottom of the hole could reduce the efficiency of drilling with this mode, especially if drilling higher aspect-ratio holes (i.e. thicker plates) than those studied here.

These results are consistent with M. Meier *et al.* 2007 and M. Kraus *et al.* 2010, who studied micro-drilling high-aspect-ratio holes in 0.5 to 3 mm thick steel plates. They found that an azimuthal polarization tends to be more efficient at drilling steel plates with a thickness above 0.5mm, whereas a radial polarization tends to be more efficient at drilling 0.5mm thick steel plates.

6.3 Micro-cutting

6.3.1 Aim of the experiment

In the experiments described in Section 6.2, I looked at the properties of radial and azimuthal polarizations for helical drilling, where the ablation front is wider than the laser focal spot. In this section, I look at micro-cutting, where high-aspect-ratio channels are typically produced with an ablation front which approximately is of the same size as the laser focal spot. In this case, the small size of the ablation front could reduce the process efficiency, with multiple reflections inside the channels leading to a poor channelling of the laser energy to the bottom. To study how polarization influences these multiple reflections, radially, azimuthally and circularly polarized beams are used to micro-cut stainless steel plates. The process efficiency and quality achieved in each case are then compared.

6.3.2 Experimental setup

Stainless steel plates (type 302) were machined using the same femtosecond laser processing setup used for the helical drilling experiments in Section 6.2 and in Chapter 4 (Figure 4.6), and the resulting cut-outs were studied. This time, the magnification telescope was removed from the beam path to reduce optical aberrations.

6.3.3 Experimental procedure

Each stainless steel test piece was machined with three square holes, one for each polarization mode (the SLM mode converter was set to produce either a radially, an azimuthally or a circularly polarized focal region). Apart from the polarization state, the same process parameters were used for each square so that the results can be compared. A range of plate thicknesses were used (200µm to 380µm) to give an insight into the way these polarization modes influence the coupling of the laser energy to the stainless steel at various depths. The machining tests were repeated using various exposure durations to compare the efficiency of the cutting.

A laser pulse energy of 75µJ was used (fluence ~24J/cm²). For all the tests, 650µm sided square beam paths were programmed into the scanning galvanometer and scanned at 5mm/s, as a continuous loop for the chosen exposure duration. This generated square cut-outs in the centre of the beam path. After exposure to the laser beam, the stainless steel plate was placed in an ultrasonic bath, so that the ultrasonic waves would clean and, if the cutting had been successful, remove the central cut-outs. This method is used to compare the cutting efficiency, the average volume of ablation and the quality of machining between each polarization state.

6.3.4 Overall cutting efficiency

6.3.4.1 Method

A comparative study of the cutting efficiency achievable with each polarization mode was undertaken by checking which of the three holes were successfully cut-out from the plate for a given exposure

duration. To find out the most efficient polarization mode, I look at which mode produces a hole in the shortest exposure time.

6.3.4.2 Results

Table 6.1 summarizes these experimental results for all the processing parameters tested. In summary, a 380μm thick plate was exposed to the beam for 9.5 minutes per hole. Subsequent exposure to ultrasonic waves successfully removed the cut-outs for all polarization modes. The experiment was repeated, shortening the laser exposure to 8.5 minutes per hole. In this case, only cut-outs machined with a radially polarized focal region were removed by the ultrasonic waves. Reducing exposure further led to the failure of cutting for all polarization modes. These experiments were repeated with a 310μm thick plate and produced the same results: a radially polarized focal region successfully produced cut-outs in the shortest exposure duration (8 minutes in this case).

Next, the experiment was repeated with a 200μm thick plate exposed to the laser beam for 4 minutes per hole. In this case, all the polarization modes produced clear cut-outs. The same plate was processed again, but with the laser exposure reduced to 3.5 minutes per hole. In that case, the cutting failed for all the polarization modes. In the case of machining a 200μm thick stainless steel plate, this comparative study did not single out one of the polarization modes as more efficient than the others.

It is noted that each machining test described here was carried out a number of times with various durations of exposure. To ensure consistency, the figures for the minimum exposure in Table 6.1 were averaged between these results.

Table 6.1: Minimum laser exposure required for cutting through stainless steel plates of various thicknesses. Results based on cutting 650μm square holes using radial, azimuthal and circular polarizations (775nm, 160fs pulses, 1kHz repetition rate, pulse energy: 75μJ).

Plate thickness	Azimuthally polarized focal region	Radially polarized focal region	Circularly polarized focal region
380μm	9.5 min.	8.5 min.	9 min.
310μm	9 min.	8 min.	8.5 min.
200μm	4 min.	4 min.	4 min.

6.3.4.3 Discussion

These machining tests revealed that a radially polarized focal region is more efficient than a circularly or azimuthally polarized one for cutting deep structures such as the ones produced in the 310 and 380μm thick stainless steel plates. Under these experimental conditions, a radially polarized focal region reduces the minimum laser exposure duration by ~5% compared to a circularly polarized one. These results are consistent with those presented in Chapter 3 (Section 3.5.2): machining with a radially or an azimuthally polarized focal region produces the same results as machining with *p*- or *s*-polarization

respectively in Chapter 3. However, when the depth of the machined structures is reduced, the comparative advantage of machining with a radially polarized mode disappears as indicated by cutting through 200µm thick plates.

The higher efficiency obtained with a radially polarized focal region for machining high-aspect-ratio channels was predicted theoretically in V. G. Niziev *et al.* 1999 and confirmed in the experimental analysis above. This increased efficiency is related to the internal reflections that occur during the machining of the micro-channels. When the laser beam is radially polarized in the focal region, it produces internal reflections which are mostly *p*-polarized. When the focal region is azimuthally polarized, the internal reflections are mostly *s*-polarized. With circular polarization, the internal reflections are an average of *p*- and *s*-polarizations. For a typical high-aspect-ratio channel geometry, the angle of incidence on the sidewalls is around 80˚. The corresponding value for the reflectivity of steel is around 47% for *p*-polarization and 94% for *s*-polarization (S. Nolte *et al.* 1999). Therefore, the intensity of light reflected from the walls during the machining is approximately twice as much with an azimuthal (*s*-) polarization compared with a radial (*p*-) polarization. This results in a higher loss of energy through the exit of the channels machined with an azimuthal polarization. On the other hand, a radial polarization increases the coupling of the laser beam energy to the sidewalls during the machining, compared with a circular or azimuthal polarization.

When lower aspect-ratio channels (depth/width < 3) are machined, fewer internal reflections occur on the sidewalls. The influence of polarization on coupling the laser energy to the work-piece is not so critical in that case, explaining the similarity in the efficiency of cutting through a 200µm thick plate between all the polarization modes. This trend was suggested in M. Meier *et al.* 2007, where the drilling efficiency through steel plates of various thicknesses above 1mm was compared between several states of polarization. The same trend is now confirmed for steel plates with a thickness below 1mm: when the aspect-ratio of the machined structures (i.e. the thickness of the plates) is reduced, the machining efficiency of the various polarization states converges.

It is noted that, due to the phase vortex of the radially/azimuthally polarized beams, the polarization purity at the focal plane is not 100%. A residual circularly polarized region is present in the centre of the focal spots produced with these beams (see Chapter 5). This could reduce the gains in processing efficiency compared with a homogenous circularly polarized beam. It is thought that using a radially polarized beam with a planar phase could further increase the efficiency of the process, since such beam produces a better polarization purity at the focal plane compared with a vortex beam. It is also noted that the slight difference in the laser spot size between the radially/azimuthally polarized vortex beams and the circularly polarized one (see Figure 4.7) could also affect the process efficiency. This is discussed further in the following section.

6.3.5 Ablation efficiency

6.3.5.1 Method

To further investigate the machining efficiency, the overall volume of ablated material was measured for each polarization mode. The cut-outs removed after machining as described above were imaged with an optical microscope. Table 6.2 (second row) shows optical micrographs of the sidewall of cut-outs removed from a 310µm thick stainless steel plate after a 9 minutes exposure to the laser beam per hole.

By measuring the cross-sectional area of the sidewalls of the cut-outs, the overall volume of ablated material can be derived for each polarization mode. Figure 6.2 shows the typical geometry of a cut-out and the dimensions required to derive the volume of ablated material. The cross-sectional area of the cut groove is $\mathbf{A_G} = \mathbf{H} \times \mathbf{L} - \mathbf{A_{CO}}$ (see Figure 6.2). $\mathbf{H}$ is the thickness of the sample plate ($\mathbf{H}$ =310µm in the example illustrated in Table 6.2). $\mathbf{L}$ is the length of a side of the (square) beam path (650µm here). $\mathbf{A_{CO}}$ is the cross-sectional area of a side of the cut-out. It is measured from the optical micrographs, using the associated imaging software. The volume of ablated material $\mathbf{V}$ can be derived by multiplying the cut groove cross-sectional area, $\mathbf{A_G}$, by the overall length of the groove: $\mathbf{V} = \mathbf{4} \times \mathbf{L} \times \mathbf{A_G}$.

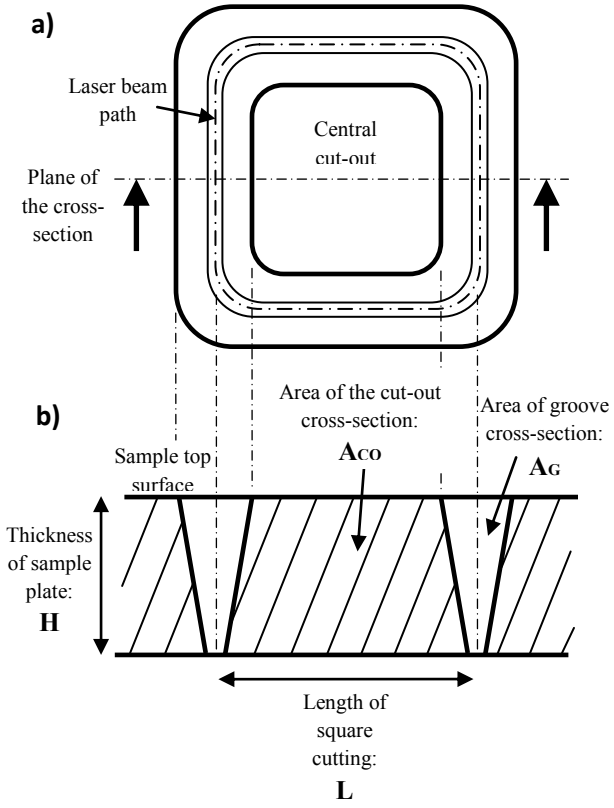

Figure 6.2: Schematic of the geometry of a cut-out from a sample plate after laser exposure: **(a)** Top view and **(b)** Side cross-section.

Table 6.2: Results of laser cutting square-shaped holes from a 310µm thick stainless steel plate, using radial, azimuthal and circular polarizations (775nm, 160fs pulses, 1kHz repetition rate, laser scanning speed: 5mm/s, pulse energy: 75µJ, duration of laser exposure: 9 minutes per hole).

	Azimuthally polarized focal region	**Radially polarized focal region**	**Circularly polarized focal region**
Bottom of the square cut-outs, showing the exit grooves	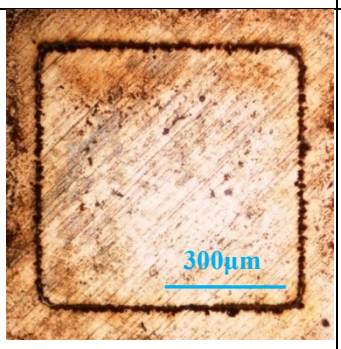	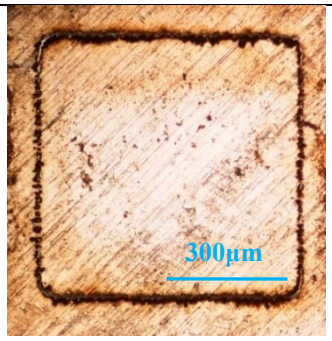	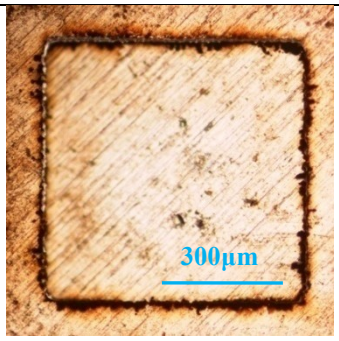
Sidewall of the square cut-outs after removal from sample plate	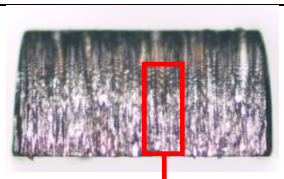	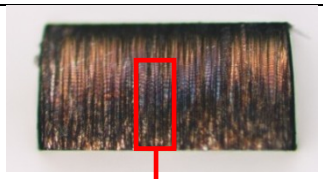	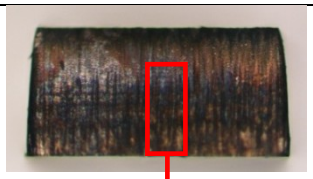
Surface profile of sidewalls Only the area highlighted in red (see above) is displayed. The colour-coded scale shows the distance from an average mid-plane, in µm. From these surface profiles, the Roughness average can be measured.	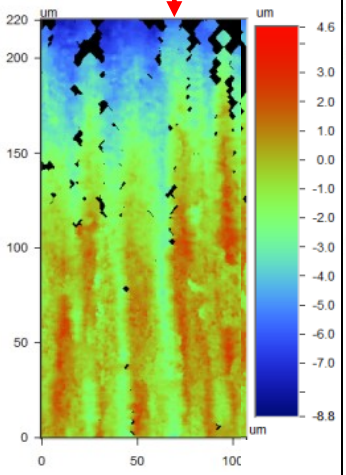	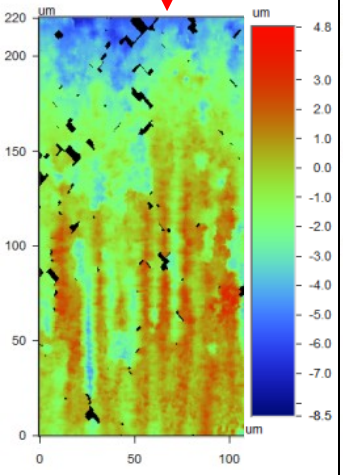	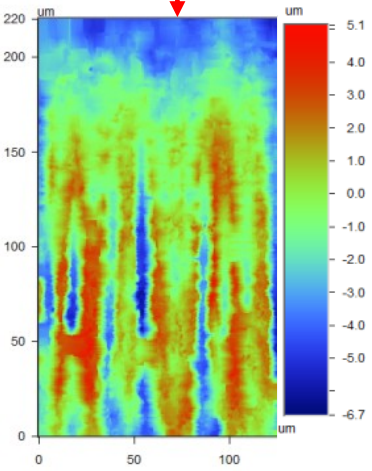
Roughness average (Ra) of sidewalls (measured on the lower half of each side wall)	1.0+/-0.4µm	1.0+/-0.7µm	0.9+/-0.4µm
Volume of material ablation	~19.1 x10^6µm^3	~19.1 x10^6µm^3	~15.8 x10^6µm^3
Overall micro-machining efficiency (see Table 6.1)	Lowest	Highest	Intermediate

6.3.5.2 Results

To ensure consistency in the results and gauge the level of uncertainty in the measurements, several cut-outs have been machined and measured for each polarization state. When 310μm thick stainless steel plates were exposed to the laser beam for 9 minutes per hole, a circularly polarized focal region ablated an average volume of ~$15.8 \times 10^6 \mu m^3$, while a radially or an azimuthally polarized focal region both ablated an average volume of ~$19.1 \times 10^6 \mu m^3$ (see Table 6.2). According to these figures, radially and azimuthally polarized beams ablated approximately 20% more material than a circularly polarized one. The difference in ablation efficiency between these beams can be explained with the difference in the size of the laser spots at the focal plane.

6.3.5.3 Discussion

When the Polarization Mode Converter was used to produce a radially or an azimuthally polarized vortex beam, the resulting laser spot at the focal plane was wider than that produced with a circularly polarized planar phase beam (32+/-5μm for linearly/circularly polarized beams versus 40+/-5μm for radially/azimuthally polarized vortex beams, see Figure 4.7 in Chapter 4). A wider spot increases the size of the ablation front, enabling a more effective channeling of laser energy inside the machined structures by avoiding excessive reflections on the sidewalls. The wider spot also facilitates ejection of the ablated material, which helps to maintain a high ablation rate when machining high-aspect-ratio structures. The result of these effects is an increased sidewall taper angle. The circularly polarized beam, which produced a smaller spot at the focal point, ablated comparatively less material and produced a smaller taper.

6.3.6 Machining quality

6.3.6.1 Method

In order to compare the quality of machining achieved with each polarization mode, the exit grooves obtained after laser cutting were examined with an optical microscope, prior to removing the cut-outs in an ultrasonic bath. Once the cut-outs had been removed, their sidewalls were studied using an optical surface profiling system (i.e. a white light interferometer WYCO NT1100) to examine the surface quality and measure the Roughness average (Ra).

6.3.6.2 Results and discussion

Table 6.2 (first row) shows optical micrographs of the exit grooves obtained from machining a 310μm thick stainless steel plate for 9 minutes per hole. It can be seen that machining with a circular polarization mode produced ripples and filaments on the edges of the exit grooves. An azimuthally polarized focal region produced a better quality than a radially or circularly polarized one, with fewer ripples and filaments distorting the shape of the exit grooves. These findings are consistent across the full range of stainless steel plate thicknesses and exposure times tested here.

In order to check if the ripples and filaments seen on the exit grooves also affect the sidewalls, the Roughness average, Ra, of the surface of the sidewalls was measured for each cut-out from a 310μm thick stainless steel plate. To ensure consistency in the results, several cut-outs have been measured and the results averaged. Ra=1.0+/-0.7μm for a radially polarized focal region, Ra=1.0+/-0.4μm for an azimuthally polarized focal region and Ra=0.9+/-0.4μm for a circularly polarized one (see Table 6.2). This

indicates that in terms of surface roughness, the machining quality was similar (within 10%) for all polarization modes. It is noted that this work is the first to compare the surface roughness of sidewalls produced from machining with these modes of polarization.

6.4 Chapter summary

The chief points of this chapter are summarized below. A more comprehensive discussion of these results is outlined in Chapter 7.

- Ultrafast laser micro-machining tests of stainless steel plates with radially and azimuthally polarized beams were conducted. The results were compared with those obtained when machining using uniforms states of polarization such as linear or circular.

- In helical drilling, where the ablation front is wider than the laser focal spot, radial polarization in the focal plane produced the best machining quality, albeit with a slightly higher sidewall taper angle. This is due to a relatively better absorption of the laser beam energy at the sidewalls, leading to fewer internal reflections during machining.

- In micro-cutting, the ablation front is typically of a similar size to the laser focal spot. Micro-cutting was tested with various plate thicknesses. Radial polarization at the focal plane was the most efficient mode for machining high-aspect-ratio channels (i.e. thicker plates). However for machining lower aspect-ratio channels (i.e. thinner plates), all the polarization modes had a similar process efficiency in these experiments.

7 Conclusions

7.1 Introduction

In this thesis, I have investigated novel liquid-crystal-based optical setups for controlling the polarization of ultrafast laser beams. These new optical setups were used for laser micro-machining stainless steel work-pieces, aiming to improve the quality and efficiency of the process.

As a first step in the experimental work, some of the optical properties of the new liquid-crystal devices used in this research were characterized. I then followed two experimental strategies for laser processing with these liquid-crystal devices: the first using dynamic control of the polarization direction of a linearly polarized beam and the second using laser beams with cylindrical polarization structures (i.e. CVBs). Both of these techniques were used to optimize the micro-machining of stainless steel plates. In this way, I have demonstrated how liquid-crystal-based optical setups can improve laser micro-processing efficiency and quality. In this chapter, I summarize the results described in the rest of this thesis and discuss potential future industrial applications and future lines of investigation.

7.2 Innovative techniques for optical diagnostic

As part of the research described in this thesis, novel optical setups were designed to control the phase and polarization of ultrashort-pulse laser beams. To characterize some of the optical properties of these new setups, two original diagnostic techniques were used: one for analyzing polarization and the other for analyzing phase-response under certain experimental conditions.

7.2.1 Method for analyzing polarization

Analyzing polarization in the focal region of a laser processing bench is a notoriously difficult thing to do. In Chapter 2, I described an original method for analyzing polarization by imprinting LIPSS on stainless steel samples placed in the focal region of our micro-processing setups. This technique was used either to imprint the state of polarization of CVBs around the focal region, or to check the direction of polarization along a beam scanning path.

Producing LIPSS requires applying ultrashort laser pulses to a surface, using laser fluences close to the ablation threshold of the material. Here, a fluence of 1.8J/cm² was used to produce LIPSS on stainless steel samples. The orientation of the produced LIPSS is orthogonal to the polarization vectors of the beam and their pitch is similar to the incident laser wavelength.

This method can be used for analysing a static, uniform state of polarization such as linear or circular at the focal plane: a linear polarization produces regular, well-defined LIPSS whereas a circular polarization produces irregular LIPSS oriented in random directions. However, an elliptical polarization

state cannot be analysed accurately using this method. Moreover, this method can only analyse the transverse components of the polarization and therefore it is not accurate for analysing the polarization in the focal region of a high NA optic.

In spite of these restrictions, this method is very powerful when analysing complex, structured polarization modes such as CVBs: thanks to the small size of the LIPSS, these structured states of polarization can be clearly visualized in the focal region. This method can help calibrate a laser bench that uses CVBs for industrial processing: by producing LIPSS at low fluence, and analysing them prior to processing the work-piece, the state of polarization in the focal region can be verified.

This method could also be useful to calibrate an industrial laser processing bench that uses a dynamically controlled polarization, such as in a *polarization trepanning* process. By imprinting LIPSS on a sample surface prior to machining the work-piece, the appropriate orientation of polarization in each region of the scanned geometry can be verified. This can be useful for example when programming a *polarization trepanning* processing bench to produce a new laser scanning geometry.

7.2.2 Method for verifying the phase-response of SLMs at high-average-power

SLMs have often been used with low-average-power laser beams in a research environment. However, their suitability for high-average-power industrial use needed to be confirmed. In Chapter 2, I described an optical diagnostic technique to check if SLMs can sustain high-average beam powers without influencing their phase modulation properties.

This was done by programming an SLM to induce a phase grating which splits the beam into a zero- and first-order laser beam. The resulting diffraction efficiency was used to evaluate the stability of the phase modulation. A fluctuation of diffraction efficiency as a result of a long exposure to a high-average-power beam would imply that the phase modulation is affected by the exposure to the beam. Here, the diffraction efficiency was measured with the SLM exposed to a laser beam with 8W of average power for 4.5 hours. It was found that the diffraction efficiency fluctuation was less than 4% under these experimental conditions. This confirmed that the SLMs are suitable for high-average-power industrial applications. Therefore the results from the experimental work that used SLMs, described in this thesis, are relevant to industrial users.

7.3 Real-time control of polarization

In Chapter 3, a real-time control of the polarization direction of laser beams was used to improve micro-machining processes. Prior to testing real-time processes, I demonstrated how a laser beam with a static state of polarization affects micro-machining.

7.3.1 Influence of polarization on micro-machining

In this thesis, I have shown how the state of polarization of an ultrashort-pulse laser beam influences its properties for micro-machining a stainless steel work-piece. For example, a laser beam with a static linear polarization tends to produce strongly distorted geometries. A beam with a circular polarization tends to produces ripples on the sidewalls of the machined structures.

The experimental results described in Chapter 3 indicate that the coupling of the laser energy to the sidewalls of the machined structures is strongly influenced by the local state of polarization in each region. In the regions of the machined structures where the laser radiation is *p*-polarized, the coupling tends to be more efficient, leading to a higher rate of ablation. In the regions where the laser radiation is *s*-polarized, the coupling is poorer and most of the laser energy is reflected. This sometimes leads to laser energy losses through the exit aperture of the machined structures, or distortions due to internal reflections on non-optically-flat sidewalls. Therefore, a novel method for maintaining the beam at a *p*- or an *s*-polarization state in real-time during machining was investigated. This method was referred to as *polarization trepanning*.

7.3.2 Dynamic polarization control for industrial micro-manufacturing

Real-time control of the polarization direction of a femtosecond laser beam was achieved using a fast-response, liquid-crystal device and this was presented in Chapter 3. Helical drilling and cutting of high-aspect-ratio microscopic structures of various geometries in a steel plate was tested, using a number of polarization driving modes such as *polarization trepanning*. These tests were performed on thin (~0.4mm thick) stainless steel sheets using a 775nm femtosecond laser at 24J/cm².

The experimental results showed that, when a *polarization trepanning* process was used to maintain the laser beam in a *p*-polarized state in real-time during processing, higher-quality structures were produced compared with other states of polarization. The sidewall-surface-roughness and edge-quality of the machined structures were improved significantly, with the dimensions of ripples and distortions divided by a factor of two. Moreover, a higher processing speed was achieved. For example, micro-cutting square cutouts with a *p*-polarized beam required a shorter processing time than a circularly polarized one. This is thought to be due to the more efficient coupling of the laser energy to the work-piece with the *p*-polarized beam.

Existing industrial laser micro-processing systems use a mechanical rotation of polarization optics to achieve *polarization trepanning*. However this opto-mechanical method is limited to producing circular holes and could suffer from undesirable mechanical motion, associated vibrational problems and maintenance downtime. To our knowledge, the research presented in this thesis was the first to achieve *polarization trepanning* using a solid-state device for micro-processing. The fast-response liquid-crystal polarization rotator presented in this thesis could emerge as a powerful alternative to existing opto-mechanical devices. As an off-the-shelf item, it can easily provide improved machining quality for industrial laser systems.

7.3.3 Future work

Future work could investigate micro-machining structures in steel with a higher aspect-ratio than those studied in this thesis. In this case, a laser beam maintained in an *s*-polarized state in real-time during machining could be desirable. When very-high-aspect-ratio micro-structures are machined, the channeling of laser energy to the bottom of the structures is critical to maintain a high process efficiency. This channeling could be facilitated by increasing internal reflections during machining. Using an *s*-polarized beam would increases these internal reflections since it has a higher reflectivity.

Due to its design characteristics, the liquid-crystal device used in this research had an angular rotation range limited to 90˚ and required a DC-balanced, 50% duty-cycle periodic driving voltage. As a result, the tests were restricted to machining axi-symmetric features. A potential line of future work could aim to assess, amongst the wide range of liquid-crystal technologies available, the most suitable ones for various drilling and machining configurations.

This thesis focused on laser processing work-pieces made of stainless steel. Future work could investigate how real-time control of the beam polarization direction could improve the machining of other metals or materials such as semiconductors and dielectrics. Another line of work could consist in looking at how real-time polarization control could help producing complex, non-circular geometries such as those produced in a medical stent device. Here the absence of inertia associated with mechanical motion could enable to flip the direction of polarization at high speed to best suit the machining process.

7.4 Spatial control of polarization: producing Cylindrical Vector Beams

7.4.1 Principle of a Polarization Mode Converter

In Chapter 4, I have demonstrated a Polarization Mode Converter that uses a liquid-crystal SLM to produce polarization structures with a cylindrical geometry, or CVBs. The optical setup of the Polarization Mode Converter was first studied theoretically using a Jones matrix analysis. The analysis confirmed that each pixel of the SLM enables rotating the direction of polarization between 0 and π radians. As each pixel is independently controllable, the Polarization Mode Converter enables a spatially dependant rotation of the polarization. By adjusting the rotation induced by each pixel, CVBs (such as radially and azimuthally polarized beams) can be produced. I have also shown that a residual phase vortex exists after the Polarization Mode Converter. For example if a radial or an azimuthal polarization are produced, the residual phase vortex has a 2π pitch. Some of the theoretical results from the Jones matrix calculations were also confirmed experimentally using a nanosecond-pulse laser test bench.

7.4.2 Experimental analysis of CVBs produced with the Polarization Mode Converter

Chapter 4 describes how the optical setup of the Polarization Mode Converter was then implemented in a 775nm femtosecond laser micro-processing bench. The Polarization Mode Converter was used to produce CVBs and the resulting polarization was analyzed with a polarizing filter, demonstrating a polarization purity better than 84%. The intensity distribution and polarization properties around the focal point of the micro-processing bench were studied by laser marking the surface of stainless steel samples at a low fluence of 1.5J/cm², less than ten times the ablation threshold (which is 0.16J/cm² for stainless steel, see P. Mannion *et al.* 2003). In particular, the properties of radially and azimuthally polarized beams were investigated, since these polarizations are expected to be beneficial for material processing.

By imprinting LIPSS at the surface of stainless steel samples, I was able to map the structure of the polarization in the focal region and check if the expected states of polarization had been achieved. At the focal plane the state of polarization was found to be orthogonal to that of the collimated beam

before the focusing lens, implying that a flip in the state of polarization had occurred. This polarization flip effect was thought to be caused by the residual vortex phase structure induced with the Polarization Mode Converter.

The three-dimensional structure of the polarization vectors in the regions around the focal point were further investigated by imprinting LIPSS above and below the focal plane. The analysis of the produced LIPSS showed that the polarization vectors "twist" along the optical axis of the focusing optics. This indicates that the state of polarization varies along the optical axis of the focusing lens. This polarization "twist" effect is an interesting discovery in the focal properties of CVBs with an orbital angular momentum. It is expected to affect laser-material interactions with these beams.

The effect of the pitch of the phase vortex induced by the Polarization Mode Converter was also investigated. I found that changing the vortex pitch affects the laser fluence profile (i.e. the intensity distribution) at the focal plane. When marking samples, lobes of various sizes are produced as a result.

In summary, I have shown that the Polarization Mode Converter provides a flexible way to control the intensity distribution and polarization structure in the focal region. As controlling these enables to optimize laser-material interactions, the Polarization Mode Converter could be a valuable tool for various industrial laser processing applications.

7.4.3 Analytical model of the CVBs produced with the Polarization Mode Converter

In Chapter 5, an analytical model of the optical setup was used to explain the experimental results described in Chapter 4. I modeled the optical setup using a geometrical approach to derive the Jones vectors and assess the state of polarization in the focal plane of the low NA focusing lens. The model also enabled to assess an approximate fluence amplitude profile in the focal plane. Various types of beams were studied using the model, including radially and azimuthally polarized beams with a planar or a vortex phase, and beams with a uniform state of polarization.

The model predicted that a radially polarized beam with a planar phase focuses as a radially polarized annular spot with a zero intensity in its center. Similarly, an azimuthally polarized beam with a planar phase focuses as an azimuthally polarized annular spot. These predictions are in agreement with recently published literature describing the focal properties of radially or azimuthally polarized beams with a planar phase, focused with low NA optics. This gave me confidence that my simplified analytical model described the focal behavior of the beams accurately.

In the case of CVBs with a vortex phase, there is no consensus in the literature since the focal properties of these beams depend on the experimental parameters. My model predicted that a radially polarized beam with a 2π pitch vortex phase produces a Gaussian type of fluence profile at the focal plane, with the highest fluence in the central region (i.e. not an annular shaped focal spot). The focal spot was predicted to be circularly polarized in its central region and mostly azimuthally polarized in the annular region around its centre. Similarly, an azimuthally polarized beam with a 2π pitch vortex phasefront was predicted to produce a focal spot mostly radially polarized in the annular region around its centre. In the focal plane, the beam was predicted to also include circularly and elliptically polarized regions and therefore the polarization purity obtained by focusing these vortex phase beams was not 100%. When compared with beams with a uniform polarization (and with planar phase fronts), the radially and azimuthally polarized vortex phase beams were found to produce a lower peak fluence with a wider beam waist at the focal plane.

The model predictions were in agreement with the experimental results described in Chapter 4. In particular, the model confirmed that the optical setup induces an inversion in the dominant state of polarization at the focal plane, compared to the state of polarization of the collimated beam.

Overall, this model clarified how the polarization and phase structures of a CVB affect its focal properties when focused with low NA optics. A specific type of CVBs can be designed to produce the desired polarization structure and intensity distribution within the focal spot, optimized for a given processing application. Before CVBs can be used in a wide range of industrial laser processing applications, a good understanding of their focal properties is necessary. Existing models available in the literature describe the focusing properties of various types of CVBs. However there is little work comparing model predictions with experimental data. In particular, very little work has been published that explains how optical aberrations such as diffraction affect the focal properties of CVBs. The analysis described here is an interesting case-study into how, under some experimental conditions, diffraction effects can cause an inversion in the dominant state of polarization at the focal plane of a CVB with a vortex phase.

7.4.4 Ultrafast laser micro-machining with CVBs

In Chapter 6, radially and azimuthally polarized laser beams were used with a high fluence (24J/cm²) for micro-machining stainless steel plates. The same femtosecond laser micro-processing system was used as in Chapter 4 (producing 160fs pulses at a central wavelength of 775nm). A comparative analysis of micro-machining with radially, azimuthally, circularly and linearly polarized beams was carried out.

In a first experiment, I looked at helical drilling ~0.4mm thick stainless steel plates. In helical drilling, the ablation front is wider than the laser focal spot. The drilling results showed that a radial polarization in the focal plane produced the best machining quality, reducing the distortions affecting the edge quality of the machined structures. This is due to a relatively better absorption of the laser beam energy at the sidewalls, leading to fewer internal reflections during machining. However, it was found that the comparatively poorer channelling of the laser energy to the bottom of the hole produced a larger sidewall taper angle, with a wider entrance cross-section compared to its exit cross-section.

A second experiment looked at micro-cutting 0.2-0.4mm thick stainless steel plates. In micro-cutting, high-aspect-ratio channels are typically produced with an ablation front which is approximately of the same size as the laser focal spot. The experimental results showed that a radially polarized beam was more efficient at drilling and cutting high-aspect-ratio features when the plate thickness was ~0.3mm or ~0.4mm. The gain in processing speed was better than 5% compared with a circularly polarized beam and better than 10% compared with an azimuthally polarized beam, under the chosen processing parameters. However the processing speed was similar for all these polarization states (radial, azimuthal and circular) when machining 0.2mm thick plates. It is noted however that these results were affected by the limited polarization purity of the beam within the focal spots, as detailed in the previous section. A radially polarized beam with a higher polarization purity is expected to produce higher gains in processing speed.

Although there is an increasing interest in laser micro-processing with CVBs, there is still relatively little publication in this field. Recent experimental work suggested that the actual benefits of using CVBs for drilling or cutting are more subtle than predicted in early theoretical studies. Depending on the

work-piece material, processing parameters and aspect-ratio of the machined structures, either a radial, an azimuthal or a circular polarization is most efficient.

The experimental results described in Chapter 6 give a further insight into this field. Recent publications available in the literature described micro-drilling high-aspect-ratio holes in 0.5 to 3 mm thick steel plates, using CVBs. These publications explained that an azimuthal polarization tends to be more efficient at drilling steel plates with a thickness above 0.5mm, whereas a radial polarization tends to be more efficient at drilling 0.5mm thick steel plates. The results presented in Chapter 6 clarified the properties of machining steel plates with a thickness below 0.5mm with these polarization modes.

7.4.5 Future work

7.4.5.1 Optical aberration correction

In the experimental results presented in Chapters 4 and 6, slight optical aberrations affected the quality of laser micro-processing with CVBs. For industrial laser micro-manufacturing applications where a very high processing quality is required, these optical aberrations would have to be corrected. Some of the optical aberrations seen in the experiments were due to the laser source (beam mode, astigmatism). These aberrations could be removed by using a laser source with a higher beam quality factor.

Some optical aberrations seen in the experiments in Chapter 4 and 6 were induced by the Polarization Mode Converter. For example, the SLM used in the experiments induced residual phase distortions due to its active liquid-crystal layers, which are not optically flat. Some, but not all of these distortions were corrected using a phase correction pattern at the SLM.

Another source of optical aberration was the phase vortex induced by the SLM, which produced a phase singularity at the optical axis. The pixels of the SLM that were very close to this central phase singularity induced significant diffraction effects, because of the rapid transverse spatial phase variations associated with the singularity. These diffraction effects produced a slight divergence of the beam. It is noted that apart from inducing diffraction, the phase vortex also affected the focusing properties of the CVBs. In particular it affected the polarization purity and produced an inversion in the dominant state of polarization at the focal plane.

A potential line of future work could look at improving the optical design of the Polarization Mode Converter to remove these optical aberrations. For example, adding a second SLM to the Polarization Mode Converter could improve its optical properties. The second SLM could induce a corrective phase pattern designed to compensate for the full phase aberrations induced by the non-optically-flat liquid-crystal layers of both SLMs. Moreover, the second SLM could also be used to compensate for the residual phase vortex and produce CVBs with a planar phase. This, in turn, would allow improving the polarization purity at the focal plane. This could be achieved by superimposing a vortex phasefront with the opposite handedness (i.e. an orbital angular momentum of opposite sign) to the wavefronts of the CVBs.

Another potential area for improving the experimental setup could be to add a spatial filtering stage after the Polarization Mode Converter. This can be done by including a 4F correlator with a spatial filter (i.e. a pin hole plate) at its focal point. Such addition to the optical system of the Polarization Mode Converter could minimize the diffraction-induced divergence of the beam and produce smaller focal spots.

7.4.5.2 Industrial processing with CVBs

In a laser micro-processing setup, the focal intensity distribution (i.e. the size and shape of the focused laser spot) is of great importance as it impacts on the quality and efficiency of the process. When beams with a uniform state of polarization (i.e. linear or circular) are used for micro-processing, the focal intensity distribution is determined by the optical properties of the setup, such as the divergence of the laser beam, the NA of the focusing optics, the diffraction induced by all the optics in the beam path, etc... The state of polarization does not influence the focal intensity distribution in those cases.

As described in this thesis, CVBs have specific properties which influence the focal intensity distribution. Industrial applications that could benefit from using CVBs include the surface processing of organic thin films, for example to produce thin photovoltaic cells or displays. Another application could be the internal structuring of transparent material such as fused silica or PMMA, to produce optical waveguides for opto-fluidic devices. Using CVBs could facilitate producing steeper-gradient intensity profiles, wider depth of focus, or sub-diffraction limited focal spot size to optimize laser-material interactions and facilitate such expensive processes.

Various industries require producing high-aspect-ratio structures such as vias or channels. For example these are produced in photovoltaic wafers. CVBs could be used to optimize the coupling of the laser beam energy at various depths within the structures and for various processing geometries. By using an appropriate CVB, the intensity distribution and coupling within the depth of high-aspect-ratio machined structures could be optimized, and a higher process efficiency and quality could be achievable.

Appendix A
Derivations supporting Chapter 4

In Chapter 4, the Polarization Mode Converter was analyzed theoretically of using Jones matrices. The results of geometrical calculations involving Jones vectors were presented. For completeness, I will now present the details of these calculations.

A.1 Calculation of Jones vectors after the SLM

In the calculations detailed here, we consider a single pixel of the SLM. As detailed in Chapter 4, we first define a reference coordinate system with horizontal (x) and vertical (y) axes, centered on the optical axis of the laser beam. The location of the pixel of interest in this coordinate system is: (x_p, y_p). The direction of the incident linear polarization is set at +45˚ with respect to the horizontal axis. The Jones vector which defines this incident polarization is:

$$\boldsymbol{J}inc_{x_p y_p} = \frac{1}{\sqrt{2}}\begin{pmatrix}1\\1\end{pmatrix} \quad \text{(B.1)}$$

The pixel of interest induces a phase shift noted Φ_p. The Jones matrix of the pixel is:

$$\boldsymbol{P}_{x_p y_p} = \begin{bmatrix}1 & 0\\ 0 & \mathrm{e}^{j\Phi_p}\end{bmatrix} \quad \text{(B.2)}$$

The Jones vector representing the polarization after the SLM is noted $\boldsymbol{J}slm_{x_p y_p}$. To obtain $\boldsymbol{J}slm_{x_p y_p}$ we multiply the matrix $\boldsymbol{P}_{x_p y_p}$ by the incident Jones vector $\boldsymbol{J}inc_{x_p y_p}$:

$$\boldsymbol{J}slm_{x_p y_p} = \boldsymbol{P}_{x_p y_p} \times \boldsymbol{J}inc_{x_p y_p} = \begin{bmatrix}1 & 0\\ 0 & \mathrm{e}^{j\Phi_p}\end{bmatrix} \times \frac{1}{\sqrt{2}}\begin{pmatrix}1\\1\end{pmatrix} = \frac{1}{\sqrt{2}}\begin{pmatrix}1\\ \mathrm{e}^{j\Phi_p}\end{pmatrix} \quad \text{(B.3)}$$

If $\Phi_p = 0$, we have: $\boldsymbol{J}slm_{x_p y_p} = \frac{1}{\sqrt{2}}\begin{pmatrix}1\\ \mathrm{e}^{0}\end{pmatrix} = \frac{1}{\sqrt{2}}\begin{pmatrix}1\\1\end{pmatrix}$. In this case: $\boldsymbol{J}slm_{x_p y_p} = \boldsymbol{J}inc_{x_p y_p}$. The polarization after the SLM is still linear, oriented at +45˚.

If $\Phi_p = \pi/2$, we have: $\boldsymbol{J}slm_{x_p y_p} = \frac{1}{\sqrt{2}}\begin{pmatrix}1\\ \mathrm{e}^{j\frac{\pi}{2}}\end{pmatrix}$. In this case, the resulting polarization is circular.

A.2 Calculation of Jones vectors after the Polarization Mode Converter

As detailed in Chapter 4, the Jones matrix of the Polarization Mode Converter is contains three terms:

$$\boldsymbol{T}_{x_p y_p} = \boldsymbol{Q} \times \boldsymbol{R} \times \boldsymbol{P}_{x_p y_p} \tag{B.4}$$

$\boldsymbol{Q}$ is the Jones matrix of a quarter-waveplate:

$$\boldsymbol{Q} = \begin{bmatrix} 1 & 0 \\ 0 & \mathrm{e}^{-j\frac{\pi}{2}} \end{bmatrix} \tag{B.5}$$

$\boldsymbol{R}$ is a rotation matrix which changes the reference coordinate system:

$$\boldsymbol{R} = \frac{1}{\sqrt{2}} \begin{bmatrix} 1 & -1 \\ 1 & 1 \end{bmatrix} \tag{B.6}$$

The Jones vector representing the polarization after the Polarization Mode Converter is noted $\boldsymbol{J}pmc_{x_p y_p}$. It is obtained by multiplying the matrix $\boldsymbol{T}_{x_p y_p}$ by the incident Jones vector $\boldsymbol{J}inc_{x_p y_p}$:

$$\boldsymbol{J}pmc_{x_p y_p} = \boldsymbol{T}_{x_p y_p} \times \boldsymbol{J}inc_{x_p y_p} = \begin{bmatrix} 1 & 0 \\ 0 & \mathrm{e}^{-j\frac{\pi}{2}} \end{bmatrix} \times \frac{1}{\sqrt{2}} \begin{bmatrix} 1 & -1 \\ 1 & 1 \end{bmatrix} \times \begin{bmatrix} 1 & 0 \\ 0 & \mathrm{e}^{j\Phi_p} \end{bmatrix} \times \frac{1}{\sqrt{2}} \binom{1}{1} \tag{B.7}$$

To obtain $\boldsymbol{J}pmc_{x_p y_p}$ we first multiply the first two terms on the right hand side in Equation (B.7):

$$\begin{bmatrix} 1 & 0 \\ 0 & \mathrm{e}^{j\Phi_p} \end{bmatrix} \times \frac{1}{\sqrt{2}} \binom{1}{1} = \frac{1}{\sqrt{2}} \binom{1}{\mathrm{e}^{j\Phi_p}} \tag{B.8}$$

We then multiply this result with the third term in Equation (B.7):

$$\frac{1}{\sqrt{2}} \begin{bmatrix} 1 & -1 \\ 1 & 1 \end{bmatrix} \times \frac{1}{\sqrt{2}} \binom{1}{\mathrm{e}^{j\Phi_p}} = \frac{1}{2} \binom{1-\mathrm{e}^{j\Phi_p}}{1+\mathrm{e}^{j\Phi_p}} \tag{B.9}$$

We now need to express the result of Equation (B.9) in polar coordinates (see Figure A.1):

$$\frac{1}{2} \binom{1-\mathrm{e}^{j\Phi_p}}{1+\mathrm{e}^{j\Phi_p}} = \frac{1}{2} \begin{pmatrix} 2.\sin\left(\frac{\Phi_p}{2}\right).e^{j\frac{\Phi_p - \pi}{2}} \\ 2.\cos\left(\frac{\Phi_p}{2}\right).e^{j\frac{\Phi_p}{2}} \end{pmatrix} = \begin{pmatrix} \sin\left(\frac{\Phi_p}{2}\right).e^{j\frac{\Phi_p - \pi}{2}} \\ \cos\left(\frac{\Phi_p}{2}\right).e^{j\frac{\Phi_p}{2}} \end{pmatrix} \tag{B.10}$$

We then multiply this result with the fourth term in Equation (B.7):

$$\begin{bmatrix} 1 & 0 \\ 0 & \mathrm{e}^{-j\frac{\pi}{2}} \end{bmatrix} \times \begin{pmatrix} \sin\left(\frac{\Phi_p}{2}\right).e^{j\frac{\Phi_p - \pi}{2}} \\ \cos\left(\frac{\Phi_p}{2}\right).e^{j\frac{\Phi_p}{2}} \end{pmatrix} = \begin{pmatrix} \sin\left(\frac{\Phi_p}{2}\right).e^{j\frac{\Phi_p - \pi}{2}} \\ \cos\left(\frac{\Phi_p}{2}\right).e^{j\frac{\Phi_p}{2}}.e^{-j\frac{\pi}{2}} \end{pmatrix} = \begin{pmatrix} \sin\left(\frac{\Phi_p}{2}\right).e^{j\frac{\Phi_p - \pi}{2}} \\ \cos\left(\frac{\Phi_p}{2}\right).e^{j\frac{\Phi_p - \pi}{2}} \end{pmatrix} = e^{j\frac{\Phi_p - \pi}{2}} \times \begin{pmatrix} \sin\frac{\Phi_p}{2} \\ \cos\frac{\Phi_p}{2} \end{pmatrix} \tag{B.11}$$

We can now express $\boldsymbol{J}pmc_{x_p y_p}$ as:

$$\boldsymbol{J}pmc_{x_p y_p} = e^{j\frac{\Phi_p - \pi}{2}} \times \begin{pmatrix} \sin\frac{\Phi_p}{2} \\ \cos\frac{\Phi_p}{2} \end{pmatrix} = e^{-j\frac{\pi}{2}} \times e^{j\frac{\Phi_p}{2}} \times \begin{pmatrix} \sin\frac{\Phi_p}{2} \\ \cos\frac{\Phi_p}{2} \end{pmatrix} \quad \text{(B.12)}$$

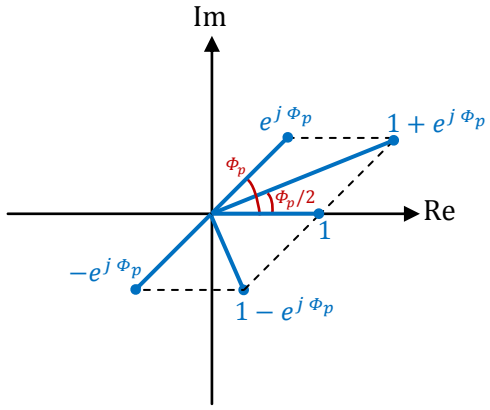

Figure A.1: Complex Plane showing how the Jones vector in Equation (B.10) is converted into polar coordinates.

Appendix B
Geometrical derivations supporting Chapter 5

The model proposed in Chapter 5 describes a CVB using eight polarization vectors equally spread around the beam profile. In Chapter 5, the results of various geometrical calculations involving these vectors were used to study the state of polarization at the focal plane of the optical setup. The details of these geometrical calculations were not described in Chapter 5. For completeness, I will now further look at these calculations, explaining how the results used in Chapter 5 were obtained. I first explain the calculation of the phase tilt factor related to each of the eight polarization vectors when focusing a tilted phase front. Then, I explain the calculation of the complex coordinates for each of the eight Jones vectors. I will also explain how I derive the vector sums geometrically in the Complex Plane in various cases of interest.

As a convention, in this appendix I use the following notations:

- $\vec{E}_i$ is one of the eight electric field (polarization) vectors used in the model to represent the incident CVBs.
- $\boldsymbol{E_i}$ is the origin point where the vector $\vec{E}_i$ applies.
- $\bar{V}$ is a geometrical distance, with either a positive or a negative value. It is either named after a letter (for example $\bar{D}$) or defined by two points (for example $\overline{\boldsymbol{E_2E_6}}$).
- $(\boldsymbol{E_iE_j})$ is a straight line that contains Point $\boldsymbol{E_i}$ and Point $\boldsymbol{E_j}$.

B.1 Calculation of the phase tilt factors in the case of a beam that focuses at Point A

As shown in Figure B.1, each vector $\vec{E}_i$ originates at a corresponding point $\boldsymbol{E_i}$ in the plane that contains the active surface of the SLM. For convenience, this plane is referred to as Horizontal Plane henceforth. As detailed in Section 5.3, we also define an Origin Plane that contains Points $\boldsymbol{E_0}$, $\boldsymbol{E_4}$ and $\boldsymbol{E_4}'$ and is parallel to the tilted phase front that focuses at Point ***A*** (see Figure B.1). Here we are interested in the distance between each point $\boldsymbol{E_i}$ and its orthogonal projection in the Origin Plane. Once this distance is known, the corresponding phase tilt factor φ_{2i} that applies to each vector $\vec{E}_i$ can be derived.

For convenience, we define $\bar{D}$ as the diameter of the beam and $\boldsymbol{E_4}'$ as the center of the beam. Therefore $\overline{\boldsymbol{E_2E_6}} = \bar{D}$ and $\overline{\boldsymbol{E_4}'\boldsymbol{E_2}} = \overline{\boldsymbol{E_4}'\boldsymbol{E_3}} = \overline{\boldsymbol{E_4}'\boldsymbol{E_5}} = \overline{\boldsymbol{E_4}'\boldsymbol{E_6}} = \frac{\bar{D}}{2}$ (see Figure B.1).

We also define Points $\boldsymbol{E_3}'$, $\boldsymbol{E_4}'$ and $\boldsymbol{E_5}'$ as the orthogonal projections on $(\boldsymbol{E_2E_6})$ of Points $\boldsymbol{E_3}$, $\boldsymbol{E_4}$ and $\boldsymbol{E_5}$ respectively. Therefore, we have:

$$\overline{\boldsymbol{E_4}'\boldsymbol{E_3}'} = \frac{\bar{D}}{2}\cos\left(\frac{\pi}{4}\right) = \frac{\sqrt{2}}{4}\bar{D} \quad \text{(B.1)}$$

Thanks to the symmetry of the problem, we have: $\overline{E_4{}'E_3{}'} = \overline{E_4{}'E_5{}'}$, therefore we also have:

$$\overline{E_4{}'E_5{}'} = \frac{\sqrt{2}}{4}\overline{D} \tag{B.2}$$

We define Points $E_2{}''$, E_3'', $E_5{}''$ and $E_6{}''$ as the orthogonal projections on the Origin Plane of Points E_2, $E_3{}'$,$E_5{}'$ and E_6 respectively. We now apply Thales's theorem:

$$\frac{\overline{E_4{}'E_3{}'}}{\overline{E_4{}'E_2}} = \frac{\overline{E_3{}'E_3{}''}}{\overline{E_2E_2{}''}} \tag{B.3}$$

We can re-write Equation (B.3) as:

$$\overline{E_3{}'E_3{}''} = \frac{\overline{E_4{}'E_3{}'} \cdot \overline{E_2{}'E_2{}''}}{\overline{E_4{}'E_2}} \tag{B.4}$$

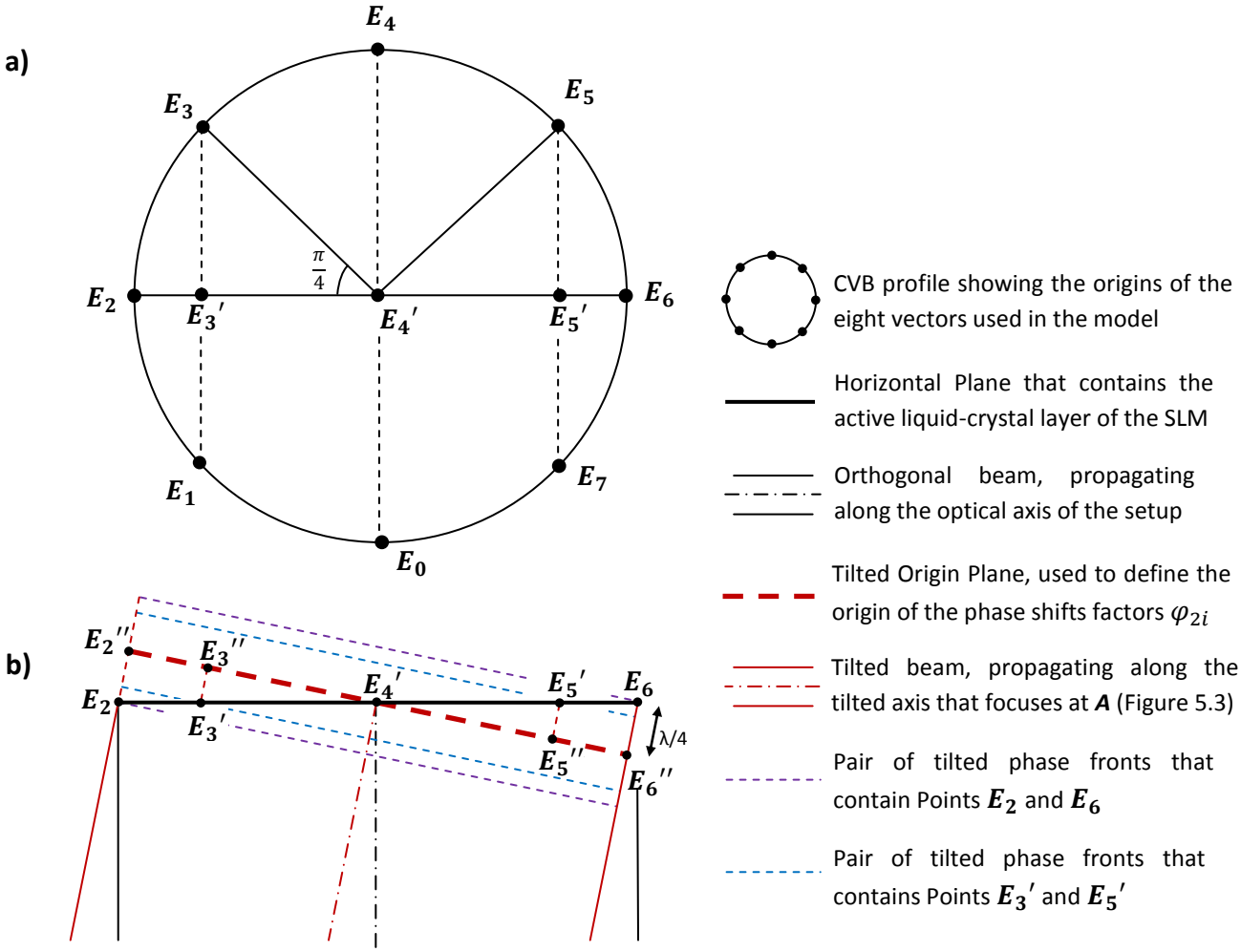

Figure B.1: Schematics showing how the CVB is represented in the model. **(a)** Front view showing the CVB profile at the Horizontal Plane (i.e. the plane that contains the active liquid-crystal layer of the SLM). Each point E_i is the origin of the corresponding vector $\vec{E}_i$ and is contained within the Horizontal Plane. **(b)** Side view showing the Horizontal Plane and the tilted Origin Plane. A phase front parallel to the Horizontal Plane focuses at Point ***O*** (see Figure 5.3). The eight vectors $\vec{E}_i$ that define this phase front do not include any phase tilt factorφ_{2i}. A phase front parallel to the tilted Origin Plane focuses at Point ***A***. Each of the eight vectors $\vec{E}_i$ that define this tilted phase front includes a phase tilt factor φ_{2i} that represents the distance between its origin Point E_i and the Origin Plane.

As explained in Section 5.3, the tilted phase front is defined so that $\overline{\boldsymbol{E_2E_2''}} = \overline{\boldsymbol{E_6E_6''}} = \frac{\lambda}{4}$

We can now replace each term in Equation B.4 with its value:

$$\overline{\boldsymbol{E_3'E_3''}} = \frac{\frac{\sqrt{2}}{4}\bar{D}.\frac{\lambda}{4}}{\frac{\bar{D}}{2}} = \frac{\sqrt{2}}{8}\lambda \quad \text{(B.5)}$$

Thanks to the symmetry of the problem, we also have:

$$\overline{\boldsymbol{E_5'E_5''}} = \overline{\boldsymbol{E_3'E_3''}} = \frac{\sqrt{2}}{8}\lambda \quad \text{(B.6)}$$

We are interested in the distance between each point $\boldsymbol{E_i}$ and its orthogonal projection in the Origin Plane. We define this distance as positive when the orthogonal projection falls above the Horizontal Plane. We define it as negative when it falls below the Horizontal Plane (see Figure B.1). We use the results above tor express each distance. We also derive the corresponding phase shifts φ_{2i} by multiplying each distance by a factor $\frac{2\pi}{\lambda}$. Table B.1 summarizes the results.

Table B.1: Optical path difference and corresponding phase term φ_{2i} induced by the phase front tilt, derived for each vector $\vec{E}_i$ that focus at Point ***A***.

Points $\boldsymbol{E_i}$ (all these points are contained within the Horizontal Plane)	Geometrical expression of the distance between Point $\boldsymbol{E_i}$ and its orthogonal projection in the Origin Plane	Distance between Point $\boldsymbol{E_i}$ and its orthogonal projection in the Origin Plane	Resulting phase tilt factor: φ_{2i}
$\boldsymbol{E_0}$	0	0	0
$\boldsymbol{E_1}$	$\overline{\boldsymbol{E_3'E_3''}}$	$\frac{\sqrt{2}}{8}.\lambda$	$\frac{\sqrt{2}}{4}.\pi$
$\boldsymbol{E_2}$	$\overline{\boldsymbol{E_2E_2''}}$	$\frac{1}{4}.\lambda$	$\frac{1}{2}.\pi$
$\boldsymbol{E_3}$	$\overline{\boldsymbol{E_3'E_3''}}$	$\frac{\sqrt{2}}{8}.\lambda$	$\frac{\sqrt{2}}{4}.\pi$
$\boldsymbol{E_4}$	0	0	0
$\boldsymbol{E_5}$	$\overline{\boldsymbol{E_5'E_5''}}$	$-\frac{\sqrt{2}}{8}.\lambda$	$-\frac{\sqrt{2}}{4}.\pi$
$\boldsymbol{E_6}$	$\overline{\boldsymbol{E_6E_6''}}$	$-\frac{1}{4}.\lambda$	$-\frac{1}{2}.\pi$
$\boldsymbol{E_7}$	$\overline{\boldsymbol{E_5'E_5''}}$	$-\frac{\sqrt{2}}{8}.\lambda$	$-\frac{\sqrt{2}}{4}.\pi$

B.2 Calculation of the complex coordinates of each Jones vector

I now explain the calculation of the complex coordinates of the Jones vectors $\vec{E}_i$ under the various experimental conditions that are relevant to the model.

B.2.1 Radially polarized beam with a planar phase, focusing at Point *O*

In this case, all the phase terms φ_i are equal to zero, since there is no phase vortex or phase tilt. This means the complex coordinates of all the Jones vectors $\vec{E}_i$ are real number (i.e. the argument φ of each complex value $r.e^{j\varphi}$ is zero, therefore $r.e^{j\varphi} = r$). Each complex coordinate is derived by projecting the vectors $\vec{E}_i$ on $\vec{\boldsymbol{X}}$ and $\vec{\boldsymbol{Y}}$. For convenience, we define the amplitude for each vector $\vec{E}_i$ as: $\left\|\vec{E}_i\right\| = 1$.

As an example we derive the complex coordinates of $\vec{E}_1$ by projecting it on $\vec{\boldsymbol{X}}$ and $\vec{\boldsymbol{Y}}$ (see Figure B.2):

$$E_{1X} = \cos\left(\frac{\pi}{4}\right).e^{j(0)} = \frac{1}{\sqrt{2}} \tag{B.7}$$

$$E_{1Y} = \sin\left(\frac{\pi}{4}\right).e^{j(0)} = \frac{1}{\sqrt{2}} \tag{B.8}$$

The complex coordinates of all the other vectors are derived in the same way. The results are summarized in Table B.2 for the X coordinates and in Table B.3 for the Y coordinates.

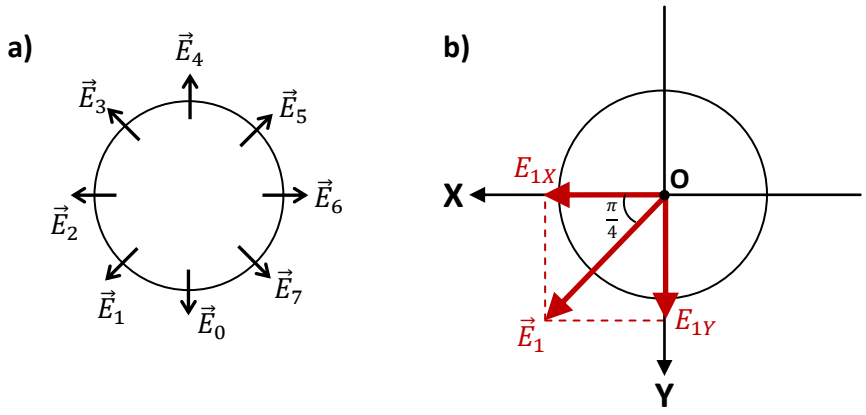

Figure B.2: (a) Schematics showing the beam profile with the eight vectors $\vec{E}_i$ and **(b)** the projection of $\vec{E}_1$ on $\vec{\boldsymbol{X}}$ and $\vec{\boldsymbol{Y}}$.

Table B.2: Case of a radially polarized beam with planar phase, focusing at Point ***O***: X components.

Vectors $\vec{E}_i$ (all these vectors focus at Point ***O***)	Amplitude term, related to the projection of $\vec{E}_i$ to X axis	Phase term, related to the topological charge (i.e. vortex structure) of the CVB	Phase term, related to the phase front tilt	Resulting complex amplitude $\boldsymbol{E_{iX}}$ $\boldsymbol{E_{iX}} = r_{iX}.e^{j(\varphi_i)}$
	r_{iX}	φ_{1i}	φ_{2i}	$\boldsymbol{E_{iX}} = r_{iX}.e^{j(\varphi_{1i}+\varphi_{2i})}$
$\vec{E}_0$	0	0	0	$0.e^{j\,(0)} = 0$
$\vec{E}_1$	$\frac{1}{\sqrt{2}}$	0	0	$\frac{1}{\sqrt{2}}.e^{j\,(0)} = \frac{1}{\sqrt{2}}$
$\vec{E}_2$	1	0	0	$1.e^{j\,(0)} = 1$
$\vec{E}_3$	$\frac{1}{\sqrt{2}}$	0	0	$\frac{1}{\sqrt{2}}.e^{j\,(0)} = \frac{1}{\sqrt{2}}$
$\vec{E}_4$	0	0	0	$0.e^{j\,(0)} = 0$
$\vec{E}_5$	$-\frac{1}{\sqrt{2}}$	0	0	$-\frac{1}{\sqrt{2}}.e^{j\,(0)} = -\frac{1}{\sqrt{2}}$
$\vec{E}_6$	-1	0	0	$-1.e^{j\,(0)} = -1$
$\vec{E}_7$	$-\frac{1}{\sqrt{2}}$	0	0	$-\frac{1}{\sqrt{2}}.e^{j\,(0)} = -\frac{1}{\sqrt{2}}$

Table B.3: Case of a radially polarized beam with planar phase, focusing at Point ***O***: Y components.

Vectors $\vec{E}_i$ (all these vectors focus at Point ***O***)	Amplitude term, related to the projection of $\vec{E}_i$ to Y axis	Phase term, related to the topological charge (i.e. vortex structure) of the CVB	Phase term, related to the phase front tilt	Resulting complex amplitude E_{iY} $E_{iY} = r_{iY}.e^{j(\varphi_i)}$
	r_{iY}	φ_{1i}	φ_{2i}	$E_{iY} = r_{iY}.e^{j(\varphi_{1i}+\varphi_{2i})}$
$\vec{E}_0$	1	0	0	$1.e^{j\,(0)} = 1$
$\vec{E}_1$	$\frac{1}{\sqrt{2}}$	0	0	$\frac{1}{\sqrt{2}}.e^{j\,(0)} = \frac{1}{\sqrt{2}}$
$\vec{E}_2$	0	0	0	$0.e^{j\,(0)} = 0$
$\vec{E}_3$	$-\frac{1}{\sqrt{2}}$	0	0	$-\frac{1}{\sqrt{2}}.e^{j\,(0)} = -\frac{1}{\sqrt{2}}$
$\vec{E}_4$	-1	0	0	$-1.e^{j\,(0)} = -1$
$\vec{E}_5$	$-\frac{1}{\sqrt{2}}$	0	0	$-\frac{1}{\sqrt{2}}.e^{j\,(0)} = -\frac{1}{\sqrt{2}}$
$\vec{E}_6$	0	0	0	$0.e^{j\,(0)} = 0$
$\vec{E}_7$	$\frac{1}{\sqrt{2}}$	0	0	$\frac{1}{\sqrt{2}}.e^{j\,(0)} = \frac{1}{\sqrt{2}}$

B.2.2 Radially polarized beam with a planar phase, focusing at Point *A*

In this case, each vector $\vec{E}_i$ has a phase terms φ_i that includes a phase tilt factor φ_{2i} as defined in Table B.1. For example $\vec{E}_0$ has a phase term $\varphi_{20} = 0$, $\vec{E}_1$ has a phase term $\varphi_{21} = \frac{\sqrt{2}.\pi}{4}$, $\vec{E}_2$ has a phase term $\varphi_{22} = \frac{\pi}{2}$ and so on.

The complex coordinates are derived by projecting each vector $\vec{E}_i$ on $\vec{\boldsymbol{X}}$ and $\vec{\boldsymbol{Y}}$ and including the appropriate phase factor in the argument. As before, we derive the complex coordinates of vector $\vec{E}_1$ by projecting it on $\vec{\boldsymbol{X}}$ and $\vec{\boldsymbol{Y}}$ and including the phase factor:

$$E_{1X} = \cos\left(\frac{\pi}{4}\right).e^{j\frac{\sqrt{2}.\pi}{4}} = \frac{1}{\sqrt{2}}e^{j\frac{\sqrt{2}.\pi}{4}} \quad \text{(B.9)}$$

$$E_{1Y} = \sin\left(\frac{\pi}{4}\right).e^{j\frac{\sqrt{2}.\pi}{4}} = \frac{1}{\sqrt{2}}e^{j\frac{\sqrt{2}.\pi}{4}} \quad \text{(B.10)}$$

The complex coordinates of all the other vectors are derived in the same way. The results are summarized in Table B.4 for the X coordinates and in Table B.5 for the Y coordinates.

Table B.4: Case of a radially polarized beam with planar phase, focusing at Point ***A***: X components.

Vectors $\vec{E}_i$ (all these vectors focus at Point ***A***)	Amplitude term, related to the projection of $\vec{E}_i$ to X axis	Phase term, related to the topological charge (i.e. vortex structure) of the CVB	Phase term, related to the phase front tilt	Resulting complex amplitude E_{iX} $E_{iX} = r_{iX}.e^{j(\varphi_i)}$
	r_{iX}	φ_{1i}	φ_{2i}	$E_{iX} = r_{iX}.e^{j(\varphi_{1i}+\varphi_{2i})}$
$\vec{E}_0$	0	0	0	$0.e^{j\,(0)} = 0$
$\vec{E}_1$	$\frac{1}{\sqrt{2}}$	0	$\frac{\sqrt{2}}{4}.\pi$	$\frac{1}{\sqrt{2}}.e^{j\,(0+\frac{\sqrt{2}}{4}.\pi)} = \frac{1}{\sqrt{2}}.e^{j\frac{\sqrt{2}}{4}.\pi}$
$\vec{E}_2$	1	0	$\frac{1}{2}.\pi$	$1.e^{j\,(0+\frac{\pi}{2})} = e^{j\frac{\pi}{2}}$
$\vec{E}_3$	$\frac{1}{\sqrt{2}}$	0	$\frac{\sqrt{2}}{4}.\pi$	$\frac{1}{\sqrt{2}}.e^{j\,(0+\frac{\sqrt{2}}{4}.\pi)} = \frac{1}{\sqrt{2}}.e^{j\frac{\sqrt{2}}{4}.\pi}$
$\vec{E}_4$	0	0	0	$0.e^{j\,(0)} = 0$
$\vec{E}_5$	$-\frac{1}{\sqrt{2}}$	0	$-\frac{\sqrt{2}}{4}.\pi$	$-\frac{1}{\sqrt{2}}.e^{j\,(0-\frac{\sqrt{2}}{4}.\pi)} = -\frac{1}{\sqrt{2}}e^{j\,(-\frac{\sqrt{2}}{4}.\pi)}$
$\vec{E}_6$	-1	0	$-\frac{1}{2}.\pi$	$-1.e^{j\,(0-\frac{\pi}{2})} = -e^{j\,(-\frac{\pi}{2})}$
$\vec{E}_7$	$-\frac{1}{\sqrt{2}}$	0	$-\frac{\sqrt{2}}{4}.\pi$	$-\frac{1}{\sqrt{2}}.e^{j\,(0-\frac{\sqrt{2}}{4}.\pi)} = -\frac{1}{\sqrt{2}}.e^{j\,(-\frac{\sqrt{2}}{4}.\pi)}$

Table B.5: Case of a radially polarized beam with planar phase, focusing at Point ***A***: Y components.

Vectors $\vec{E}_i$ (all these vectors focus at Point ***A***)	Amplitude term, related to the projection of $\vec{E}_i$ to Y axis	Phase term, related to the topological charge (i.e. vortex structure) of the CVB	Phase term, related to the phase front tilt	Resulting complex amplitude E_{iY} $E_{iY} = r_{iY}.e^{j(\varphi_i)}$
	r_{iY}	φ_{1i}	φ_{2i}	$E_{iY} = r_{iY}.e^{j(\varphi_{1i}+\varphi_{2i})}$
$\vec{E}_0$	1	0	0	$1.e^{j\,(0)} = 1$
$\vec{E}_1$	$\frac{1}{\sqrt{2}}$	0	$\frac{\sqrt{2}}{4}.\pi$	$\frac{1}{\sqrt{2}}.e^{j\,(0+\frac{\sqrt{2}\pi}{4})} = \frac{1}{\sqrt{2}}.e^{j\frac{\sqrt{2}\pi}{4}}$
$\vec{E}_2$	0	0	$\frac{1}{2}.\pi$	$0.e^{j\,(0+\frac{\pi}{2})} = 0$
$\vec{E}_3$	$-\frac{1}{\sqrt{2}}$	0	$\frac{\sqrt{2}}{4}.\pi$	$-\frac{1}{\sqrt{2}}.e^{j\,(0+\frac{\sqrt{2}\pi}{4})} = -\frac{1}{\sqrt{2}}.e^{j\frac{\sqrt{2}\pi}{4}}$
$\vec{E}_4$	-1	0	0	$-1.e^{j\,(0)} = -1$
$\vec{E}_5$	$-\frac{1}{\sqrt{2}}$	0	$-\frac{\sqrt{2}}{4}.\pi$	$-\frac{1}{\sqrt{2}}.e^{j\,(0-\frac{\sqrt{2}\pi}{4})} = -\frac{1}{\sqrt{2}}e^{j\,(-\frac{\sqrt{2}\pi}{4})}$
$\vec{E}_6$	0	0	$-\frac{1}{2}.\pi$	$0.e^{j\,(0-\frac{\pi}{2})} = 0$
$\vec{E}_7$	$\frac{1}{\sqrt{2}}$	0	$-\frac{\sqrt{2}}{4}.\pi$	$\frac{1}{\sqrt{2}}.e^{j\,(0-\frac{\sqrt{2}\pi}{4})} = \frac{1}{\sqrt{2}}.e^{j\,(-\frac{\sqrt{2}\pi}{4})}$

B.2.3 Radially polarized beam with a vortex phase, focusing at Point O

In this case, each vector $\vec{E}_i$ has a phase terms φ_i that includes a vortex factor defined as: $\varphi_{1i} = i \times \frac{\pi}{4}$. Table B.6 summarizes these phase terms.

For example $\vec{E}_0$ has a vortex phase term $\varphi_{10} = 0$, $\vec{E}_1$ has a vortex phase term $\varphi_{11} = \frac{\pi}{4}$, $\vec{E}_2$ has a phase term $\varphi_{12} = \frac{\pi}{2}$ and so on. As before, the complex coordinates are derived by projecting each vector $\vec{E}_i$ on $\vec{X}$ and $\vec{Y}$ and including the appropriate phase factor in the argument. As an example we derive the complex coordinates of vector $\vec{E}_1$ by projecting it on $\vec{X}$ and $\vec{Y}$ and including the vortex phase factor in the argument:

$$E_{1X} = \cos\left(\frac{\pi}{4}\right).e^{j\frac{\pi}{4}} = \frac{1}{\sqrt{2}}e^{j\frac{\pi}{4}} \quad \text{(B.11)}$$

$$E_{1Y} = \sin\left(\frac{\pi}{4}\right).e^{j\frac{\pi}{4}} = \frac{1}{\sqrt{2}}e^{j\frac{\pi}{4}} \quad \text{(B.12)}$$

The coordinates of all the other vectors are derived in the same way. The results are summarized in Table B.7 for the X coordinates and in Table B.8 for the Y coordinates.

Table B.6: Phase terms induced by the vortex phase structure of the beam.

Vectors $\vec{E}_i$	Vortex phase $\varphi_{1i} = i \times \frac{\pi}{4}$
$\vec{E}_0$	0
$\vec{E}_1$	$\frac{\pi}{4}$
$\vec{E}_2$	$\frac{\pi}{2}$
$\vec{E}_3$	$\frac{3\pi}{4}$
$\vec{E}_4$	π
$\vec{E}_5$	$\frac{5\pi}{4}$
$\vec{E}_6$	$\frac{3\pi}{2}$
$\vec{E}_7$	$\frac{7\pi}{4}$

Table B.7: Case of a radially polarized beam with a 2π vortex phase, focusing at Point ***O***: X components.

Vectors $\vec{E}_i$ (all these vectors focus at Point ***O***)	Amplitude term, related to the projection of $\vec{E}_i$ to X axis	Phase term, related to the topological charge (i.e. vortex structure) of the CVB	Phase term, related to the phase front tilt	Resulting complex amplitude E_{iX} $E_{iX} = r_{iX}.e^{j(\varphi_i)}$
	r_{iX}	φ_{1i}	φ_{2i}	$E_{iX} = r_{iX}.e^{j(\varphi_{1i}+\varphi_{2i})}$
$\vec{E}_0$	0	0	0	$0.e^{j\,(0)} = 0$
$\vec{E}_1$	$\frac{1}{\sqrt{2}}$	$\frac{1}{4}.\pi$	0	$\frac{1}{\sqrt{2}}.e^{j\,(\frac{\pi}{4}+0)} = \frac{1}{\sqrt{2}}.e^{j\frac{\pi}{4}}$
$\vec{E}_2$	1	$\frac{1}{2}.\pi$	0	$1.e^{j\,(\frac{\pi}{2}+0)} = e^{j\frac{\pi}{2}}$
$\vec{E}_3$	$\frac{1}{\sqrt{2}}$	$\frac{3}{4}.\pi$	0	$\frac{1}{\sqrt{2}}.e^{j\,(\frac{3\pi}{4}+0)} = \frac{1}{\sqrt{2}}.e^{j\frac{3\pi}{4}}$
$\vec{E}_4$	0	π	0	$0.e^{j\,(\pi+0)} = 0$
$\vec{E}_5$	$-\frac{1}{\sqrt{2}}$	$\frac{5}{4}.\pi$	0	$-\frac{1}{\sqrt{2}}.e^{j\,(\frac{5\pi}{4}+0)} = -\frac{1}{\sqrt{2}}e^{j\frac{5\pi}{4}}$
$\vec{E}_6$	-1	$\frac{3}{2}.\pi$	0	$-1.e^{j\,(\frac{3\pi}{2}+0)} = -e^{j\frac{3\pi}{2}}$
$\vec{E}_7$	$-\frac{1}{\sqrt{2}}$	$\frac{7}{4}.\pi$	0	$-\frac{1}{\sqrt{2}}.e^{j\,(\frac{7\pi}{4}+0)} = -\frac{1}{\sqrt{2}}e^{j\frac{7\pi}{4}}$

Table B.8: Case of a radially polarized beam with a 2π vortex phase, focusing at Point ***O***: Y components.

Vectors $\vec{E}_i$ (all these vectors focus at Point ***O***)	Amplitude term, related to the projection of $\vec{E}_i$ to Y axis	Phase term, related to the topological charge (i.e. vortex structure) of the CVB	Phase term, related to the phase front tilt	Resulting complex amplitude E_{iY} $E_{iY} = r_{iY}.e^{j(\varphi_i)}$
	r_{iY}	φ_{1i}	φ_{2i}	$E_{iY} = r_{iY}.e^{j(\varphi_{1i}+\varphi_{2i})}$
$\vec{E}_0$	1	0	0	$1.e^{j\,(0)} = 1$
$\vec{E}_1$	$\frac{1}{\sqrt{2}}$	$\frac{1}{4}.\pi$	0	$\frac{1}{\sqrt{2}}.e^{j\,(\frac{\pi}{4}+0)} = \frac{1}{\sqrt{2}}.e^{j\frac{\pi}{4}}$
$\vec{E}_2$	0	$\frac{1}{2}.\pi$	0	$0.e^{j\,(\frac{\pi}{2}+0)} = 0$
$\vec{E}_3$	$-\frac{1}{\sqrt{2}}$	$\frac{3}{4}.\pi$	0	$-\frac{1}{\sqrt{2}}.e^{j\,(\frac{3\pi}{4}+0)} = -\frac{1}{\sqrt{2}}.e^{j\frac{3\pi}{4}}$
$\vec{E}_4$	-1	π	0	$-1.e^{j\,(\pi+0)} = 1$
$\vec{E}_5$	$-\frac{1}{\sqrt{2}}$	$\frac{5}{4}.\pi$	0	$-\frac{1}{\sqrt{2}}.e^{j\,(\frac{5\pi}{4}+0)} = -\frac{1}{\sqrt{2}}.e^{j\frac{5\pi}{4}}$
$\vec{E}_6$	0	$\frac{3}{2}.\pi$	0	$0.e^{j\,(\frac{3\pi}{2}+0)} = 0$
$\vec{E}_7$	$\frac{1}{\sqrt{2}}$	$\frac{7}{4}.\pi$	0	$\frac{1}{\sqrt{2}}.e^{j\,(\frac{7\pi}{4}+0)} = \frac{1}{\sqrt{2}}e^{j\frac{7\pi}{4}}$

B.2.4 Radially polarized beam with a vortex phase, focusing at Point *A*

In this case, each vector $\vec{E}_i$ has a phase terms φ_i that includes a phase tilt factor φ_{2i} as defined in Table B.1, and a phase vortex factor φ_{1i} as defined in Table B.6. Therefore, each term φ_i is derived by adding both phase factors: $\varphi_i = \varphi_{1i} + \varphi_{2i}$. For example $\vec{E}_0$ has a phase term $\varphi_0 = 0$, since both phase factors are nil. $\vec{E}_1$ has a phase term $\varphi_1 = \varphi_{11} + \varphi_{21} = \frac{\pi}{4} + \frac{\sqrt{2}.\pi}{4}$, $\vec{E}_2$ has a phase term $\varphi_2 = \varphi_{12} + \varphi_{22} = \frac{\pi}{2} + \frac{\pi}{2}$ and so on.

As before, the complex coordinates are derived by projecting each vector $\vec{E}_i$ on $\vec{X}$ and $\vec{Y}$ and including the phase factors in the argument. As an example, we derive here the complex coordinates of vector $\vec{E}_1$ by projecting it on $\vec{X}$ and $\vec{Y}$ and adding the appropriate phase factors in the arguments:

$$E_{1X} = \cos\left(\frac{\pi}{4}\right).e^{j(\frac{\sqrt{2}.\pi}{4}+\frac{\pi}{4})} = \frac{1}{\sqrt{2}}e^{j\frac{1+\sqrt{2}}{4}\pi} \quad \text{(B.13)}$$

$$E_{1Y} = \sin\left(\frac{\pi}{4}\right).e^{j(\frac{\sqrt{2}.\pi}{4}+\frac{\pi}{4})} = \frac{1}{\sqrt{2}}e^{j\frac{1+\sqrt{2}}{4}\pi} \quad \text{(B.14)}$$

The complex coordinates of all the other vectors are derived in the same way. The results are summarized in Table B.9 for the X coordinates and in Table B.10 for the Y coordinates.

Table B.9: Case of a radially polarized beam with a 2π vortex phase, focusing at Point ***A***: X components.

Vectors $\vec{E}_i$ (all these vectors focus at Point ***A***)	Amplitude term, related to the projection of $\vec{E}_i$ to X axis	Phase term, related to the topological charge (i.e. vortex structure) of the CVB	Phase term, related to the phase front tilt	Resulting complex amplitude E_{iX} $E_{iX} = r_{iX}.e^{j(\varphi_i)}$
	r_{iX}	φ_{1i}	φ_{2i}	$E_{iX} = r_{iX}.e^{j(\varphi_{1i}+\varphi_{2i})}$
$\vec{E}_0$	0	0	0	$0.e^{j(0)} = 0$
$\vec{E}_1$	$\frac{1}{\sqrt{2}}$	$\frac{1}{4}.\pi$	$\frac{\sqrt{2}}{4}.\pi$	$\frac{1}{\sqrt{2}}.e^{j(\frac{\pi}{4}+\frac{\sqrt{2}\pi}{4})} = \frac{1}{\sqrt{2}}.e^{j\frac{1+\sqrt{2}}{4}.\pi}$
$\vec{E}_2$	1	$\frac{1}{2}.\pi$	$\frac{1}{2}.\pi$	$1.e^{j(\frac{\pi}{2}+\frac{\pi}{2})} = e^{j\pi} = -1$
$\vec{E}_3$	$\frac{1}{\sqrt{2}}$	$\frac{3}{4}.\pi$	$\frac{\sqrt{2}}{4}.\pi$	$\frac{1}{\sqrt{2}}.e^{j(\frac{3\pi}{4}+\frac{\sqrt{2}\pi}{4})} = \frac{1}{\sqrt{2}}.e^{j\frac{3+\sqrt{2}}{4}.\pi}$
$\vec{E}_4$	0	π	0	$0.e^{j(\pi+0)} = 0$
$\vec{E}_5$	$-\frac{1}{\sqrt{2}}$	$\frac{5}{4}.\pi$	$-\frac{\sqrt{2}}{4}.\pi$	$-\frac{1}{\sqrt{2}}.e^{j(\frac{5\pi}{4}-\frac{\sqrt{2}\pi}{4})} = -\frac{1}{\sqrt{2}}e^{j\frac{5-\sqrt{2}}{4}.\pi}$
$\vec{E}_6$	-1	$\frac{3}{2}.\pi$	$-\frac{1}{2}.\pi$	$-1.e^{j(\frac{3\pi}{2}-\frac{\pi}{2})} = -e^{j\pi} = 1$
$\vec{E}_7$	$-\frac{1}{\sqrt{2}}$	$\frac{7}{4}.\pi$	$-\frac{\sqrt{2}}{4}.\pi$	$-\frac{1}{\sqrt{2}}.e^{j(\frac{7\pi}{4}-\frac{\sqrt{2}\pi}{4})} = -\frac{1}{\sqrt{2}}.e^{j\frac{7-\sqrt{2}}{4}.\pi}$

Table B.10: Case of a radially polarized beam with a 2π vortex phase, focusing at Point ***A***: Y components.

Vectors $\vec{E}_i$ (all these vectors focus at Point ***A***)	Amplitude term, related to the projection of $\vec{E}_i$ to the Y axis	Phase term, related to the topological charge (i.e. vortex structure) of the CVB	Phase term, related to the phase front tilt	Resulting complex amplitude E_{iY} $E_{iY} = r_{iY}.e^{j(\varphi_i)}$
	r_{iY}	φ_{1i}	φ_{2i}	$E_{iY} = r_{iY}.e^{j(\varphi_{1i}+\varphi_{2i})}$
$\vec{E}_0$	1	0	0	$1.e^{j\,(0)} = 1$
$\vec{E}_1$	$\frac{1}{\sqrt{2}}$	$\frac{1}{4}.\pi$	$\frac{\sqrt{2}}{4}.\pi$	$\frac{1}{\sqrt{2}}.e^{j\,(\frac{\pi}{4}+\frac{\sqrt{2}\pi}{4})} = \frac{1}{\sqrt{2}}.e^{j\,\frac{1+\sqrt{2}}{4}.\pi}$
$\vec{E}_2$	0	$\frac{1}{2}.\pi$	$\frac{1}{2}.\pi$	$0.e^{j\,(\frac{\pi}{2}+\frac{\pi}{2})} = 0$
$\vec{E}_3$	$-\frac{1}{\sqrt{2}}$	$\frac{3}{4}.\pi$	$\frac{\sqrt{2}}{4}.\pi$	$-\frac{1}{\sqrt{2}}.e^{j\,(\frac{3\pi}{4}+\frac{\sqrt{2}\pi}{4})} = -\frac{1}{\sqrt{2}}.e^{j\,\frac{3+\sqrt{2}}{4}.\pi}$
$\vec{E}_4$	-1	π	0	$-1.e^{j\,(\pi+0)} = 1$
$\vec{E}_5$	$-\frac{1}{\sqrt{2}}$	$\frac{5}{4}.\pi$	$-\frac{\sqrt{2}}{4}.\pi$	$-\frac{1}{\sqrt{2}}.e^{j\,(\frac{5\pi}{4}-\frac{\sqrt{2}\pi}{4})} = -\frac{1}{\sqrt{2}}e^{j\,(\frac{5-\sqrt{2}}{4}.\pi)}$
$\vec{E}_6$	0	$\frac{3}{2}.\pi$	$-\frac{1}{2}.\pi$	$0.e^{j\,(\frac{3\pi}{2}-\frac{\pi}{2})} = 0$
$\vec{E}_7$	$\frac{1}{\sqrt{2}}$	$\frac{7}{4}.\pi$	$-\frac{\sqrt{2}}{4}.\pi$	$\frac{1}{\sqrt{2}}.e^{j\,(\frac{7\pi}{4}-\frac{\sqrt{2}\pi}{4})} = \frac{1}{\sqrt{2}}.e^{j\,(\frac{7-\sqrt{2}}{4}.\pi)}$

B.2.5 Linearly polarized beam with a planar phase, focusing at Point *O*

In this case, all the phase terms φ_i are equal to zero, since there is no phase vortex or phase tilt. All the Jones vector $\vec{E}_i$ have the same coordinates. We choose: $E_{iX} = 0$ and $E_{iY} = 1$ (see Figure B3).

The coordinates of all the vectors are in Table B.11 (X coordinates) and in Table B.12 (Y coordinates).

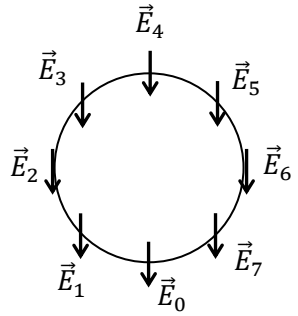

Figure B.3: Schematic showing the beam profile with the eight vectors $\vec{E}_i$ in the case of a linear polarization oriented along the Y axis.

Table B.11: Case of a linearly polarized beam with planar phase, focusing at Point ***O***: X components.

Vectors $\vec{E}_i$ (all these vectors focus at Point ***O***)	Amplitude term, related to the projection of $\vec{E}_i$ to X axis	Phase term, related to the topological charge (i.e. vortex structure) of the CVB	Phase term, related to the phase front tilt	Resulting complex amplitude $\boldsymbol{E_{iX}}$ $\boldsymbol{E_{iX}} = r_{iX}.e^{j(\varphi_i)}$
	r_{iX}	φ_{1i}	φ_{2i}	$\boldsymbol{E_{iX}} = r_{iX}.e^{j(\varphi_{1i}+\varphi_{2i})}$
$\vec{E}_0$	0	0	0	$0.e^{j\,(0)} = 0$
$\vec{E}_1$	0	0	0	$0.e^{j\,(0)} = 0$
$\vec{E}_2$	0	0	0	$0.e^{j\,(0)} = 0$
$\vec{E}_3$	0	0	0	$0.e^{j\,(0)} = 0$
$\vec{E}_4$	0	0	0	$0.e^{j\,(0)} = 0$
$\vec{E}_5$	0	0	0	$0.e^{j\,(0)} = 0$
$\vec{E}_6$	0	0	0	$0.e^{j\,(0)} = 0$
$\vec{E}_7$	0	0	0	$0.e^{j\,(0)} = 0$

Table B.12: Case of a linearly polarized beam with planar phase, focusing at Point ***O***: Y components.

Vectors $\vec{E}_i$ (all these vectors focus at Point ***O***)	Amplitude term, related to the projection of $\vec{E}_i$ to Y axis	Phase term, related to the topological charge (i.e. vortex structure) of the CVB	Phase term, related to the phase front tilt	Resulting complex amplitude E_{iY} $E_{iY} = r_{iY}.e^{j(\varphi_i)}$
	r_{iY}	φ_{1i}	φ_{2i}	$E_{iY} = r_{iY}.e^{j(\varphi_{1i}+\varphi_{2i})}$
$\vec{E}_0$	1	0	0	$1.e^{j\,(0)} = 1$
$\vec{E}_1$	1	0	0	$1.e^{j\,(0)} = 1$
$\vec{E}_2$	1	0	0	$1.e^{j\,(0)} = 1$
$\vec{E}_3$	1	0	0	$1.e^{j\,(0)} = 1$
$\vec{E}_4$	1	0	0	$1.e^{j\,(0)} = 1$
$\vec{E}_5$	1	0	0	$1.e^{j\,(0)} = 1$
$\vec{E}_6$	1	0	0	$1.e^{j\,(0)} = 1$
$\vec{E}_7$	1	0	0	$1.e^{j\,(0)} = 1$

B.2.6 Linearly polarized beam with a planar phase, focusing at Point *A*

In this case, each vector $\vec{E}_i$ has a phase terms φ_i that includes a phase tilt factor φ_{2i} as defined in Table B.1. The coordinates of each vector $\vec{E}_i$ are summarized in Table B.13 (X coordinates) and in Table B.14 (Y coordinates).

Table B.13: Case of a linearly polarized beam with planar phase, focusing at Point ***A***: X components.

Vectors $\vec{E}_i$ (all these vectors focus at Point ***A***)	Amplitude term, related to the projection of $\vec{E}_i$ to X axis	Phase term, related to the topological charge (i.e. vortex structure) of the CVB	Phase term, related to the phase front tilt	Resulting complex amplitude $\boldsymbol{E_{iX}}$ $\boldsymbol{E_{iX}} = r_{iX}.e^{j(\varphi_i)}$
	r_{iX}	φ_{1i}	φ_{2i}	$\boldsymbol{E_{iX}} = r_{iX}.e^{j(\varphi_{1i}+\varphi_{2i})}$
$\vec{E}_0$	0	0	0	$0.e^{j\,(0)} = 0$
$\vec{E}_1$	0	0	$\frac{\sqrt{2}}{4}.\pi$	$0.e^{j\,(0+\frac{\sqrt{2}}{4}.\pi)} = 0$
$\vec{E}_2$	0	0	$\frac{1}{2}.\pi$	$0.e^{j\,(0+\frac{\pi}{2})} = 0$
$\vec{E}_3$	0	0	$\frac{\sqrt{2}}{4}.\pi$	$0.e^{j\,(0+\frac{\sqrt{2}}{4}.\pi)} = 0$
$\vec{E}_4$	0	0	0	$0.e^{j\,(0)} = 0$
$\vec{E}_5$	0	0	$-\frac{\sqrt{2}}{4}.\pi$	$0.e^{j\,(0-\frac{\sqrt{2}}{4}.\pi)} = 0$
$\vec{E}_6$	0	0	$-\frac{1}{2}.\pi$	$0.e^{j\,(0-\frac{\pi}{2})} = 0$
$\vec{E}_7$	0	0	$-\frac{\sqrt{2}}{4}.\pi$	$0.e^{j\,(0-\frac{\sqrt{2}}{4}.\pi)} = 0$

Table B.14: Case of a linearly polarized beam with planar phase, focusing at Point ***A***: Y components.

Vectors $\vec{E}_i$ (all these vectors focus at Point ***A***)	Amplitude term, related to the projection of $\vec{E}_i$ to Y axis	Phase term, related to the topological charge (i.e. vortex structure) of the CVB	Phase term, related to the phase front tilt	Resulting complex amplitude E_{iY} $E_{iY} = r_{iY}.e^{j(\varphi_i)}$
	r_{iY}	φ_{1i}	φ_{2i}	$E_{iY} = r_{iY}.e^{j(\varphi_{1i}+\varphi_{2i})}$
$\vec{E}_0$	1	0	0	$1.e^{j\,(0)} = 1$
$\vec{E}_1$	1	0	$\frac{\sqrt{2}}{4}.\pi$	$1.e^{j\,(0+\frac{\sqrt{2}\pi}{4})} = e^{j\frac{\sqrt{2}\pi}{4}}$
$\vec{E}_2$	1	0	$\frac{1}{2}.\pi$	$1.e^{j\,(0+\frac{\pi}{2})} = e^{j\frac{\pi}{2}}$
$\vec{E}_3$	1	0	$\frac{\sqrt{2}}{4}.\pi$	$1.e^{j\,(0+\frac{\sqrt{2}\pi}{4})} = e^{j\frac{\sqrt{2}\pi}{4}}$
$\vec{E}_4$	1	0	0	$1.e^{j\,(0)} = 1$
$\vec{E}_5$	1	0	$-\frac{\sqrt{2}}{4}.\pi$	$1.e^{j\,(0-\frac{\sqrt{2}\pi}{4})} = e^{j\,(-\frac{\sqrt{2}\pi}{4})}$
$\vec{E}_6$	1	0	$-\frac{1}{2}.\pi$	$1.e^{j\,(0-\frac{\pi}{2})} = e^{j\,(\frac{\pi}{2})}$
$\vec{E}_7$	1	0	$-\frac{\sqrt{2}}{4}.\pi$	$1.e^{j\,(0-\frac{\sqrt{2}\pi}{4})} = e^{j\,(-\frac{\sqrt{2}\pi}{4})}$

B.3 Vectorial calculation in the Complex Plane

Here, I explain how I derive the Jones vectors at Points ***O*** and ***A*** by summing all the contributing vectors $\vec{E}_i$ geometrically in the Complex Plane.

B.3.1 Radially polarized beam with a planar phase, focusing at Point *O*

In this case, each vector coordinate E_{iX} or E_{iY} is cancelled out by that of another vector of similar amplitude and opposite direction in the Complex Plane. For example in Figure B.4, E_{1X} is cancelled out by E_{5X} , E_{2X} is cancelled out by E_{6X} and E_{3X} is cancelled out by E_{7X}. Therefore, the complex vector resulting from summing all these contributing vectors is nil. In the same way, the complex vector resulting from summing all the vector coordinates in Y is also nil. Therefore, the Jones vector produced with a radially polarized beam with a planar phase focusing at Point ***O*** is: $\binom{0}{0}$. This result implies a zero amplitude at Point ***O***.

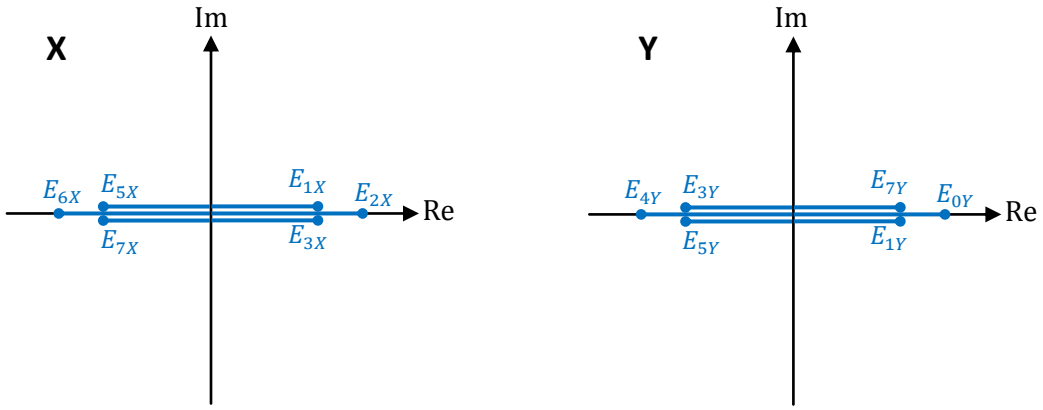

Figure B.4: Complex Planes showing the X and Y components (E_{iX} and E_{iY}) of the Jones vectors $\vec{E}_i$ at Point ***O***.

B.3.2 Radially polarized beam with a planar phase, focusing at Point *A*

In this case, the sum of all the coordinates in X is derived geometrically. As seen in Figure B.5, we can sum pairs of vectors to simplify the calculation. For example, E_{1X} and E_{5X} have real parts that cancel each other out. The sum of these two vectors is an imaginary number: $E_{1X} + E_{5X} = 2 \times \frac{1}{\sqrt{2}} \sin\left(\frac{\sqrt{2}.\pi}{4}\right).e^{j\frac{\pi}{2}}$. In the same way, $E_{3X} + E_{7X} = 2 \times \frac{1}{\sqrt{2}} \sin\left(\frac{\sqrt{2}.\pi}{4}\right).e^{j\frac{\pi}{2}}$. We also have $E_{2X} + E_{6X} = 2 \times e^{j\frac{\pi}{2}}$. So overall, we have:

$$\sum_{i=0}^{i=7} E_{iX} = 2 \times \frac{1}{\sqrt{2}} \sin\left(\frac{\sqrt{2}.\pi}{4}\right).e^{j\frac{\pi}{2}} + 2 \times e^{j\frac{\pi}{2}} + 2 \times \frac{1}{\sqrt{2}} \sin\left(\frac{\sqrt{2}.\pi}{4}\right).e^{j\frac{\pi}{2}} \approx 4.53 \times e^{j\frac{\pi}{2}} \quad \text{(B.15)}$$

If we normalize this result, we have:

$$\frac{1}{8}\sum_{i=0}^{i=7} E_{iX} \approx 0.57 \times e^{j\frac{\pi}{2}} \quad \text{(B.16)}$$

When the sum of all the coordinates in Y is derived geometrically in the Complex Plane, it is found that each vector coordinate E_{iY} is cancelled out by that of another vector of similar amplitude and opposite direction. For example in Figure B.5, E_{0Y} is cancelled out by E_{4Y}, E_{1Y} is cancelled out by E_{3Y}

and E_{5X} is cancelled out by E_{7X} . The complex vector resulting from summing all the vector coordinates in Y is nil. Therefore, the Jones vector produced with a radially polarized beam with a planar phase focusing at Point ***A*** is: $0.57e^{j(\frac{\pi}{2})} \times \binom{1}{0}$. It is noted that this Jones vector defines a linear polarization oriented along the X axis.

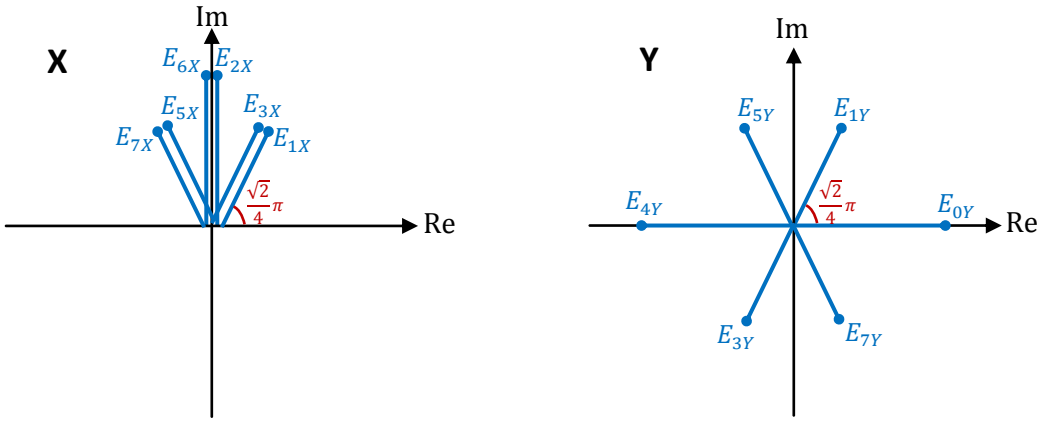

Figure B.5: Complex Planes showing the X and Y components (E_{iX} and E_{iY}) of the Jones vectors $\vec{E}_i$ at Point ***A***.

B.3.3 Radially polarized beam with a vortex phase, focusing at Point *O*

We now derive the sum of all the contributing vectors in the case of a radially polarized beam with a vortex phase focusing at Point ***O***. First, the sum of all the coordinates in X is derived geometrically. As seen in Figure B.6, we can sum pairs of vectors to simplify the calculation. For example, E_{1X} and E_{3X} have real parts that cancel each other out. The sum of these two vectors is an imaginary number: $E_{1X} + E_{3X} = 2 \times \frac{1}{\sqrt{2}} \sin\left(\frac{\pi}{4}\right) . e^{j\frac{\pi}{2}}$. In the same way, $E_{5X} + E_{7X} = 2 \times \frac{1}{\sqrt{2}} \sin\left(\frac{\pi}{4}\right) . e^{j\frac{\pi}{2}}$. We also have $E_{2X} + E_{6X} = 2 \times e^{j\frac{\pi}{2}}$. So overall, we have:

$$\sum_{i=0}^{i=7} E_{iX} = 2 \times \frac{1}{\sqrt{2}} \sin\left(\frac{\pi}{4}\right) . e^{j\frac{\pi}{2}} + 2 \times e^{j\frac{\pi}{2}} + 2 \times \frac{1}{\sqrt{2}} \sin\left(\frac{\pi}{4}\right) . e^{j\frac{\pi}{2}} = 4 \times e^{j\frac{\pi}{2}} \quad \text{(B.17)}$$

If we normalize this result, we have:

$$\frac{1}{8} \sum_{i=0}^{i=7} E_{iX} = 0.5 \times e^{j\frac{\pi}{2}} \quad \text{(B.18)}$$

We also derive the sum of all the coordinates in Y. As seen in Figure B.6, we can sum pairs of vectors to simplify the calculation. For example, E_{1Y} and E_{3Y} have imaginary parts that cancel each other out. The sum of these two vectors is a real number: $E_{1Y} + E_{3Y} = 2 \times \frac{1}{\sqrt{2}} \cos\left(\frac{\pi}{4}\right)$. In the same way, $E_{5Y} + E_{7Y} = 2 \times \frac{1}{\sqrt{2}} \cos\left(\frac{\pi}{4}\right)$. We also have $E_{0Y} + E_{4Y} = 2$. So overall, we have:

$$\sum_{i=0}^{i=7} E_{iY} = 2 \times \frac{1}{\sqrt{2}} \cos\left(\frac{\pi}{4}\right) + 2 + 2 \times \frac{1}{\sqrt{2}} \cos\left(\frac{\pi}{4}\right) = 4 \quad \text{(B.19)}$$

If we normalize this result, we have:

$$\frac{1}{8} \sum_{i=0}^{i=7} E_{iY} = 0.5 \quad \text{(B.20)}$$

Therefore, the Jones vector produced with a radially polarized beam with a vortex phase focusing at Point ***O*** is: $0.5\times\begin{pmatrix} e^{j(\frac{\pi}{2})} \\ 1 \end{pmatrix}$. It is noted that this Jones vector defines a circular polarization.

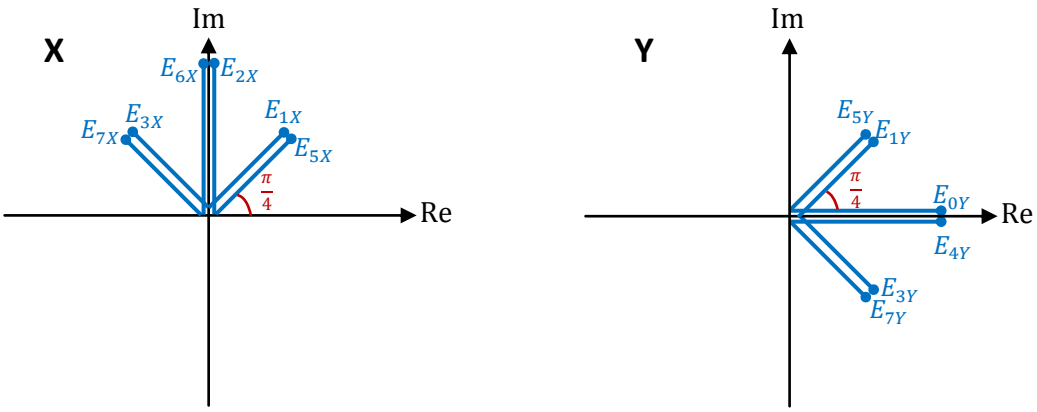

Figure B.6: Complex Planes showing the X and Y components (E_{iX} and E_{iY}) of the Jones vectors $\vec{E}_i$ at Point ***O***.

B.3.4 Radially polarized beam with a vortex phase, focusing at Point *A*

We now derive the sum of all the contributing vectors in the case of a radially polarized beam with a vortex phase focusing at Point ***A***. First, the sum of all the coordinates in X is derived geometrically. As seen in Figure B.7, we can sum pairs of vectors to simplify the calculation. For example, E_{1X} and E_{7X} have real parts that cancel each other out. The sum of these two vectors is an imaginary number: $E_{1X}+E_{7X}=2\times\frac{1}{\sqrt{2}}\sin\left(\frac{\sqrt{2}.\pi}{4}\right).e^{j\frac{\pi}{2}}$. In the same way, $E_{3X}+E_{5X}=-2\times\frac{1}{\sqrt{2}}\sin\left(\frac{5\pi}{4}-\frac{\sqrt{2}\pi}{4}\right).e^{j\frac{\pi}{2}}$. We also have $E_{2X}+E_{6X}=0$. So overall, we have:

$$\sum_{i=0}^{i=7}E_{iX}=2\times\frac{1}{\sqrt{2}}\sin\left(\frac{\sqrt{2}.\pi}{4}\right).e^{j\frac{\pi}{2}}-2\times\frac{1}{\sqrt{2}}\sin\left(\frac{5\pi}{4}-\frac{\sqrt{2}\pi}{4}\right).e^{j\frac{\pi}{2}}\approx 0.8\times e^{j\frac{\pi}{2}} \quad \text{(B.21)}$$

If we normalize this result, we have:

$$\frac{1}{8}\sum_{i=0}^{i=7}E_{iX}\approx 0.1\times e^{j\frac{\pi}{2}} \quad \text{(B.22)}$$

We also derive the sum of all the coordinates in Y. As seen in Figure B.7, we can sum pairs of vectors to simplify the calculation. For example, E_{1Y} and E_{7Y} have imaginary parts that cancel each other out. The sum of these two vectors is a real number: $E_{1Y}+E_{7Y}=2\times\frac{1}{\sqrt{2}}\cos\left(\frac{\pi}{4}+\frac{\sqrt{2}\pi}{4}\right)$. In the same way, $E_{3Y}+E_{5Y}=-2\times\frac{1}{\sqrt{2}}\cos\left(\frac{3\pi}{4}+\frac{\sqrt{2}\pi}{4}\right)$. We also have $E_{0Y}+E_{4Y}=2$. So overall, we have:

$$\sum_{i=0}^{i=7}E_{iY}=2\times\frac{1}{\sqrt{2}}\cos\left(\frac{\pi}{4}+\frac{\sqrt{2}\pi}{4}\right)-2\times\frac{1}{\sqrt{2}}\cos\left(\frac{3\pi}{4}+\frac{\sqrt{2}\pi}{4}\right)+2\approx 2.9 \quad \text{(B.23)}$$

If we normalize this result, we have:

$$\frac{1}{8}\sum_{i=0}^{i=7}E_{iY}\approx 0.4 \quad \text{(B.24)}$$

Therefore, the Jones vector produced with a radially polarized beam with a vortex phase focusing at Point ***A*** is: $\begin{pmatrix} 0.1\times e^{j(\frac{\pi}{2})} \\ 0.4 \end{pmatrix}$. This Jones vector defines an elliptical polarization with a strong elongation along the Y axis. The axial ratio is 0.25

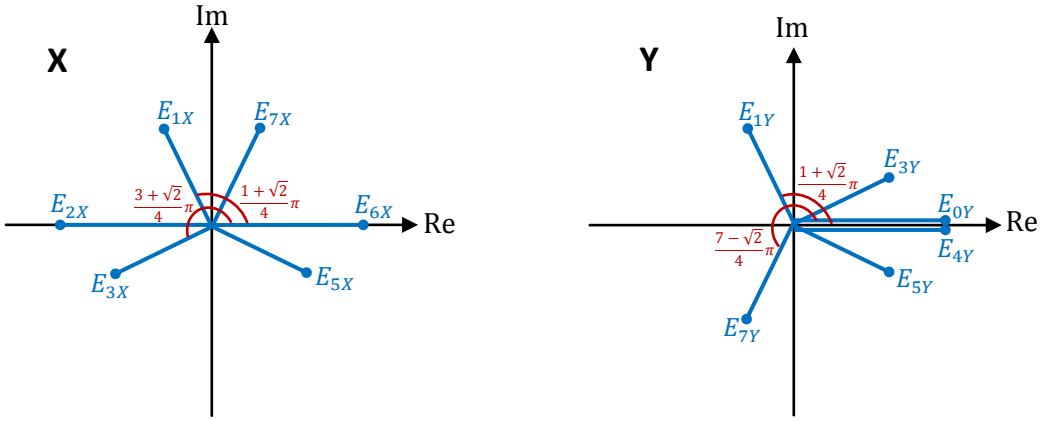

Figure B.7: Complex Planes showing the X and Y components (E_{iX} and E_{iY}) of the Jones vectors $\vec{E}_i$ at Point ***A***.

B.3.5 Linearly polarized beam with a planar phase, focusing at Point *O*

In this case, all the vectors $\vec{E}_i$ have the same coordinates. In the example shown in Figure B.3, the coordinates in X of all the vectors are nil and the coordinates in Y are all equal to one. This is shown in Figure B.8. As a result, the normalized Jones vector produced at Point ***O*** is: $\binom{0}{1}$. As expected, this represents a linear polarization oriented along the Y axis.

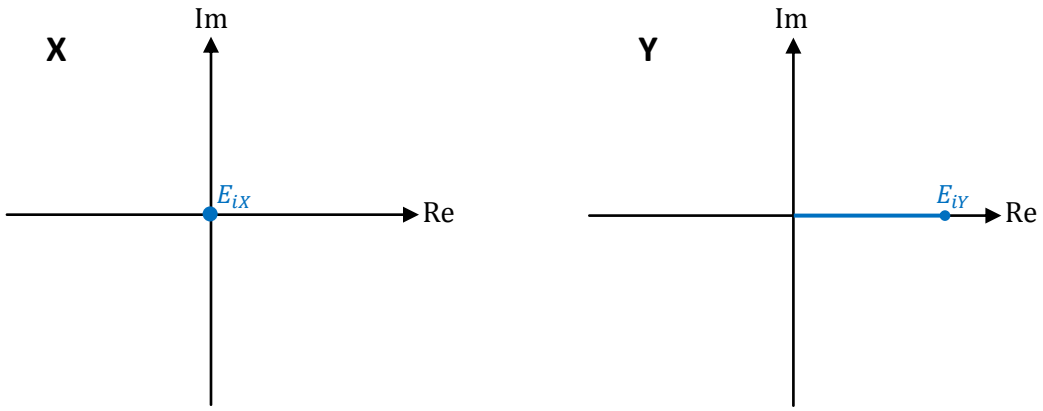

Figure B.8: Complex Planes showing the X and Y components (E_{iX} and E_{iY}) of the Jones vectors $\vec{E}_i$ at Point ***O***.

B.3.6 Linearly polarized beam with a planar phase, focusing at Point *A*

As before, the sum of the coordinates in X and Y is derived geometrically (see Figure B.9).

$$\frac{1}{8}\sum_{i=0}^{i=7} E_{iX} = 0 \quad \text{(B.25)}$$

$$\frac{1}{8}\sum_{i=0}^{i=7} E_{iY} = \frac{1}{8}\left(4 \times \cos\left(\frac{\sqrt{2}\pi}{4}\right) + 2\right) \approx 0.47 \quad \text{(B.26)}$$

The Jones vector at Point ***A*** is: $0.47 \times \binom{0}{1}$. This Jones vector defines a linear polarization oriented along the Y axis.

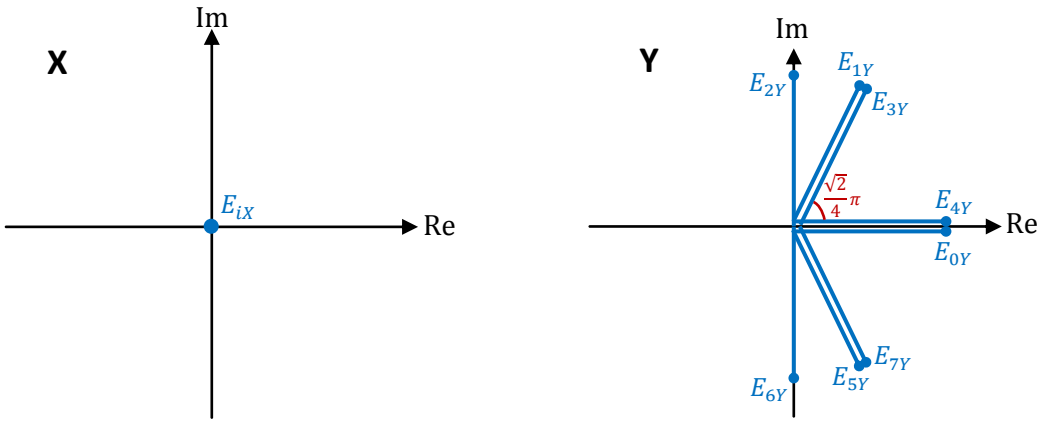

Figure B.9: Complex Planes showing the X and Y components (E_{iX} and E_{iY}) of the Jones vectors $\vec{E}_i$ at Point ***A***.

B.3.7 Irradiance at focal plane, produced with a linearly polarized beam with a planar phase

I first derive the irradiance at Point ***O***. As detailed in Chapter 5, the irradiance, noted I, is obtained from the Jones vector coordinates (E_X ; E_Y): $I = {E_X}^2 + {E_Y}^2$. At Point ***O***, I have $E_X = 0$ and $E_Y = 1$ (see results in Section B.3.5). Hence the irradiance at Point ***O*** is: $I_O = 1$.

At Point ***A***, I have $E_X = 0$ and $E_Y = 0.47$ (see results in Section B.3.6). Hence the irradiance at Point ***A*** is: $I_A = 0.47^2 = 0.22$. The ratio I_O/I_A is 4.5 .

Appendix C
Abbreviations, acronyms and definitions

C.1 Abbreviations and acronyms

This thesis contains the following abbreviations and acronyms:

CVB	Cylindrical Vector Beam
CW laser	Continuous Wave laser
DPSS laser	Diode-Pumped Solid State laser
FLC	Ferroelectric Liquid-crystal
ITO	Indium Tin Oxide
LCOS	Liquid-Crystal On Silicon
LIPSS	Laser Induced Periodic Surface Structures
NA	Numerical Aperture
Nd:YAG laser	Neodymium-doped Yttrium Aluminum Granet laser
OAM	Orbital Angular Momentum
PMMA	Poly(Methyl Methacrylate)
SLM	Spatial Light Modulator
Ti:Sapphire laser	Titanium-doped Sapphire laser

C.2 Definitions

4F correlator	A 4F correlator, or 4F telescope, is a system of two identical lenses separated by a distance equal to twice the focal length
Acousto-optic modulator	An acousto-optic modulator uses acousto-optic effects to diffract and shift the frequency of an incident light beam. It generally uses a piezoelectric transducer attached to a glass or quartz substrate. The piezoelectric transducer induces a periodic change in the index of refraction of the glass or quartz substrate. As a result, the incident light beam is diffracted into several orders
Anisometry	Anisometry is a geometrical property used to describe the shape of objects such as molecules. An anisometric molecule for example, is a molecule with strongly elongated along one direction (i.e. a rod-like molecule) or two directions (i.e. a disc-like molecule)

Anisotropy	Anisotropy is the property of being directionally dependent (as opposed to isotropy, which implies identical properties in all directions)
Axial ratio	The axial ratio of an ellipse is the ratio of its short axis over its long axis.
Birefringence	Birefringence is the optical property of materials having a refractive index that depends on the polarization and propagation direction of light
Continuous wave laser	A continuous wave laser is a laser whose beam has a constant power output (i.e. not a pulsed laser). It is sometimes referred to as CW laser
Diffraction efficiency	In this thesis, the diffraction efficiency is defined as the power ratio of a first-order beam over the full beam power
Ferroelectricity	Ferroelectricity is a property of certain materials which have a spontaneous electric polarization that can be reversed by the application of an external electric field
Fluence	Energy density (J/cm2)
Gaussian function	A Gaussian function has a characteristic symmetric bell shaped curve defined by f(x)=exp(-a.x). A number of physical phenomenons follow a distribution characterized by a Gaussian function
Gaussian laser beam	A Gaussian laser beam has a beam profile whose intensity distribution follows a Gaussian function: f(x)=exp(-a.x)
Longitudinal mode	A longitudinal mode of a resonant cavity is a particular standing wave confined in the cavity. The longitudinal modes correspond to the wavelengths of the wave which interfere constructively after many reflections from the reflecting surfaces of the cavity. Longitudinal modes are also sometimes referred to as electromagnetic field modes
Nematic liquid-crystal	A nematic liquid-crystal is a type of liquid-crystal whit elongated, rod-shaped organic molecules which self-align to have a long-range directional order with their long axes roughly parallel
Orbital angular momentum	The orbital angular momentum of a light beam is the component of angular momentum that is dependent on the field spatial distribution (i.e. dependent on the phase of light and not its polarization)
Saturable absorption	Saturable absorption is a property of materials where the absorption of light decreases with increasing light intensity
Spatial filter	A spatial filter is an optical device used to remove aberrations in a laser beam due to imperfect, dirty or damaged optics. Typically it consists of a pinhole (i.e. a screen with a small hole) placed at the Fourier plane of a telescope
Topological charge	The topological charge of a light beam is a property of its orbital angular momentum. It describes the amplitude of orbital angular momentum. It can be compared with the pitch of a screw thread

Appendix D
Symbols

The following constants, variables and units have been used throughout this thesis (see also G. Woan, 2000):

D.1 Constants, units and notations

Symbol	Description	Units
α	Incidence angle	deg
A	Cross-sectional area	mm²
D	Laser beam diameter	mm
e	Euler's number [~2.718]	
E	Laser pulse energy	J
$\vec{\boldsymbol{E}}$, $\vec{\boldsymbol{H}}$	Electric / magnetic field vector	
$\left\|\vec{E}\right\|$, E	Electric field amplitude	N/C
$\boldsymbol{Ei}$, $\boldsymbol{Er}$	Electric field amplitude of incident and reflected light	N/C
f	Focal length	mm
F	Fluence	J/cm²
H	Hole depth / cutting thickness	mm
I	Irradiance	W/cm²
j	Unit imaginary (complex) number	
k	Extinction coefficient	
$\vec{\boldsymbol{k}}$	Wave vector	
L	Side-length of beam scanning path	mm
λ	Wavelength of light	nm
M^2	Laser beam quality factor	
n	Index of refraction	
Δν	Gain bandwidth	THz
P	Average power	W
$\boldsymbol{PP}$	Polarization purity	%
π	Pi [~3.142]	
$\boldsymbol{q}$	Amplitude ratios of the reflected to incident electric fields	
$\boldsymbol{R}$	Reflectivity of light	
Ra	Surface roughness average	µm

T	Wave period	s
τ	Temporal pulse-length	s
θ	Polar angle	rad
ω_0	Radius at beam waist	mm
$\boldsymbol{O}, \boldsymbol{A}, \boldsymbol{E}'$	Geometrical points	
$\bar{V}$, $\overline{\boldsymbol{AB}}$	Geometrical distances	
$\vec{\boldsymbol{X}}$, $\vec{\boldsymbol{Y}}$	Unit vectors along the x and y axes of a Cartesian coordinate system	

D.2 Variables

Symbol	Description
$\vec{\boldsymbol{E}}$, $\boldsymbol{J}$	Electric field vector / Jones vector representing the electric field
i	Index number
$\boldsymbol{P}$, $\boldsymbol{Q}$, $\boldsymbol{T}$	Jones matrices
$\boldsymbol{R}$	Rotation matrix
Re, Im	Real and imaginary parts of a complex number, expressed in Cartesian coordinates
r, φ	Amplitude and phase of a complex number, expressed in polar coordinates
Φ, Δ_φ	Relative phase delay

References

Abate J. A., Lund L., Brown D., Jacobs S., Refermat S., Kelly J., Gavin M., Waldbilling J., Lewis O., 1981, *Active mirror: a large-aperture medium-repetition rate Nd:glass amplifier*, Appl. Optics **20** (2): 351-361

Banks P. S., Feit M. D., Rubenchik A. M., Stuart B. C., Perry M. D., 1999, *Material effects in ultra-short pulse laser drilling of metals*, Appl. Phys. A **69**: S377-S380

Basov N. G., Danilychev V. A., Popov Yu. M., 1970, Zh. Eksp. Fiz. i Tekh. Pis'ma. Red. **12**: 473

Beresna M., 2011, *Polarization sensitive elements fabricated by femtosecond laser nanostructuring of glass*, Opt. Materials Express **1** (4): 783-795

Beversluis M. R., Novotny L., Stranick S. J., 2006, *Programmable vector point-spread function engineering*, Opt. Express **14** (7): 2650-2656

Breitling D., Ruf A., Dausinger F., 2004a, *Fundamental aspects in machining of metals with short and ultrashort laser pulses*, Proc. SPIE **5339**: 49-63

Breitling D., Fohl C., Dausinger F., Kononenko T., Konov V., 2004b, *drilling of metals*, Femtosecond Technology for Technical and Medical Applications, Topics Appl. Phys. **96**: 131-156, published by Springer-Verlag Berlin, Heidelberg, Germany

Cavalieri A., 2010, *Beyond ultrafast*, Physics World **23** (5): 47-51

Cheng J., 2010, *Ultrafast Picosecond Laser Micromachining of Metallic Materials*, Ph.D. thesis, University of Liverpool, UK

Crafer R., Oakley P. J., 1993, *Laser Processing in Manufacturing* published by Chapman & Hall, London, UK

Curran A., Lee M. P., Padgett M. J., Cooper J. M., Leonardo R. Di., 2012, *Partial Synchronization of Stochastic Oscillators through Hydrodynamic Coupling*, Phys. Rev. Lett. **108**: 240601

Dausinger F., Shen J., 1993, *Energy Coupling Efficiency in Laser Surface Treatment*, ISIJ International **33** (9): 925-933

Dausinger F., 2003, *Femtosecond technology for precision manufacturing: Fundamental and technical aspects*, RIKEN Review **50**, Focused on Laser Precision Microfabrication (LPM 2002): 77-82

De Genne P., 1976, *The Physics of Liquid Crystals* published by Oxford University Press, Oxford, UK

Eichstadt J., Romer G. R. B. E., Huis in't Veld A. J., 2011, *Towards Friction Control using Laser-induced Periodic Surface Structures*, Physics Procedia **12**: 7-15

Föhl C., Dausinger F., 2003, *High precision deep drilling with ultrashort pulses*, Proc. SPIE **5063**: 346-351

Föhl C., Breitling D., Dausinger F., 2003, *Precise drilling of steel with ultrashort pulsed solid-state lasers*, Proc. SPIE **5121**: 271–279

Föhl C., Dausinger F., 2006, *High precision laser drilling with ultra short pulses - fundamental aspects and technical applications*, Proc. PICALO **2**: 281-286

Fu Y. H., Ho F. H., Lin W. C., Liu W. C., Tsai D. P., 2003, *Study of the focused laser spots generated by various polarized laser beam conditions*, Journal of Microscopy **210** (3): 225-228

Fuhr P. L., 1984, *Direct-current polarization characteristics of various AlGaAs laser diodes*, Opt. Lett. **9** (10): 438-440

Garanin S. G., Manachinsky A. N., Starikov F. A., Khokhlov S. V., 2012, *Phase Correction of Laser Radiation with the Use of Adaptive Optical Systems at the Russian Federal Nuclear Center - Institute of Experimental Physics*, Optoelectronics, Instrumentation and Data Processing **48** (2): 134-140

Geusic J. E., Marcos H. M., Van Uitert L. G., 1964, *Laser oscillations in nd-doped yttrium aluminum, yttrium gallium and gadolinium garnets*, Appl. Phys. Lett. **4** (10): 182-184

Gray G. W., Harrison K. J., Nash J. A., 1973, *New family of nematic liquid crystals for displays*, Electron. Lett. **9** (6): 130-131

Guosheng Z., Fauchet P. M., Siegman A. E., 1982, *Growth of spontaneous periodic surface structures on solids during laser illumination*, Phys. Rev. B **26** (10): 5366-5381

Hahne S., Johnston B. F., Withford M. J., 2007, *Pulse-to-pulse polarization-switching method for high-repetition-rate lasers*, Appl. Opt. **46** (6): 954-958

Hall R. N., Fenner G. E., Kingsley J. D., Soltys T. J., Carlson R. O., 1962, *Coherent light emission from GaAs junctions*, Phys. Rev. Lett. **9** (9): 366-368

Hecht J., 2010, *The bubble legacy*, Physics World **23** (5): 36-40

Hendow S. T., Shakir S. A., 2010, *Structuring materials with nanosecond laser pulses*, Opt. Express **18** (10): 10188-10199

Hnatovsky C., Shvedov V., Krolikowski W., Rode A., 2011, *Revealing Local Field Structure of Focused Ultrashort Pulses*, Phys. Rev. Lett. **106**: 123901

Iglesias I., Vohnsen B., 2007, *Polarization structuring for focal volume shaping in high-resolution microscopy*, Opt. Commun. **271**: 40-47

Jain K., Willson C. G., Lin B. J., 1982, *Ultrafast deep-UV lithography with excimer lasers*, IEEE Electron. Device Let. **3** (3): 53-55

Kang H., Jia B., Gu M., 2010, *Polarization characterization in the focal volume of high numerical aperture objectives*, Opt. Express **18** (10): 10813-10821

Klug U., Dusing J. F., Sato T., Washio K., Kling R., 2010, *Polarization converted laser beams for micromachining applications*, Proc. of SPIE **7590**: 759006-1

Kraus M., Abdou-Ahmed M., Michalowski A., Voss A., Weber R., Graf T., 2010, *Microdrilling in steel using ultrashort pulsed laser beams with radial and azimuthal polarization*, Opt. Express **18** (21): 22305-22313

Kuang Z., Liu D., Perrie W., Edwardson S., Sharp M., Fearon E., Dearden G., Watkins K., 2009a, *Fast parallel diffractive multi-beam femtosecond laser surface micro-structuring*, Appl. Surf. Sci. **255**, 13-14: 6582-6588

Kuang Z., Perrie W., Liu D., Edwardson S., Cheng J., Dearden G., Watkins K., 2009b, *Diffractive multi-beam surface micro-processing using 10 ps laser pulses*, Appl. Surf. Sci. **255** (22): 9040-9044

Le Harzic R., Dorr D., Sauer D., Neumeier M., Epple M., Zimmermann H., Stracke F., 2011, *Large-area, uniform, high-spatial-frequency ripples generated on silicon using a nanojoule-femtosecond laser at high repetition rate*, Opt. Lett. **36** (2): 229-231

Lekner J., 2003, *Polarization of tightly focused laser beams*, J. Opt. A: Pure Appl. Opt. **5**: 6-14

Liu D., Kuang Z., Perrie W., Scully P. J., Baum A., Edwardson S. P., Fearon E., Dearden G., Watkins K. G., 2010, *High-speed uniform parallel 3D refractive index micro-structuring of poly(methyl methacrylate) for volume phase gratings*, Appl. Phys. B: Laser Optic **101** (4): 817-823

Machavariani G., Lumer Y., Moshe I., Jackel S., 2007, *Effect of the spiral phase element on the radial-polarization (0, 1)* LG beam*, Opt. Commun. **271**: 190-196

Mannion P., Magee J., Coyne E., O'Connor G. M., 2003, *Ablation thresholds in ultrafast laser micro-machining of common metals in air*, Proc. SPIE **4876**: 470-478

Marrucci L., Karimi E., Slussarenko S., Piccirillo B., Santamato E., Nagali E., Sciarrino F., 2011, *Spin-to-orbital conversion of the angular momentum of light and its classical and quantum applications*, J. Opt. **13** (6): 064001

Meier M., Romano V., Feurer T., 2007, *Material processing with pulsed radially and azimuthally polarized laser radiation*, Appl. Phys. A **86**: 329-334

Mellor L., 2011, *Periodic Structuring of Metallic Surfaces Using Picosecond Laser System*, Ph.D. thesis, University of Liverpool, UK

Moser T., Balmer J., Delbeke D., Muys P., Verstuyft S., Baets R., 2006, *Intracavity generation of radially polarized CO2 laser beams based on a simple binary dielectric diffraction grating*, Appl. Opt. **45** (33): 8517-8522

Moulton P. F., 1986, *Spectroscopic and laser characteristics of Ti:Al2O3*, J. Opt. Soc. Am. B **3** (1): 125-133

Nathan M. I., Dumke W. P., Burns G., Dill F. H., Lasher G., 1962, *Stimulated emission of radiation from GaAs p-n junctions*, Appl. Phys. Lett. **1** (3): 62-64

Nee S. F., 2000, *Polarization Measurement* published by CRC Press LLC, USA

Niziev V. G., Nesterov A. V., 1999, *Influence of Beam Polarization on Laser Cutting Efficiency*, J. Phys. D: Appl. Phys. **32**: 1455-1461

Nolte S., Momma C., Kamlage G., Ostendorf A., Fallnich C., Alvensleben F., Welling H., 1999, *Polarization effects in ultrashort-pulse laser drilling*, Appl. Phys. A **68**: 563-567

O'Shea D. C., 1985, *Elements of Modern Optical Design* published by J. Wiley & Sons, Inc., New York, USA

Ouyang J., 2011, *Control of Polarization in Laser Materials Processing*, Masters thesis, University of Liverpool, UK

Patel C. K. N., 1964, *Continuous-Wave Laser Action on Vibrational-Rotational Transitions of CO2*, Phys. Rev. **136** (5A): A1187-A1193

Pedrotti F. L. , Pedrotti L. S., 1993, *Introduction to Optics* published by Prentice-Hall, Inc., New Jersey, USA

Perez J. P., 1996, *Optique* published by Masson S.A., Paris, France

Perkowitz S., 2010, *From ray-gun to Blu-ray*, Physics World **23** (5): 16-20

Riley K. F., Hobson M. P., Bence S. J., 2002, *Mathematical Methods for Physics and Engineering* published by Cambridge University Press, Cambridge, UK

Rizvi N. H., 2003, *Femtosecond laser micromachining: Current status and applications*, RIKEN Review **50**, Focused on Laser Precision Microfabrication (LPM 2002): 107-112

Sakamoto M., Endriz J. G., Scifres D. R., 1992, *20W CW monolithic AlGaAs (810 nm) laser diode arrays*, Electron. Lett. **28**: 197-199

Schlup P., Masihzadeh O., Xu L., Trebino R., Bartels R. A., 2008, *Tomographic retrieval of the polarization state of an ultrafast laser pulse*, Opt. Lett. **33** (3): 267-269

Stalder M., Schadt M., 1996, *Linearly polarized light with axial symmetry generated by liquid-crystal polarization converters*, Opt. Lett. **21** (23): 1948-1950

Steen W. M., 1998, *Laser Material Processing* published by Springer-Verlag London Limited, London, UK

Tönshoff H. K., Momma C., Ostendorf A., Nolte S., Kamlage G., 2000, *Microdrilling of metals with ultrashort laser pulses*, J. Laser Applications **12** (1): 23-27

Venkatakrishnan K., Tan B., 2006, *Interconnect microvia drilling with a radially polarized laser beam*, J. Micromech. Microeng. **16**: 2603-2607

Weber R., Michalowski A., Abdou-Ahmed M., Onuseit V., Rominger V., Kraus M., Graf T., 2011, *Effects of Radial and Tangential Polarization in Laser Material Processing*, Physics Procedia **12**: 21-30

Woan G., 2000, *The Cambridge handbook of physics formulas* published by Cambridge university press, New York, USA

Wu G., Lou Q., Zhou J., Dong J., Wei Y., 2007, *Focal shift in focused radially polarized ultrashort pulsed laser beams*, Appl. Opt. **46** (25): 6251-6255

Yariv A., Yeh P., 1984, *Optical waves in crystal* published by J. Wiley & Sons, Inc., New York, USA

Yew E. Y. S., Sheppard C. J. R., 2007, *Second harmonic generation polarization microscopy with tightly focused linearly and radially polarized beams*, Opt. Commun. **275**: 453-457

Yoshiki K., Hashimoto M., Araki T., 2005, Three dimensional polarization control and its applications to SHG imaging, Proc. CLEO **2005**, 1569537: 655-656

Zhan Q., Leger J. R., 2002, *Focus shaping using cylindrical vector beams*, Opt. Express **10** (7): 324-331

Zhan Q., 2009, *Cylindrical vector beams: from mathematical concepts to applications*, Advances in Optics and Photonics **1**: 1-57